An Experimental Study of Mantle Convection

A Thesis

Submitted for the Degree of

MASTER OF SCIENCE (ENGINEERING)

by

VIVEK N. PRAKASH

ENGINEERING MECHANICS UNIT
JAWAHARLAL NEHRU CENTRE FOR ADVANCED
SCIENTIFIC RESEARCH
(A Deemed University)
Bangalore – 560 064

OCTOBER 2009

DECLARATION

I hereby declare that the matter embodied in the thesis entitled "**An Experimental Study of Mantle Convection**" is the result of investigations carried out by me at the Engineering Mechanics Unit, Jawaharlal Nehru Centre for Advanced Scientific Research, Bangalore, India under the supervision of Prof. K. R. Sreenivas and that it has not been submitted elsewhere for the award of any degree or diploma.

In keeping with the general practice in reporting scientific observations, due acknowledgement has been made whenever the work described is based on the findings of other investigators.

_____

Vivek N. Prakash

CERTIFICATE

I hereby certify that the matter embodied in this thesis entitled "**An Experimental Study of Mantle Convection**" has been carried out by Mr. Vivek N. Prakash at the Engineering Mechanics Unit, Jawaharlal Nehru Centre for Advanced Scientific Research, Bangalore, India under my supervision and that it has not been submitted elsewhere for the award of any degree or diploma.

_____

Prof. K. R. Sreenivas

(Research Supervisor)

To

my family

Acknowledgements

I am deeply indebted to my supervisor Prof. K.R. Sreenivas who has been the backbone of my education and career in research. I had a wonderful experience working with him and gained many valuable lessons from him. He has always been there for me when I needed him the most. If it were not for his support during difficult times, I would not be writing this thesis today.

Prof. Jaywant H. Arakeri has played a very important role in shaping the way my research has progressed. Discussions with him have been very fruitful and have thought me how to think better. I have learnt a lot from my advisors and working with them has been a privilege.

The culmination of this thesis is the result of my work at jnc for the past four years, the first two when I was a summer student and the last two during my masters. My stint at jnc has changed me for the better. I have had many experiences at jnc that have left a deep impression on me.

Prof. R. Narasimha has been and will always be a source of inspiration. I thank Prof. Rama Govindarajan for her constant encouragement during my stay at jnc. I also thank Prof. Meheboob Alam for his advice and support.

I thank Manikandan, Shreyas, Mukund, Mallappa and Rajapandiyan who helped me in the lab when I was a summer student. During my masters, I had very close friends at jnc who really cared for me and did everything possible to cheer me up when I was in agony, this included Aditya, Rakshith and Rahul. Aditya, was my roommate for two years and is one of my best friends. Rakshith understood my problems better than anyone else and helped me face them. In the end, he took the pains to print and submit my thesis. Rahul always gave objective and healthy criticism. We had a very nice time together and I will miss them. Mukund was the counselor for my day to day problems. Lengthy discussions with Mukund have given me insights into many new things, both academic and non-academic. Towards the end, he helped me with the thesis and analysis. The ‘upstairs gang’ consisting of Harish, Anubhab, Ratul, Sumesh, Vishwanath, Dabade, Gayathri, Ponnu, Ashish and Saurabh have been very good friends. I thank Harish for helping me write the Matlab code. Harish and Anubhab opened my eyes to consider Europe as an option for further studies. Devranjan and Vishwanath provided good company in the lab and outside. Dinesh and Dhiraj have been helpful labmates. The summers provided a valuable but tiring experience of advising the summer students. But the summer students were fun and in particular I spent good times with Subrahmanyam and Veera. I also thank my other good friends at jnc, Sonia, Avinash, Ronak, Arti, Shruti and Abhishek for a wonderful time.

I acknowledge Prof. G. U. Kulkarni and Radha for the mesh measurements and Prof. V. Kumaran and Madhusudan from IISc for viscosity measurements.

Finally, I thank my parents, sister, uncle and aunt for their unconditional love, support and encouragement.

CONTENTS

Synopsis

Mantle convection in the earth is an important process by which heat is transported from the core to the surface. Mantle convection is responsible for geophysical phenomena like volcanism, plate tectonics and orography. Hot plumes detach from the thermal boundary layer on the core and rise through a viscous ambient mantle. The mantle has a complicated rheology and chemical composition and plume dynamics in these conditions is not well understood. Convection in the mantle corresponds to a regime of high Rayleigh number (Ra) in the limit of high Prandtl number (Pr). In this thesis, we report on the findings from laboratory experiments conducted to study convection in this regime of high Rayleigh and Prandtl numbers. We focus on the role of viscosity contrast between the plume fluid and the surrounding fluid on the structure and dynamics of plumes.

The experiments have been conducted in a square cross-section tank that is divided into two chambers by a permeable mesh. The convection is driven by concentration differences across the mesh using sugar solution in the upper chamber and water in the bottom chamber of the tank. We use an external setup that delivers water to the bottom chamber from below at a constant flow rate using gravity feed at a constant head. We employ the Planar-Laser-Induced-Fluorescence (PLIF) technique to visualize and photograph the plume structures above the mesh in the near wall planform, side section views and in 3D.

We study the effect of viscosity ratio (U) on the plume structure. Na-CarboxyMethylCellulose(CMC) has been used to enhance the viscosity of the fluid. CMC solutions have been used in the upper chamber of the tank to study convection regimes where $U>1$ and in the bottom chamber of the tank for the $U<1$ regime. The viscosity enhancement increases the Schmidt numbers (Sc) (which is a proxy for the Prandtl number) and makes the parameter regime in our experiment comparable to mantle convection. We have studied regimes ranging from $U = 0.003$ to 2500, $Ra = 10^8$ to 10^{11} and $Sc = 10^3$ to 10^6 with a constant buoyancy flux. We have also studied the effect of varying buoyancy flux on the plume structure.

The planform (top view) plume structures near-wall (just above) on the mesh exhibit a well known dendritic structure at $U = 1$. We have found that the planform plume structures change

their morphology from line plumes to discrete circular blob structures as U is increased (U >> 1). Also, the average plume spacings and plume thicknesses increase with U >> 1. When U << 1, the formation of cellular patterns is favored. The sizes of the cells are largest at lowest U (0.003) and decrease with increase in U till U =1. We quantify this over a set of experiments by using image processing techniques in Matlab. An autocorrelation based code has been developed which gives information on distribution of plume spacings and plume thickness.

In the vertical section, as U is increased, we observe changes in the plume structure: The plume size increases and the shape of line plume with a mushroom-like head structure changes to a spherical blob. As U is increased, theplumes retain their identity for longer distance and rise to the surface due to reduced mixing with the ambient viscous fluid. At high U, low viscosity remnant conduits are established by rising starting plumes.Future ascending plumes prefer to flow through these conduits as they offer a low resistance path. Tailgating is also seen where two or more starting plumes merge with each other as they rise and accelerate upwards. Another phenomenon studied is the motion of a plume across an interface of viscosity contrast which causes a rapid vertical acceleration and formation of a dipolar vortical structure. In experiments where U < 1, the plumes rise as long columns and detach. The heights of the columns are maximum for the smallest U (0.003) and decrease with increase in U. The boundary layer thickness is largest for the smallest U (0.003) and decreases with increase in U. The velocities have been estimated from the vertical sections and it is observed that the plume rise velocities are highest for U = 1 and decrease with increasing U (U>>1). A traverse setup has been built that enables the movement of a horizontal laser sheet in the vertical direction at a constant predetermined speed. The traverse setup can be used to visualize the plume structure in 3D. Another important aspect is the mixing of plumes with the ambient fluid. Data from the traverse experiments are used to quantify the mixing at different heights in the flow field and at different times. We have found that the mixing is maximum for the U = 1 case and decreases as U increases (U>1 cases). The mixing also decreases when U decreases (U<1 cases).

Chapter - 1

Introduction

In this thesis, we report results from laboratory experiments conducted to study mantle convection. Mantle convection corresponds to a regime of high Rayleigh and Prandtl numbers. In this chapter, we first give a brief introduction to high Rayleigh number natural convection. We then move on to describe mantle convection and review previous work done from a fluid dynamics perspective. Finally, we touch upon the relevance of our experiments in understanding mantle convection.

1.1 High Rayleigh number convection

Natural convection from a horizontal surface occurs when the fluid adjacent to the surface becomes unstable and starts rising. In the presence of gravity, the fluid layer rises because of a buoyancy force when it becomes lighter than the surrounding fluid. Once the motion starts, the potential energy of the fluid is converted to kinetic energy in the form of buoyant motion and is finally dissipated. The source of the buoyancy force is a density difference that can be created either by thermal heating or by concentration differences (compositional buoyancy). Natural convection from a horizontal surface has been widely studied in different types of configurations. The main types are Rayleigh-Benard Convection (RBC), unsteady non-penetrative (UNP) convection, unsteady penetrative convection (UPC), steady penetrative convection, planetary boundary layer and horizontal flat plate convection (HPC) (Puthenveettil 2004). Figure 1 shows a schematic of some of these types of natural convection configurations. The Rayleigh-Benard Convection (RBC) setup consists of steady convection occurring in a fluid layer bound between two horizontal plates, heated

from below and cooled from above. Unsteady non-penetrative convection (UNP) occurs when the top plate in a RBC system is made adiabatic(insulated). In the case of horizontal flat plate convection (HPC) there is steady convection over a horizontal flat plate kept in a vast expanse of a stationary fluid.

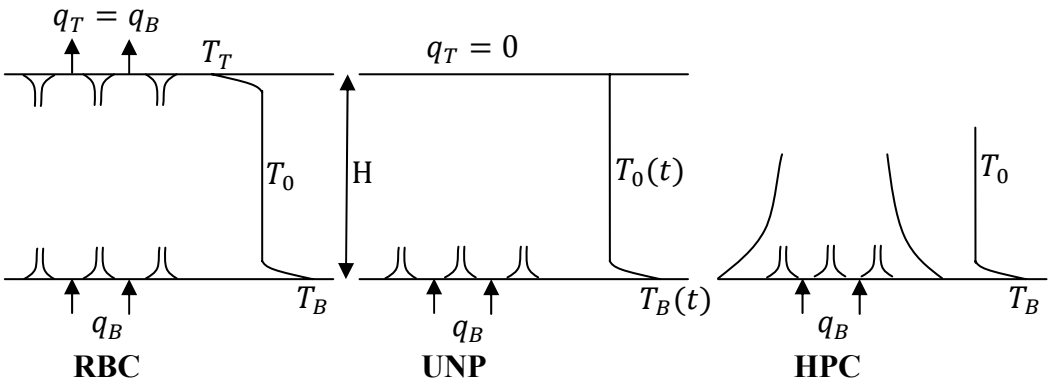

Figure 1: A schematic of some types of natural convection over a horizontal surface. RBC: Rayleigh-Benard Convection, UNP: Unsteady Penetrative Convection, HPC: Horizontal Flat Plate Convection (Puthenveettil 2004)

The governing non-dimensional parameters in natural convection are:

Rayleigh number, $Ra = \frac{g\beta_T \Delta T H^3}{\nu\alpha}$ (1)

Prandtl number, $Pr = \frac{\nu}{\alpha}$ (2)

Aspect ratio, $AR = \frac{L}{H}$ (3)

Here, g = acceleration due to gravity, β_T = coefficient of thermal expansion, ΔT = temperature difference between the walls, H = height of the fluid layer, ν = kinematic viscosity, α = thermal diffusivity of the fluid, L = horizontal dimension of the fluid layer. If the convection is unsteady, then the ratio of the fluxes at the top and bottom walls is also a parameter. The Rayleigh number is the ratio of a diffusive time scale to the convective time scale while the Prandtl number is a ratio of the kinematic viscosity to the thermal diffusivity and is a property of the fluid.

Depending on the magnitudes of Ra and Pr, different convection regimes have been observed. For RBC, the regimes have been identified by the landmark experiments of Krishnamurti (1970). The heat transfer through the fluid occurs through conduction alone till a critical Rayleigh number of Ra_{cr}= 1708. Beyond this, convection sets in the form of steady laminar rolls. Unsteady laminar rolls appear at Rayleigh numbers ~ 10^4 which lead to turbulent natural convection at Rayleigh numbers greater than 10^5. For Ra > 10^7, based on experiments using Helium gas, Heslot et al. (1987) proposed a 'Hard Turbulence' regime.

Turbulent natural convection between horizontal surfaces in its different configurations, occurs in many situations in natural processes like mantle convection, atmospheric convection and in technological applications like metallurgy, electronic cooling, and nuclear energy. Thus, turbulent natural convection has been described as a "ubiquitous" phenomenon (see for example, Grossmann and Lohse, 2000, Niemala et al 2000) and high Rayleigh number convection in general has been an important field of investigation in physics. Another reason for the great interest in studying turbulent natural convection is that the turbulence is generated by buoyancy and is different from shear turbulence. A recent review on turbulent RBC has been written by Guenter Ahlers et al. (2009). There are other excellent reviews on high Rayleigh number convection (Siggia, 1994, Kadanoff, 2001).

In turbulent natural convection, the heat transport mainly occurs through structures called plumes and thermals. A plume is defined as the continuous release of buoyant fluid from a source and a thermal is defined as an intermittent release of buoyant fluid. Plumes and thermals are the coherent structures in turbulent convection and

play a crucial role in determining the flow characteristics. Hence, it is important to understand their structure and dynamics.

Here, we briefly review previous work on turbulent natural convection relevant to our study. Theerthan (Theerthan and Arakeri, 1998) proposed a two-dimensional model for the near-wall dynamics in Rayleigh-Benard convection and in general for convection over heated horizontal surfaces. According to them, turbulent free convection over a horizontal surface consists essentially of line plumes near the walls. They propose that line plumes can be modeled as a periodic array of steady laminar two-dimensional plumes that are fed on either side by boundary layers on the wall. The results of their model are obtained using similarity solutions for the boundary layer and plume as well as numerical simulations of a two-dimensional flow field in a two-dimensional rectangular cavity. The outcome of the model is a prediction for the plume spacing as a function of the Rayleigh number. They also derive expressions for the mean temperature and fluctuations of temperature and velocity near the wall. Theerthan (Theerthan and Arakeri, 2000) carried out experiments on a heated surface to visualize and analyze the planform structure and the heat transfer under different conditions with water as the working fluid.

Puthenveettil (Puthenveettil and Arakeri, 2005, 2008) studied turbulent natural convection using the method of driving convection across a fine membrane using salt to create an unstable density difference. They focused on understanding the near wall plume structure. Their experimental setup consisted of a square cross section tank separated into two chambers by a permeable membrane. The upper chamber has a layer of brine and the bottom chamber has distilled water. The membrane is permeable enough to allow a small flow across it at higher driving potentials.

Depending on the mode of transport across the membrane, they have identified three regimes of convection namely an advection regime (2008), a diffusion regime (2005) and a combined regime. In the advection regime, there is a strong through flow across the membrane. Expressions for mean plume spacing as a function of Rayleigh number in the three regimes have been derived and compared with their experiments.

Very large eddy simulations of RBC for Pr=0.71 over a 10 decade range of Rayleigh numbers (Ra = 10^5 – 10^{15}) have been carried out Kenjeres and Hanjalic (2002). Their results reveal a dramatic thinning of the wall boundary layer with an increase in the Ra number. Also, they find that fingerlike plumes in the planform become thinner and sparsely spaced, but much more vigorous.

Another fluid instability of interest in our study is the Rayleigh-Taylor (RT) instability. This results due the unstable equilibrium of two fluid layers with the heavier fluid on top of the lighter fluid. A schematic is shown in Figure 2. The two fluids in this configuration overturn as the system seeks to minimize its potential energy. The main focus of RT studies is to study the mixing and turbulence that results as a consequence of the overturning fluids. The RT instability, like RBC, is also a very well studied phenomenon in literature. See for example Young et al 2001, where a numerical investigation of the RT instability of miscible fluids has been carried out. The RT instability is relevant in fields like astrophysics and geophysics and in technological applications like nuclear fusion reactors.

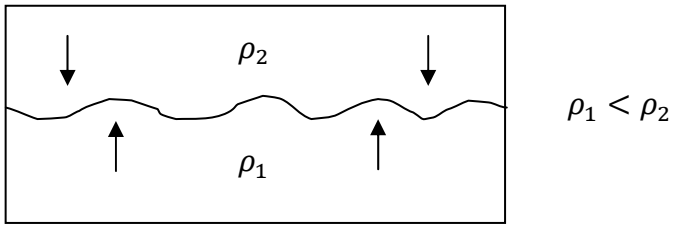

Figure 2: A schematic illustrating the Rayleigh-Taylor instability

1.2 Mantle Convection

It has been well accepted that thermal convection occurs in the mantle and is responsible for transporting heat from the core to the lithosphere. Morgan (Morgan 1971) put forward the hypothesis that 'mantle plumes' are responsible for the origin of 'hotspots' on the earth. Hotspots are localized, long-term sources of volcanic activity. Mantle plumes are considered to be hot, low-viscosity material rising buoyantly through the mantle. The source of buoyancy is a combination of thermal and compositional buoyancy. The hotspots are a surface expression of the plumes and manifest as anomalies – bathymetric swells, volcanic chains, voluminous flood basalt events. The number of hotspots is estimated to be around 40-50 (Sleep 1990). Figure 3 shows a cartoon of the cross section of the earth (from Courtillot et al. 2003) illustrating how plumes form and rise through the mantle.

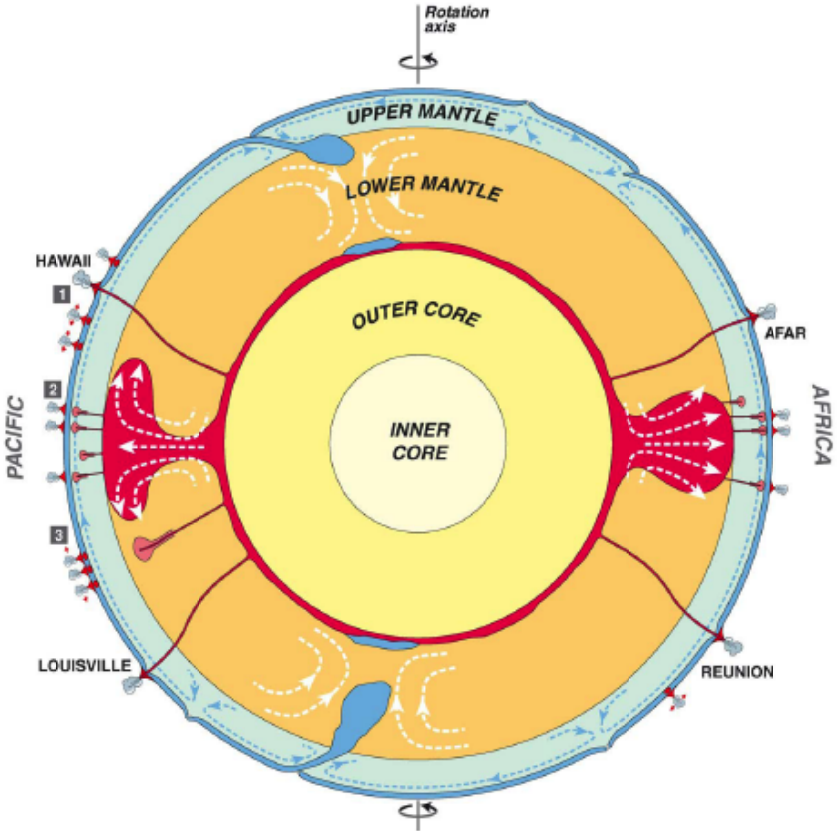

Figure 3: A cartoon of the cross section of the earth (taken from Courtillot et. al. 2003). At the Core-Mantle Boundary (CMB), heat is removed from the core which causes a thermal boundary layer to develop (shown in red). Plumes detach from the thermal boundary layer (being lighter and less viscous due to higher temperature) and rise in a viscous ambient mantle. The subduction of plates (shown in blue) are essentially cold plumes sinking into the mantle.

The average radius of the earth is about 6370 km. Starting from the surface or 'crust', the lithosphere extends from 10 km to a depth of 100 km. The region from 100 km to 660 km is referred to as the upper mantle. It is believed that there is a seismic discontinuity at 660 km which defines the boundary between the upper and lower mantle. The lower mantle extends from 660 km till the Core-Mantle Boundary (CMB) at a depth of about 2800 km. A layer exists on the CMB called the D" layer, which extends to a height of about 140 km. The D" layer is denser and has a complicated composition. The D" layer consists of both a thermal and a compositional boundary layer. The outer core extends from the CMB at 2800 km to a depth of 5000 km (Geoffrey Davies 1999).The inner solid core exists beneath the outer core. The earth is hottest at the core and loses heat through the mantle and the lithosphere through mantle plumes. The thermal structure of the earth makes plumes in the mantle inevitable.

The mantle primarily consists of molten silicate rock which can be regarded to behave as a fluid at geological timescales. Let us estimate the Rayleigh and Prandtl numbers for convection in the mantle. Assuming a layer height of H = 3000 km (whole mantle), density ρ = 4000 kg/m^{-3}, Coefficient of thermal expansion β_T = 2 x 10^{-5} /^{o}C, temperature gradient ΔT = 1400 ^{o}C, thermal diffusivity α = 10^{-6} m^2/s, and absolute viscosity = 10^{22} Pas, (all values are taken from Geoffrey Davies 1999) using the definition for Rayleigh and Prandtl number from (1) and (2), we get Ra = 3 x 10^6 and Pr = 2.5 x 10^{24}. Therefore, Mantle convection corresponds to a regime of high Rayleigh numbers (~10^6) and high Prandtl numbers (~10^{24}).

The structure and dynamics of plumes in general are quite well understood for simple laboratory systems. But, mantle plumes are not yet well understood mainly because they are difficult to observe. Information about mantle plumes is obtained indirectly from detailed seismic imaging studies both on a global and regional scale, where slow seismic velocity anomalies have been found beneath the hotspots (Zhao, 2001) . Even though there have been many advances, there is still a lack of understanding on many questions about the mantle plumes: their existence, depth of origin, morphology and longevity. The confusion is due to the fact that different geophysical observations at hotspots can be explained by different plume models (Foulger and Natland, 2003). The plume dynamics is complicated by the rheological and chemical complexity inherent in the mantle. Also, in the literature, there are different types of physical models invoked to explain mantle plumes. The source of buoyancy can be compositional or thermal, the buoyancy source can be continuous or intermittent. Plumes have been modeled as arising from boundary layer instabilities on one end and arising from point heat sources on the other end.

Mantle convection being an important problem in geophysics, has received a lot of attention. Several reviews have been written on different aspects of mantle plumes. Whitehead (1988), reviewed work on fluid models of hotspots, existing studies on high Rayleigh number convection with constant and varying viscosities, instabilities of the bottom boundary layer, plumes and conduits in constant and varying viscosity conditions and effect on shear on the rising plumes. Duncan and Richards (1991) have have focused their review on geophysical aspects of hotspots: whether hotspots are stationary, how mantle plumes interact with the shear (‘mantle wind’) produced due to plate tectonic movements in the upper mantle, and plume initiation in the lower mantle. Jellinek and Manga (2004) review recent work on the possible links between

hotspots, mantle plumes, D" layer and plate tectonics. They summarize recent findings on the origin of mantle plumes and highlight the role of viscosity variations at the CMB on plume dynamics. They also explain the different models explaining the D" layer and its effect on the longevity and geochemistry of mantle plumes. A recent overview of mantle plumes from the fluid dynamics perspective has been written by Neil Ribe (Neil Ribe et. al. 2007). In the sections that follow we summarize previous work on mantle plumes from the viewpoint of fluid dynamics relevant to our study.

1.2.1 Plumes from a point source of buoyancy

Early studies of mantle plumes considered the simple case of an isolated laminar 'starting plume' rising from a point source of buoyancy. This is an easier approach to adopt in laboratory studies, as it is difficult to study plumes arising as thermal boundary layer instabilities in vigorously convecting fluids. Experiments on isolated laminar plumes have been conducted with both compositional buoyancy (Whitehead and Luther 1975, Olson and Singer 1985) and thermal buoyancy (Griffiths 1986, Griffiths and Campbell 1990). These studies led to the standard accepted model of a mantle plume: a large, bulbous 'head' or 'cavity' trailed by a narrow conduit or 'tail' connecting it with its source. Figure 4 shows the morphology of the starting plumes (taken from Olson and Singer 1986, Griffiths and Campbell 1990). According to this plume model, massive flood basalts are produced when the plume head arrives at the base of the lithosphere and the trailing conduit is responsible for the subsequent volcanic track. This model has successfully explained features of several prominent hotspots (Sleep 1990, Olson and Singer 1985).

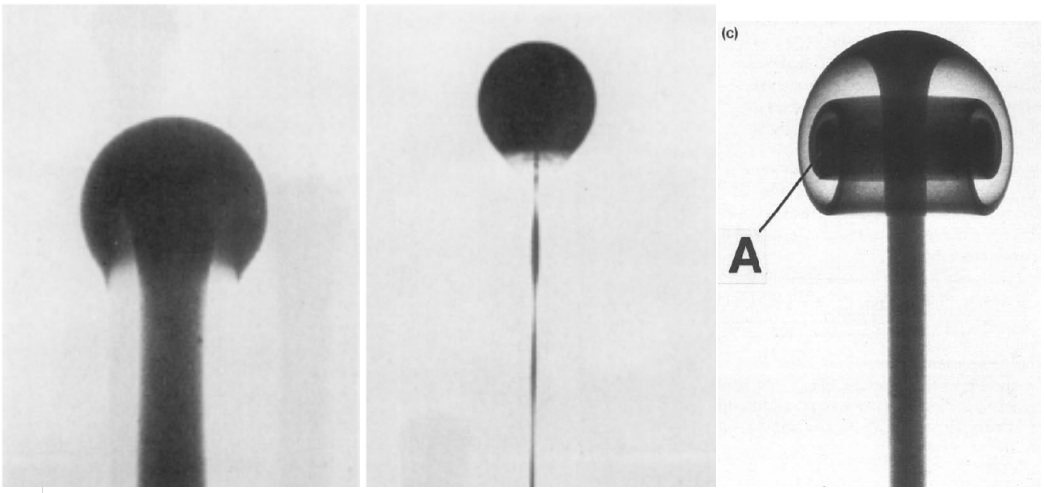

(a) (b) (c)

Figure 4: The morphology of starting plumes from a point source. (a) Diapiric plume, plume viscosity being equal to the ambient fluid. (b) Cavity plume, the plume fluid viscosity is much less than the ambient fluid. (In both (a) and (b), the plumes are formed by compositional buoyancy and the photographs are taken from Olson and Singer, 1985). (c) Starting plume formed due to thermal buoyancy (taken from Griffiths and Campbell, 1990)

Whitehead and Luther (1975) conducted the first experiments to investigate the dynamics of a thin layer of fluid bounded below by a flat horizontal boundary and moving buoyantly through another immiscible fluid of different viscosity and density. They found that the thin horizontal layer of fluid is observed to go unstable and forms spouts that rise through a denser fluid of another viscosity. The structural features were strongly dependent on which fluid is more viscous. Long buoyant columns were formed if the buoyant fluid was more viscous. On the other hand, when the buoyant fluid was less viscous, the features were dramatically different. The protrusions formed spherical pockets of fluid that gradually developed an overhang to the point where the neck of the spherical pockets pinched off from the source fluid feeding it and left behind a trailing tiny pipe. The spherical pockets travelled through the viscous fluid as almost perfect spheres. These features have been described theoretically by a linear Rayleigh-Taylor stability analysis. The wave numbers and growth rates for the most unstable modes show a strong dependence on the viscosity ratio between the fluid layers. They go on to conduct experiments from a point source

to further model the unstable buoyant rising structures. They provide a theory for the dynamics of low viscosity domes and plumes rising in a viscous ambient fluid, using the stokes approximations for a rising sphere. They derive expressions for the critical time and radius for lift-off of the buoyant spherical ball (plume head) from the source. After lift-off, the dynamics depend strongly on the viscosity ratio. Expressions have been derived for the terminal velocity and radius of the sphere.

Olson and Singer (1985) conducted experiments using glucose solutions to determine the morphology and ascent rate of buoyant plumes in a viscous fluid. A glucose solution was injected through a small orifice into another glucose solution of different density, resulting in the formation of plumes. They investigated two classes of plumes- Diapiric plumes, for which the plume viscosity is same as that of the ambient fluid, and Cavity plumes, for which the plume fluid viscosity is much less than the ambient fluid viscosity (Figure 4 (a) and (b) show Diapiric and Cavity plumes). They found that the ascent velocity of cavity plumes increases with time as $t^{2/5}$ and that the ascent velocity of diapirs is proportional to the terminal velocity of a cylinder moving parallel to its axis. They also note that remnant fossil conduits left over by cavity plumes act as low-resistance ascent paths for future plumes. Their presence alters the morphology of cavity plumes and increases their rate of ascent. They have also studied the effect of a large-scale background circulation on the cavity plumes, by towing the plume generation source steadily through the viscous fluid. These experiments have shown that the deep mantle plumes can produce hotspots that are nearly fixed, in spite of the presence of a background circulation in the mantle.

Olson and Christensen (1986), and Scott et al. (1986), have shown that waves of large amplitude can propagate upwards without change in shape through the stem of a chemically buoyant plume. These are called solitary waves and it has been found that they can transport chemically distinct material over long distances with higher velocities and with little contamination. This could explain the episodic magma production at weak hotspots and surges of activity at stronger hotspots.

The viscosity of the mantle material decreases strongly with increasing temperature. Therefore, a majority of the previous studies have focused on plumes generated by thermal buoyancy using fluids with temperature-dependent viscosity. These thermal starting plumes resemble cavity plumes with a large head and narrow stem. Griffiths and Campbell (1990) studied the dynamics of a starting thermal plume by injecting hot glucose syrup into a cooler reservoir of the same fluid at a constant rate. Figure 4 (c) shows the morphology of the starting thermal plume in their experiment. They found that the spherical head entrains ambient material due to thermal effects as it rises. They analyze the effects of entrainment on the structure and dynamics of the starting plume. Compositionally buoyant plumes have also been found to entrain the ambient fluid through which they rise. (See for e.g. Kumagai 2002)

Numerical simulations have also been carried out to study mantle plumes. Van keken (1997) performed numerical simulations to match the conditions of the laboratory experiments by Griffiths and Campbell (1990), and in addition different rheological models for the ambient fluid were used. Mantle plumes have been studied in complex and ‘earthlike’ configurations by Kellogg and King (1997). Through numerical simulations, they studied the evolution of plumes in a spherical annulus of fluid with

temperature-dependent viscosity. Both numerical simulations mentioned above have found reasonable agreement with the experiments of Olson and Singer (1985) and Griffiths and Campbell (1990).

In studies of plumes from point sources of buoyancy, there are many different approaches that have been used. Considerable work has been done to determine power-law scalings which would be valid in a limited range. However, It is difficult to compare between the different laws to see how they are related to each other. As of now, there is a lack of complete scaling laws which describe all the regimes and transitions between them.

1.2.2 Plumes arising as boundary layer instabilities

Plumes modeled from point sources of buoyancy have been useful to provide a conceptual understanding of the physics. In the mantle, a more realistic scenario would be that plumes arise as instabilities of hot thermal boundary layers.

As mentioned before, convection in the mantle corresponds to high Rayleigh numbers ($\sim 10^6$) and high Prandtl numbers. Previous studies of convection at high Rayleigh number (particularly RBC) have revealed that above $Ra \sim 10^6$, well defined cells or rolls do no exist and heat is transported by plumes that form as instabilities of the upper cold and lower hot thermal boundary layers. Traditionally, majority of the previous experimental work to study mantle convection at high Rayleigh and Prandtl numbers have used heating to drive the convection, and the fluids used have a temperature-dependent viscosity. The reader is referred to two recent experimental studies on convection relevant to the mantle convection regime (Manga and Weeraratne (1999) and Lithgow et al (2001)). In these experiments, the thermal buoyancy is usually supplied gradually and kept constant. When the convection

becomes fully developed, the plume generation is a cyclic process in which the thermal boundary layers grow by thermal diffusion, become unstable and then empty themselves rapidly into plumes, and the cycle begins again. In the mantle, once plumes are formed they must be able to reach the surface to produce a hotspot. In a RBC system heated from below and cooled from above in a constant-viscosity fluid, the hot plumes tend to lose their identity before reaching the upper surface and the cold plumes also a lose their identity before reaching the lower surface. The reasons for this is due to the interaction of hot and cold plumes which tend to disrupt each other (Schaeffer and Manga 2001) and also the interaction between plumes of same kind which can cause merging or clustering (Manga 1997, Kelly and Bercovici 1997) leading to a large scale circulation (Xi et al, 2004).

Plumes in convecting homogeneous fluids are transient features and do not resemble the 'cavity plume' model of Olson and Singer (1985). We therefore have a conflict: cavity plumes are favored in the presence of high viscosity contrasts, but are not observed in fully developed convection in fluids with temperature-dependent viscosity. The reason for the conflict is that most of the temperature drop in a system with fully developed convection occurs across a stagnant high-viscosity 'lid' at the top of the layer, leaving only a small temperature drop across the bottom (Manga et al. 2001). Generation of cavity plumes in fluids with temperature-dependent viscosity requires a larger temperature contrast across the lower thermal boundary layer under statistically steady-state conditions. Impulsive heating from below can produce the required large contrasts in temperature (Davaille and Vatteville 2005) but only in a transient manner. If the hypothesis that large plume heads occur under hotspots is true, a permanent mechanism is required to keep the large temperature difference

across the bottom thermal boundary layer. Experiments carried out by Jellinek et al. (2002) have shown that one possible mechanism can be the transport of cold material from the top layer to the bottom by subducting tectonic plates, which increases the temperature gradient. Another possible mechanism could be due to the chemical heterogeneity in the lowermost mantle. This has led to the study of thermochemical convection by Anne Davaille and co-workers. In thermochemical convection the density of the fluids depends on both temperature and composition and a layered system of fluids is studied. This type of a study and its implications was first reported by Davaille (1999a and 1999b). See Davaille et al (2003) for a review on thermochemical convection. Experiments by Davaille et al (2002) and Jellinek (Jellinek and Manga, 2002) have shown that plumes can be anchored by the presence of a chemically stratified layer and hotspots produced by such plumes could persist for longer times and be relatively fixed. There is yet another way to model high viscosity contrasts across the bottom thermal boundary layer and that is by using compositional buoyancy to drive the convection. This is the approach we have adopted in our study and below we review similar work done by Jellinek et al. (1999a).

Jellinek (Jellinek et al. 1999a) conducted laboratory experiments to quantify the different situations under which fluids can be mixed by natural convection at high flux Rayleigh numbers using compositional buoyancy. In their experimental setup, light buoyant fluid is injected into an overlying ambient fluid of different viscosity at a fixed rate from a planar, horizontally uniform source. The study is more complicated than the case of a plume from a point source. Here the planar geometry does not impose constraints on the buoyancy flux of each plume and results in a

random field of plumes that can interact with one another. In all of their experiments, the flux Rayleigh number was large ($>10^{11}$) and so the velocity fields were always unsteady and the motions complex. They have pointed out that the viscosity ratio (U) which is a measure of relative importance of viscous stresses in the two fluids influences the spacing and structure of buoyant plumes (Whitehead and Luther, (1975), Olson and Singer, (1985)). They have studied mixing for cases ranging from U<<1 to U>>1 and have defined a Reynolds number with a suitable velocity scale that can be used along with U to rationalize the results across the entire range of conditions. They quantified mixing in the Re-U space by defining a mixing efficiency and have provided a mixing efficiency contour map. They apply their experimental results on mixing to arrive at conclusions for the differentiation of the earth's core, mixing in the earth's mantle (Jellinek et al. 1999a) and also to the differentiation of magma chambers and lava flows (Jellinek et al. 1999b).

Studies of the planforms of mantle convection and their scaling with the Rayleigh number are important to understand the spatial distribution of hotspots in the mantle. Busse (Busse and Whitehead 1971) conducted experiments to study the instabilities of convection rolls in a high Prandtl number fluid. In the planforms of RBC, convection will first emerge in the form of hexagonal rolls when the Rayleigh number is raised above the critical value. Increase in Rayleigh number leads to the formation of rolls, and further increase ($Ra \sim 10^4$) leads to a three-dimensional pattern called 'bimodal convection' (Busse and Whitehead 1971). White (1988) studied the planforms and onset of convection in a fluid with strongly temperature dependent viscosity. Rayleigh numbers of $6x10^4$ were reached and viscosity variations of upto1000 were achieved. In addition to the rolls and hexagons reported by Busse and Whitehead (1971), a new

planform of squares was observed at large viscosity variations. Numerical simulations have been used to study the effect of depth-dependent viscosity in the planform of mantle convection using a three-dimensional spherical shell model (Bunge et al. 1996). However, the near wall convective planforms have not been studied for large viscosity variations across the bottom boundary layer.

1.3 Present work

Plume dynamics in mantle convection is not well understood because of the complicated rheology and chemical composition in the mantle and other factors like the influence of large scale flow due to plate tectonic movements. Convection in the mantle corresponds to a regime of high Rayleigh number (Ra) in the limit of high Prandtl number (Pr). In this work, we have set out to investigate the role of viscosity contrast between the plume fluid and surrounding fluid on the structure and dynamics of plumes.

In our experiments, we have used compositional buoyancy to drive the convective flow. A heavier layer of sugar solution rests on top of a layer of water in a glass tank of square cross-section. The two layers are separated by a permeable mesh and the concentration difference provides the buoyancy. The water in the lower layer is forced through the mesh at a small constant rate using an external setup. The fluid viscosities in both the upper and lower layer have been enhanced in different cases using Na-CarboxyMethylCellulose (CMC). This enables us to study the effect of viscosity ratio (U) on the plume structure and reach regimes relevant to mantle convection. The Planar-Laser-Induced-Fluorescence (PLIF) technique is used to visualize and

photograph the plume structure and dynamics above the mesh in the near wall planform, side section views and in 3D using a traversing laser sheet.

The primary questions we address are:

- What is the effect of the viscosity ratio on the spacing and morphology of plumes in the near wall planform?
- How does the viscosity ratio change the structure and dynamics of the rising plumes?
- How does the viscosity ratio determine the extent of mixing?

In 'classical' convection experiments driven by thermal buoyancy, the buoyancy flux and fluid viscosity are coupled. Using compositional buoyancy gives the advantage of being able to study the effect of viscosity alone on the plume structure, decoupled from other parameters. In previous work (Whitehead and Luther 1975, Olson and Singer 1985), compositional buoyancy was used to study plumes rising from point sources of buoyancy, but in our study, plumes arise as boundary layer instabilities from a planar source, which makes it more realistic. Also, we are able to study plumes rising from the boundary layer at large viscosity contrasts, which is not possible when thermal buoyancy is used for the study. We have studied convection over a range of viscosity ratios, corresponding to a wide range of Rayleigh and Prandtl numbers. The primary motivation for our experiments is to understand plume structure in mantle convection, but the parameter regimes we cover also make our study of fundamental interest. Very few experimental works have been able to reach high Rayleigh and Prandtl numbers simultaneously, and the use of compositional buoyancy to reach these regimes make our study novel. We have conducted preliminary experiments to

study the dynamics of a plume moving across an interface of large viscosity contrast. Another set of preliminary experiments have explored the effects of variation of buoyancy flux on the plume structure.

The experimental setup of Puthenveettil (Puthenveettil and Arakeri, 2005, 2008) used a similar concept but they do not have an externally imposed through flow across the mesh. Also we vary the fluid viscosities and study in detail the role of viscosity on plume dynamics. This changes the fluid dynamical regime of our system to something in between a Rayleigh-Taylor instability and Rayleigh-Benard convection system. To the best of our knowledge, we are not aware of any theoretical or numerical work in this regime. The only similar work has been the experiments of Jellinek et al. (1999). Their experimental setup was similar, but the primary motive was to study mixing in different regimes of viscosity ratios. We focus on studying the plume structure and dynamics at different viscosity ratio regimes. They only give a qualitative description of the flow, whereas besides visualizing the flow details, we also quantify the features. We have studied the planforms in detail for the first time. We quantify the changes in plume spacing and thickness at different viscosity ratios in the near-wall planforms. We also determine the dependence of plume rise velocities and plume sizes with varying viscosity ratios. Finally, we quantify mixing over a range of viscosity ratios from our data.

This thesis is organized as follows: The experimental details are given in Chapter 2. Chapter 3 describes the results and analysis of our experiments. We make some conclusions from our study in Chapter 4.

Chapter 2
Experiments

The experiments have been conducted in a square cross-section tank that is divided into two chambers by a permeable mesh. The convection is driven by a concentration difference across the mesh between sugar solution in the upper chamber and tap water in the bottom chamber. The viscosity of the solutions is enhanced and we study in detail the effect of viscosity ratio between the plume fluid and surrounding fluid on the plume structures. In this chapter, we describe the experimental setup and methodology in detail.

2.1 Test section

The test section of the experimental setup consists of a square section glass tank of cross section dimensions 20.3 cm x 20.3 cm and height 45.7 cm. Float glass with a thickness of 10 mm has been used for construction of the tank. The tank has a central hole (6mm diameter) in the bottom through which fluid is forced from below using a constant head setup. A permeable mesh divides the tank into two chambers – a top and bottom chamber. The tank is open at the top and rests on a metal (mild steel) stand that is provided with screws for leveling the test section horizontally. Figure 5 shows a schematic of the construction details of the tank. The permeable mesh is glued onto a square stainless steel frame of dimensions 20.3 cm x 20.3 cm and thickness 0.8 cm using a strong adhesive. Extreme care has been taken to ensure that the glue has not spread beyond the steel frame to affect the test section. The frame has 1 cm diameter holes on the sides to accommodate screws as shown in Figure 5(b).

The frame also has two small threaded holes to fix rods used for lowering and lifting. This frame is screwed tightly onto another square steel frame using M5 (5mm standard) allen screws. This bottom steel frame is of the same dimensions as the top one but with a thickness of 1.5 cm. It is provided with a slot for a 0.5cm soft rubber O-ring and threaded holes for the allen screws. It is part of a permanent assembly in the bottom chamber and is glued onto glass slabs using a silicone sealant. It is supported by rectangular glass slabs that rest on the tank base (slabs are 2.5 cm thick and 17.8 cm high).

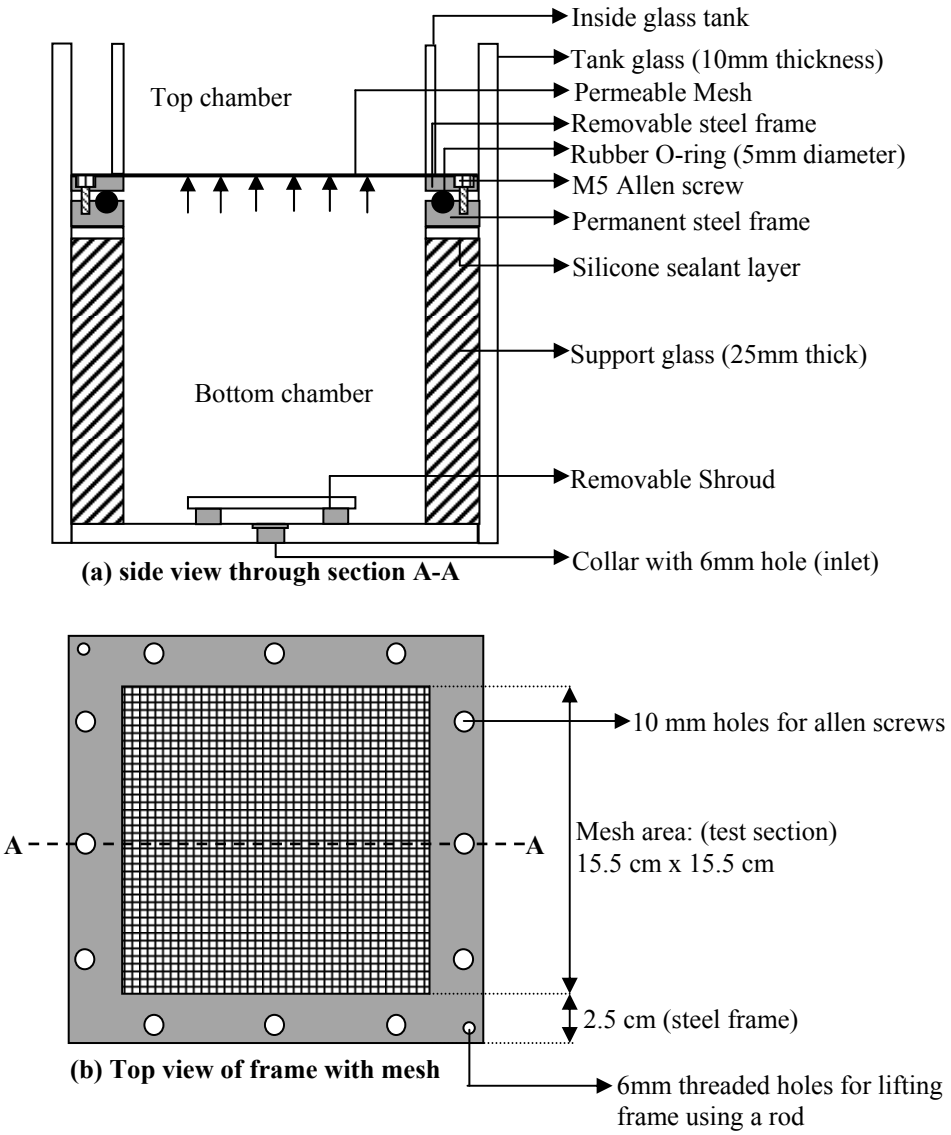

Figure 5: Detailed view of construction details of frames and mesh (not drawn to scale)
(a) Side cross-sectional view through section A-A shown below.
(b) Top view of frame with mesh

The rubber O-ring is compressed between the two steel frames and provides a seal to prevent leakage of fluid from the sides. The O-ring ensures that the only possible interaction between the fluids in the top and bottom chambers is through the mesh. A smaller square glass tank of dimensions 16 cm x 16 cm x 30 cm is placed on the steel frame before the start of the experiment. This ensures that the test section essentially is a rectangular box of cross section 15.5 cm x 15.5 cm extending from the base of the tank to a height of 26 cm above the mesh.

A small shroud is placed on tank base covering the region of the inlet hole in the bottom chamber. This shroud is a small glass plate (10 cm x 10cm x 0.8 cm) placed on intervening spacers. The purpose of the shroud is to avoid the impingement of a direct jet of fluid from the inlet hole on the lower surface of the mesh. The shroud results in a reasonably uniform upward fluid flow across the mesh.

2.2 Permeable Meshes

The mesh separates the tank into the two chambers and provides a horizontal planar boundary for the release of buoyant fluid. We have used two types of meshes in our experiments – a nylon mesh and a steel mesh. Table 1 lists the properties of both the meshes.

Mesh	Material	Mean pore size (μm)	Open area factor Γ
Nylon140s	Nylon	29	0.2
Steel40	Stainless steel	427	0.45

Table 1: The properties of the permeable meshes

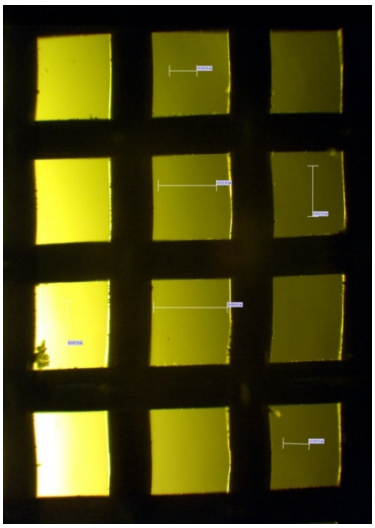

Figure 6: Optical microscope image of Steel40 mesh

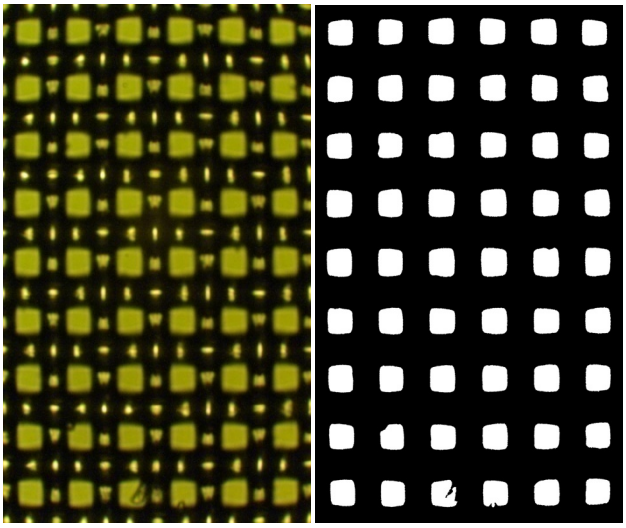

(a) (b)

Figure 7: Calculation of open area factor for the nylon140s mesh. (a) optical microscope image (b) binary image obtained by thresholding

An optical microscope (LABEN instruments, India) was used to image the meshes to determine the pore size and open area factor. Small samples of the mesh (2cm x 2cm) were imaged under the optical microscope at magnifications of 5X, 10X and 20X. Pore size measurements were determined using the ImageJ software (freeware) using the length scale provided by the optical microscope software. The meshes have a square opening and the pore size is taken to be the length of the side of the square.

The open area factor (Γ) is a measure of the total area of the pores as compared to the total mesh area. It is an indication of the permeability of the mesh. The open area factor would be small for a fine mesh (like the nylon140s) and would be higher for a coarser mesh (like the steel40). The optical microscope images were converted into binary using Matlab. A suitable threshold was applied so as to retain the major features in the image. Once the binary image was obtained, the open area factor was calculated as:

$$\Gamma = \frac{Total\ Area\ of\ all\ the\ pores(squares) in\ the\ image}{Total\ Area\ of\ the\ image} \qquad (4)$$

The nylon140s mesh is made of a nylon fabric and is used in screen printing. The mesh has a mean pore size of $29\mu m$. Figure 7 (a) shows an optical microscope image of a small region of the nylon 140s mesh. The binary version of the optical microscope image is shown in Figure 7 (b). The nylon140s mesh was found to have an open area factor, $\Gamma = 0.2$

The steel40 mesh is coarser than the nylon140s mesh. Figure 6 shows the optical microscope image of the steel40 mesh. The mesh has a mean pore size of $427\mu m$ and an open area factor $\Gamma = 0.45$

The selection of the mesh depends on the experiment. The nylon140s mesh has been used in experiments where the viscosity ratio, U >> 1, i.e. where water was forced through the mesh with the top chamber fluid being viscous. The steel40 mesh was used in experiments where U << 1, i.e. where viscous fluid was forced from the bottom chamber through the mesh. It is difficult to force viscous fluids through the mesh as they do not flow easily. The steel40 mesh had to be used in the U<<1 experiments as it has a greater pore size and is rigid. The nylon140s mesh would bulge and would not allow viscous fluids to flow through easily because of its small pore size.

2.3 Constant Pressure Head Setup

The constant pressure head setup is used for forcing the fluid through the bottom chamber of the tank to the top chamber across the mesh. It has been constructed based on the experimental setup of Debopam Das et al. (1993). The objective is to deliver fluid to the tank through the inlet at the bottom at a constant flow rate. This is

achieved by maintaining a constant level of fluid at a particular height, thereby ensuring a constant pressure head fluid supply. A schematic of the setup is shown in Figure 8. The setup consists of two aspirator bottles containing the inlet fluid with dye and connected to the tank inlet at the bottom. The upper 5L aspirator bottle is closed with a cork. A small tube is inserted through the cork and left open to the atmosphere.

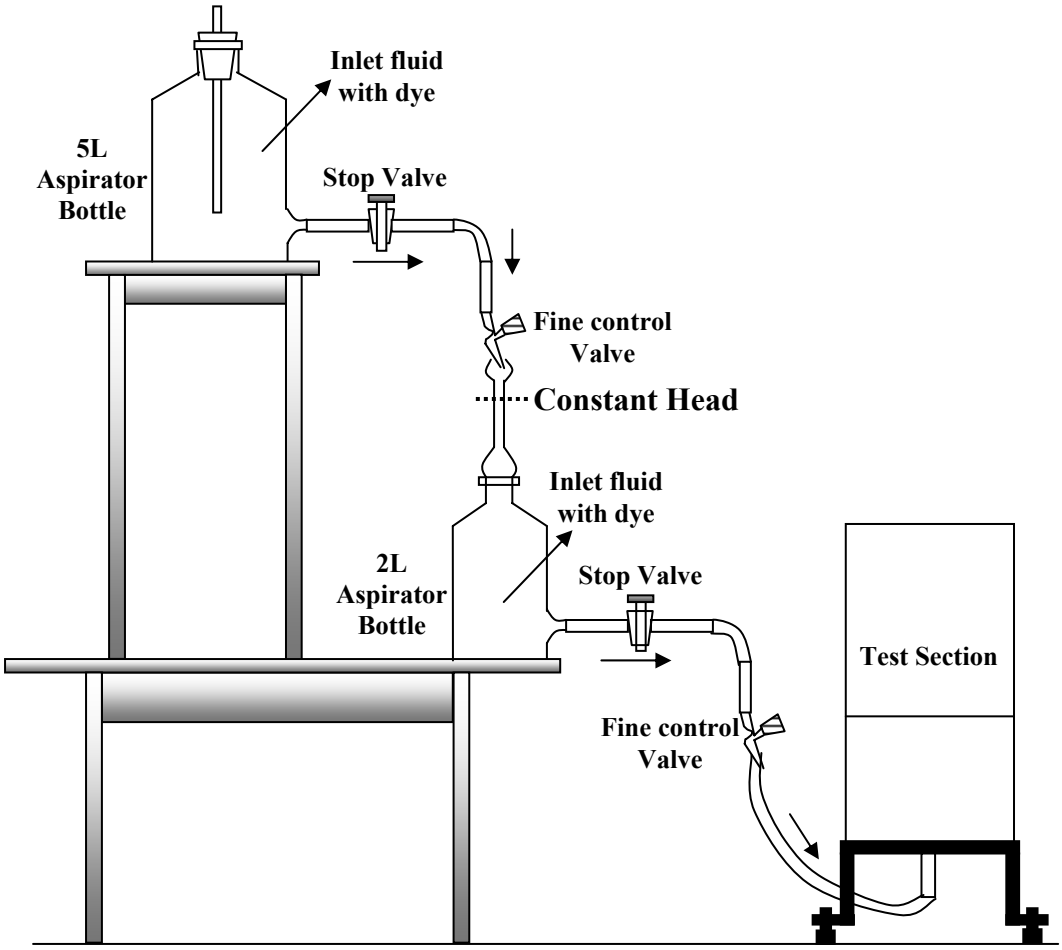

Figure 8: The constant head setup

This is the commonly known 'marriott's bottle' and the fluid flows out of the bottle at a constant flow rate till the meniscus drops below the tube. The stop valves (open/close valves) are adjusted to either allow or stop the flow. The desired flow rate is set carefully using the Fine control valve. These valves have been modified from the standard burette valves and they allow a drop by drop control. The flow rate is

measured by the jet issuing out of the fine control valve. This jet is open to the atmosphere and can be diverted to make flow rate measurements. The flow rate is measured by noting down the time taken to fill a finite volume of fluid in a measuring cylinder using a stopwatch. The average value of a number of trials is taken to be the flow rate. Once the desired flow rate is set, the next task is to ensure that the constant head level is maintained in the capillary as shown in Figure 8. Before this is done, the bottom aspirator bottle and piping are connected to the bottom of the tank and all bubbles are removed from the system. Once the experiment begins, both the stop valves are opened. The fine control valve (placed after the 2L aspirator) is adjusted to maintain a constant level in the capillary tube, thereby ensuring a constant flow rate through the mesh.

2.4 Viscosity enhancement

The viscosity of the fluid was enhanced using Sodium-CarboxyMethylCellulose (Na-CMC). Na-CMC finds applications in food, pharmaceutical and cosmetic industries where it is used for several functions - as a thickener, suspension aid, binder, stabilizer and film-former. CMC is basically an anionic water-soluble polymer derived from cellulose. CMC is a cellulose ether, produced by the reaction of alkali cellulose with sodium monochloroacetate under controlled conditions. We have used the commercial 'Aqualon' brand '7H4F' grade CMC available from Hercules, Inc, USA (refer Booklet 250, Aqualon, 1999 for technical details).

Viscosity enhancement is the single most important property of CMC solutions. The viscosity of CMC solutions increases rapidly with concentration. Generally, CMC solutions are non-newtonian because they change in viscosity with change in shear

rate. CMC solutions generally exhibit a pseudoplastic behavior, i.e. the solutions show a time-independent, shear-thinning behavior under application of shear. Figure 9 shows a plot of apparent viscosity v/s shear rate for Newtonian and pseudoplastic fluids.

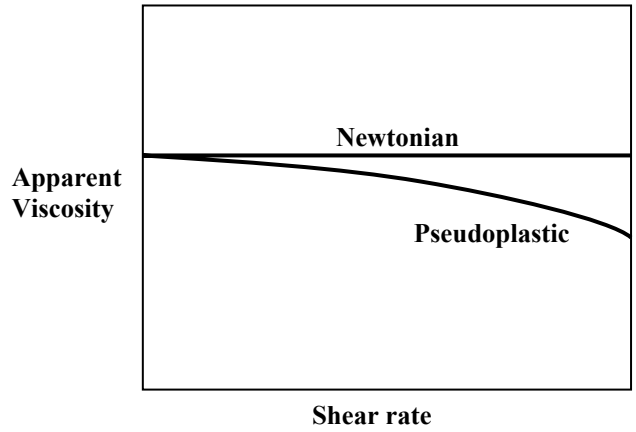

Figure 9: Apparent viscosity v/s shear rate for a general fluid

It is evident from Figure 9 that Newtonian fluids have a constant viscosity at different shear rates. On the other hand, for pseudoplastic fluids, the viscosity decreases as shear rate increases. Although CMC solutions are generally pseudoplastic, they approach Newtonian behavior at very low shear rates (~ 0.1 to 1 s^{-1}). The shear rates in our experiments correspond to ~ 1 s^{-1}, hence the CMC solutions in our experiment may be considered as Newtonian fluids. CMC solutions are also known to exhibit thixotropy: a time-dependent change in viscosity. This occurs mainly in cases where the solutions are left undisturbed to rest for long periods of time. But, thixotropy does not play a role in our experiments.

The CMC solutions were prepared by adding a carefully weighed quantity (with an accuracy of 0.01g) of the required amount of CMC powder into distilled water. Initially clumps (large aggregates of CMC) are formed and when sufficiently wet by

water they are manually squashed into smaller clumps. This is done carefully only once and from then on the solutions are periodically stirred using a powerful hand blender (400W Morphy Richards). The solutions are kept in containers with frequent stirring for a time period of 24 hours. It is visually ensured that the solution is homogeneous before using it in the experiments. In our experiments, we have added a maximum of 1% by weight of CMC in water. The changes in density are negligible for CMC additions of less than 1% by weight in water. Ageing also plays a role in affecting the viscosity of CMC solutions, but since we uniformly prepare and use the solutions after 24 hours, it is not a consideration in our experiments.

Salt solutions have dissociated ions which can affect the properties of CMC solutions. Hence, we have used sugar to increase the density of the fluid in our experiments.

We have measured the viscosity by two methods – using a rheometer and falling ball method. A computer-controlled rheometer (Rheolyst series AR1000) manufactured by TA Instruments, USA, was used for viscosity measurements. A parallel plate geometry was used with a 400 μm gap between the stationary and rotating plate. It is possible to measure the viscosity at different shear rates varying with time.

We measured the viscosities of a number of samples of CMC solutions of different concentrations. Figure 10 shows a plot of the Absolute viscosity of CMC solutions (in mPas) v/s the concentration of CMC in solution (% weight) measured using the rheometer and falling ball method. The falling ball method was used to measure viscosity of CMC solutions in a few cases (shown in Figure 10). This method uses the Stokes law for a sphere falling through a fluid at low Reynolds numbers.

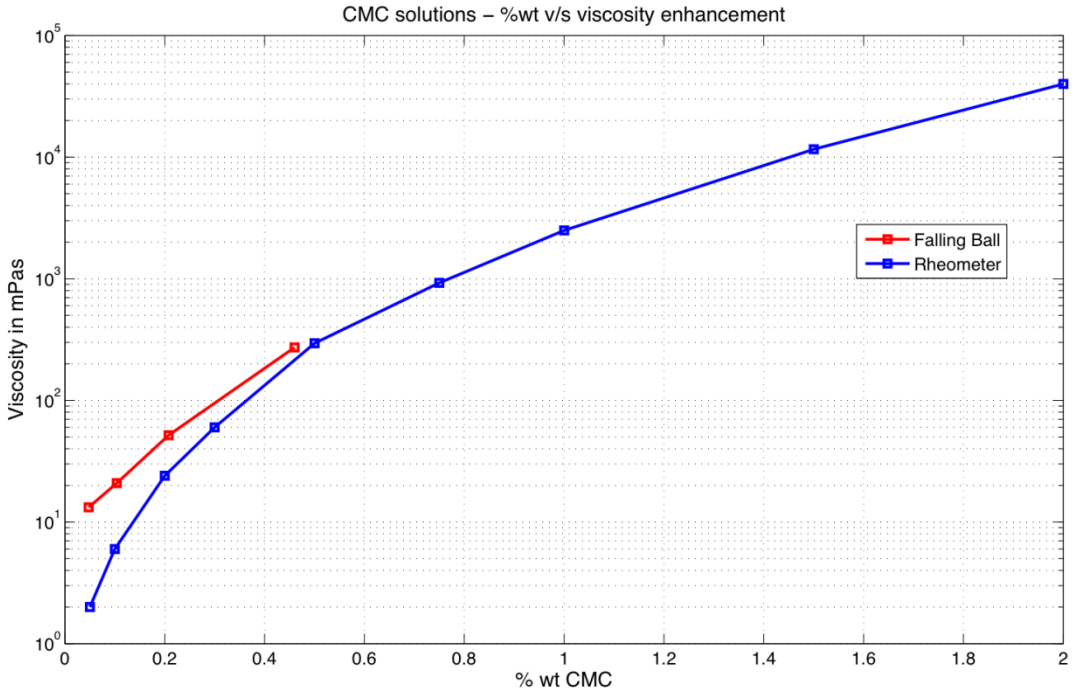

Figure 10: Viscosity v/s concentration of CMC

The Stokes law gives the drag force exerted by a viscous fluid on a spherical object moving through the fluid with constant velocity: $F_{drag} = 6\pi\mu rv$, where μ is the absolute viscosity of the fluid, r is the radius, and v is the terminal velocity. Stokes law is valid for Reynolds numbers less than 80, where the flow surrounding the sphere would be laminar. For the spherical object to be in force equilibrium, the viscous drag force and the buoyancy force exerted by the fluid balance its weight: $V_{ball}(\rho_{ball} - \rho_{fluid})g = F_{drag} = 6\pi\mu rv$ (5), where, V_{ball} is the volume of the spherical ball, ρ_{ball} is the density of the ball, $\rho_{fluid}$is the density of the fluid, g is the acceleration due to gravity. Small spherical plastic balls (diameter ~ 6 mm) of different densities were dropped into the fluid whose viscosity was to be measured. The balls were allowed to fall through a 1m column of fluid. The terminal velocity was estimated by noting the time taken for the ball to travel 50 cm. The viscosity value is calculated from the terminal velocity. Figure 10 shows that the viscosity measurements using the falling ball method shows reasonable agreement with the measurements using the rheometer.

We have a set of measurements of viscosity of CMC solutions at discrete values of concentrations from the rheometer (shown in Figure 11). To find values of viscosity of CMC solutions at intermediate values of concentration (% weight), we fit a 5th order polynomial curve to the data and get an expression for the viscosity as a function of concentration:

$$\mu = 1300c^5 - 1549c^4 + 3139c^3 - 564.7c^2 + 173.5c - 8.2 \quad (6)$$

Where, μ is the absolute viscosity in mPas and c is the concentration of CMC in solution expressed as % weight of CMC in solution.

2.5 Flow Visualization

The primary source of data in our experiments is from flow visualization using the Planar-Laser-Induced-Fluorescence (PLIF) technique. The plume structures in the test section above the mesh have been studied by using a laser light source for illumination. The laser beam is converted into a planar sheet using a plano-concave lens (12mm x 10mm x 4mm). Horizontal planar sheets of light are used to visualize the planform structures and vertical planar light sheets are used to study the plumes structures in vertical sections. Figure 11 shows a schematic of the flow visualization process. A small amount (~ 0.5 ppm) of fluorescent Rhodamine-6G dye is dissolved in the inlet fluid forced from below and also in the fluid in the bottom chamber. Our laser light is of green color (wavelength of 532 nm) which matches the absorption peak for the Rhodamine dye. Hence, Rhodamine-6G it is the preferred dye for our experiments. The small amount of dye added does not affect the flow and the dye acts as a passive tracer.

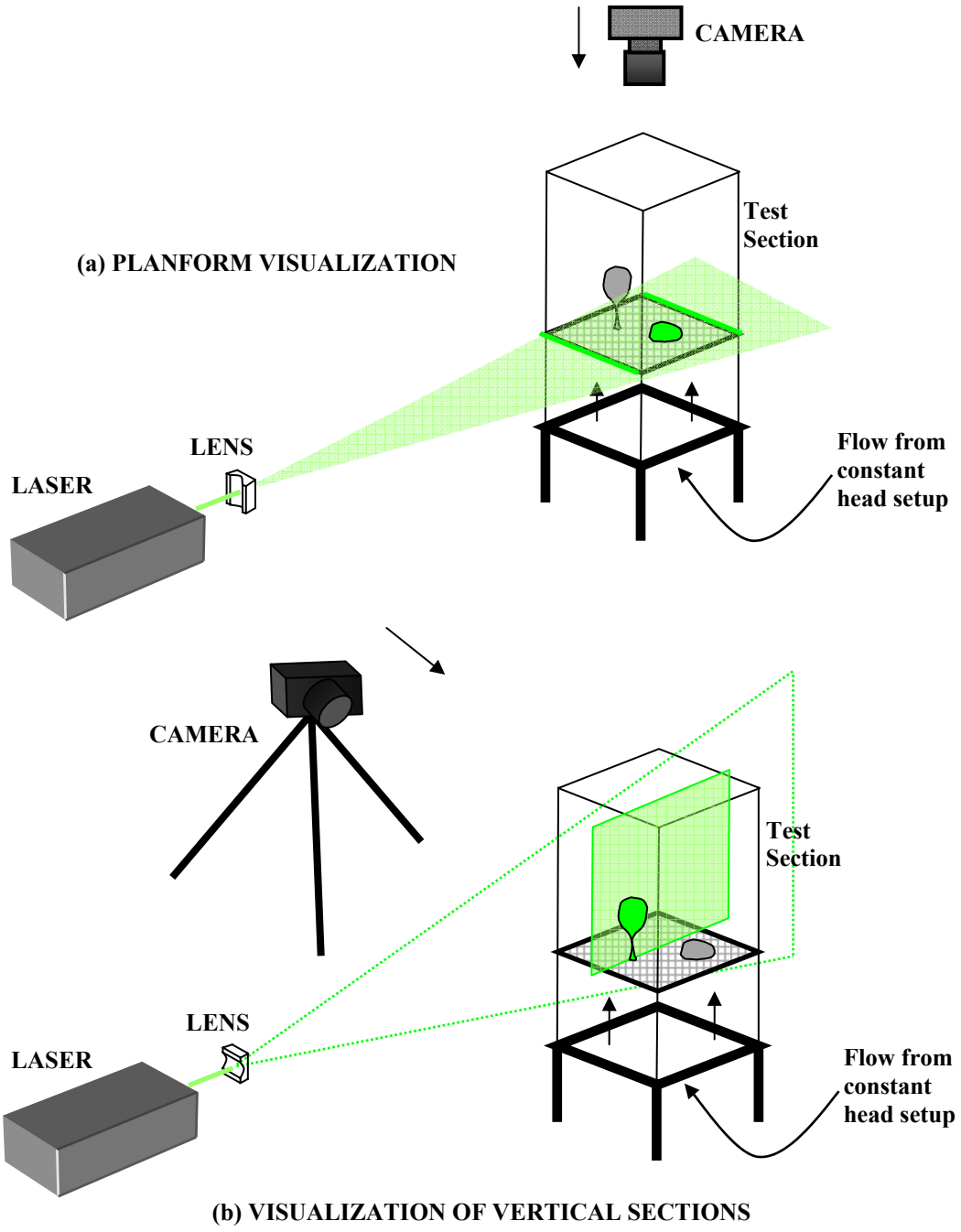

Figure 11: A schematic of the flow visualization process
(a) Planform visualization
(b) Visualization of the vertical sections

The fluid from the bottom chamber (plume fluid) passing through the mesh and laser sheet (horizontal or vertical) fluoresces because of the presence of the dye and this image is captured by a camera. Note that we see fluorescence from only the laser sheet illuminated area in a 2D plane; the rest of the flow details are invisible to us. This is the essence of the PLIF method.

In our initial experiments (Experiments: PExpt1 to PExpt12 in Table 2), the laser used was a 532 nm 10Hz Nd-YAG pulsed laser (Brilliant Twins laser by Quantel, France). This laser was used to visualize the planform structures just above the mesh. Images were captured form above at intervals of 5 seconds using a Canon Digital SLR camera (model: EOS 350D). The light from the laser was deflected twice using 90^o deflecting prisms and then passed through the plano-concave lens. The plano-concave lens expands the laser beam into an expanding plane sheet of light. The plano-concave lens is rotated suitably depending on whether we need a horizontal or vertical sheet of light (a 90^o rotation of the lens changes the plane). A condensing convex-convex lens of 48cm focal length was placed in front of the plano-concave lens to obtain a thin light sheet (thickness ~1-2 mm).

In all subsequent experiments (Experiments: TExpt1 to TExpt7, VExpt1 to VExpt6 in Table 2), we used a continuous laser for flow visualization. The laser was a 532 nm solid-state semiconductor diode laser of 50 mW power (manufactured by Shangai Dream Lasers, China). In these experiments, we captured videos of the flow using either a Nikon D90 Digital SLR camera (video mode) or Sony DVD Handycam (model: DCR DVD201E). Occasional photographs were also taken using the Nikon camera. Image and video processing for analysis is described in detail in the next chapter.

2.6 Traverse Setup

We designed and fabricated a Traverse setup which enabled the controlled and precise movement of a horizontal laser sheet in the vertical direction. A vertical section view of the Traverse setup is shown schematically in Figure 12.

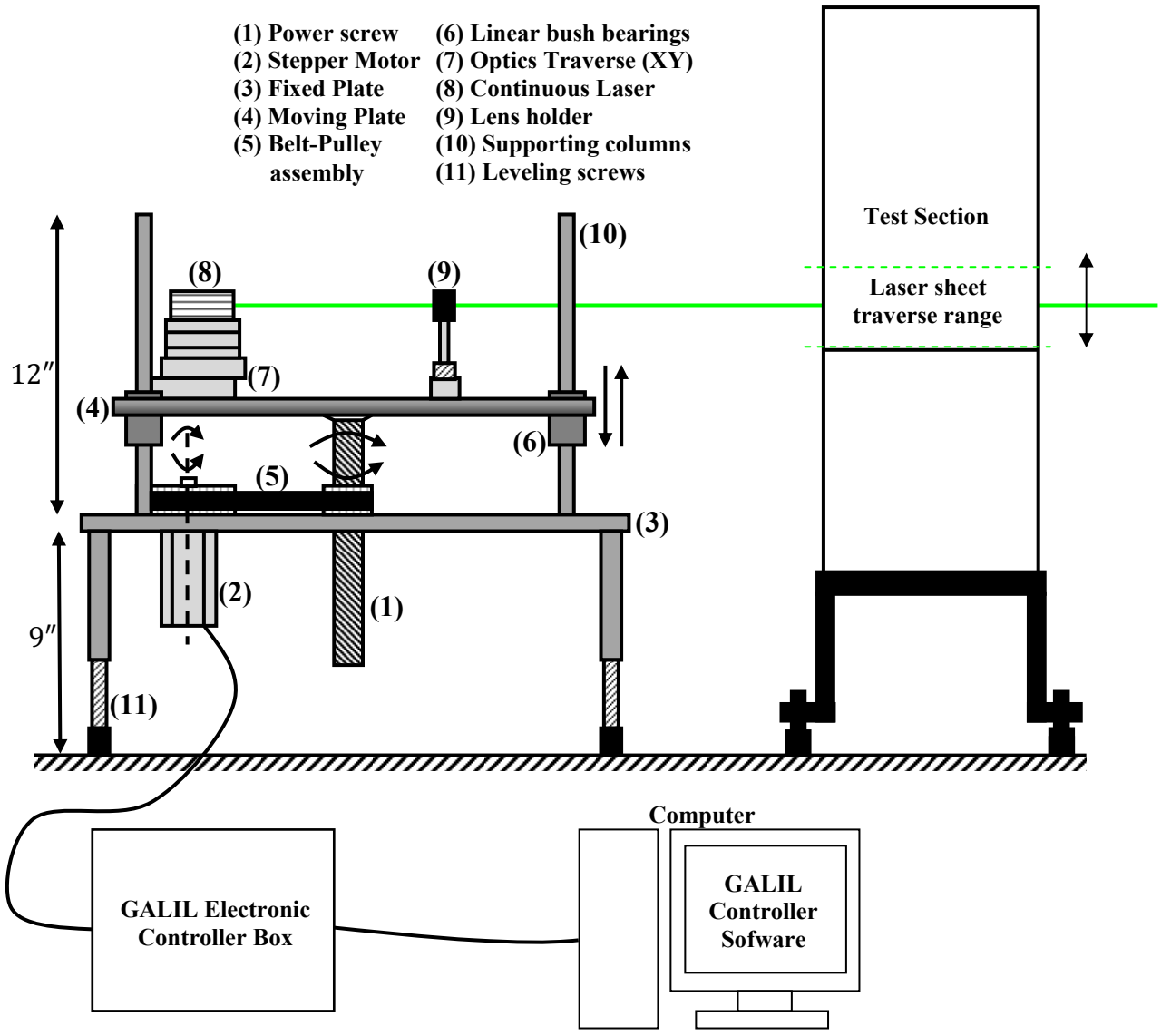

Figure 12: A schematic of the Traverse setup (vertical section view)

Referring to Figure 12, the Traverse setup consists of a rotating power screw(1) (20mm diameter) which moves an Aluminium plate(4) (38 cm x 45.7 cm dimensions, 8 mm thickness) up and down. The continuous green laser(8) is mounted on the moving plate. The optical adjustment mechanisms(7,9) are allow a precise positioning

of the laser beam with respect to the lens. Linear bush bearings(6) fitted on the moving plate enables it to slide smoothly on four supporting columns(10). The power screw(1) is driven by a belt-pulley system(5) which in turn are driven by a stepper motor(2) (Mycom Inc., Taiwan, model: PF468-02A). The power screw, belt-pulley system and motor are attached to the fixed plate. The fixed plate(3) (made of steel) rests on leveling screws(11) so an accurate horizontal positioning of the laser sheet is possible. The motor is a 4 phase stepping motor with ratings of 4.5 volt, 2 amperes and has a least count rotation of 1.8 degrees per step. The motor is computer controlled using the DMC smart terminal software and electronic controller manufactured by GALIL Motion Control Inc., USA. The motor has been programmed using the software to automate the up and down movement of the horizontal laser sheet. Any of the parameters, i.e. the traverse speed, number of cycles and range can be varied in the program. In our experiments, we have set the traverse speed of the laser sheet to 3 mm s^{-1}. The laser sheet moves up and down for a fixed number cycles (~10) and covers a fixed range (~5 cm) in every cycle. The Traverse setup allowed the study of plume structures in different horizontal sections in a controlled manner. The traverse setup can also be used to visualize horizontal sections at different heights without the motor driving it. Further details on the use of Traverse setup in our experiments and analysis are described in the next chapter.

2.7 Experimental Procedure

A typical experiment was conducted in the following manner:

1. The plume fluid, consisting of the bottom chamber fluid and fluid in the constant head setup, was prepared by adding the required amount of rhodamine dye (0.5 ppm by mass) into a known quantity of tap water. If the

experiment is a case of U < 1, then the CMC solution was prepared with the dye dissolved.

2. The constant head setup is cleaned and then filled with the freshly prepared fluid mentioned in the previous step. It is connected to the tank after the bottom chamber fluid is filled almost to the level of the mesh. Care is taken to ensure that there are no bubbles present in the circuit. The shroud is placed in the bottom chamber and the required flow rate is set.
3. The mesh is cleaned under a jet of water immediately after every experiment. Also, it is cleaned before the start of the experiment and left to dry. The O-ring is tightly placed in its slot on the permanent steel frame. The mesh frame is lowered and screwed tightly onto the permanent steel frame.
4. The stop valves are opened and the constant head setup starts delivering fluid to the bottom chamber. The valves are open till the fluid passes through the mesh and not through the sides; this is a check for leaks. After ensuring there are no leaks, the small amount of fluid on the mesh is carefully removed using a sponge. A circular spirit level is placed on the mesh and the tank is leveled to make it horizontal. A small glass plate is then placed on the mesh.
5. The top chamber fluid is prepared before the experiment. To have the upper chamber fluid being denser, 48.24g of sugar (Parry's double refined sugar) was dissolved in 6.5 L of water. If the experiment was a case of U > 1, the sugar was dissolved in the CMC solution. This fluid is slowly poured into the top chamber and left to rest for a while.
6. The camera is positioned in the required location (on top for the planform and traverse experiments, on a tripod for the vertical section experiments). The camera is focused on the test section with an optimal zoom.

7. The laser is turned on and the laser sheet is carefully set to the required position.
8. The glass plate on the mesh is removed very slowly to minimize the disturbance. The inside glass tank is inserted slowly and placed accurately on the mesh frame. The disturbance is left to settle down for a few minutes. All external lights are switched off and the experiment is started by opening the stop valves. The capillary level in the constant head setup is adjusted and kept constant by operating the fine control valve. The cameras are turned on and recording of photos/videos is started.

2.8 Experiments – Methodology and other Details

As mentioned before, in our experiments, the convection is driven by compositional buoyancy resulting from a concentration difference across the mesh between sugar solution in the upper chamber and tap water in the bottom chamber. We use the analogy between heat transfer and mass transfer phenomena and modify the thermal Rayleigh number (Ra) to define a compositional Rayleigh number, (Ra_c) as:

$$Ra = \frac{g\beta_T \Delta T H^3}{\nu\alpha} \quad \Longrightarrow \quad Ra_c = \frac{g\frac{\Delta\rho}{\rho}H^3}{\nu\alpha_m} \tag{7}$$

The Schmidt number (Sc) is the proxy for Prandtl number (Pr):

$$Pr = \frac{\nu}{\alpha} \quad \Longrightarrow \quad Sc = \frac{\nu}{\alpha_m} \tag{8}$$

The viscosity ratio (U) is defined as:

$$U = \frac{\nu_a}{\nu_p} \tag{9}$$

The aspect ratio (AR) is defined as:

$$AR = \frac{L}{H} \qquad (10)$$

Here, g = acceleration due to gravity, β_T = coefficient of thermal expansion, ΔT = temperature difference between the walls, H = height of the fluid layer, ν = kinematic viscosity, α = thermal diffusivity of the fluid, L = horizontal dimension of the fluid layer, $\Delta\rho$ = density difference between the ambient fluid and plume fluid, ρ = density of the plume fluid, α_m = mass diffusivity of sugar in water, ν_a = kinematic viscosity of the ambient fluid, ν_p = kinematic viscosity of the plume fluid.

The Rayleigh number (Ra_c) is usually based on the kinematic viscosity of the ambient fluid unless mentioned otherwise. We are able to achieve large values of Sc, due to the smaller value of mass diffusivity of sugar in water compared to thermal diffusivity. Note that the viscosity ratio (U) can also be considered to be the ratio of the kinematic viscosity of the fluid in the upper chamber to the kinematic viscosity of the fluid in the bottom chamber.

We start the experiments with the top chamber fluid filled till 15.5 cm height. The starting Aspect ratio is 1 and goes on decreasing as the experiment progresses. We have an externally imposed flow of water from below using the constant head setup described in section 2.3. Hence, the height of the fluid layer in the top chamber rises with time due to the influx of fresh lighter fluid from below. Our region of interest for visualization is the top chamber since the forced through flow across the mesh prevents the flow of fluid from the top chamber into the bottom chamber. A typical experiment would last for about 20 minutes. The experiment is stopped when the

height of the fluid layer reaches the brim of the tank and the aspect ratio AR = 0.62 at the end of the experiment.

The convection is unsteady in the sense that the height of the fluid layer is increasing. However, we observed that the convection is initially transient and settles down to a quasi-steady state in a statistical sense. We have considered data from the quasi-steady state in our analysis.

Our experiments can be broadly divided into 2 sets: In set (1), we have varied the viscosity ratio systematically keeping other parameters constant. The set (2) consists of preliminary experiments which will be discussed separately in section 3.2 in Chapter 3. The discussions throughout the thesis except in section 3.2 in Chapter 3 refer to set (1) experiments.

The parameter ranges we have covered are: U = 0.003 to 2500, Ra_c = 10^8 to 10^{11}, Sc =10^3 to 10^6 with a constant buoyancy flux. An initial density difference of $\Delta\rho$ = 2.4 kg m^{-3} was maintained constant in all of the experiments. The through flow rate is also held constant at $Q = 4$ mL s^{-1}, i.e. the buoyancy flux is held constant throughout the duration of the experiment in all the cases where U>1. Across the mesh, this corresponds to a through flow velocity, $V_i = 0.083$ cm s^{-1}. We have ensured that the through flow velocity is small (~1/10th) compared to the plume rise velocities. In experiments where U<1, there were limitations in maintaining a constant flow rate as viscous fluid had to be forced through the mesh. In the U<1 experiments, the through flow rates quoted (Table 3) are averaged over the duration of the experiment.

Table 2 lists the all the experiments. The naming convention is described below.
The Planform (top view) experiments are labelled PExpt(#), where, # = experiment number. The vertical section experiments are labelled VExpt(#) and experiments

using the Traverse setup are labelled TExpt(#). A few experiments were conducted using the Traverse setup without using the motor. The laser sheet was moved without using the motor to capture horizontal sections at different heights, these experiments are labelled MExpt(#). Table 3 lists the relevant parameters for all the experiments.

Experiment #	U	Planform PExpt	Vertical VExpt	Traverse TExpt	Mixing MExpt
1	1	PExpt1	VExpt1	TExpt1	
2	3	PExpt2			
3	5	PExpt3			
4	7	PExpt4			
5	15	PExpt5			
6	25	PExpt6	VExpt2		
7	65	PExpt7		TExpt2, m	
8	130	PExpt8			
9	300	PExpt9	VExpt3	TExpt3	
10	470	PExpt10			
11	930	PExpt11		TExpt4, m	
12	2500	PExpt12	VExpt4	TExpt5	
13	1/300		VExpt5	TExpt6,8, m	
14	1/130		VExpt6		MExpt1
15	1/65		VExpt7	TExpt7, m	
16	1/25				MExpt2

Table 2: A list of all the experiments and their labels

Experiment #	CMC %wt	U	Ra_c x 10^8	Sc x 10^3	Q (mL s^{-1})
1	0	1	2934	2	4
2	0.025	3	978	6	4
3	0.05	5	586	10	4
4	0.1	7	419	14	4
5	0.15	15	195	30	4
6	0.2	25	117	50	4
7	0.3	65	45	131	4
8	0.4	130	22	262	4
9	0.5	300	9.78	604	4
10	0.6	470	6.24	946	4
11	0.75	930	3.15	1873	4
12	1	2500	1.17	5035	4
13	0.5	1/300	2934	2	2
14	0.4	1/130	2934	2	3.2
15	0.3	1/65	2934	2	3.7
16	0.2	1/25	2934	2	4

Table 3: Experimental Parameters

Chapter 3
Results and Analysis

Our objective is to study the effect of viscosity ratio (U) and buoyancy flux on the plume structure and dynamics in high Rayleigh number convection. In this chapter, we report the results and analyses from our experiments.

3.1 Role of Viscosity Ratio (U) on plume structure and dynamics

Here, we consider experiments where the viscosity ratio U has been changed over a range of U = 0.003 to 2500, and other parameters have been kept constant. The density difference was $\Delta\rho$ = 2.4 kg m^{-3} and the through flow rate (and hence buoyancy flux) was $Q = 4$ ml s^{-1} for all the experiments (except in a few cases which will be highlighted).

3.1.1 Near-wall planform plume structure

As mentioned before, the planforms of high Rayleigh number convection relevant to mantle convection have not been understood well. In particular, there is no previous experimental study that focuses on understanding the role of viscosity ratio on the planform plume structures using compositionally driven buoyancy to drive the convection.

The planform refers to horizontal sections that are perpendicular to the direction of flow. These refer to the convective structures seen from the top. Here, we report results from our study on convective planforms in the near wall region. In the section on traverse experiments, we describe studies of planform structures at different horizontal sections. The study of the planforms in the near-wall region is important to

understand the dynamics of plume formation and their eventual detachment from the boundary layer. We have carried out experiments to visualize the near-wall planform structures at different viscosity ratios. The objective is to characterize the geometry and statistics of the near-wall planform structures. We have studied the effect of the viscosity ratio (U) on the plume spacing and thickness. The near-wall planforms obtained from two different sets of experiments is analyzed. In the first planform analysis set (PSet1), we use data from experiments PExpt1 to PExpt12 (refer Table 2) for cases where U > 1, and experiments TExpt6, MExpt1, TExpt7 and MExpt2 (refer Table 2) for cases where U < 1. Thus, PSet1 consists of data from 16 experiments. In the second planform analysis set (PSet2), we use data from experiments TExpt1 to TExpt7, a total of 7 experiments. Next, we compare results from both sets.

Figure 13(a) and (b) show montages of the near-wall plume structures for PSet1. The raw images from the experiment are shown in Figure 13(a) and the corresponding binary images are shown in Figure 13(b). The image size is 2052 x 2052 pixels corresponding to a resolution of 0.075 mm per pixel. The binary images make it easier to identify the changes and are used for quantitative analysis. In Figure 13(a) and (b), there is a progressive increase in the viscosity ratio U as we go from cases [1] to [16] (U = 1/300, 1/130, 1/65, 1/25, 1, 3, 5, 7, 15, 25, 65, 130, 300, 470, 930, 2500). It has been mentioned before, that in our experiments, the convection is initially transient and takes time to reach a quasi-steady state. The images selected in PSet1 have been taken with this consideration to ensure that quasi-steady state has been reached. Also, the images have been selected to ensure that the structures have been uniformly distributed on the test section.

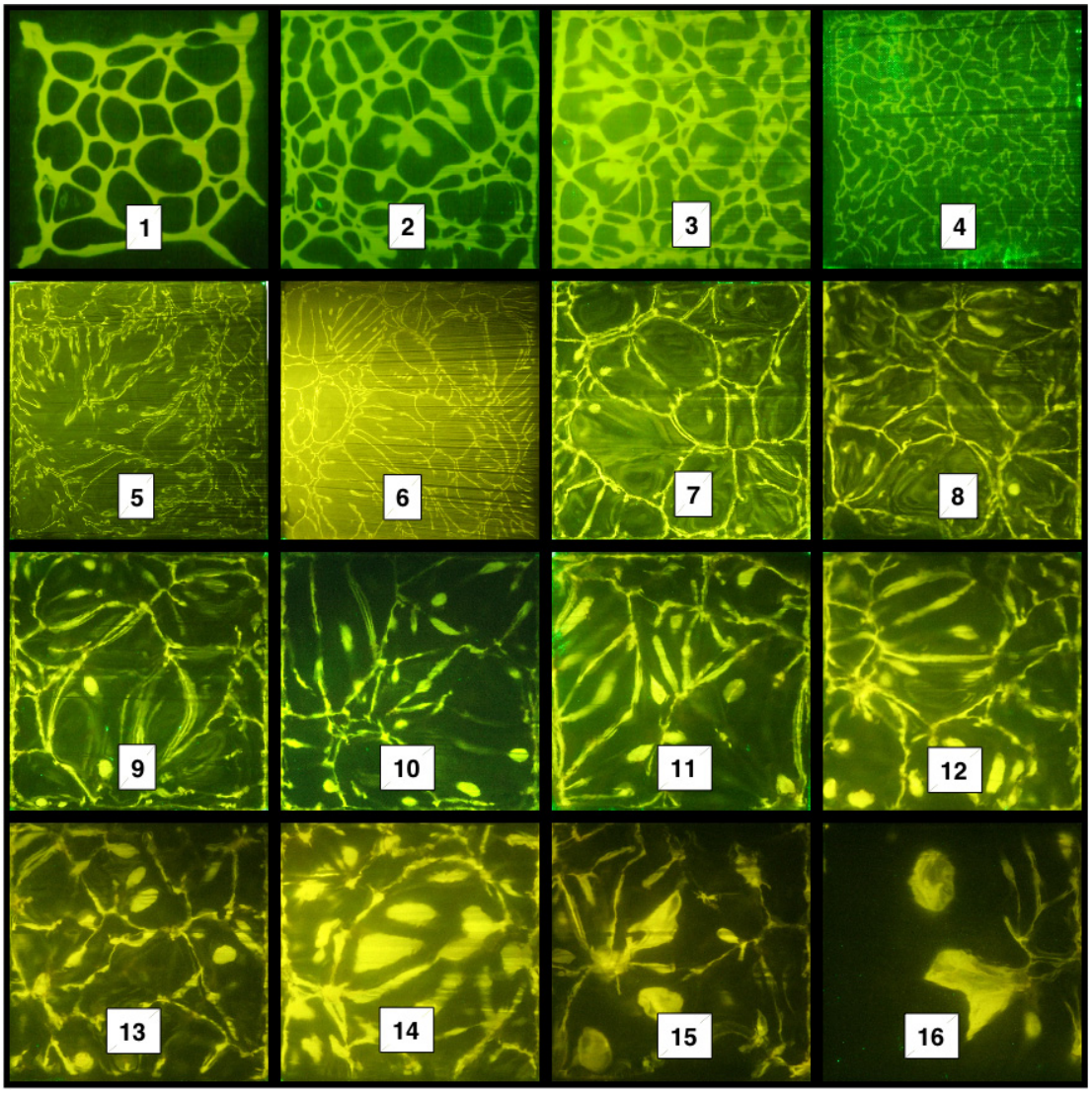

Figure 13(a): Near-wall plan view images of plume structures in a set 16 experiments.
The set of images shown above are raw images (2052 x 2052 pixels) from the experiment.
The viscosity ratio U is increased progressively (U = 1/300, 1/130, 1/65, 1/25, 1, 3, 5, 7, 15, 25, 65, 130, 300, 470, 930, 2500) in cases[1] to [16].

A repetition of some cases (PExpt1 and 7) showed that the planform structures have the same characteristics in an average sense. Let us assume that time t = 0 seconds at the start of the experiment (when the fluid from bottom chamber started flowing across the mesh). The images in PSet1 were selected at: t = 75, 310, 135, 185, 130, 110, 110, 285, 420, 400, 650, 465 seconds. These correspond to cases [5] to [16] (PExpt1 to PExpt12) shown in Figure 13(a) and (b). It is evident from this data that the convection takes more time to settle to a quasi-steady state as U increases.

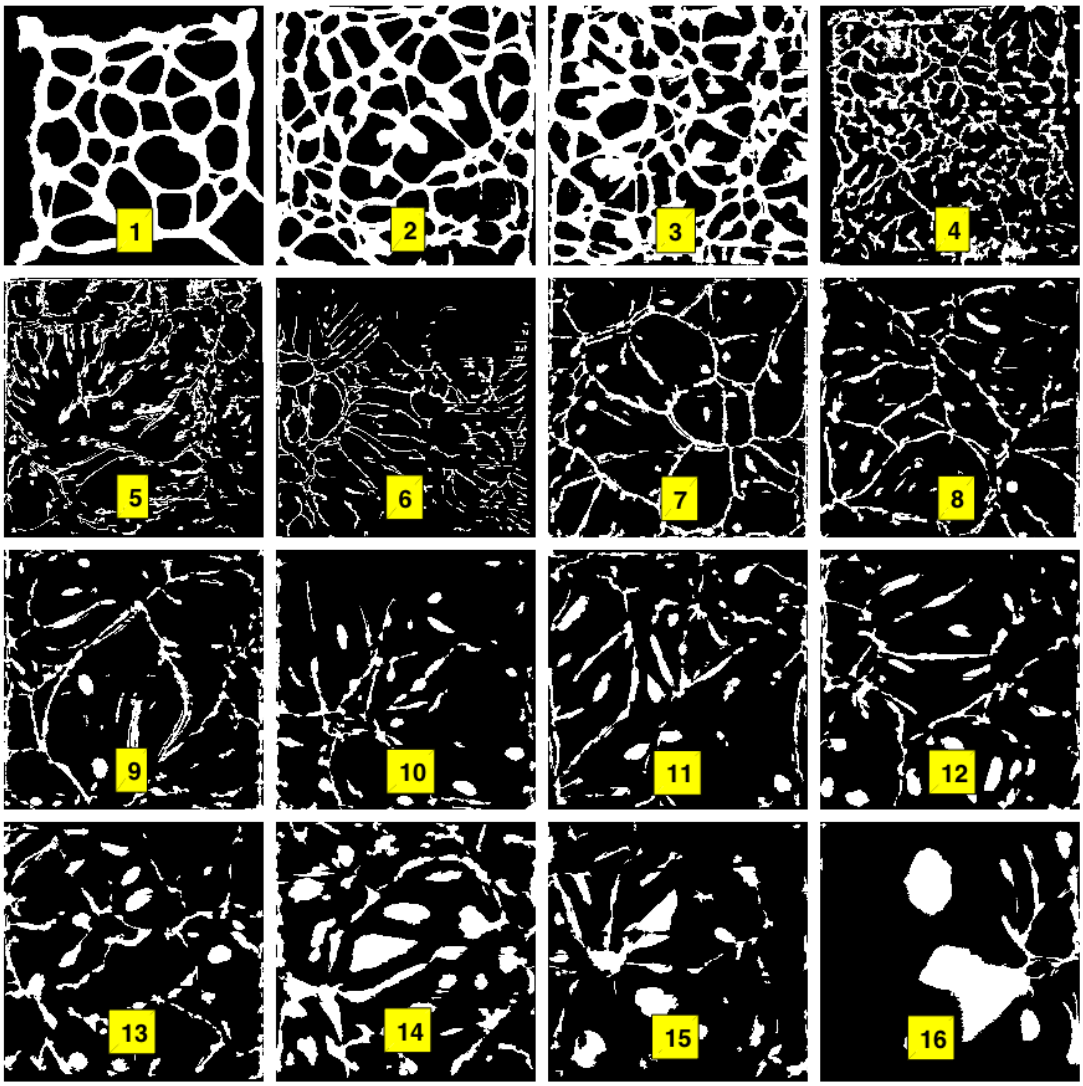

Figure 13(b): Near-wall plan view images (binary) of plume structures in a set 16 experiments. The raw set of images shown in Fig 13(a) have been converted into binary images. The structures in white colour correspond to plumes and the background is black. The viscosity ratio U is increased progressivley (U = 1/300, 1/130, 1/65, 1/25, 1, 3, 5, 7, 15, 25, 65, 130, 300, 470, 930, 2500) in cases [1] to [16].

All the experiments where U < 1 have been conducted using the traverse setup and we have selected images from TExpt6, MExpt1, TExpt7 and MExpt2. The considerations taken into account for selecting images from PSet1 have been used here also. The images were selected at t = 254, 348, 205, 207 seconds and correspond to cases [1] to [4] shown in Figure 13(a) and (b). There is an additional consideration for these experiments where U < 1. It has been observed that there is a formation of a thick boundary layer (~ 2 to 4 mm thickness) above the mesh in these experiments. So there

is an uncertainty about the selection of an image representative of the near-wall planform structure. In experiments where U > 1, the near-wall planform structures are those which are just above the mesh (~ 1mm above the mesh). In experiments where U<1, there is a formation of cellular patterns just above the thick boundary layer. We select images of the planform structures at a height above the mesh beyond which the cells walls start to disintegrate. This would correspond to a height of ~ 1 to 2 mm above the thick boundary layer.

We now give a qualitative description of the changes in the near-wall planform structure. The planform mainly consists of line plumes with a dendritic structure at U = 1 (case [5], Figure 13 (a) and (b)). This is a familiar structure seen in previous experimental studies (e.g. Puthenveettil and Arakeri 2008). In our case, the spacing between the line plumes is higher than that found by Puthenveettil and Arakeri 2008, mainly because of the forced through flow across the mesh. As the viscosity ratio increases to U = 3,5,7, the spacing between the line plumes as well as their thickness increases (cases [6] to [8], Figure 13 (a) (b)). With increase in U, from U=15 (case [9]) onwards there is a transition from line plumes to discrete circular blobs which start dominating the morphology with further increase in U. The line plumes become thicker and gradually lose their prominence at U = 300 (case [13]) where the blobs are the characteristic structures. As U increases even more, the blobs increase in size. Finally, at U = 2500 (case [16]), there are mainly ~ 2 to 3 isolated large blobs. The slenderness ratio (width/length) of the plumes in the planform tends to unity as U increases from 1 to 2500 (cases [5] to [16]). In the other regime when U < 1, the formation of cellular patterns is favoured. When U = 1/300 (case [1]), the plumes are connected to form approximately round cells. The cell size decreases as U increases till U = 1/65 (case [3]). When U increases to 1/25 (case [4]) cells are no longer able to

form and the structure approaches the U = 1 case (case [5]). The plumes in case [4] are thicker and have a uniform size than in case [5] and the spacing is smaller (more densely spaced).

We now consider the second planform analysis set (PSet2). This set consists of 7 cases with images taken from experiments TExpt1 to TExpt7 (refer Table 2). In these experiments, the traverse setup provided a precise positioning (< 1mm) and control of the moving horizontal laser sheet. Figure 14(a) and (b) show montages of the near-wall plume structures for PSet2. The raw images from the experiment are shown in Figure 14(a) and the corresponding binary images are shown in Figure 14(b). The image size is 720 x 720 pixels corresponding to a resolution of 0.21 mm per pixel. The viscosity ratio U is progressively increased (U = 1/300,1/65,1, 65,300,930,2500) in cases[1] to [7] respectively. The images were selected at time t = 245, 161, 129, 190, 154, 273, 691 seconds for cases [1] to [7] shown in Figure 14. The Qualitative changes are similar to those reported for PSet1.

When U increases (>1) the plume spacing and thickness increases (cases [3] to [7]) accompanied by the transition from line plumes to discrete blobs. The blobs start dominating the morphology from case [5] (U=300). On the other end of the regime, when U<1, the cell size is largest for case [1] (U=1/300) and decreases as we move towards U = 1.

To demonstrate the transient to quasi-steady state nature of the convection in our experiments, we have put together a collection of images in Figures 15 (a) to (g). Images of the near-wall planforms have been extracted at successive time intervals in each of the traverse experiments (TExpt1 to TExpt7) and displayed as a montage in Figures 15 (a) to (g).

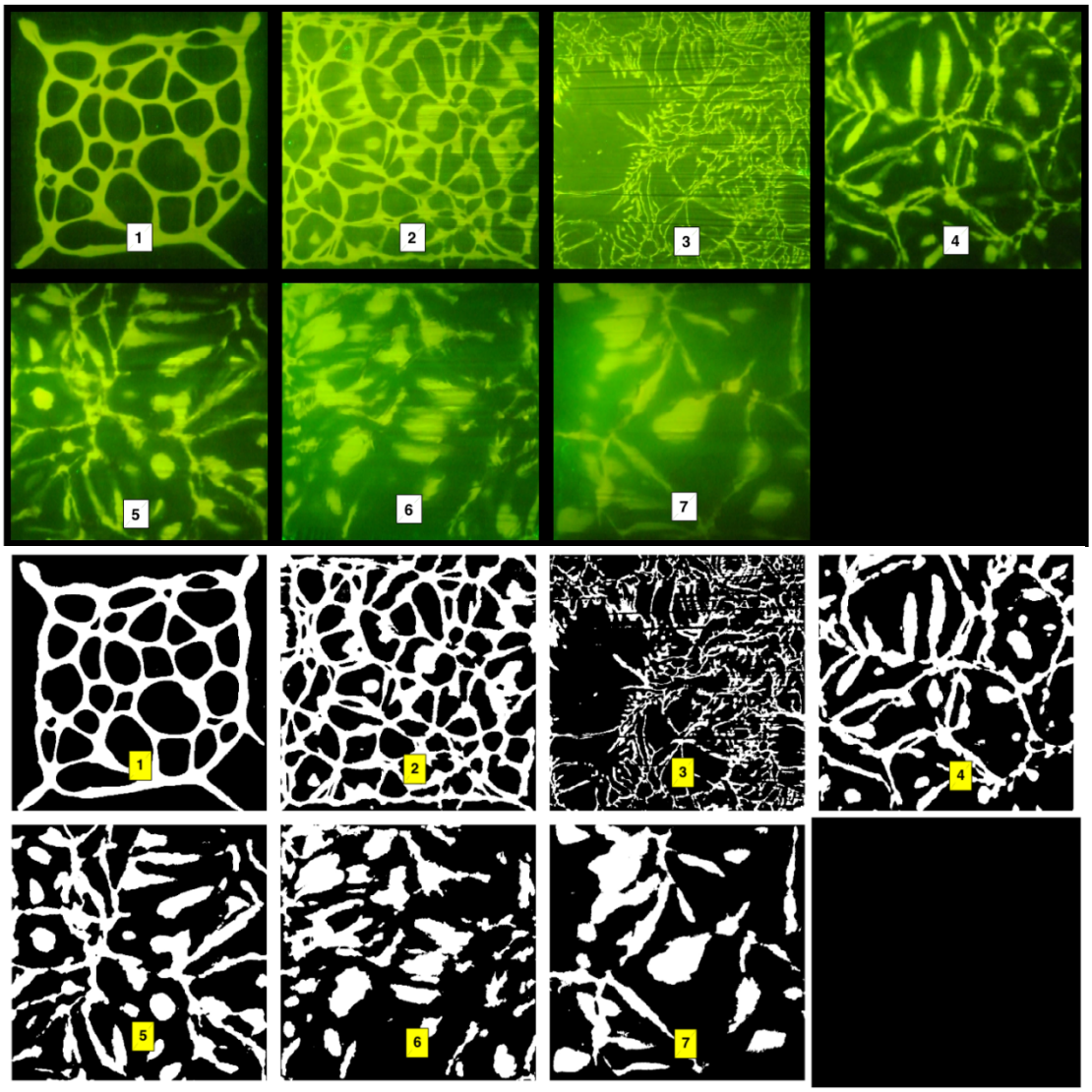

Figure 14: Near-wall plan view images of plume structures in a set of 7 experiments (PSet2). The set of images shown on top are raw images from the experiment and the set shown below are the corresponding images in binary. The viscosity ratio U is increased progressively (U = 1/300,1/65,1, 65,300,930,2500) corresponding to cases[1],[2],[3],[4],[5],[6] and [7].

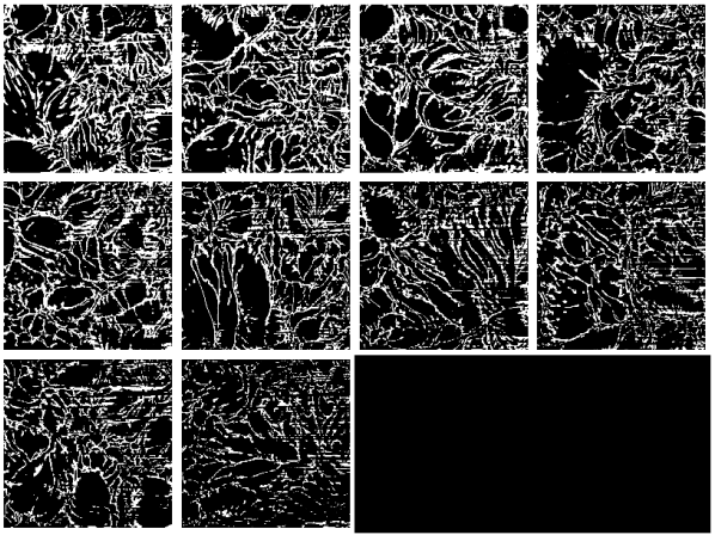

Figure 15: (a) Images from TExpt1, U = 1, Images are shown in ascending order of time from start of experiment: t = 42s, 71s, 100s, 129s, 158s, 188s, 217s, 246s, 275s, 305s.

Figure 15: Near-wall plan view images of plume structures showing transient to steady state transitions

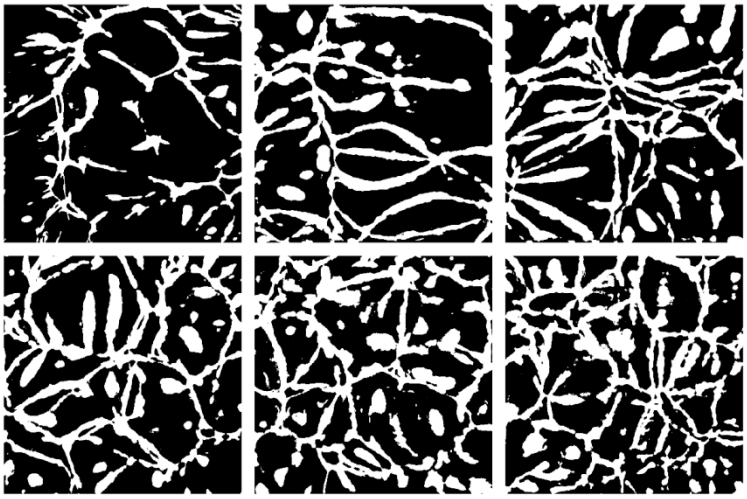

Figure 15: (b) Images from TExpt2, U = 65, Images are shown in ascending order of time from start of experiment: t = 46s, 92s, 141s, 190s, 240s, 289s.

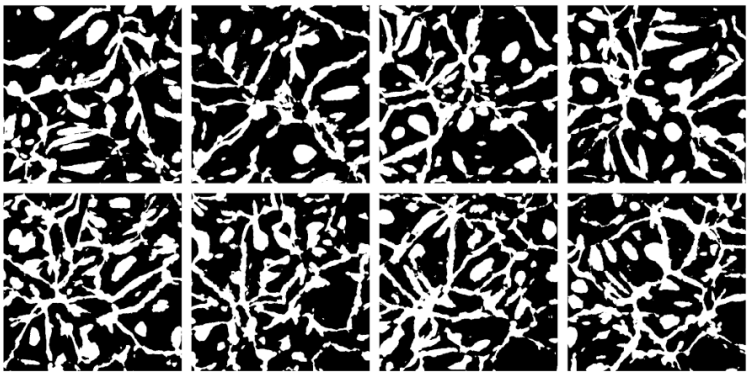

Figure 15: (c) Images from TExpt3, U = 300, Images are shown in ascending order of time from start of experiment: t = 35s, 74s, 114s, 154s, 194s, 233s, 273s, 313s

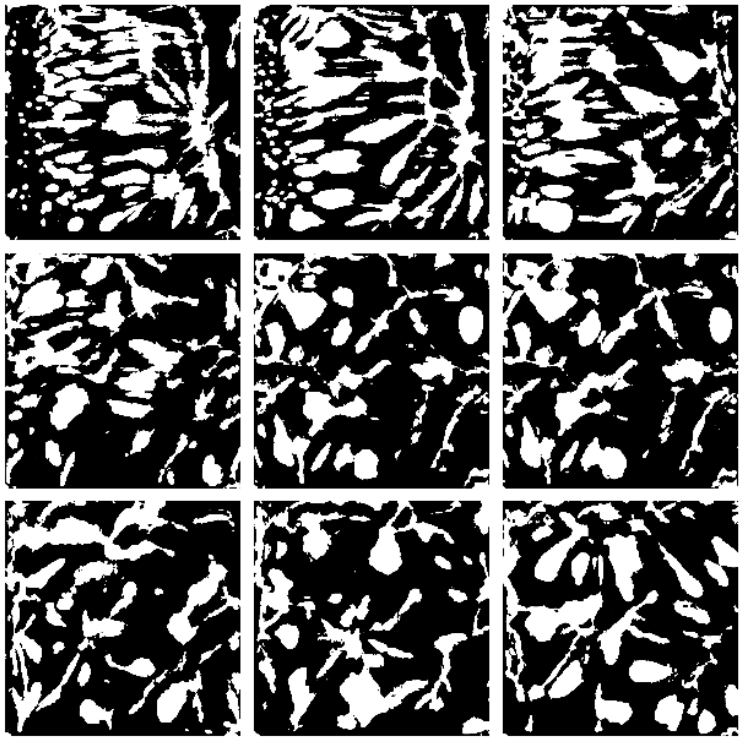

Figure 15: (d) Images from TExpt4, U = 930, Images are shown in ascending order of time from start of experiment: t = 126s, 175s, 224s, 273s, 319s, 331s, 380s, 429s, 478s

Figure 15: Near-wall plan view images of plume structures showing transient to steady state transitions

Figure 15: (e) Images from TExpt5, U = 2500, Images are shown in ascending order of time from start of experiment: t = 571s, 611s, 651s, 691s, 731s, 771s, 811s, 851s

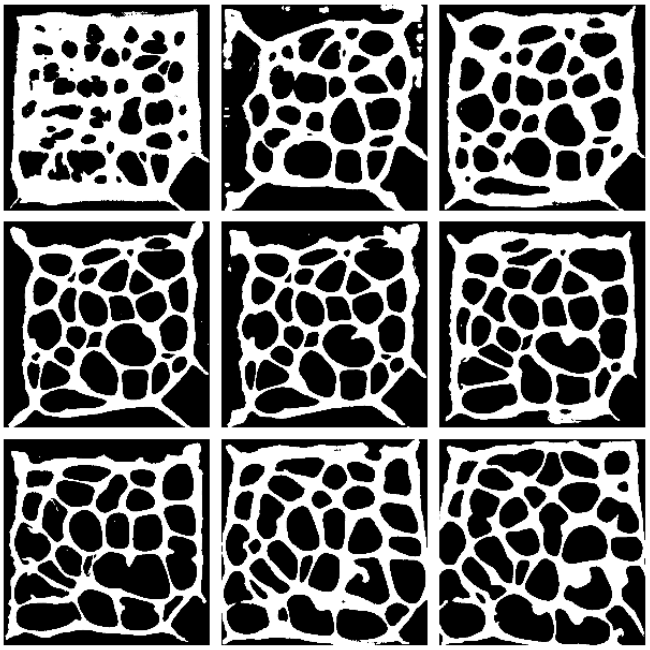

Figure 15: (f) Images from TExpt6, U = 1/300, Images are shown in ascending order of time from start of experiment: t = 103s, 154s, 205s, 245s, 254s, 305s, 356s, 407s, 458s.

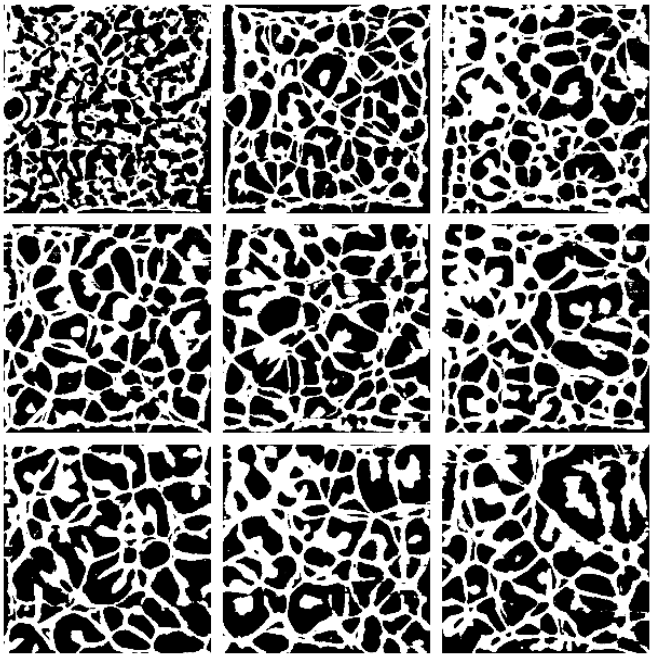

Figure 15: (g) Images from TExpt7, U = 1/65, Images are shown in ascending order of time from start of experiment: t = 14s, 63s, 112s, 161s, 210s, 259s, 303s, 352s, 401s.

Figure 15: Near-wall plan view images of plume structures showing transient to steady state transitions

Figure 15 gives an idea of the changes in planform structures over time in different experiments. In Figure 15 (a) (U = 1) we see that the structures are almost the same in all the images at different times. When U>1, the transients take time to settle; In Figure 15 (b) (d) and (e) the convection takes time till the fourth frame to settle to a quasi-steady state. When U<1, the cellular patterns become stable only from the fourth frame onwards (Figure 15 (f) and (g)). We have selected the fourth frame in each of the cases ((a) to (g)) in Figure 15 for the analysis in PSet2.

So far we have described the changes in plume structure qualitatively. Now, we describe the approaches we have used for a quantitative analysis of plume spacing and thickness for cases of different viscosity ratio. We have a written a code in Matlab to read the selected image and analyze it to give distributions of plume spacing and thickness as output. The code first reads a raw image and uses the adaptive histogram equalization technique in the image processing toolbox in Matlab. This is an important step as the images generally have a non-uniform intensity. Raw images also have lines caused due to a lensing effect by small plumes. These irregularities in the image pose problems for conversion to a binary image. The adaptive histogram technique greatly helps us overcome these problems. Care is taken to retain all the major features of the raw image, when the image is converted into a binary image by using a suitable thresholding value. From the binary image, the code calculates an autocorrelation of each row (or column) (hereafter referred to as a line) of the image in horizontal and vertical directions. The autocorrelation is computed using fast fourier transforms for each line. The result is a plot with a prominent central autocorrelation peak and other neighboring peaks which have lesser magnitudes on y-axis and the x-axis gives the length scale. The plot is symmetric about the central peak. The distance between the central peak and the centre of the next largest peak is

the value of characteristic plume spacing in that line. Half of the thickness of the central autocorrelation peak gives the value of the thickness of the plumes. The code thus outputs a value for the characteristic plume spacing and thickness for every line. Figure 16 shows a binary image of the near-wall planform image corresponding to PExpt1 (U = 1). The length scales of plume spacing and thickness that are obtained as outputs from the code are listed on the right side of Figure 17, and the lengths are drawn to the scale of the test section shown (15.5 cm). The distribution of plume spacings is plotted in a histogram as shown in Figure 17. The histogram shown in Figure 17 is for case [1] in PSet1, where U = 1 (PExpt1) and is the output from the code for all horizontal lines covered. The code picks up many different spacing values and thus there is a wide distribution seen in the histogram. However, we consider the largest peaks in the histogram to be the indicative of typical plume spacing in the image. In Figure 17, the characteristic spacing is 0.4 cm with a frequency of 32. A similar histogram for spacing is obtained from the code for the vertical lines in the image. The horizontal and vertical line distributions of plume spacing are added up to give combined histogram as shown in Figure 18. In this combined histogram of plume spacings from horizontal and vertical lines, we remove the jitters in the peaks and obtain a smooth curve fit on the distribution to identify the most characteristic spacing value. This is done by taking a fourier transform of the curve with jitters. Higher wavenumbers corresponding to the jitters are cut-off in frequency space and an inverse fourier transform is taken to obtain the smooth fit. This process of obtaining a smooth curve fit results in a spurious peak at the end, which is ignored. In the histogram shown in Figure 18, the characteristic spacing value is identified as 0.4 cm with a frequency of 120, other spacing values are 0.77cm (frequency of 50). The plume thickness is also determined in a similar manner. The code also outputs a

histogram of the plume thickness obtained from autocorrelations of horizontal and vertical lines of the image. Figure 19 shows such a histogram plot for case [1] in PSet1, where U = 1 (PExpt1). Like the plume spacings, the thickness histograms from horizontal and vertical line autocorrelations are added up to give a joint histogram as shown in Figure 20. We run the code for images in all the cases and obtain the characteristic plume spacing and thickness values and compare them later. Appendix-1 contains all the plume spacing and thickness histograms for PSet1.

In the literature, we do not find an expression for plume spacing over the entire parameter range covered in the present study. Hence, we compare existing theoretical estimates for plume spacing as a function of Rayleigh number for similar systems. Theerthan and Arakeri (1998) have derived an expression that predicts the near-wall plume spacing as a function of the Rayleigh number for Rayleigh-Benard convection and also in general for convection over heated horizontal surfaces.

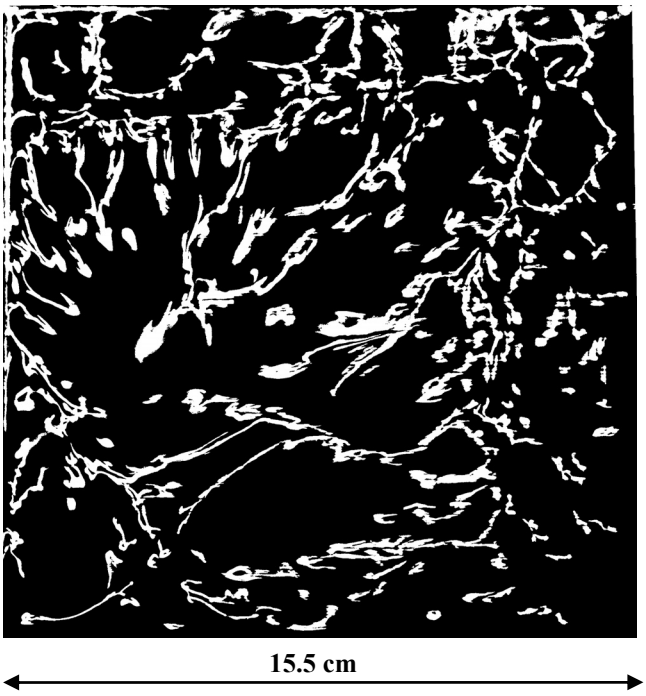

Spacing in cm (frequency of occurrence)

0.4(120)
0.77(50)
1.12(40)
2.85(32)
4.8(32)

0.4 cm

0.77 cm

1.12 cm

Thickness in cm (frequency of occurrence)

0.26(430)
0.57(60)
0.46(40)

Figure 16: The near-wall planform binary image corresponding to PExpt1 is shown above. The test section length scale of 15.15 cm is also shown. On the right side, the lengths correspond to the spacing values obtained form the code. Above and below the length scales, typical plumes spacing and thickness are listed along with their frequencies

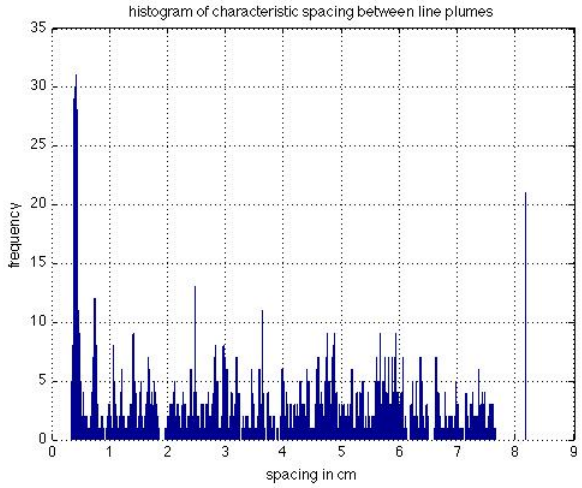

Figure 17: Histogram of characteristic plume spacing obtained from the code. This is the histogram of plume spacings obtained from taking autocorrelations of horizontal lines of the image.

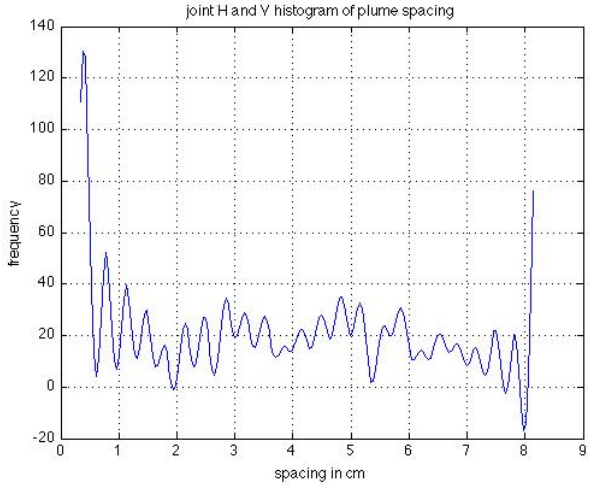

Figure 18: A combined histogram of characteristic plume spacing obtained from the code. This is the histogram of combined distributions of plume spacings obtained from taking autocorrelations of horizontal and vertical lines of the image.

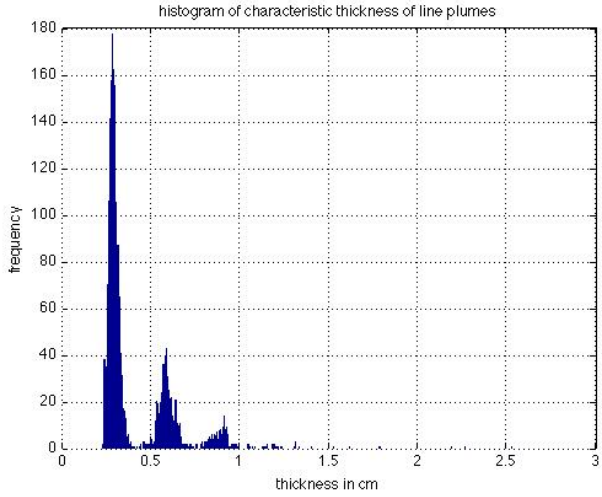

Figure 19: Histogram of characteristic plume thickness obtained from the code. This is the histogram of the plume thickness obtained from taking autocorrelations of horizontal lines of the image.

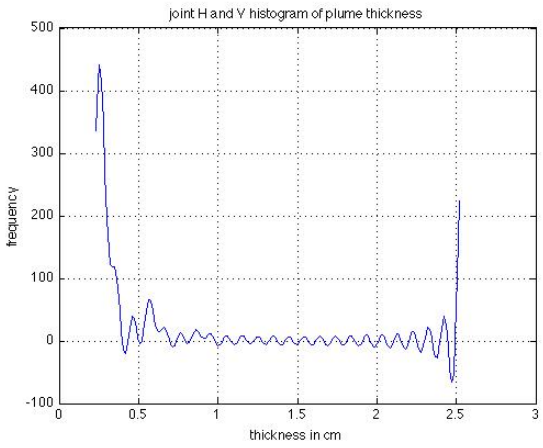

Figure 20: A combined histogram of characteristic plume thickness obtained from the code. This is the histogram of combined distributions of plume thickness obtained from taking autocorrelations of horizontal and vertical lines of the image.

The plume spacing λ_c normalized by the characteristic length D, is derived to be:

$$\frac{\lambda_c}{D} = 67(Ra)^{-1/3} \qquad (11)$$

where, Ra = Rayleigh number, $Ra = \frac{g\beta T \ \ \Delta T D^3}{\nu\alpha}$

Puthenveettil and Arakeri (2005, 2008) studied turbulent natural convection using the method of driving convection across a fine membrane using salt to create an unstable density difference. Depending on the mode of transport across the membrane, they have identified three regimes of convection namely an advection regime (2008), a diffusion regime (2005) and a combined regime. The theoretical prediction for plume spacing in the diffusion regime at Sc ~ 600 is:

$$Ra_\lambda^{1/3} = \frac{\bar{\lambda}}{Z_w} \cong 92 \qquad (12)$$

where, Ra_λ is the Rayleigh number based on mean plume spacing $\bar{\lambda}$ in the diffusion regime. Z_w is a near-wall length scale for turbulent natural convection, $z_w = \left[\frac{\gamma\alpha}{g\beta\Delta c_w}\right]^{1/3}$. Appendix – 2 gives detailed calculations and descriptions. In the advection regime, there is a strong through flow across the membrane. The situation is closely relevant to our system when U = 1. The theoretical prediction for plume spacing in the advection regime is:

$$Ra_{\lambda}^{1/3} = \frac{\bar{\lambda}}{Z_w} = 2K^{2/3}Ra^{1/6}\sqrt{\frac{Z_v}{H}}Sc^{1/6} \qquad (13)$$

where, $Z_v = \frac{\nu}{V_i}$ is the length scale due to advection, ν is the kinematic viscosity of the ambient fluid V_i is the through flow velocity, K is a constant, H is the characteristic length and Sc is the Schmidt number.

Kerr (Kerr 1994) conducted experiments on melting driven by vigorous compositional convection. Scaling analysis is used to determine the velocity V of the melt layer when melting of a solid overlain by a fluid of higher temperature leads to vigorous compositional convection. The timescale and wavelength for exponential growth of the fastest growing instabilities of this buoyant melt layer is predicted by a linear Rayleigh Taylor stability analysis. The thickness of the melt layer h_m is given by:

$$h_m \sim \left(\frac{PV\mu_m}{g(\rho_f - \rho_m)}\right)^{1/2} \qquad (14)$$

where, $P = f\left(\frac{\mu_f}{\mu_m}\right)$, μ_m is the viscosity of the melt layer, μ_f is the viscosity of the fluid, ρ_m and ρ_f are the densities of the melt layer and fluid respectively, and g is acceleration due to gravity. The plume spacing, λ is given by:

$$\lambda = Q\pi h_m \qquad (15)$$

Where, $Q = f\left(\frac{\mu_f}{\mu_m}\right)$ $\qquad \lambda \cong \pi h_m \qquad for\ \mu_f \sim \mu_m$

$$\lambda \cong h_m\left(\frac{\mu_f}{\mu_m}\right)^{1/3} \qquad for\ \mu_f \gg \mu_m$$

We have quantified the dependence of plume spacing and thickness in our experiments as a function of the compositional Rayleigh number and viscosity ratio using the code. We have compared our results to the existing estimates of plume spacing from previous work mentioned above. (refer Appendix – 2 for detailed

calculations). Table 4 lists values of plume spacings obtained from the expressions derived by previous work (equations 11 to 15) and compares them with the results from our experiments. The Plume spacing is plotted as a function of Rayleigh number in Figure 21 for the U>1 regime. We identify the characteristic plume spacings and thicknesses for each case from the code output and write down their corresponding frequencies. Each case has typically 3 to 5 characteristic values of plume spacing and thickness. We define a weighted average as follows:

$$\lambda_{wavg} = \frac{\sum_i \lambda_i f_i}{\sum_i f_i} \qquad (16)$$

Where, λ_{wavg} is the weighted average plume spacing, λ_i is a plume spacing value and f_i is its corresponding frequency of occurrence. Note that the frequency is used as the weight in the definition of weighted average. A similar weighted average is defined for the plume thickness. The last column in Table 4 lists weighted average values obtained from the code for PSet1 experiments. We have used the weighted average definition to define the plume spacing and thickness for each experiment in PSet1 and PSet2. Note that in Figure 21 we only have considered cases where U > 1. Figure 21 also has curves obtained from the expressions (equations 11 to 15) given by Kerr (1994), Puthenveettil and Arakeri (2005), and Theerthan and Arakeri (1998). We carried out another set of analysis by considering a central 50% area of the total area of the image. The code was run on these images which resulted in the trend shown by the cyan curve in Figure 21. The black curve in Figure 21 represents the plume spacing values obtained in U>1 experiments for PSet1. The magenta curve represents the spacing values for U>1 experiments in PSet2. Both the curves for PSet1 and PSet2 do not match any of the curves from previous theories. Both however, represent a similar trend of showing an initial increase in plume spacing with decrease in compositional Rayleigh number with a peak between $Ra_c \sim 10^9$ and $Ra_c \sim 10^{10}$ and a

subsequent decrease in plume spacing with further decrease in Rayleigh number. The cyan curve represents the plume spacing data from the 50 % area set, this shows a uniformly increase in spacing with decrease in Rayleigh number. We have also plotted the thickness values obtained from the weighted average of the various plume thicknesses from PSet1. This agrees reasonably well with the plume spacing predictions of Theerthan.

Tables 5 and 7 tabulate the raw values of plume spacing and the corresponding frequency of occurrence for PSet1 and PSet2 respectively. Tables 6 and 8 tabulate the raw values of plume thickness and the corresponding frequency of occurrence for PSet1 and PSet2 respectively. The weighted average calculation in Table 4 uses the raw data in Tables 5.

U	Ra_c x 10^8	Sc x 10^3	Theerthan cm	Puthenveettil diffusion cm	Puthenveettil advection cm	Kerr cm				PSet1 λ_{wavg} (cm)
						h_m	$\lambda 1$	$\lambda 2$	$\lambda 3$	
1	2934	2	**0.15**	**0.21**	*0.05*	0.046	*0.17*	*0.14*	**0.046**	**1.37**
3	978	6	**0.22**	**0.30**	*0.14*	0.055	*0.21*	*0.17*	**0.08**	**1.55**
5	586	10	**0.26**	**0.36**	*0.21*	0.065	*0.3*	*0.2*	**0.11**	**2.34**
7	419	14	**0.29**	**0.40**	*0.29*	0.073	*0.38*	*0.23*	**0.14**	**2.15**
15	195	30	**0.38**	**0.52**	*0.54*	0.094	*0.63*	*0.29*	**0.23**	**2.74**
25	117	50	**0.45**	**0.62**	*0.82*	0.11	*0.88*	*0.34*	**0.32**	**2.42**
65	45	131	**0.62**	**0.86**	*1.8*	0.15	*1.65*	*0.47*	**0.6**	**3.15**
130	22	262	**0.78**	**1.08**	*3.2*	0.19	*2.63*	*0.6*	**0.96**	**4.89**
300	9.78	604	**1.04**	**1.43**	*6.5*	0.25	*4.58*	*0.78*	**1.67**	**3.42**
470	6.24	946	**1.2**	**1.66**	*9.5*	0.29	*6.17*	*0.91*	**2.25**	**4.46**
930	3.15	1873	**1.5**	**2.08**	*16.8*	0.37	*9.89*	*1.16*	**3.61**	**2.88**
2500	1.17	5035	**2.1**	**2.89**	*38.4*	0.51	*18.9*	*1.6*	**6.92**	**3.36**
1/300	2934	2				0.29	0.85			**4.41**
1/130	2934	2				0.23	0.69			**4.53**
1/65	2934	2				0.19	0.57			**5.26**
1/25	2934	2				0.12	0.35			**1.87**

Table 4: A tabulation of plume spacings (values in bold have been plotted in Figure 20)

U	λ_1 (cm)	f_1	λ_2 (cm)	f_2	λ_3 (cm)	f_3	λ_4 (cm)	f_4	λ_5 (cm)	f_5	λ_6 (cm)	f_6	λ_7 (cm)	f_7	λ_{avg} (cm)
1	0.4	120	0.77	55	1.12	40	2.85	32	4.8	32					1.37
3	0.4	85	0.77	50	1.45	45	3.45	35	1.9	30	3.9	28			1.55
5	0.39	60	1.4	35	3.65	35	5.5	35	2.1	27					2.34
7	0.39	50	3.75	38	2.1	35	4.45	33	0.75	33					2.15
15	0.4	80	4.9	55	2.1	30	1.45	30	7	30					2.74
25	2.2	45	0.9	40	1.75	40	4.7	40	2.65	35					2.42
65	0.4	75	5.1	45	2.7	38	3	38	5.4	35	7	35			3.15
130	7	60	6.65	50	5.1	35	2.65	30	0.35	30	4.3	30			4.89
300	7.45	50	6.65	45	2.25	45	1.85	45	1.5	45	0.4	45			3.42
470	6.55	50	3.8	48	2.75	40	7.6	35	1.1	35	4.6	35			4.46
930	0.35	70	0.73	55	3.9	50	4.35	40	5.2	38	6	32			2.88
2500	0.35	90	4.4	35	7.4	40	1.1	40	6.5	30	5.8	30			3.36
1/300	4.4	18	3.05	17	6.35	17	3.65	14	5.7	11	5.2	10	2.05	9	4.41
1/130	5.25	28	4.4	14	3	11	5.8	12	6.2	11	1.6	10			4.53
1/65	7.05	18	3.5	15	5.3	15	5	14	4	12	6.4	11			5.26
1/25	1.05	17	0.73	14	1.4	13	3.55	12	3	12	2.1	11			1.87

Table 5: A tabulation of raw values of plume spacing and frequency of occurrence for PSet1 which are used to calculate the average plume spacing values shown in Table 4.

U	λ_1 (cm)	f_1	λ_2 (cm)	f_2	λ_3 (cm)	f_3	λ_4 (cm)	f_4	λ_5 (cm)	f_5	λ_6 (cm)	f_6	λ_{avg}(cm)
1	0.38	60	0.73	43	1.08	19							0.61
65	5.65	22	7	18	2.7	13	4.8	13	3.4	12	2	12	4.58
300	2.75	18	6.4	16	5.25	15	3.6	13	1.7	13			3.99
930	3.9	19	1.1	18	0.72	16	6.4	15	3.4	14			3.03
2500	3.5	20	1.1	15	2.1	13	5.6	12	2.8	11			2.98
1/300	4.2	16	3.8	15	5.75	14	7.2	14	3	13			4.78
1/65	2.6	14	3	13	5.1	12	5.7	12	1.4	11	4.4	10	3.67

Table 6: A tabulation of raw values of plume spacing and frequency of occurrence for PSet2

U	λ_1 (cm)	f_1	λ_2 (cm)	f_2	λ_3 (cm)	f_3	λ_4 (cm)	f_4	λ_5 (cm)	f_5	λ_6 (cm)	f_6	λ_7 (cm)	f_7	λ_{avg} (cm)
1	.26	430	0.57	60	0.46	200									0.31
3	0.26	200	0.58	20	0.05	170									0.18
5	0.26	140	0.4	80	0.55	45	0.6	45							0.38
7	0.29	200	0.5	60	0.58	50	0.7	25							0.4
15	0.26	200	0.35	80	0.61	60	0.9	20							0.37
25	0.47	70	0.62	65	0.88	65	1.18	13							0.68
65	0.58	100	0.43	90	0.25	85	0.8	35	1	12	1.2	8			0.5
130	0.9	135	0.6	125	0.28	70	1.45	60	2.1	13					0.82
300	0.88	120	0.58	70	0.42	50	1.22	30	1.52	15					0.79
470	0.9	100	1.58	70	0.64	60	1.2	50	1.85	30	2.7	10			1.19
930	0.58	100	0.28	80	0.88	58	1.14	48	1.54	25	1.8	10	2.57	10	0.8
2500	1.25	80	1.6	75	0.65	60	2.2	30	3.45	23	4.1	23	4.7	15	1.86
1/300	1.26	40	1.6	35	0.91	28	1.9	17							1.36
1/130	0.88	53	0.77	37	1.03	23	0.6	23							0.82
1/65	1.21	34	0.64	24	1.52	20	0.86	16							1.07
1/25	0.7	30	0.32	28	0.56	23	1.06	13							0.6

Table 7: A tabulation of raw values of plume thickness and frequency of occurrence for PSet1

U	λ_1 (cm)	f_1	λ_2 (cm)	f_2	λ_3 (cm)	f_3	λ_4 (cm)	f_4	λ_5 (cm)	f_5	λ_{avg} (cm)
1	0.22	70	0.67	54							0.46
65	0.88	28	1.3	27	0.64	19	1.7	11			1.06
300	0.92	26	1.35	24	1.22	17	0.65	14	1.65	14	1.15
930	1.25	30	0.92	24	1.85	18	2.4	15	0.6	14	1.36
2500	1.22	39	1	27	1.52	22	0.6	9	1.7	7	1.2
1/300	1.15	48	0.93	44	1.32	34	1.55	23	1.85	15	1.24
1/65	0.94	35	0.75	23	1.1	12	0.65	11			0.8

Table 8: A tabulation of raw values of plume thickness and frequency of occurrence for PSet2

Figure 21 and 22 are plots of plume spacing v/s viscosity ratio and plume thickness v/s viscosity ratio. Both show a similar trend of having a minimum at U = 1 and increase on either sides of U = 1. The weighted average definition has been used in both these plots. Figures 21 and 22 have compared plume spacing and thickness values from PSet1 and PSet2 and show that the trend matches with each other. We can conclude from Figure 21 and 22 that the characteristic plume spacing and plume thickness increase with increase in viscosity ratio when U > 1. Also, the plume spacing and thickness increase with decrease in viscosity ratio when U < 1.

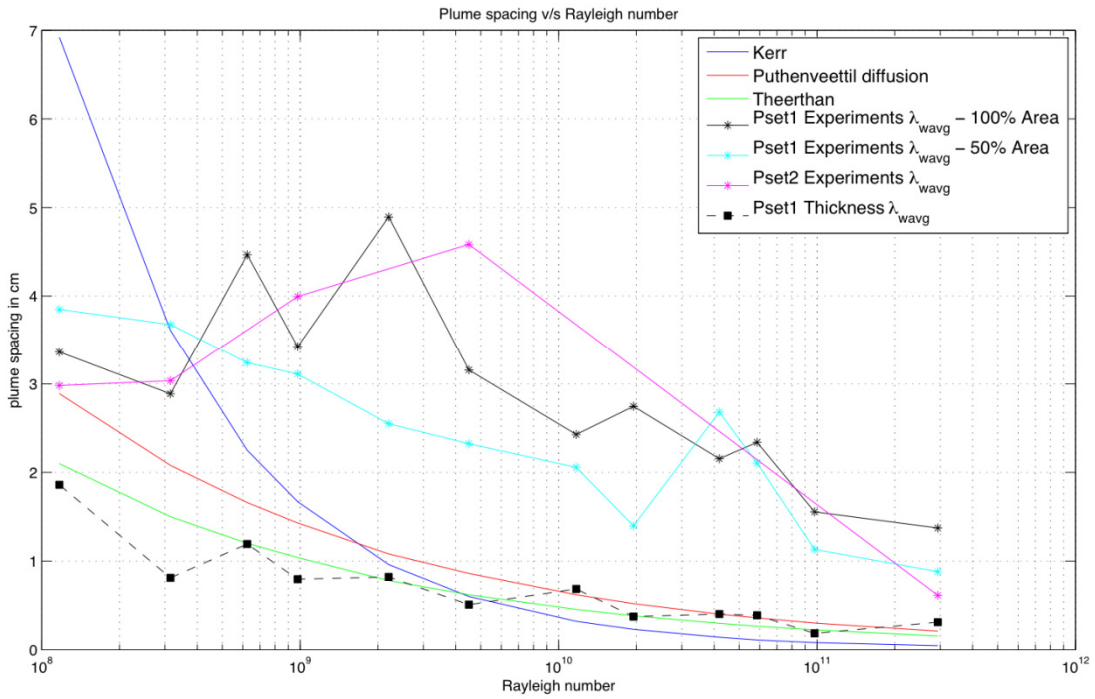

Figure 21: A plot of plume spacing (in cm) v/s Rayleigh number

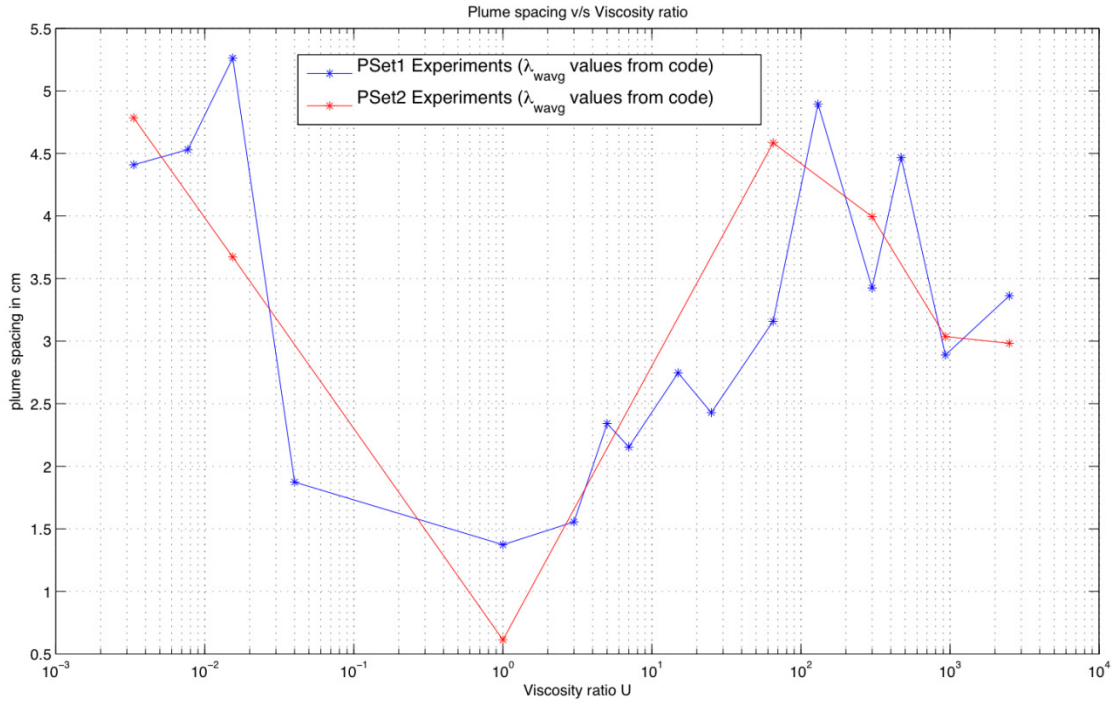

Figure 22: A plot of plume spacing (in cm) v/s viscosity ratio U

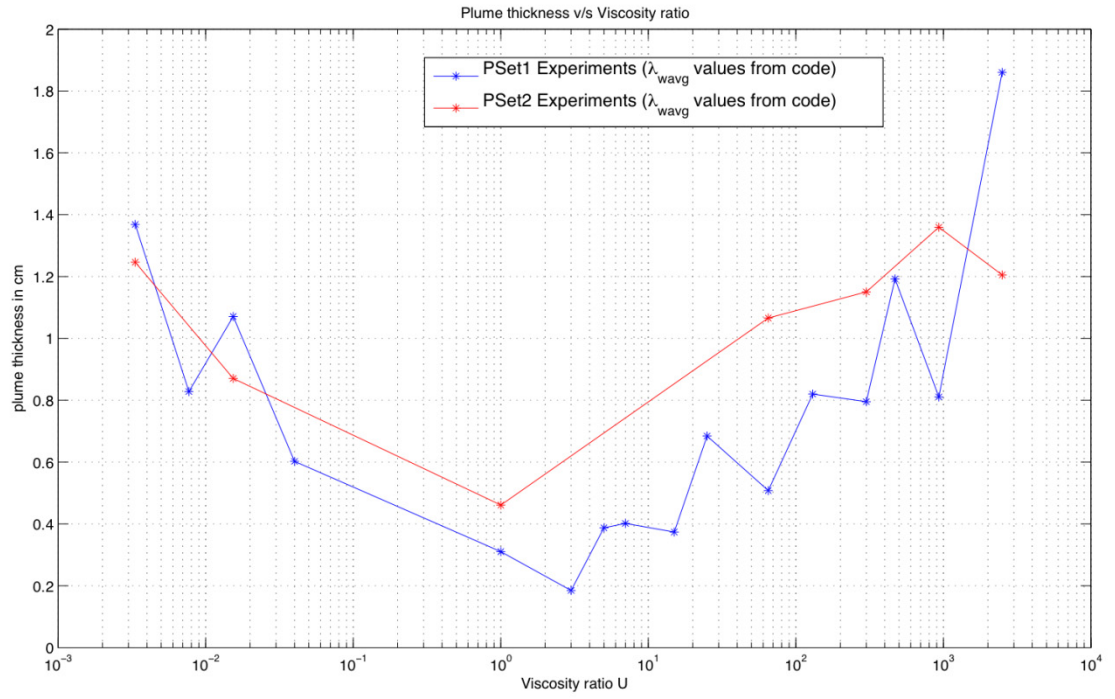

Figure 23: A plot of plume thickness (in cm) v/s viscosity ratio U

3.1.2 Plume Structure in Vertical Sections

In the vertical section views, we visualize and study the structure and dynamics of the rising plumes. Here, we report results from experiments VExpt1 to VExpt7 (see Table 2). The laser sheet illuminates a vertical section perpendicular to the mesh and the flow is captured from two sides using cameras. The thin vertical laser sheet is positioned in the middle section of the tank and the laser sheet illuminates almost the entire test section area. Occasionally the sheet is moved back and forth (~ 1-3 cm) to look at the flow in different vertical sections. Videos and Images are simultaneously captured from opposite sides of the tank. We have mainly used the videos for analysis as it is possible to cover the flow for the entire duration of the experiment. The videos were captured using the Sony handycam in experiments VExpt1 to VExpt4 and using the video mode in the Nikon D90 camera in experiments VExpt5 to VExpt7. Short videos have been included in a CD enclosed with this thesis. We refer to the videos wherever relevant in the sections that follow. Here, the objective is to study the changes the effect viscosity ratio U on plume structure (size and shape), changes in the rise velocity of the plumes, and other dynamics.

Figure 24 (b) shows a montage of raw images of the plume structure in vertical sections from experiments VExpt1 to VExpt7 (VExpt6 is not shown) and in (a) their corresponding near-wall planforms are shown. The viscosity is progressively increased in Figure 24 - U = 1/300, 1/65, 1, 25, 300, 2500. We first describe the changes in plume structure qualitatively. In Figure 24 (b) the green line at the bottom of the images is the boundary layer on the mesh and the flow direction is upwards. When U = 1, the plumes are small, heads are mushroom shaped and rapidly mix into the ambient fluid as seen in the vertical section image in Figure 24 (b). We observe changes in the plume structure with changes in U. The plume head

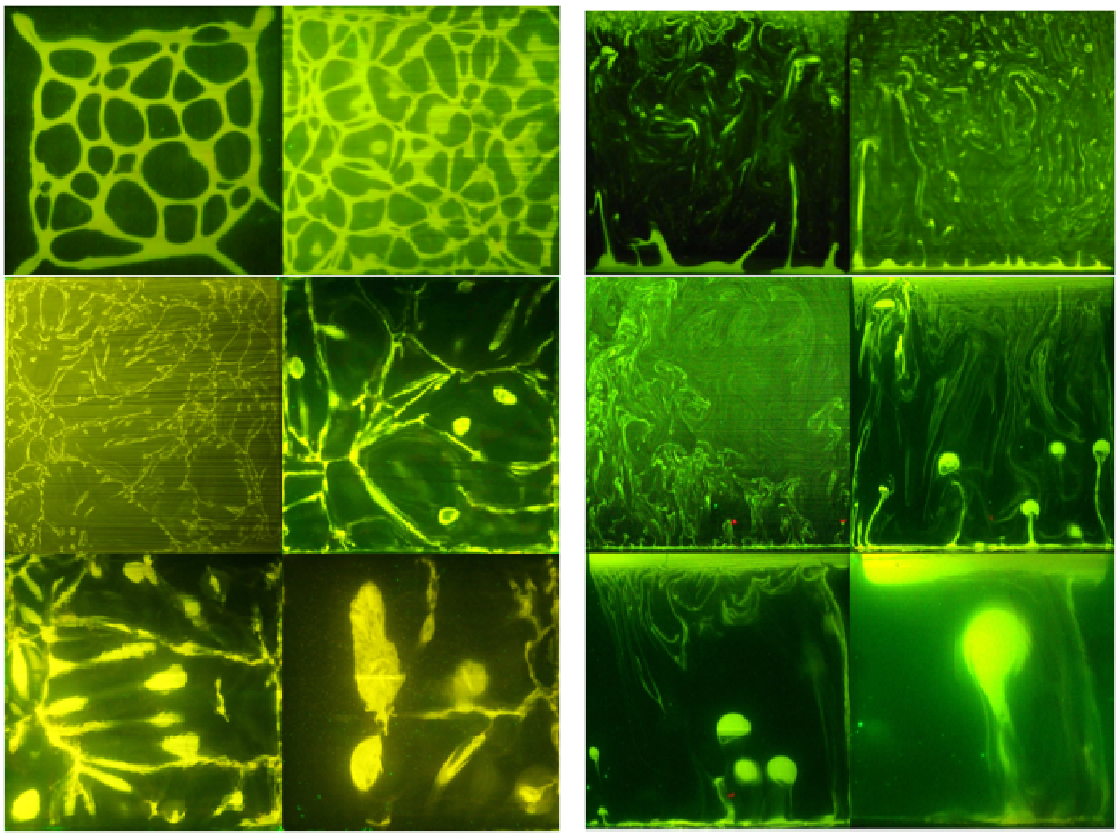

(a) (b)

Figure 24: Images from experiments where viscosity ratio U = 1/300, 1/65, 1, 25, 300, 2500 (a) Near-wall planforms of the plume structures just above the mesh. (b) Corresponding vertical section views of rising plume structures.

size increases as U is increased beyond 1 (Figure 24 (b) cases U = 25, 300, 2500). In cases where U > 1 from U = 25 onwards, the shape of the plume head changes from a mushroom-like structure to a spherical blob resembling the classic 'cavity plume' head shape reported by Olson and Singer (1985). Figure 25 shows a schematic of the two head shapes - a mushroom-like 2D structure and a spherical cavity plume in 3D.

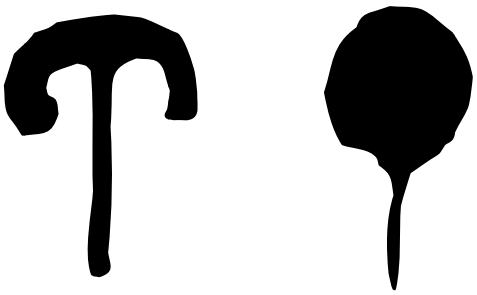

(a) (b)

Figure 25: A schematic of the two plume head shapes (a) Mushroom-like 2D (b) Cavity plume 3D

As U increases (U>1) the plumes retain their identity for a longer distance and rise to the surface due to reduced mixing with the ambient viscous fluid. The plume heads rise and pond to form a distinct layer of buoyant fluid at the top of the test section. The height of this ponded layer is maximum when U = 2500.

In cases where U>1, the starting plume heads leave behind a trailing low viscosity conduits (also seen in the experiments of Olson and Singer, 1985). Subsequent plumes that arise near the remnant conduits tend to flow through them as they offer a low resistance path. The plume heads align themselves towards the conduits and rise in an inclined trajectory. The plume head deforms when it interacts with a conduit and accelerates. The conduits are also known to support solitary waves (Olson and Christensen, 1986, and Scott et al. 1986). We see instances of such solitary waves in a few cases.

In cases where U>1, the plume heads also interact with each other (Manga 1997, Kelly and Bercovici, 1997) if they are in sufficient proximity to each other. This 'Clustering' of plumes results in the merging of two or more starting plume heads into a single larger plume head. In a typical clustering scenario, the plume head above draws in a nearby plume head which deforms and accelerates to merge with the upper plume head.

In experiments where U < 1 (see Figure 24 (b) U = 1/300,1/65 cases), the plumes rise as long columns and detach. The head of the columns is not well defined and sometimes the rising columns resemble 'diapir plumes' reported by Olson and Singer (1985). The height of the columns are maximum for the smallest U (=1/300) and decrease with increase in U. The boundary layer thickness is largest for the smallest U (=1/300) and decreases with increase in U. The boundary layer has many undulations which makes it difficult to define a specific thickness. The average boundary layer

thicknesses are ~ 0.5, 0.4 and 0.3 cm for U = 1/300, 1/130 and 1/65 cases respectively. The velocities have been estimated from the vertical section videos and it is observed that the plume rise velocities are highest for U = 1 and decrease with increasing U (U>1) and also with decreasing U (U<1).

Now, we describe individual experiments in detail and later move on to quantitative analysis. In VExpt1, U = 1, (see videoVExpt1 on CD) there is rapid turbulent mixing of the plume with the ambient fluid. Large scale flows can be identified which in turn affect the formation of near wall plumes. The large scale flow can be clockwise or anticlockwise and extend throughout the test section. The Large scale circulation changes between the two states (a) or (c) and (b) in Figure 26.

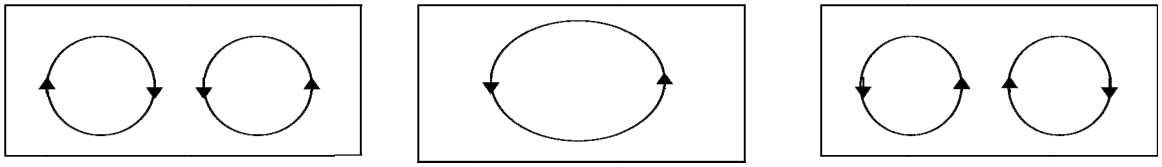

(a) (b) (c)

Figure 26: Directions of Large scale circulation in the test section in the U=1 experiment.

In our experiment, there is no top cooling as in RBC, so downwelling cold plumes (heavier plumes) are not present. There are local regions of vorticity caused by the vortex-ring like structures in the mushroom shaped plume head mixing into the ambient fluid. The downward flow of heavier fluid, on an average is into the centre as in Figure 26(a). The large scale circulation rarely switches to the configuration in Figure 26(c).

In VExpt2, U = 25 (see videoVExpt2 on CD), the initial 'transient' state consists of small 'diapir plumes' that interact with each other and rapidly coalesce to form bigger plumes. The plume heads are circular and are hollow with small 'holes' in between

the head and tail. Clustering of plumes is commonly observed in this case. When plumes interact with remnant low-viscosity conduits, they deform and rise inside the conduit like solitary waves. The plume heads sometimes break up into smaller fragments. The extent is mixing of plumes into ambient is to a large extent determined by the presence of the low-viscosity conduits. The plumes rise in an inclined direction due to the conduits and not because of a large scale flow. The ambient viscous fluid flows downwards in columns adjacent to conduits and sometimes split the rising plume heads.

In VExpt3, U = 300 (see videoVExpt3 on CD), we again see an initial transient state with small scale plumes. The small scale plume heads merge into a bigger spherical head that detaches from the boundary layer and rises. We see clustering of multiple plumes heads. A large scale circulation is setup initially, but when the downward flow reaches the entire layer depth, the large scale circulation is suspended and the plumes start rising from the center. The density of remnant conduits is lesser than in VExpt2. The acceleration of plume heads due to interactions with conduits and clustering is responsible for the head to detach from the tail. The flow details in experiments VExpt3 and VExpt4 are similar except that sizes of the plume-heads are different.

In VExpt4, U = 2500 (see videoVExpt4 on CD), the ‘cavity’ plumes rise and pond at the top forming a low viscosity layer. There are many instances of clustering observed. The plume head tip and shape are drastically influenced by low viscosity conduits. Sometimes, the plume head does not even form and buoyant fluid escapes into conduits from the boundary layer (solitary waves). The interaction between the plume heads and conduits is complex. The conduit diameter enlarges accompanied by the deformation (elongation in the direction of the conduit) of the plume head shape. This is followed by an increase in velocity of the plume in the conduit.

We now describe the analysis carried out using data from the videos of the vertical section experiments. The Analysis was done to determine the plume sizes and the rise velocity of the plumes in different cases of U. The videos from the Sony handycam were taken at 25 fps with a resolution of 704 x 576 pixels for a total duration of about 20 minutes of the experiment. Individual frames were extracted using Avidemux software (freeware) and saved as jpeg images in different folders. The frames are numbered in order and this enables us to accurately determine the time between two frames.

In each experiment, the individual plumes were tracked by analyzing each and every frame for obtaining size and velocity of plumes. The plume sizes were estimated using ImageJ software (freeware). A rising plume is selected at mid height and the corresponding frame is cropped accurately to display only the test section. The test section length scale is set in ImageJ software. This enables length measurement of any line drawn in the image. The maximum diameter of the sample plume was measured in the horizontal plane (this is referred to as the size of the plume). Measuring the plume head diameter is not possible in VExpt1 (U = 1) because of the small size of the plumes and rapid mixing into the ambient. However, the typical plume head size was estimated using ImageJ to be ~0.3 cm and the plume stem width to be ~0.1 cm. In VExpt2 (U = 25) the sizes of 42 sample plumes were measured and the histogram distribution of sizes has a peak value (characteristic size) at 1 cm. Figure 27 shows a comparison of the histogram distributions of plume size for VExpt2, 3 and 4. For VExpt3, 4 (U = 300, 2500), the characteristic plume sizes (31 and 17 samples) estimated is 1.8 cm and 3 cm respectively. In VExpt4 (U = 2500), the largest plume heads measured is about 4.5 cm in size and the smallest sizes correspond to VExpt1 (U = 1).

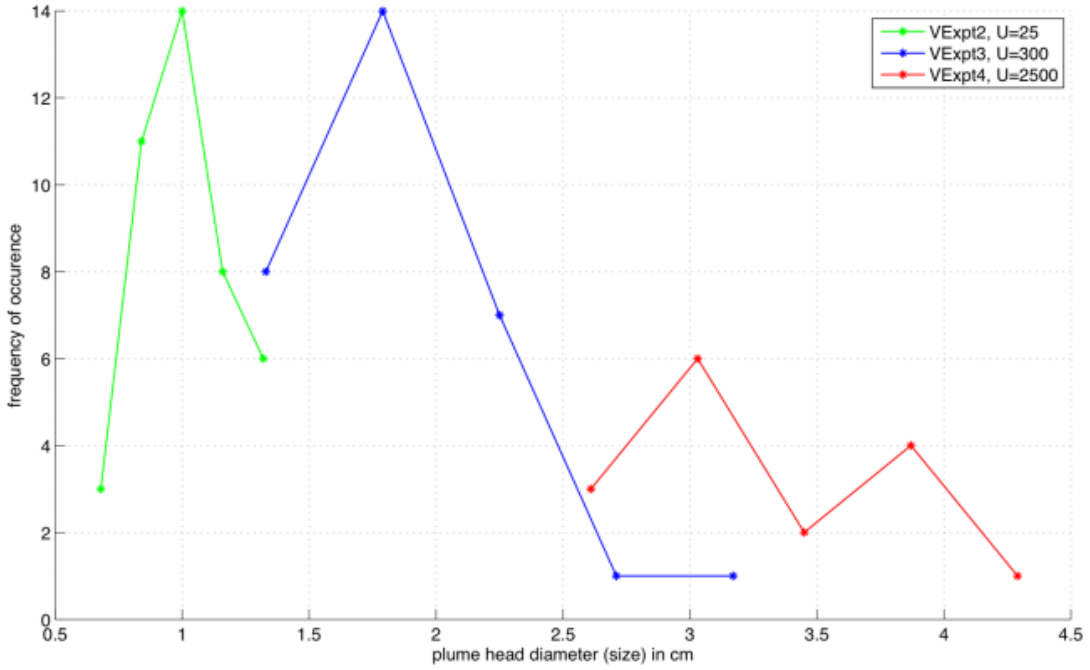

Figure 27: Comparison of distributions of plume size for VExpt 2, 3 and 4

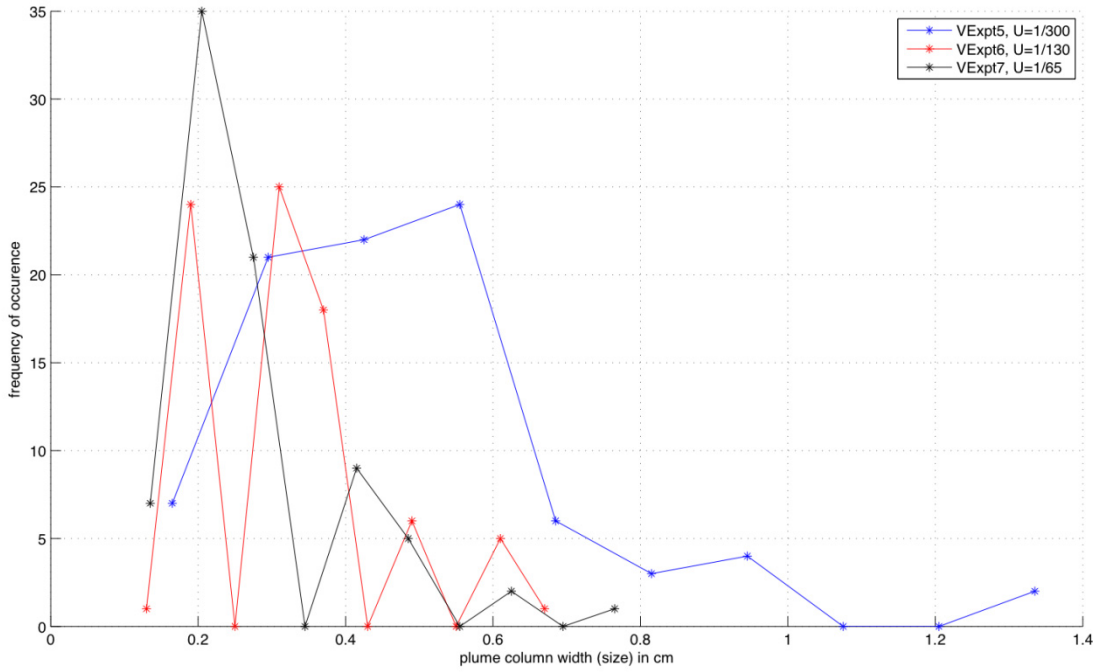

Figure 28: Comparison of distributions of plume size for VExpt 5, 6 and 7

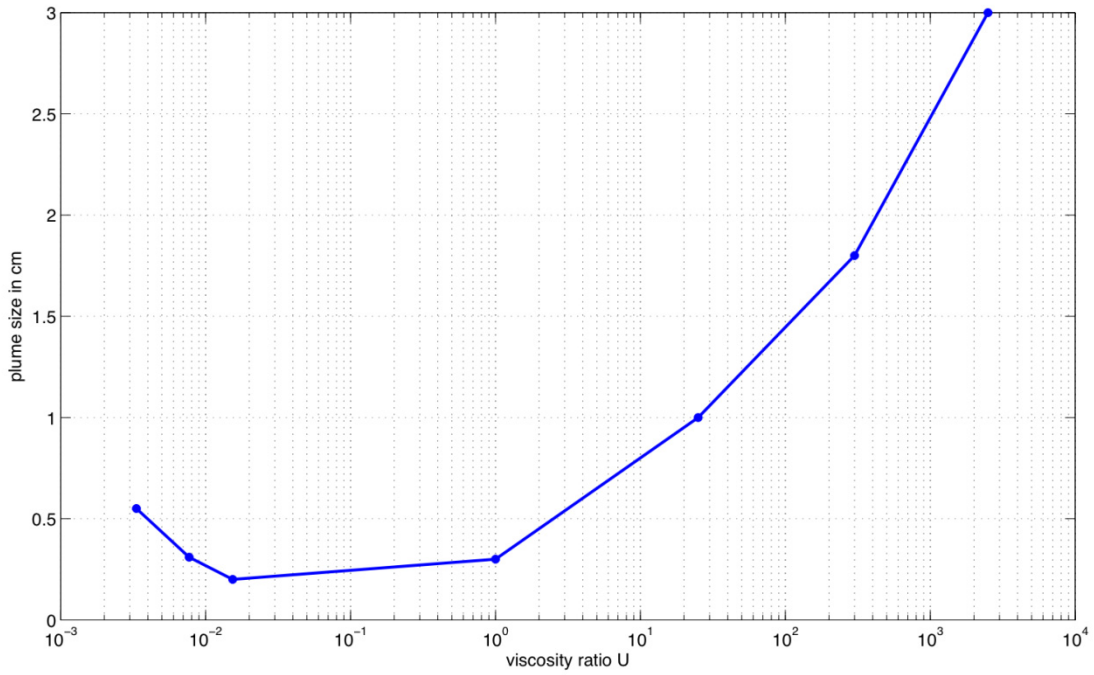

Figure 29: A plot of Plume size v/s U

In experiments where U < 1, (i.e. VExpt5, 6 and 7), estimating the plume sizes is subjective. The column widths vary as they rise. The plume size was hence taken to be the peak in the distribution for a large number (~80) of sample measurements of the columns. Figure 28 shows a comparison of the histogram distributions of plume size for VExpt5, 6 and 7. The characteristic plume size was measured to be 0.55 cm, 0.31 cm and 0.2 cm for VExpt5, 6 and 7 respectively. Figure 29 shows a plot of plume size versus the viscosity ratio U including all the vertical section experiments. From Figure 29, we conclude that the plume size increases as the viscosity ratio increases when U > 1 and also as the viscosity ratio decreases when U < 1.

The velocities of the rising plumes were estimated by tracking the vertical position of the plume-head tip over time. The different plumes for tracking were identified from the video frames. The extracted frames were converted into binary using Matlab. The thresholding for the binary was decided by the inbuilt graythresh command in Matlab.

It was not possible to manually threshold each frame as the number of frames were huge and the task had to be automated. A Matlab code was written to read a finite number of images (frames), crop them as required, convert them into grayscale and then to binary. After converting to binary, artificial marker lines were added to the image at known locations. This was possible as the length scale of the image is known. The plume crossing the different length markers at different times (frames) is noted down for each individual plume sample. From this, we obtain a height versus time plot for that plume. Figure 30 shows an example of the velocity estimation method for VExpt4 (U=2500). Figure 30 (a) shows the extracted image from the video and (b) shows the binary version with marker lines used for obtaining height measurements versus time. Figure 31 shows the height versus time data for experiments VExpt1 to VExpt7. Here, each plume starts at time = 0 as the actual starting time is subtracted from the final time. This means that the plot contains height of plume-head tip v/s time data for plumes in the experiment.

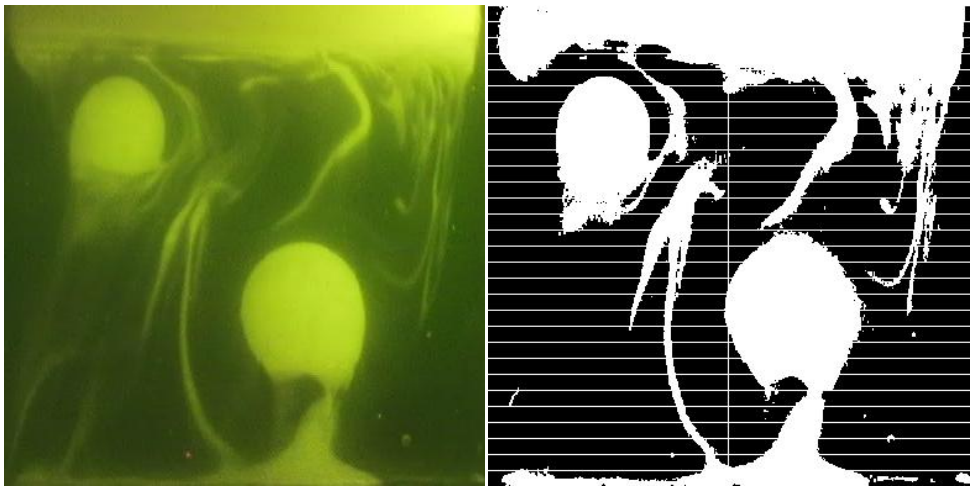

(a) **(b)**

Figure 30: Determination of height versus time for a plume. (a) Image extracted and cropped from the video. (b) Binary version of Image in (a) with marker length scales to help track height of plume tip with increasing time.

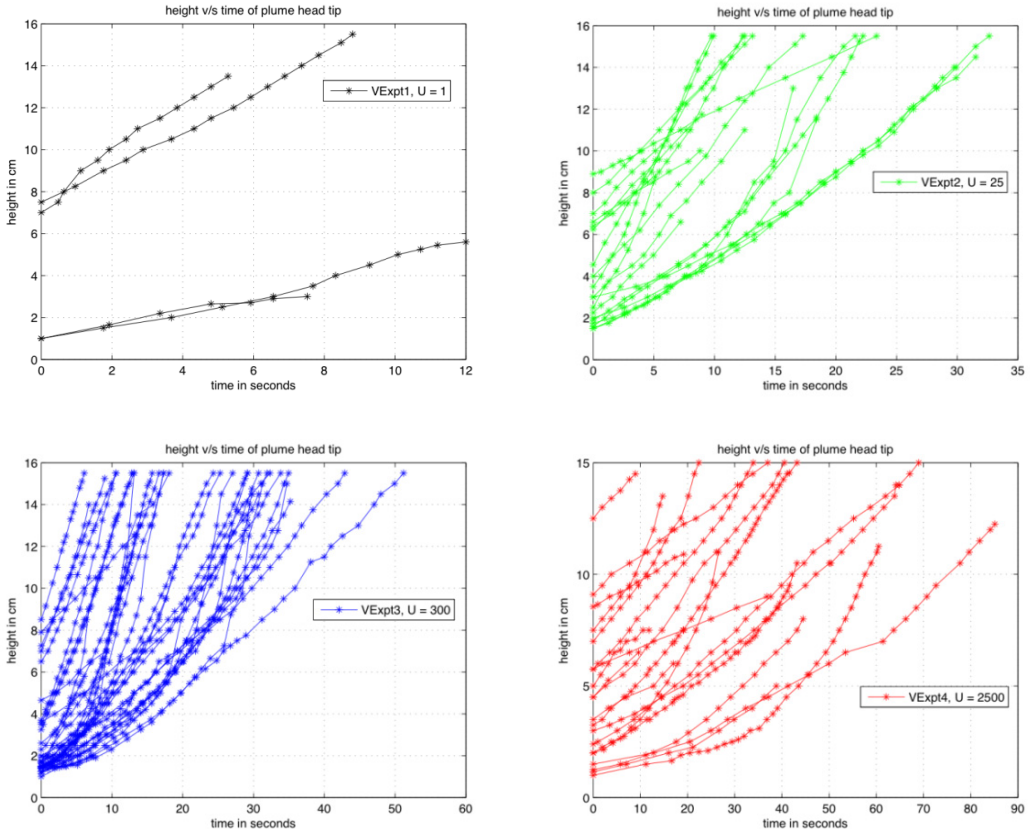

Figure 31: Height v/s time data for experiments VExpt1 to VExpt4

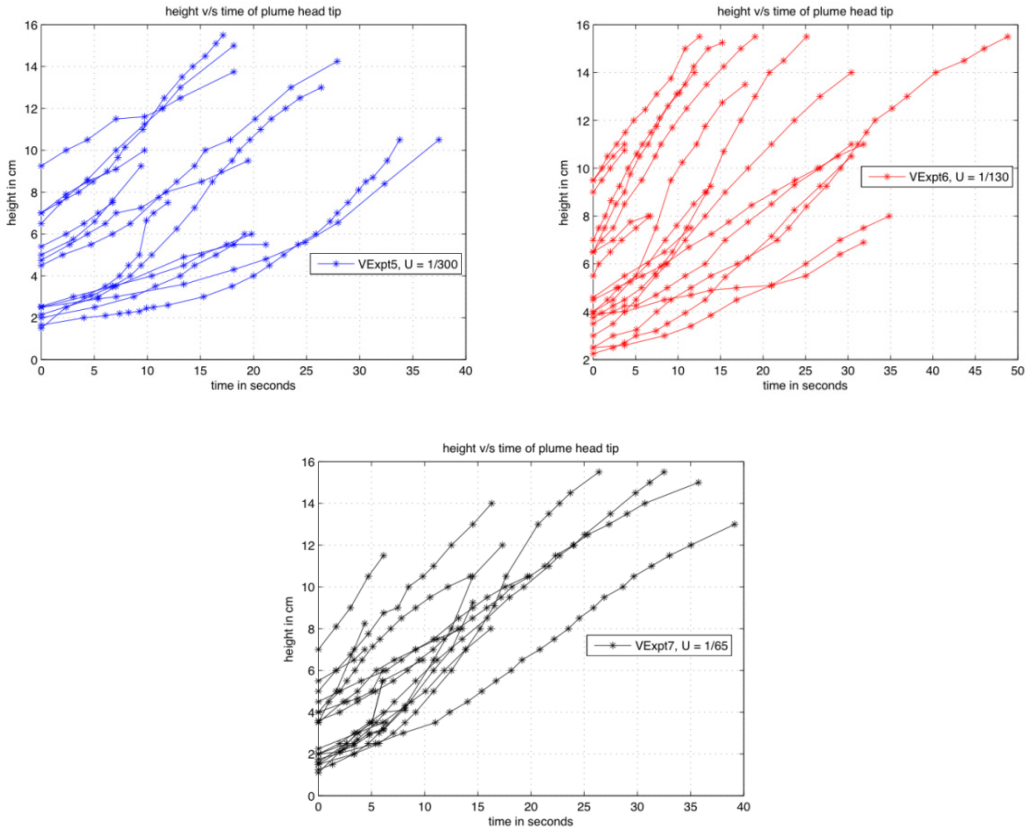

Figure 31: Height v/s time data for experiments VExpt5 to VExpt7

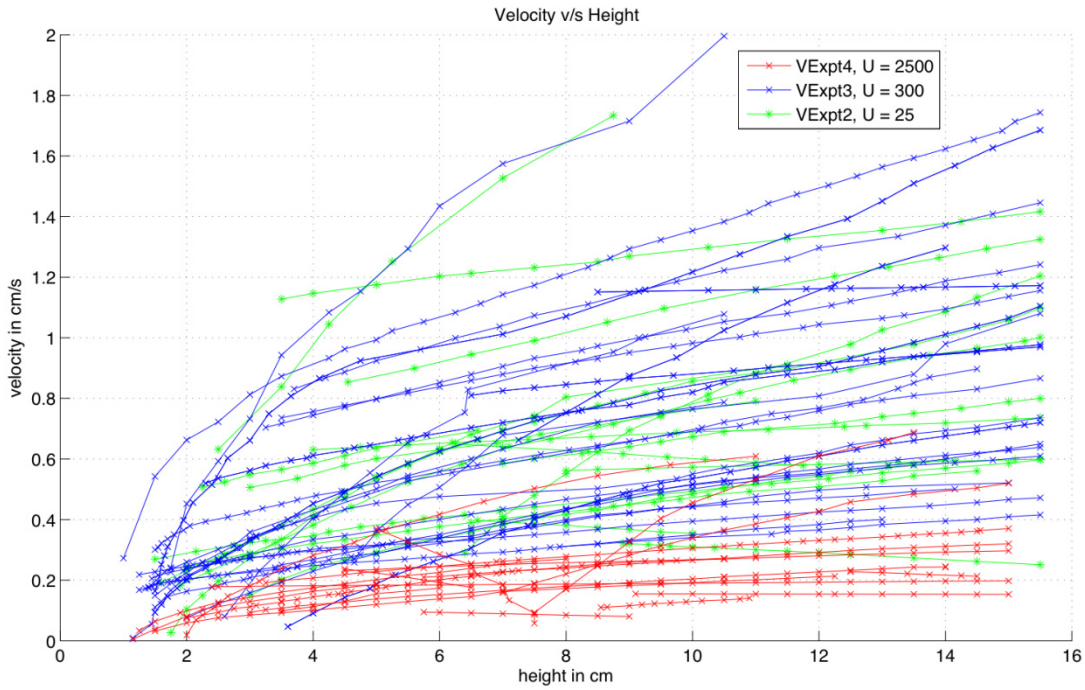

Figure 32: Velocity v/s height data for experiments VExpt1 to VExpt4

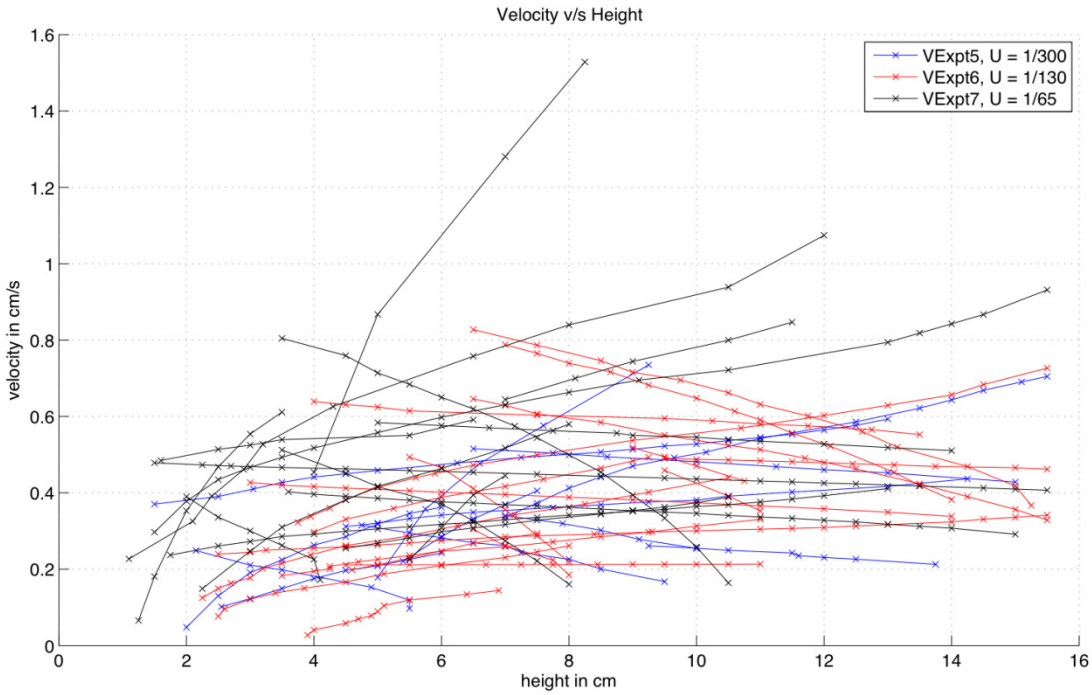

Figure 33: Velocity v/s height data for experiments VExpt5 to VExpt7

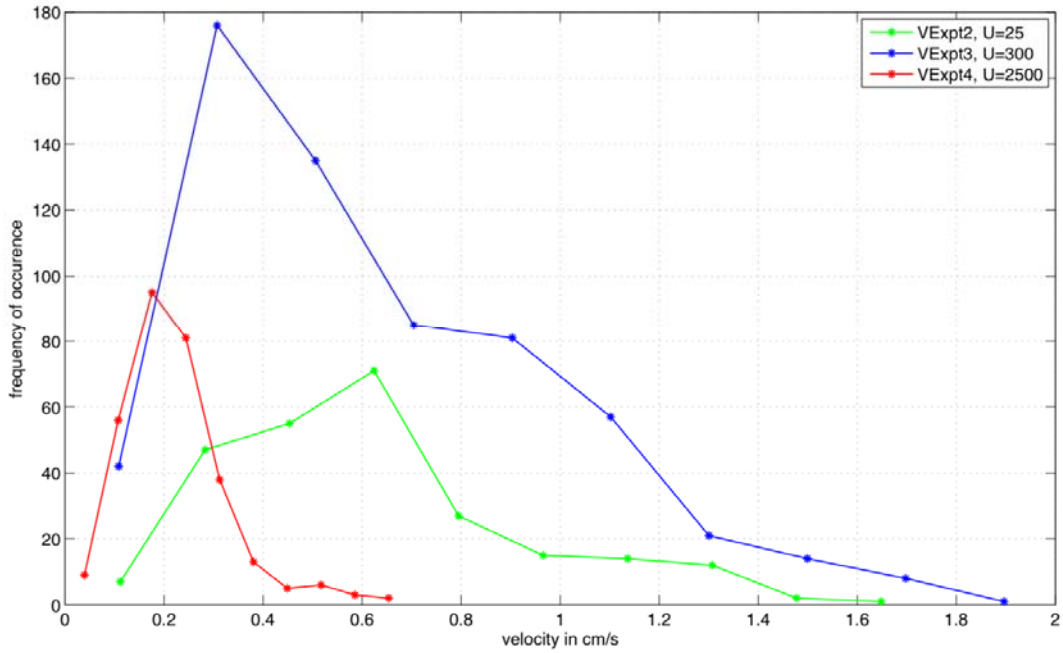

Figure 34: Comparison of distributions of plume velocities for VExpt 2, 3 and 4
(including data of plumes of different sizes at different heights)

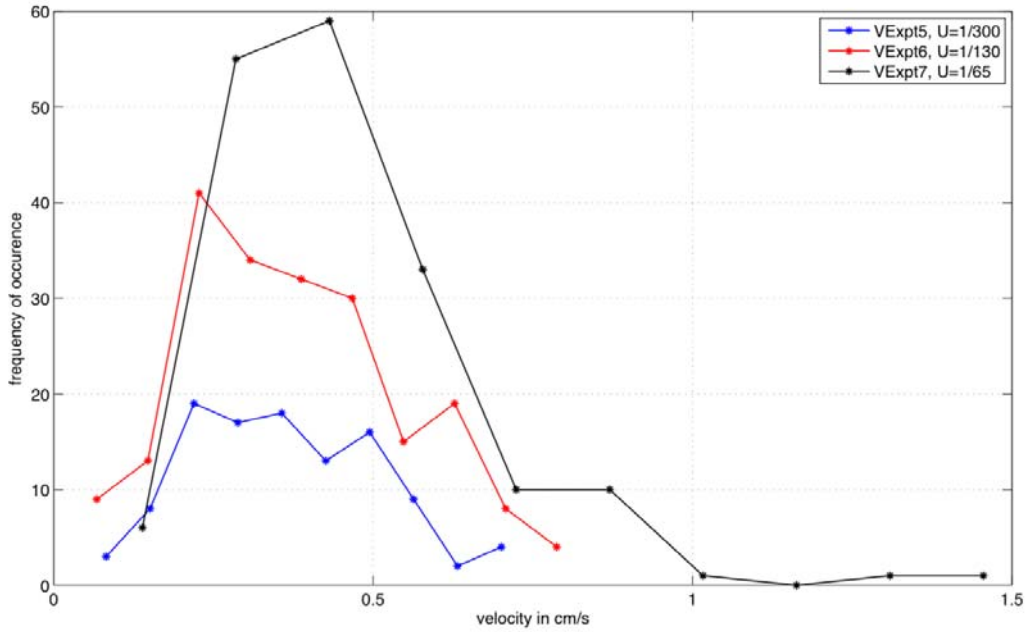

Figure 35: Comparison of distributions of plume velocities for VExpt 5, 6 and 7
(including data of plumes of different sizes at different heights)

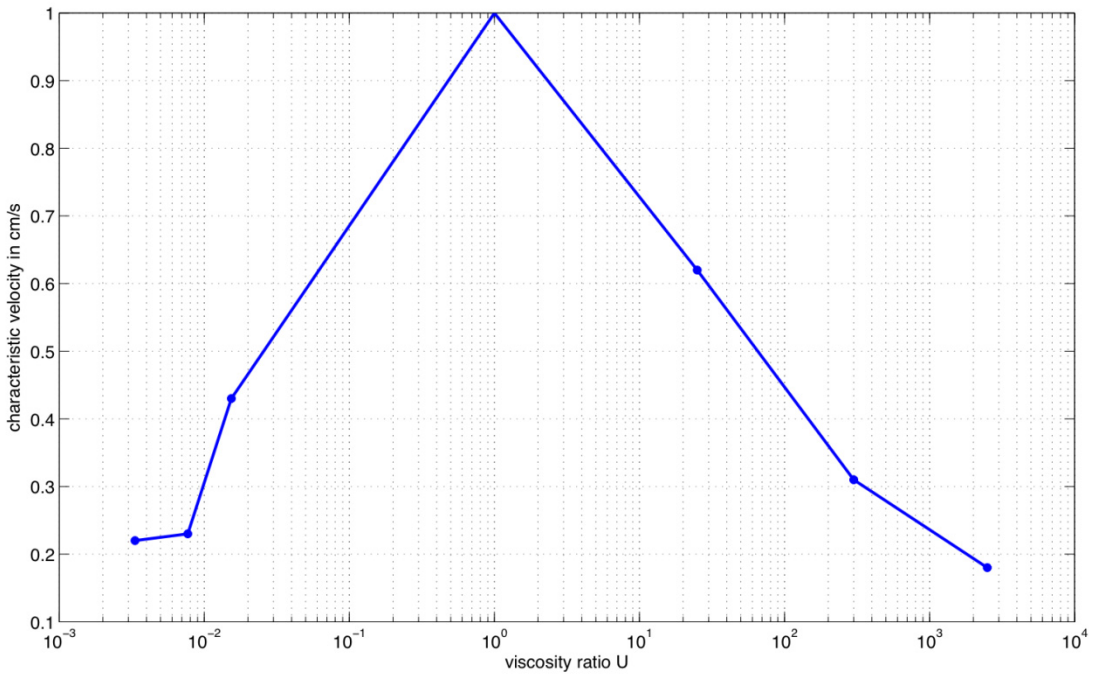

Figure 36: A plot of plume velocities v/s U

Figure 31 shows that the time taken for the plumes to rise to the maximum height increases with U. A polynomial of order 2 was fit onto the height v/s time data and the first derivative gives the velocity. Figure 32 shows a plot of plume velocity versus height for VExpt2 to VExpt4 and Figure 33 shows a plot of plume velocity versus height for VExpt5 to VExpt7. The plume velocities in VExpt4 (U=2500) (Figure 32) show minimum variation with height. Figure 34 shows the comparisons of histograms of the velocities obtained in experiments VExpt2 to VExpt4. The peak of the distribution is taken to be the characteristic velocity for each case. The characteristic velocity is 0.62, 0.31 and 0.18 cm/s for experiments VExpt2 to VExpt4 (U = 25, 300, 2500). The characteristic velocity for VExpt1 (U = 1) is taken be ~ 1 cm/s. Figure 35 shows the comparisons of histograms of the velocities obtained in experiments VExpt5 to VExpt7. The characteristic velocity is taken as 0.22 , 0.23 and 0.43 cm/s for experiments VExpt5 to VExpt7 (U = 1/300, 1/130, 1/65). Finally, Figure 36 shows a plot of characteristic plume velocity v/s viscosity ratio U for all the vertical

section experiments. We conclude from Figure 36 that the plume velocity is highest for U = 1 case and decreases with increasing U (for U>1) and decreases with decreasing U (for U<1). The plume size has a minimum value when U = 1 and velocity has maximum value when U = 1.

3.1.2 Planform plume structures at different heights from the mesh

In this section, we describe studies of the planform plume structures at different horizontal sections. The traverse setup was used to visualize the plume structures at different heights from the mesh. As mentioned before, the traverse setup provides a controlled and precise movement of a horizontal laser sheet in the vertical direction. Videos were taken from the top using the Nikon D90 camera in its video mode at 24 fps. Here, we use the data from the traverse experiments (TExpt1 to TExpt7, see Table 2) for analysis. Data from the traverse experiments is used to study the variation of the plume rise velocities and the amount of mixing between the plume and ambient fluid at different heights. Also, the data is used to reconstruct the plume structure in three dimensions to give a detailed visualization of the flow field.

Short videos of selected traverse experiments are included in the CD with the thesis (see videoTExpt1, videoTExpt3, videoTExpt5, and videoTExpt6 corresponding to traverse experiments TExpt1, 3, 5 and 6 on CD). In these experiments, the horizontal laser sheet is moved up and down at a constant speed of 3 mm s^{-1} and covers the required vertical range starting from the mesh. The vertical range covered is 3.5, 6.5, 4.8, 6.2, 4.5, 5.5, and 6 cm respectively for experiments TExpt1 to TExpt7. The near-wall planform is visible in all the included videos. The laser sheet starts from below the mesh, illuminates the near-wall planform, rises to the set traverse height and

pauses for 1-2 seconds. There are small markers placed on the side of the glass tank which cast a shadow on the horizontal section when the light sheet reaches the pre-set traverse height. The laser sheet moves down illuminating all horizontal sections it passes through. The sheet finally goes below the mesh and again pauses for 1-2 seconds. The cycle then begins again. In the TExpt1 (U=1) case, the near-wall dendritic line plumes rapidly start mixing into the ambient fluid in horizontal sections. As U increases, (U>1) there is lesser lateral motion of the plumes in horizontal directions and reduced mixing with the ambient fluid. The increase in plume size with increase in U is evident from the videos. Sometimes, (in TExpt5, U = 2500) the plume head is cut by the moving laser sheet for a long time. This occurs when the laser sheet is moving upwards, and the plume head stays in the illuminated moving sheet for a long time as the rise velocities are almost the same. The downward moving laser sheet tends to illuminate rising plumes which appear and disappear fast. This is because the laser sheet is moving in the opposite direction of the flow. The low viscosity remnant conduits appear as static objects in the moving light sheet. In experiments where U<1 (TExpt6, 7) the thick boundary layer is visible when the light sheet moves above the mesh for a few seconds. The formation of cells and their break-up into fragments are visible. In the U = 1/300 case (TExpt6), we also see the reforming of cells from the columns when the laser sheet moves downwards. In the U<1 experiments, the motion in the horizontal plane increases with height.

If the entrainment (or mixing) is small, the total area occupied by the plumes in a horizontal section is inversely proportional to the rise velocity. Hence, the area fraction provides a measure of the plume velocities. We analyze the data to determine the fractional area occupied by the plumes at different horizontal sections across

different viscosity ratio experiments. The Nikon D90 camera records movies at 24 fps and a resolution of 1280 x 720 pixels. Frames are extracted from the videos using Avidemux software and numbered in order so that it is possible to track the time evolution of the images. A Matlab code has been written to read images automatically in sequence for a specified range of frames, at periodic intervals (here 24 frames ~ 1 second). After reading the image into the Matlab workspace, the code first crops the image and then converts it into a grayscale image. We again use the adaptive histogram equalization technique in the image processing toolbox to correct for the non-uniformity of intensities in the image. The code uses the 'graythresh' Matlab command to determine the optimum threshold for converting the grayscale image into binary. The binary image and the cropped image are saved for later reference. Montages of the raw images used for processing are shown in Appendix – 3. After the binary is obtained, the code finds the total area occupied by the plumes (in white) in the image. This area is divided by the total area of the image to calculate the fractional area of plumes in the horizontal cross-section. Figure 37 shows a plot of the area fraction versus the height traversed above the mesh for TExpt1. Similar plots for all experiments (TExpt2 to TExpt7) have been made automatically from the code output (given in Appendix-3). For each experiment, there are 5 sets of observations, each set corresponding to one cycle of traverse. The area fraction obtained from the upward traverse is indicated by a solid line and the downward traverse by a dotted line. The analysis is carried out for 5 consecutive cycles of the traverse. When we look at the corresponding montage sets (Appendix-3), we find that in some cases (TExpt1, TExpt5 and Texpt7) the binary image is not a good representation of the raw image. This problem is caused due to the automatic thresholding procedure adopted.

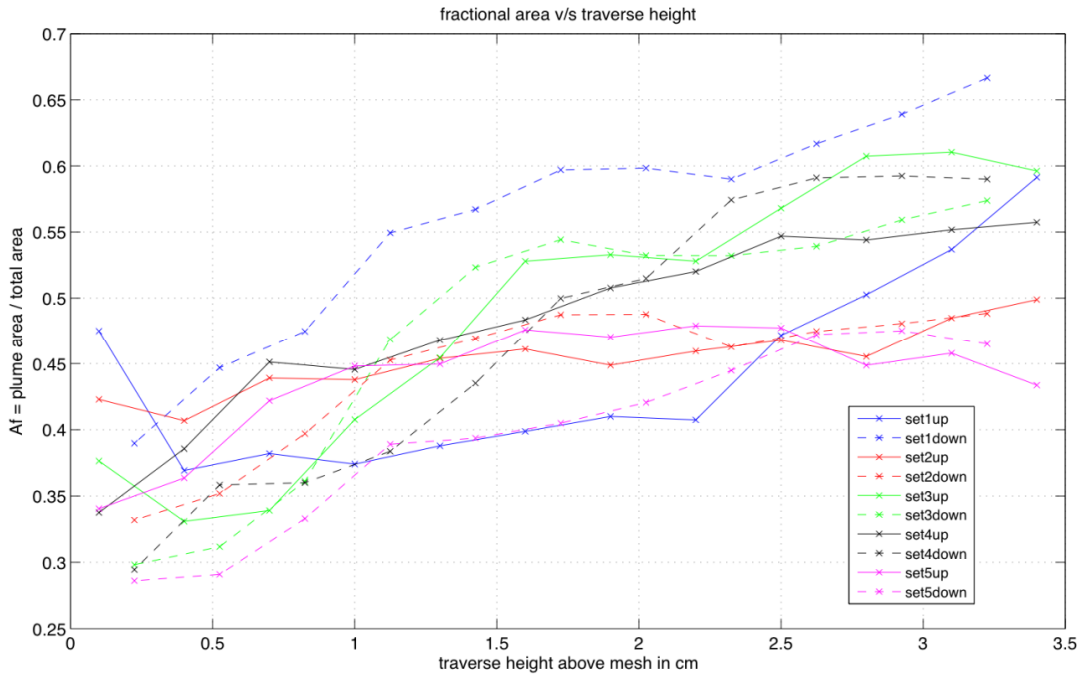

Figure 37: Fractional area v/s traverse height, TExpt1, U = 1

Hence, we consider the data from the remaining cases for further analysis. In these cases, the fractional area would be initially high and drops to a constant value. This makes sense as we would expect the velocities to increase as the plumes rise. Figure 38 shows a combined plot of fractional area v/s height for cases TExpt2, TExpt3, TExpt4 and TExpt6 considering the first two sets (traverse cycles).

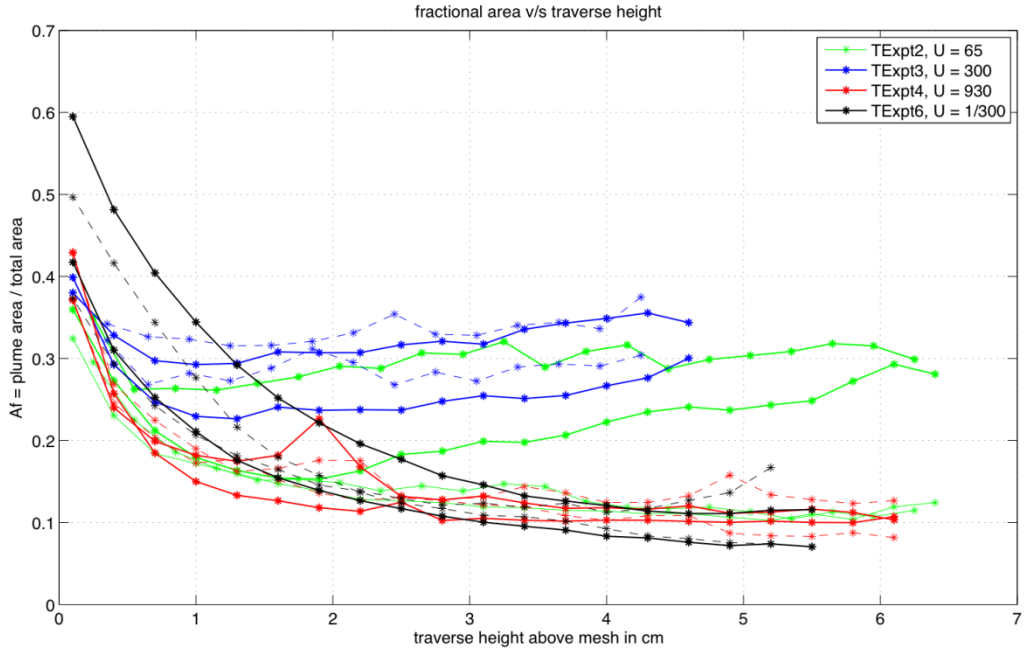

Figure 38: Fractional area v/s traverse height for cases TExpt2, 3, 4, 6 considering first two traverse cycles

The planforms in the horizontal sections can indicate how much mixing of the plume fluid into the ambient is taking place across different viscosity ratio regimes. We adopt an analysis procedure similar to that of the fractional area determination. The frames are extracted and a code is written to read the images and crop them. Then the images are converted to grayscale. To quantify the mixing, we define a measure of mixing as:

$$f_{mix} = \frac{standard\ deviation}{mean}$$

Here, the standard deviation and mean are computed from the grayscale image of the same set of images analyzed for the area fraction. The mean would correspond to the average background intensity of the pixels in the image. The standard deviation is a measure of how much variation there is from the mean intensity of the pixels. In an image where there is very less mixing, the plumes would appear clearly and would result in a high value of the standard deviation. Whereas, when there is good mixing, the image would be homogeneous and there would be smaller deviations from the mean. Hence, the ratio of the standard deviation to the mean would provide an estimation of the efficiency of mixing.

Figure 39 (a)-(g) shows a plot of Mixing versus height of traverse above the mesh for experiments TExpt1 to TExpt7. The corresponding grayscale images used for the calculation of the mixing efficiency are shown as montages in Appendix-3 for all the experiments. In Figure 39 (a)-(g) there are 5 sets shown corresponding to 5 cycles of traverse. Data from images taken during upward traverse is shown in solid lines and data from downwards traverse is shown in dotted lines.

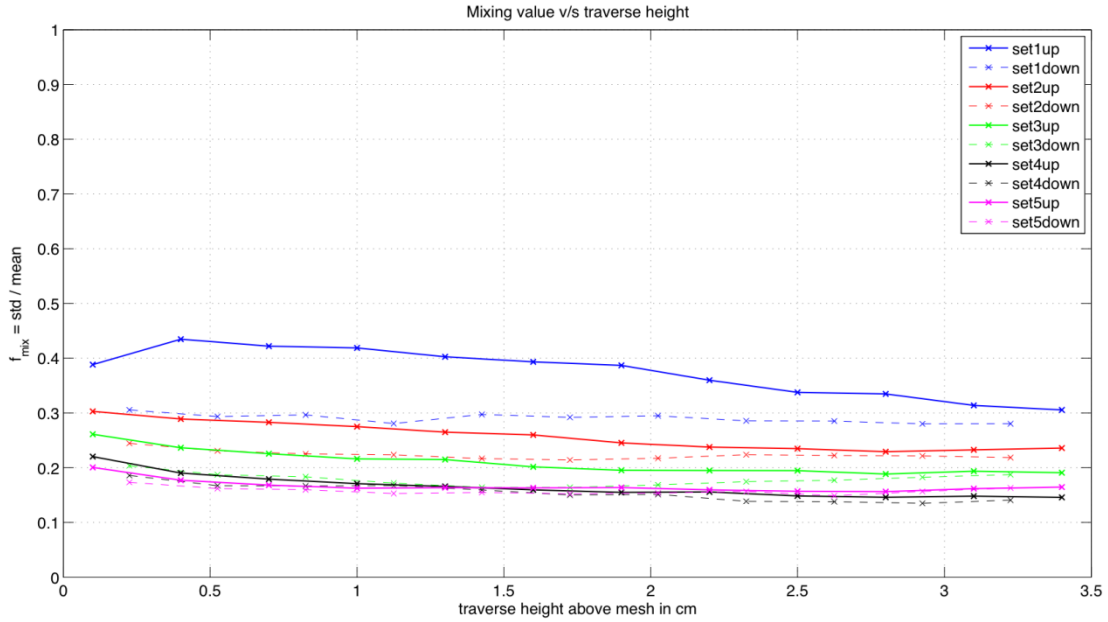

Figure 39: (a) Mixing v/s traverse height for TExpt1, U = 1

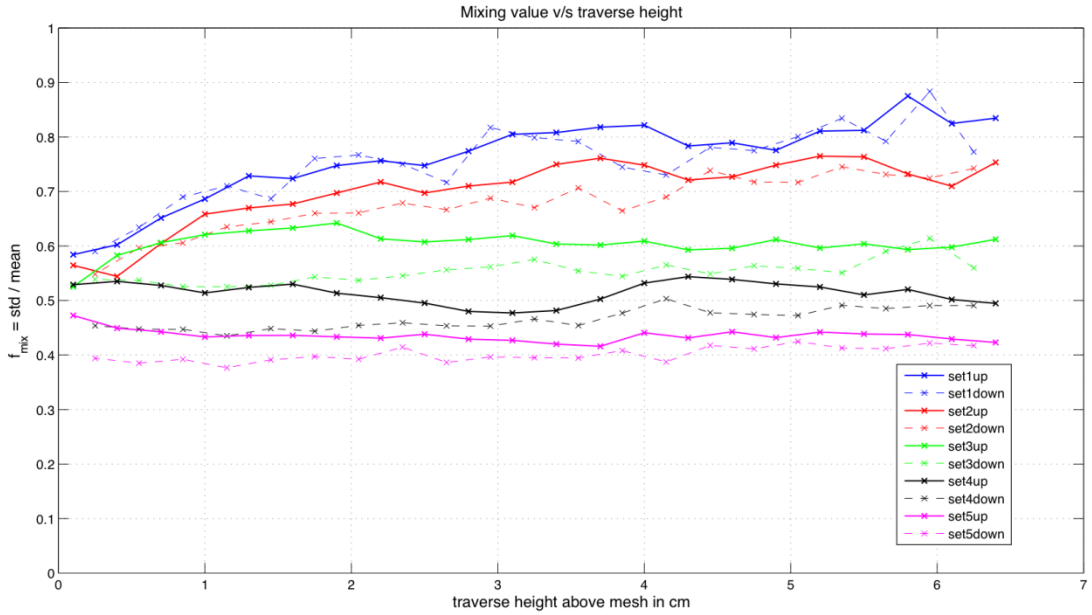

Figure 39: (b) Mixing v/s traverse height for TExpt2, U = 65

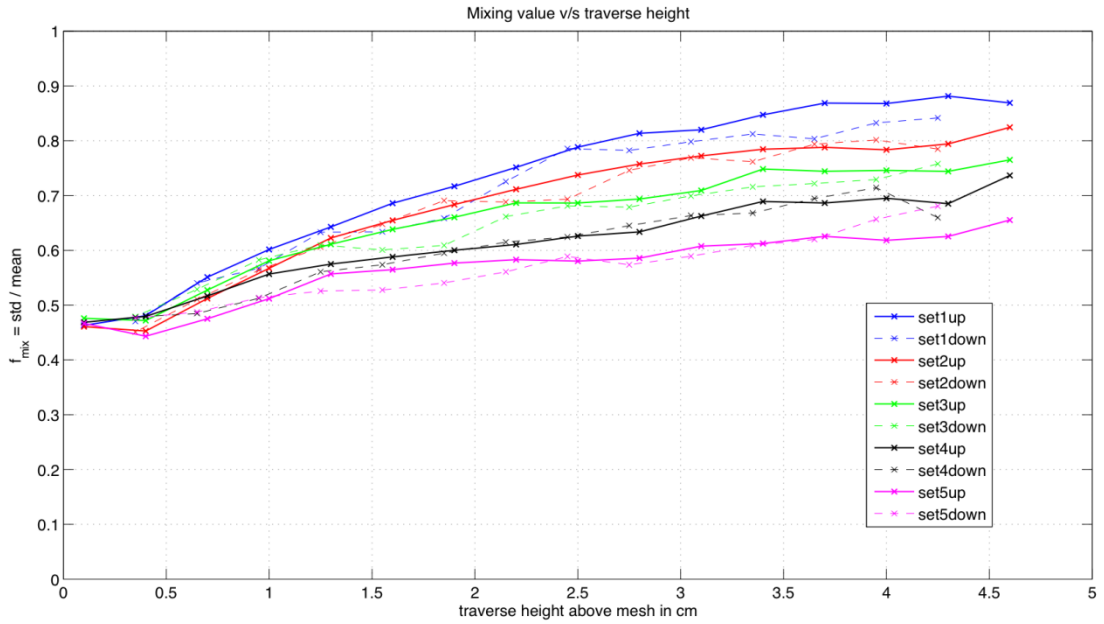

Figure 39: (c) Mixing v/s traverse height for TExpt3, U = 300

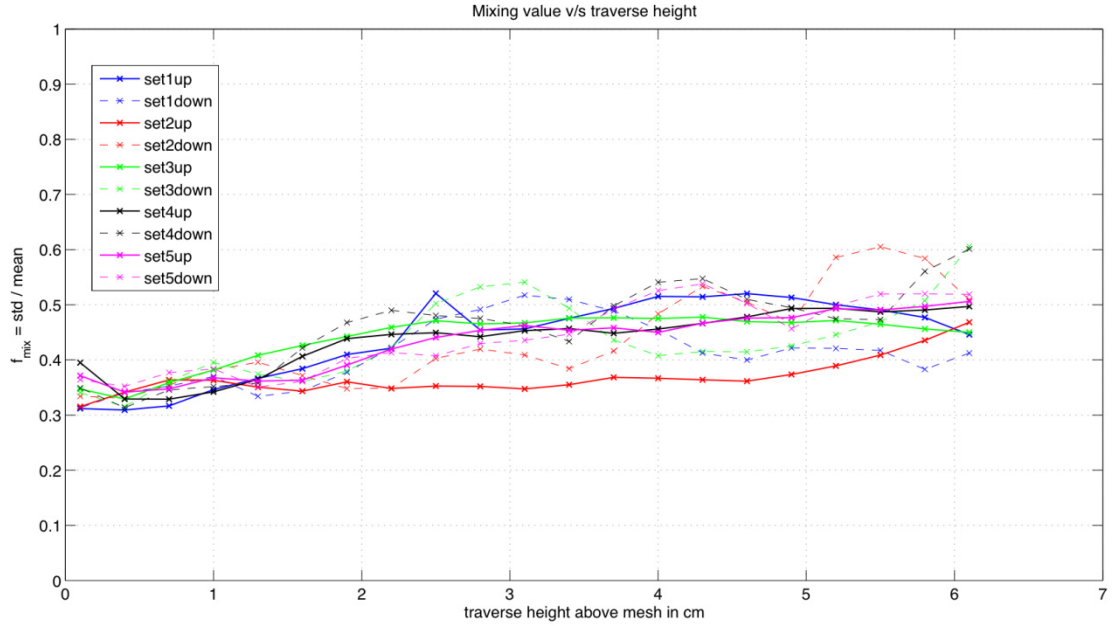

Figure 39: (d) Mixing v/s traverse height for TExpt4, U = 930

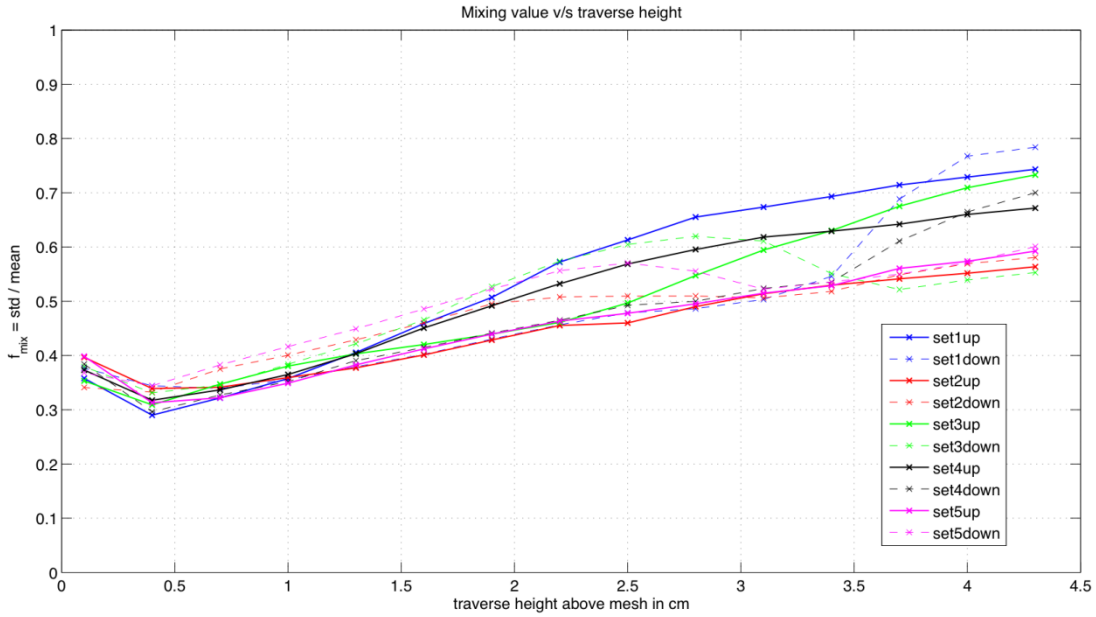

Figure 39: (e) Mixing v/s traverse height for TExpt5, U = 2500

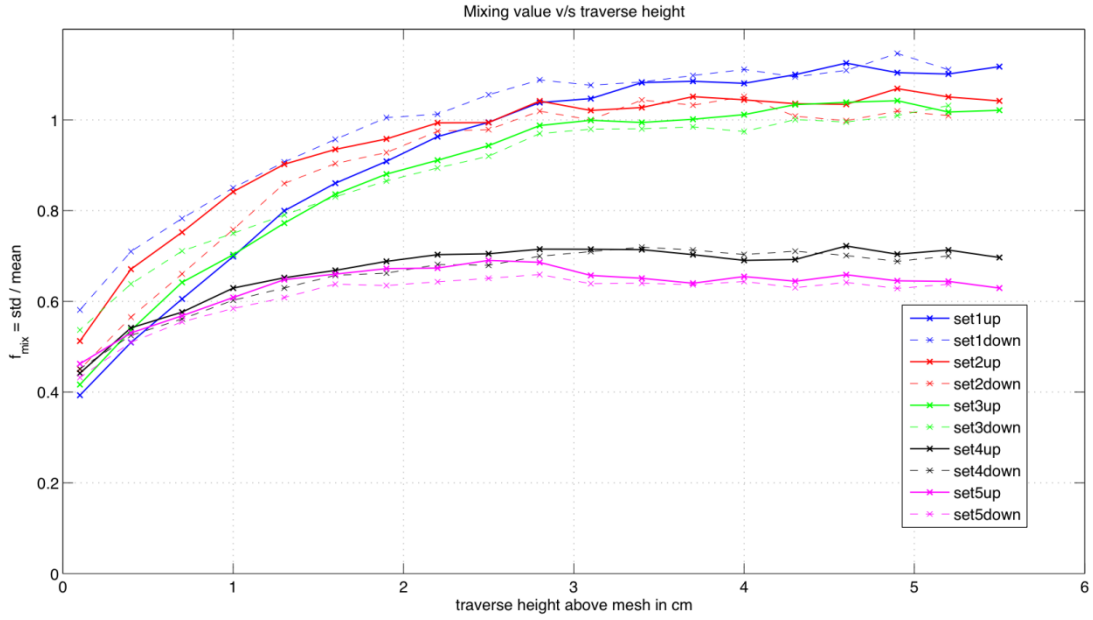

Figure 39: (f) Mixing v/s traverse height for TExpt6, U = 1/300

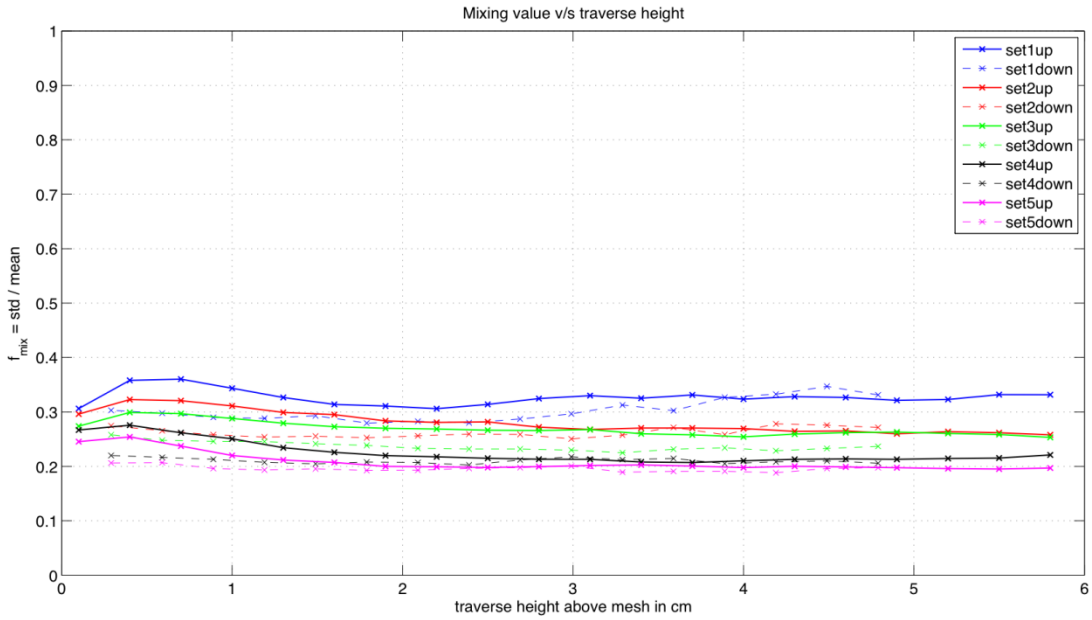

Figure 39: (g) Mixing v/s traverse height for TExpt7, U = 1/65

In Figure 39 (a)-(g) a lower value of f_{mix} means that the mixing is good and higher value indicates that the mixing is not very efficient. For the case of TExpts 1, 2, 4, 7 (Figure 39 (a), (b), (d), (g)), we see that the mixing value is almost constant with height. In TExpts 3, 5, 6 (Figure 39 (c), (e), (f)) we see a uniform trend where the mixing efficiency reduces with increase in height above the mesh. In TExpt7 (Figure 39 (g)) we find that the mixing profile is similar to that in TExpt1.

We have determined the average values of the mixing (taking last two cycles, set4 and set5) at heights of 1, 2, 3 cm above the mesh and compare it across the different regimes of viscosity ratio U. Figure 40 shows a plot of Mixing versus the viscosity ratio U with profiles at 1, 2, 3 cm above the mesh. The 3 height profiles show a similar trend. We conclude from Figure 40 that the mixing is best at U = 1 and decreases either if U increases (U>1) or if U decreases (U<1). Our results on mixing contradict the results reported by Jellinek et al. (1999) in the U<1 regime.

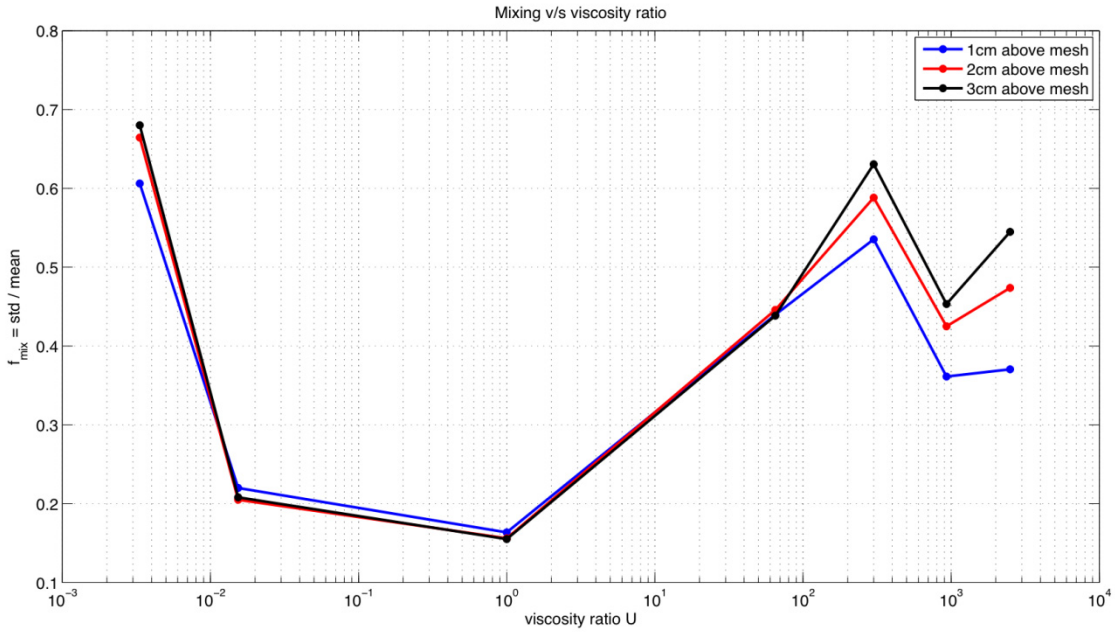

Figure 40: Plot of Mixing v/s viscosity ratio U comparing data from all the traverse experiments

The images from the traverse experiments can be used to reconstruct the plume structure in three-dimensions. This is done using a code similar to the one adopted before by selecting frames at regular intervals and converting the images to binary. The images basically stacked on each other in the z axis (height) and are stored in a single matrix. Tecplot software has been used for postprocessing. We plot the isosurfaces after loading the data file into tecplot. The data between two frames in interpolated and the plume surfaces are plotted as isosurfaces. Figure 41 shows an example of such a 3D reconstruction for TExpt3 (U=300). This 3D reconstruction method provides a valuable tool to visualize the flow structure in 3 dimensions. Another way to visualize the data is to take slices through the flow and move the slices throughout the test section. The region in the slice can be highlighted and the other regions can be made invisible. The movement of slices in x,y or z direction can be exported into videos (see videos in the videoTecplot folder on enclosed CD).

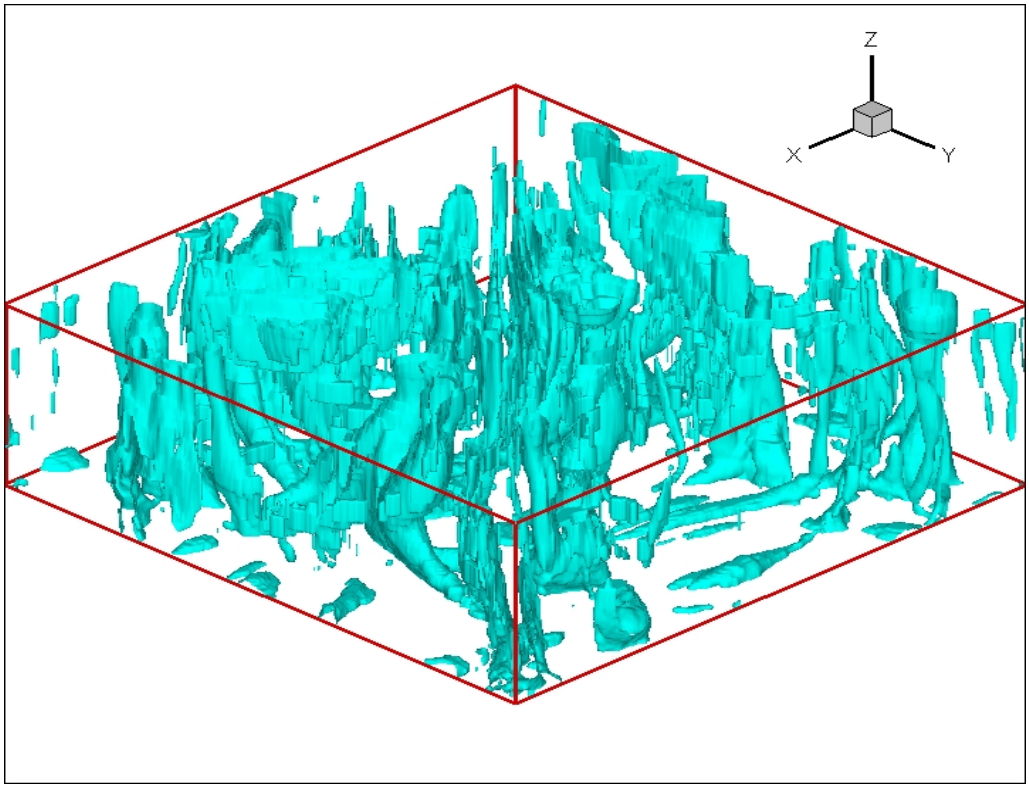

Figure 41: A 3D reconstructed isometric view of the plume structure for TExpt3, U = 300

3.2 Role of Buoyancy flux on plume structure and dynamics

In this section, we report results from preliminary experiments conducted to study the effect of buoyancy flux on plume structure and dynamics. Set 1 experiments were those in which the viscosity ratio U was varied with other parameters kept constant. The experiments reported here are referred to as Set 2 experiments. Table 9 summarizes the parameters varied in these experiments.

Experiment #	**U**	**wt% CMC**	**Flow rate Q** in ml s^{-1}	**Experiment Details**
Expt17 a, b, c, d	1	0	(a)1 (b)2 (c)3 (d)4	Variation of Flow rate
Expt18 a, b	930	0.75	(a)4 (b)1	Variation of Flow rate
Expt19	1/300	0.5	2	Doubling $\Delta\rho$
Expt20	2500	1	4	Viscosity contrast layer

Table 9: Parameters varied in Set 2 experiments

In Set 2 experiments, the buoyancy flux was varied in Experiments 17, 18 and 19. In Experiment 20, we studied the motion of a plume across an interface of viscosity contrast. In the sections that follow, we describe each experiment separately.

The buoyancy flux in our experiments is basically $g\frac{\Delta\rho}{\rho}v_i$, where g is the acceleration due to gravity, $\Delta\rho$ is the density difference between the upper chamber fluid and the bottom chamber fluid and v_i is the through flow velocity across the mesh. The buoyancy flux can be varied in two ways: One is to vary $\Delta\rho$ and the other way is to vary v_i. Varying the through flow rate Q corresponds to varying v_i across the mesh. In Experiments 17 and 18, we have varied the flow rate Q. Experiment 17 (d) corresponds to U = 1 (like TExpt1), but here we have varied the flow rates progressively (Q = 1, 2, 3, 4 ml s^{-1}) in separate experiments (Expt17 (a) to (d)). Figure 42 shows a montage of the near-wall planforms obtained in Experiment 17. Figure 42 shows the variation of the near-wall planform plume structure at different flow rates. Each row in Figure 42 shows the variation of structures with time, and here it is assumed that a quasi-steady state has been reached. We can clearly see that the plume spacing is smallest at the smallest flow rate (Q = 1 ml s^{-1}) and is the maximum for the highest flow rate (Q = 4 ml s^{-1}). Hence, we can conclude that the plume spacing increases as the flow rate increases (also reported by Kenjeres and Hanjalic (2002). As the flow rate is increased, the line plumes seem to be thicker.

Also, in some cases, there are empty regions without plumes on the mesh. These regions are probably caused by the downwelling ambient fluid. These empty regions are transients that keep moving all over the mesh area and are prominent in the high flow rate case (Q = 4 ml s^{-1}). In general we see movement of the line plumes in horizontal planes. The lateral movement of plumes is more pronounced in the high flow rate cases.

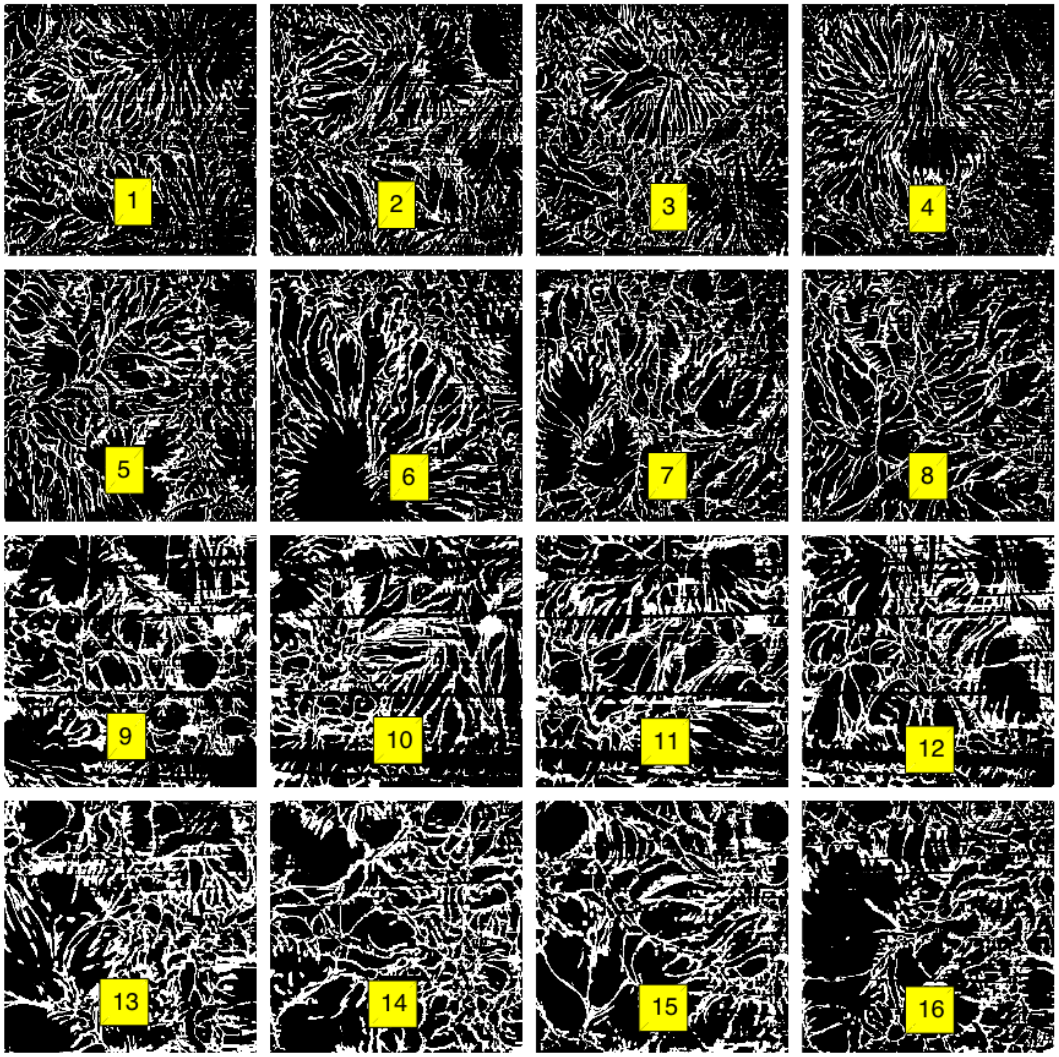

Figure 42: Near-wall plan view images (binary) of plume structures in Experiment 17(a)-(d). The structures in white colour correspond to the plumes and the background is black. Each row represents the near-wall planforms for a specific flow rate. The four cases in each row shows the variation of the planform structures with time. Cases 1-4 correspond to Q = 1 ml s^{-1} and t = 68, 97, 126, 155 seconds. Cases 5-8 correspond to Q = 2 ml s^{-1} and t = 54, 83, 112, 141 seconds. Cases 9-12 correspond to Q = 3 ml s^{-1} and t = 41, 70, 99, 128 seconds. Cases 13-16 correspond to Q = 4 ml s^{-1} and t = 42, 71, 100, 129 seconds.

The effect of varying flow rate was also studied for the U = 930 case (Experiment 18 (a) and (b)). Figure 43 (a) (b) shows a near-wall planform plume structure for Experiment 18. In Figure 43 (a) the planform corresponds to a flow rate Q = 4 ml s^{-1} and in Figure 43 (b) the flow rate is Q = 1 ml s^{-1}.

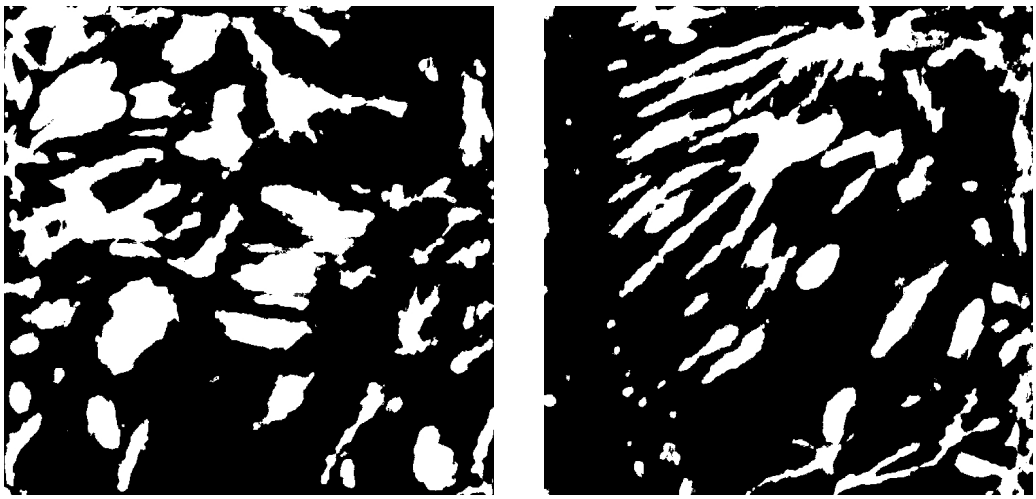

(a) (b)

Figure 43: Near-wall plan view images (binary) of plume structures in Expt18 (U = 930). The structures in white colour correspond to the plumes and the background is black. In (a) the flow rate is Q = 4 ml s^{-1} and in (b) the flow rate is Q = 1 ml s^{-1}

We see in Figure 43 (b) that the convection looks more like the transient state of (a). In Figure 43 (a) however, the convection has reached a quasi-steady state. In Figure 43 (b), line plumes have appeared. Line plumes usually disappear when the experiment corresponds to U = 300 onwards. It might be that the lower flow rate favors the formation of line plumes. One more observation is that the activity of the convection is less in (b) compared to (a) where the convection is more vigorous.

Another way of varying the buoyancy flux is to change $\Delta\rho$, the density difference between the upper chamber fluid and the lower chamber fluid. We conducted Experiment 19 (U = 1/300) to study the changes in the plume structure when $\Delta\rho$ is doubled. Figure 44 (a) and (b) show raw images of the near-wall planform plume structure for Expt19. Figure 44 (a) corresponds to a case of U = 1/300 as seen in our previous experiments (TExpt6). Figure 44 (b) corresponds to the near-wall planform seen in a case when U = 1/25 (see Figure 13 (a) case 4). Figure 44 suggests that the effect of doubling the initial $\Delta\rho$ resulted in an apparent increase of the viscosity ratio U from (1/300 to 1/25).

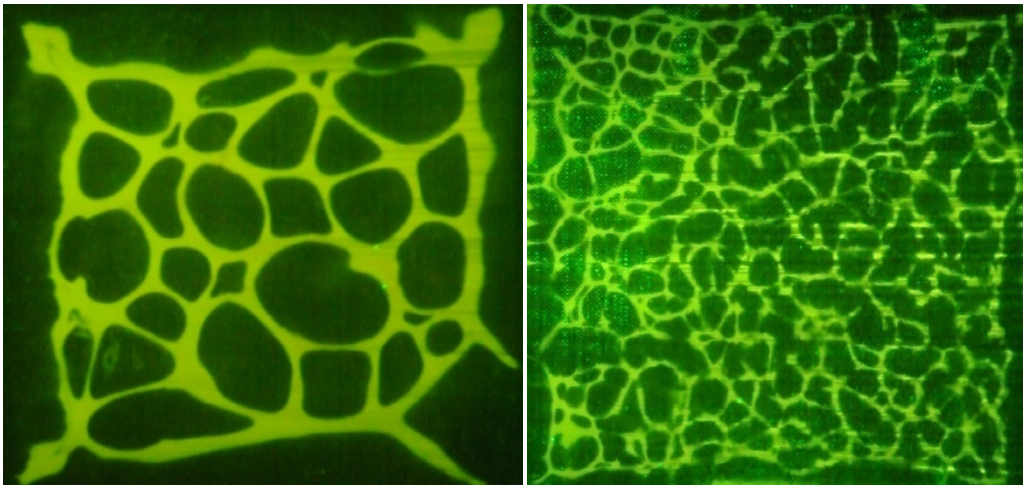

(a) **(b)**

Figure 44: Near-wall plan view images of plume structures in Experiment 19 (U = 1/300). In (a) the initial $\Delta\rho$ was 2.4 kg m^{-3} and in (b) the initial $\Delta\rho$ = 4.8 kg m^{-3} (double of (a))

We conducted an experiment (Expt20) to study the motion of a plume across a viscosity interface. Figure 45 shows a sequence of images of a plume moving across an interface with a viscosity contrast of 2500 (see video_viscinterface on CD).

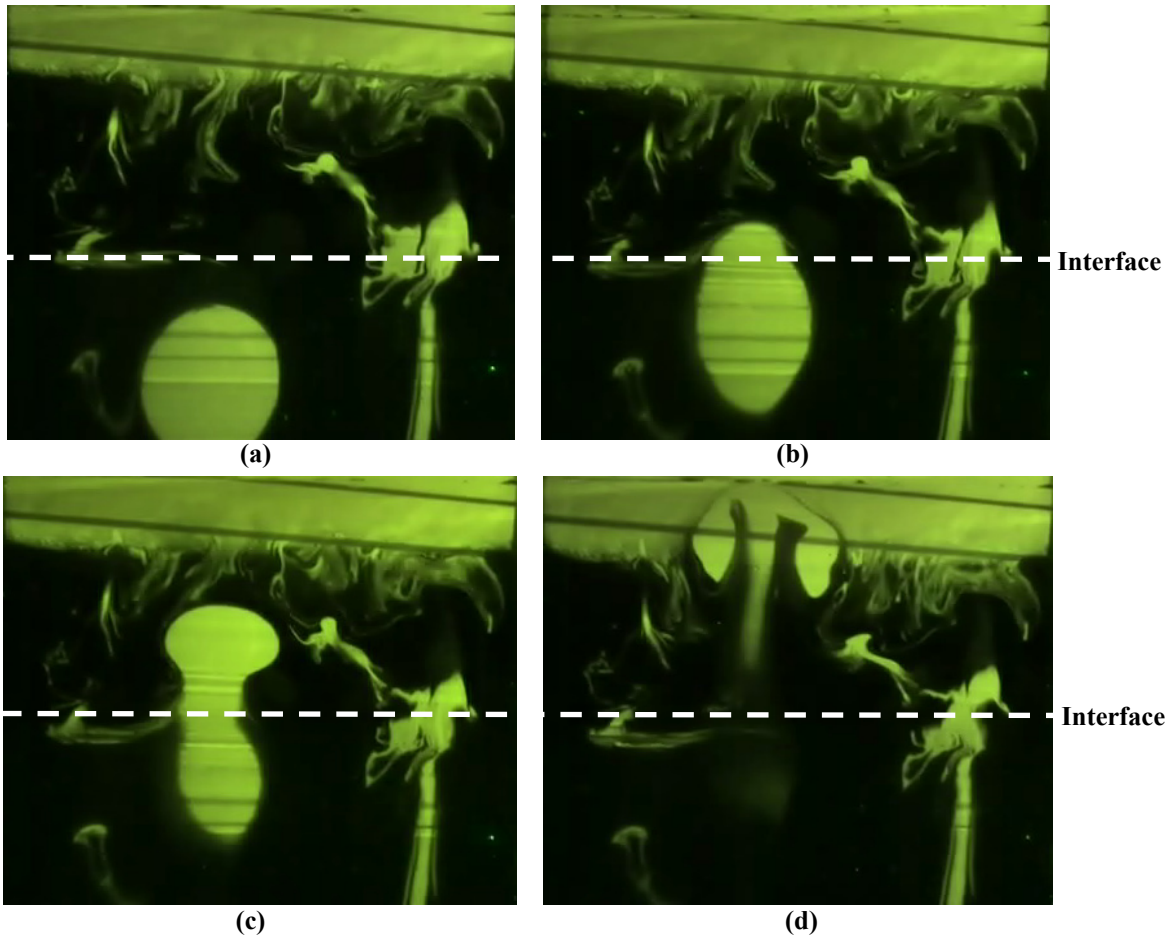

Figure 45 (a) (b) (c) (d): A sequence of images showing the motion of a plume across an interface having a viscosity contrast of 2500, showing the formation of a dipolar structure.

In this experiment, a 5 cm layer of water was slowly poured onto a pre-existing 15.5 cm high layer of viscous fluid. This corresponds to an experiment similar to VExpt4 (U = 2500) except that here we have an additional 5 cm layer of tap water. Here, we focus on studying the motion of the plume across the viscosity interface. Figure 45 (a) shows the plume head approaching the viscosity interface. In Figure 45 (b), the plume head-tip penetrated through the viscosity interface. The viscous interface is expanded and the plume head-tip breaks through with a 'pinch-off' effect. This results in an elongation of the plume-head tip as seen in Figure 45 (b). The remaining buoyant fluid in the plume flows through a smaller opening at the viscosity interface and hence there is a net acceleration in the upward direction (Figure 45 (c)). The acceleration results in formation of a dipolar vortical structure as seen in Figure 45 (d). This dipolar structure impinges on the surface and spreads beneath horizontally. This phenomenon is of interest in the earth's mantle where there is a density and viscosity discontinuity (interface) at a depth of ~ 660 km below the crust. Existing studies related to this phenomenon in literature have considered plume motion across a density interface. Kumagai and Kurita (2000) studied the motion of a compositionally buoyant plume across an interface with a density contrast and focused on effects of entrainment on the plume head. Kumagai et al. (2007) have studied the motion of thermally buoyant plumes across density interfaces. In their experiments, the interface viscosity contrast is ~ 10 relevant to the conditions in the earth's mantle. We have not come across any previous study reporting observations of the motion of a plume across an interface of viscosity contrast ~ 1000. This is an interesting phenomenon that can be studied in future experiments with our setup.

Chapter 4

Conclusions

We studied the effect of viscosity ratio U and buoyancy flux on the plume structure in high Rayleigh number and high Prandtl convection in a regime relevant to convection in the Earth's mantle. We conducted experiments in a glass tank of square cross-section that is divided into two chambers by a permeable mesh. The convection is driven by compositional buoyancy using sugar solution in the upper chamber and water in the lower chamber. The viscosity of the fluids is enhanced using Sodium-CarboxyMethylCellulose (Na-CMC) which enables us to achieve high viscosity ratios (U) across the mesh. The viscosity enhancement increases the Schmidt numbers (Sc) (which is a proxy for the Prandtl number). We have studied regimes ranging from U = 0.003 to 2500, Ra = $10^8$to 10^{11} and Sc = 10^3 to 10^6 for different buoyancy fluxes. A constant pressure head setup is used to deliver fluid to the bottom chamber of the tank at a constant flow rate. We use the Planar-Laser-Induced-Fluorescence (PLIF) technique to visualize the plume structures above the mesh in the near-wall planform, side section views and in 3D.

A cartoon of the characteristic plume structures in various regimes is shown in Figure 46. For U = 1, the near-wall (just above the mesh) planform (top view) plume structures have a dendritic structure. As U is increased (U >> 1), the near-wall planform plume structures change their morphology from line plumes to discrete circular blob structures. The average plume spacings and plume thicknesses also increase with an increase in U (U >> 1). When U << 1, the plumes organize themselves in cellular patterns over the boundary layer. The sizes of the cells are largest at lowest U (0.003) and the size decreases with increase in U till U =1. The changes in plume

spacing and thickness with changing viscosity ratios have been quantified using image processing techniques.

In the vertical section, changes in the plume structure can be clearly seen as U is increased. As the viscosity ratio increases (U>>1), the plume size increases and plume head shape changes from a 2-D mushroom-like structure to a spherical blob. At high U, the plumes retain their identity over a longer distance and rise to the surface due to reduced mixing with the ambient viscous fluid. Also, rising plumes leave behind low viscosity conduits. Subsequent plumes arising near these conduits prefer to flow through these conduits as they offer a low resistance path. Clustering is also seen where two or more starting plumes merge with each other as they rise and accelerate upwards. . In experiments where U < 1, the plumes rise as long columns and detach. The height of the columns are maximum for the smallest U (0.003) and decrease with increase in U. The boundary layer thickness is largest for the smallest U (0.003) and decreases with increase in U. The velocities have been estimated from the vertical sections. The plume rise velocities are highest at U = 1 and decrease with either an increase or decrease of U from U =1. On the other hand, the characteristic plume size is the smallest for U = 1 and shows an increase with either an increase or decrease of U.

When U = 1, as the buoyancy flux is increased, the plume spacing and thickness increases. Another phenomenon studied is the motion of a plume across an interface of viscosity contrast which causes a rapid vertical acceleration and formation of a dipolar vortical structure.

A traverse setup that enables the movement of a horizontal laser sheet in the vertical direction at a constant predetermined speed is used to visualize the plume's structure in 3D. An important aspect of the study is the mixing of plumes with the ambient fluid. Data from the traverse experiments are used to quantify the mixing at different heights in the flow field and at different

times. We have found that the mixing is maximum for the U = 1 case and decreases as U increases (U>1 cases). The mixing also decreases when U decreases (U<1 cases). This result is contrary to the mixing results reported by Jellinek et al. (1999).

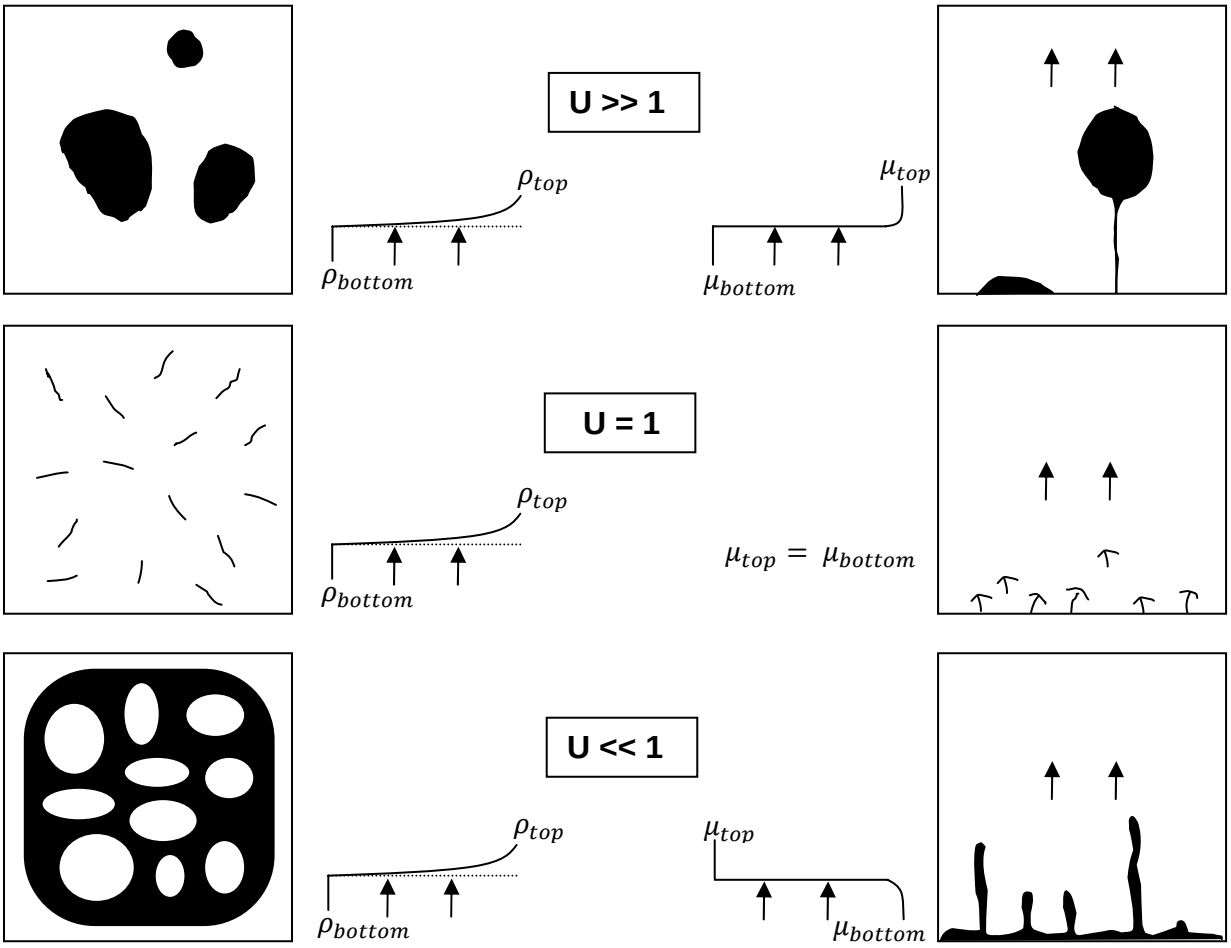

Figure 46: A cartoon of the different regimes of U and their characteristic structures. The near wall planform plume structures are shown on the left and the vertical section views are shown on the right. The density and viscosity profiles are also shown. The arrows indicate direction of flow.

Appendix – 1

Near-wall plume spacing and thickness data (PSet1)

The binary image used for analysis is shown for each case in PSet1. The histograms of plume spacing and thickness are shown separately for autocorrelations taken on Horizontal (H) and Vertical (V) rows (or columns) of the image. Combined distributions of H and V rows (or columns) for plume spacing and thickness are also shown for all cases. Raw values of the plume spacing and thickness have been tabulated in Table 5 and 7.

PExpt1: U = 1

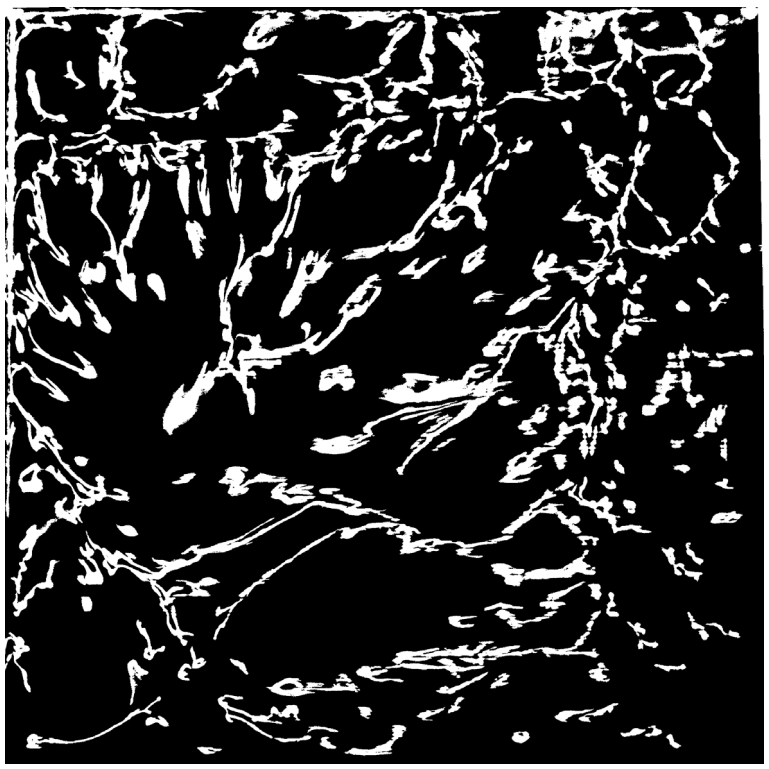

Spacing in cm (frequency of occurrence)
0.4(120)
0.77(50)
1.12(40)
2.85(32)
4.8(32)

Thickness in cm (frequency of occurrence)
0.26(430)
0.57(60)
0.46(40)

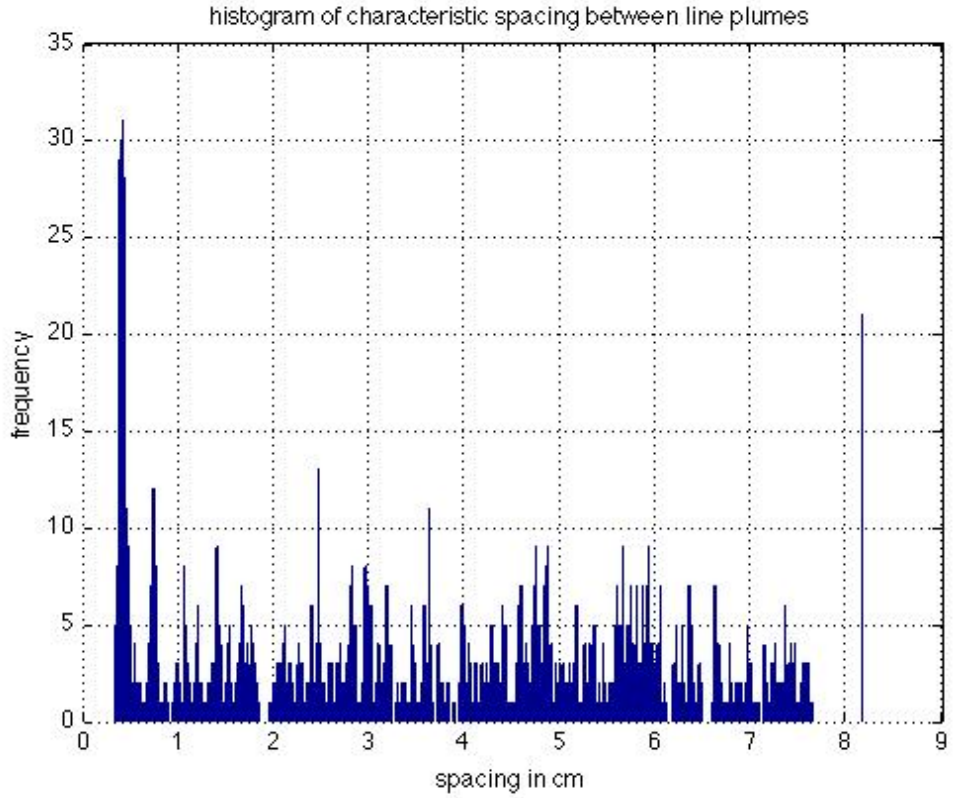
histogram of characteristic spacing between line plumes
frequency
spacing in cm
0
5
10
15
20
25
30
35
0
1
2
3
4
5
6
7
8
9

(H)

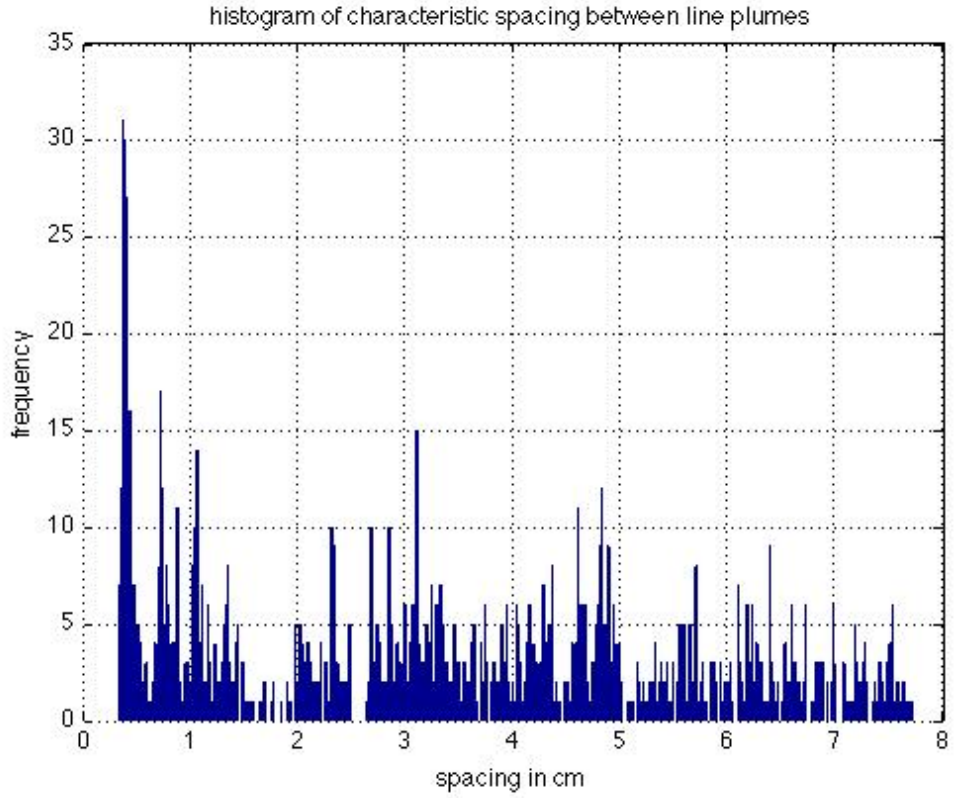
histogram of characteristic spacing between line plumes
frequency
spacing in cm
0
5
10
15
20
25
30
35
0
1
2
3
4
5
6
7
8

(V)

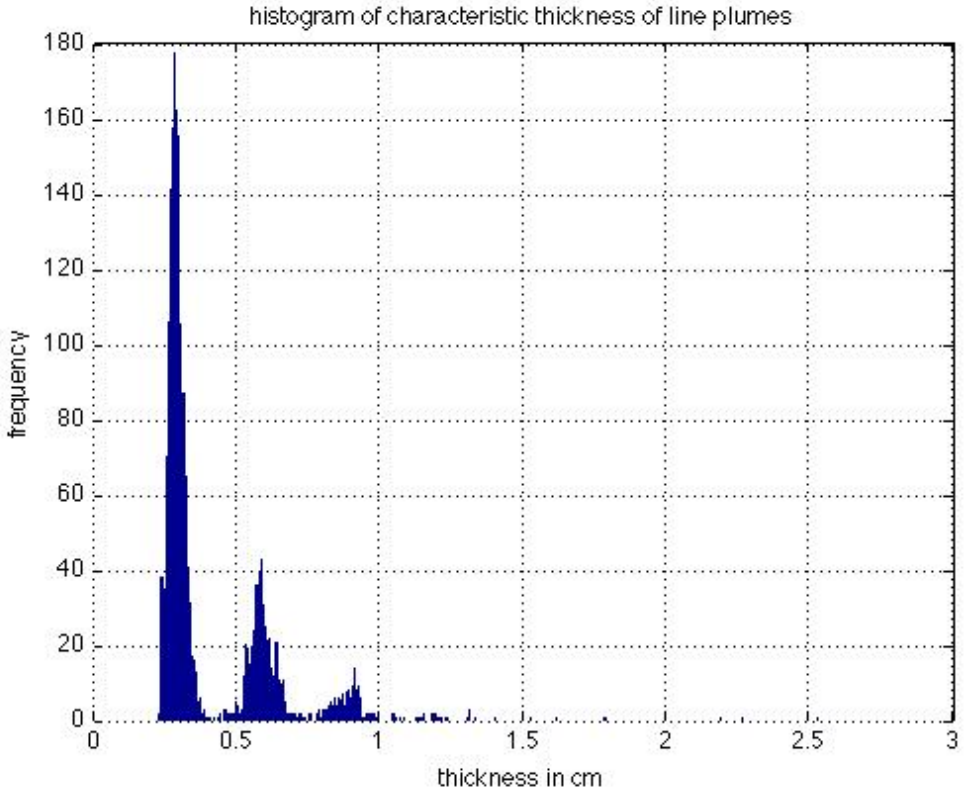
histogram of characteristic thickness of line plumes
frequency
thickness in cm
0
20
40
60
80
100
120
140
160
180
0
0.5
1
1.5
2
2.5
3

(H)

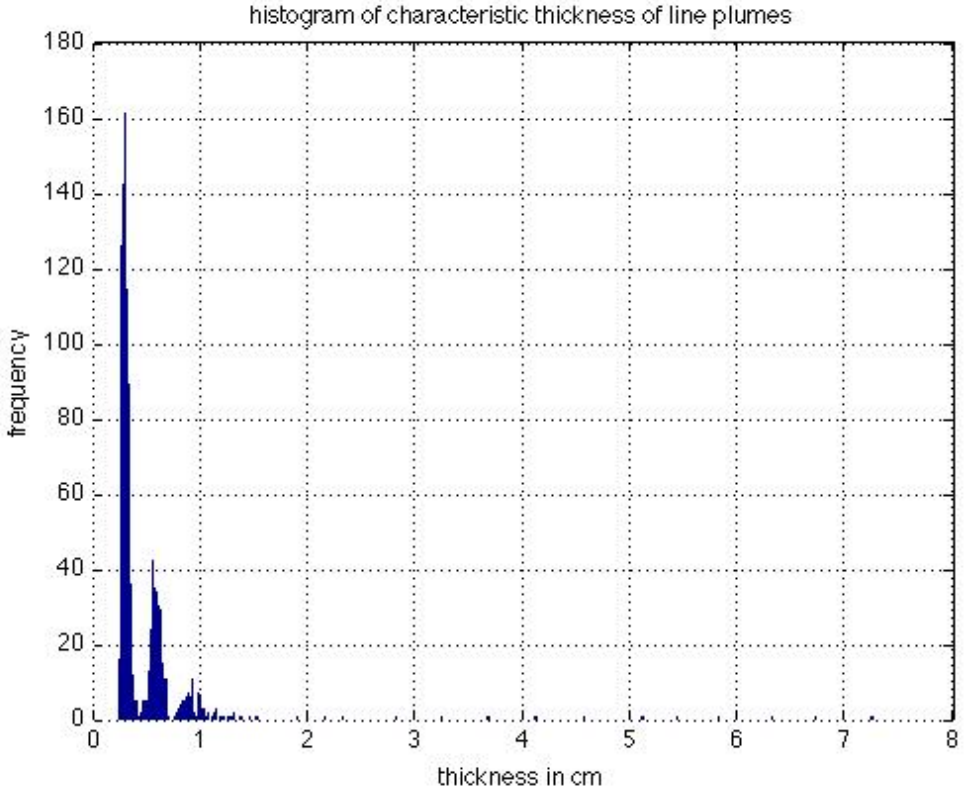
histogram of characteristic thickness of line plumes
frequency
thickness in cm
0
20
40
60
80
100
120
140
160
180
0
1
2
3
4
5
6
7
8

(V)

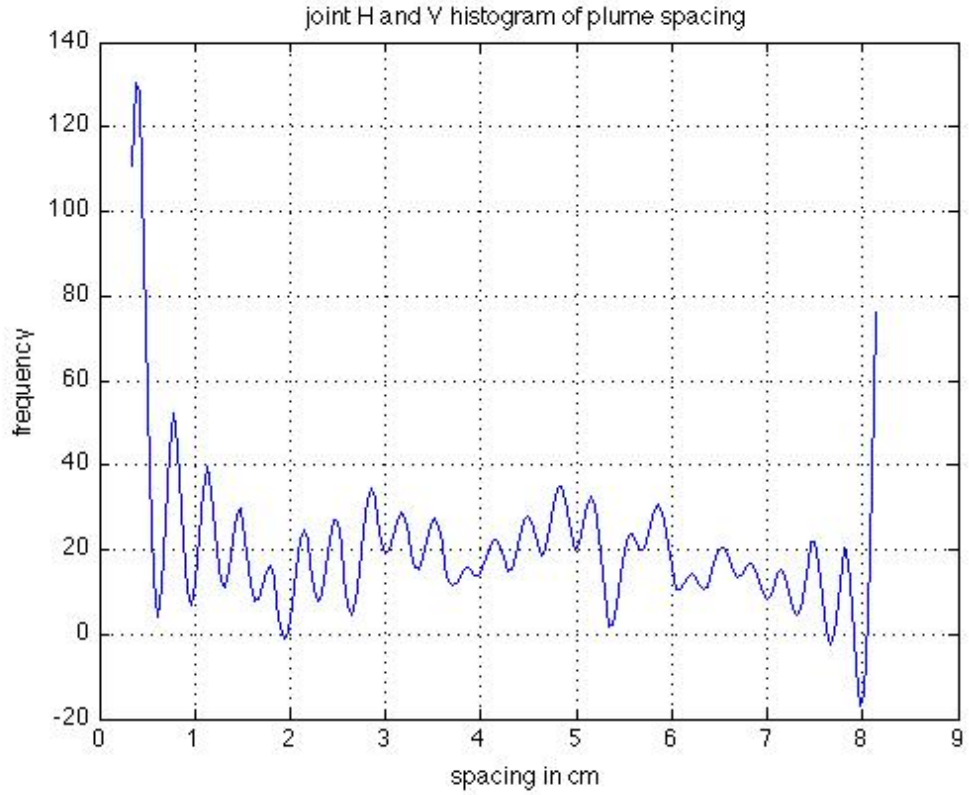
joint H and V histogram of plume spacing
frequency
spacing in cm
140
120
100
80
60
40
20
0
-20
0
1
2
3
4
5
6
7
8
9

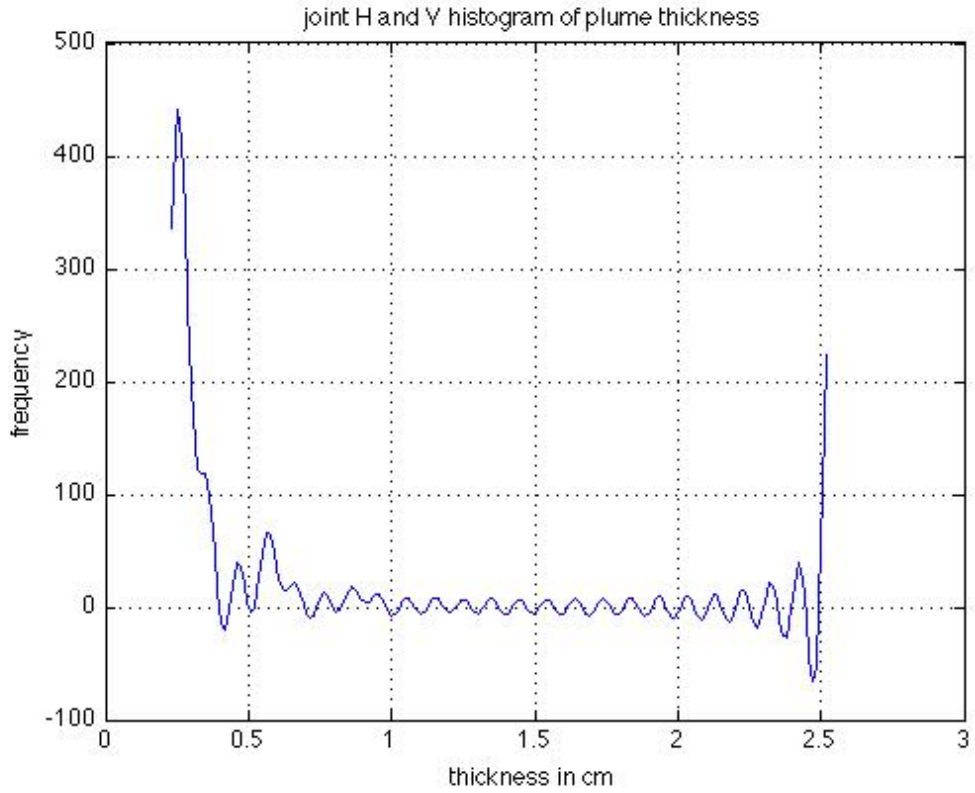
joint H and V histogram of plume thickness
frequency
thickness in cm
500
400
300
200
100
0
-100
0
0.5
1
1.5
2
2.5
3

PExpt2, U = 3

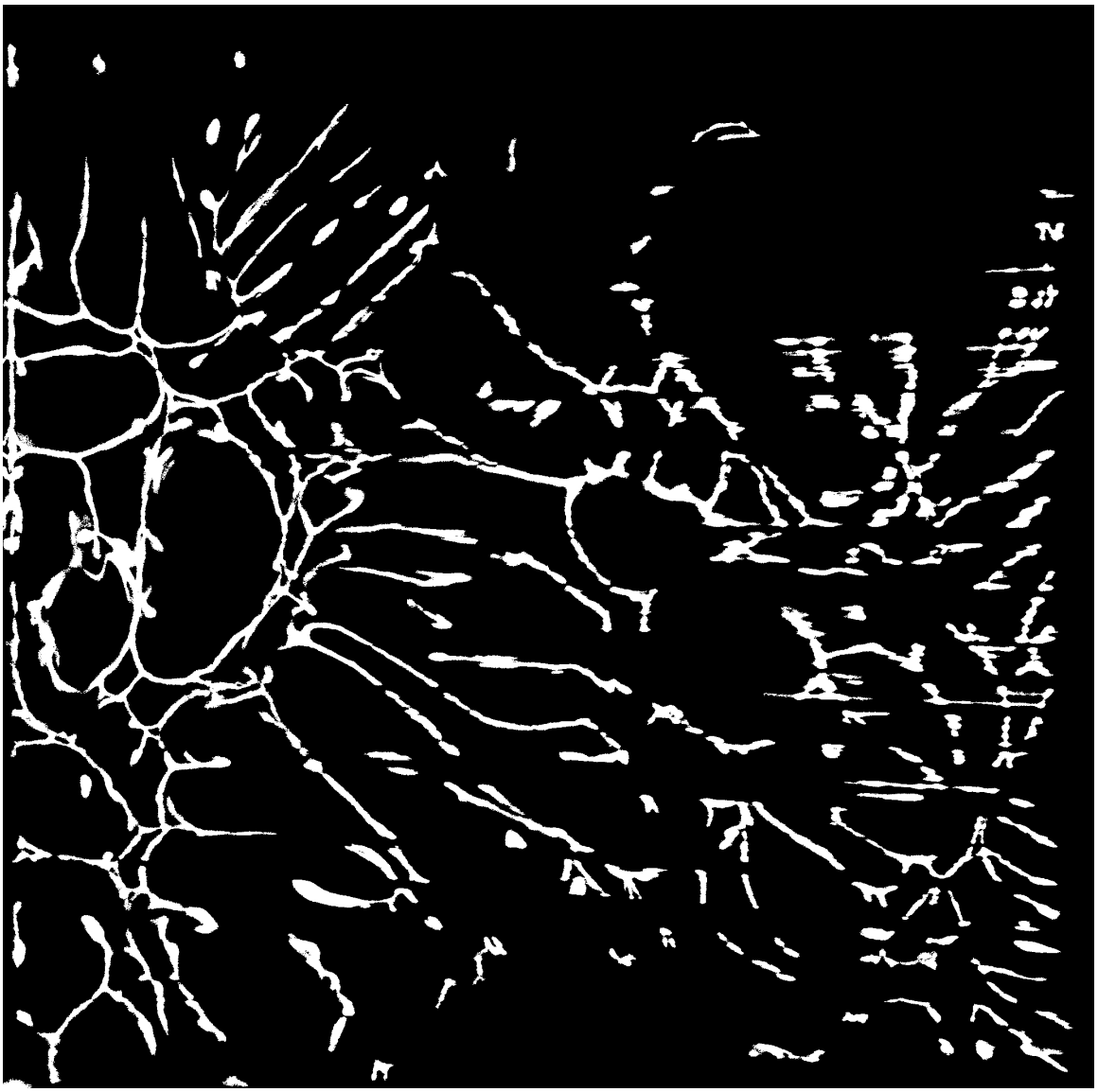

Spacing in cm (frequency of occurrence)

0.4(85)
0.77(50)
1.45(45)
3.45(35)
1.9(30)
3.9(28)

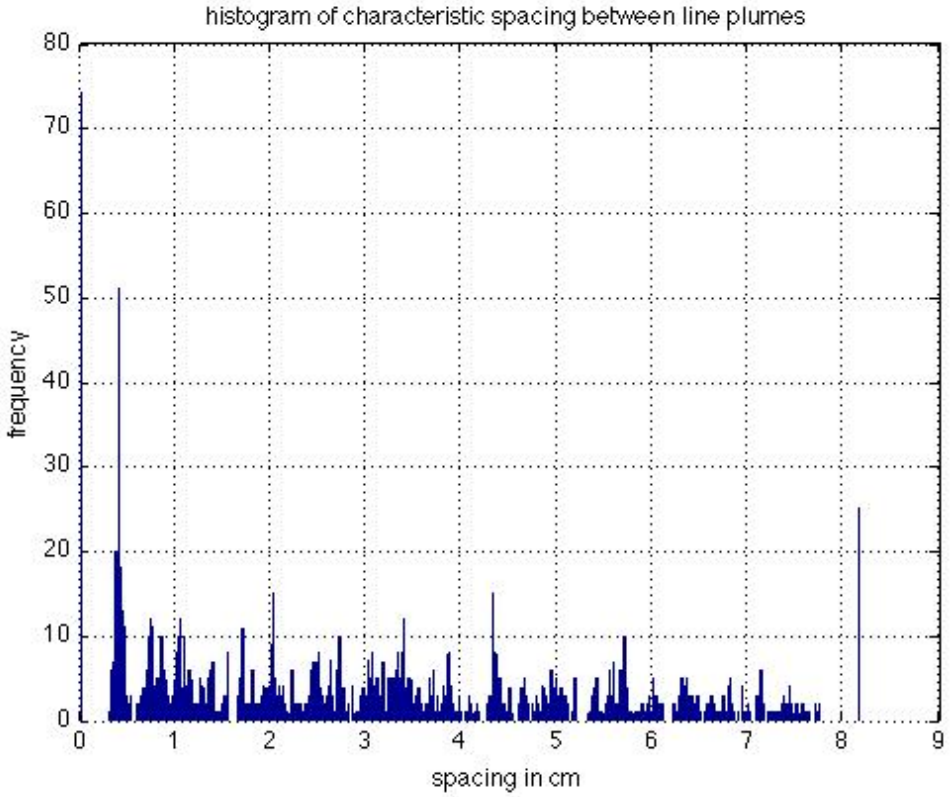
histogram of characteristic spacing between line plumes
frequency
spacing in cm
0
10
20
30
40
50
60
70
80
0
1
2
3
4
5
6
7
8
9

(H)

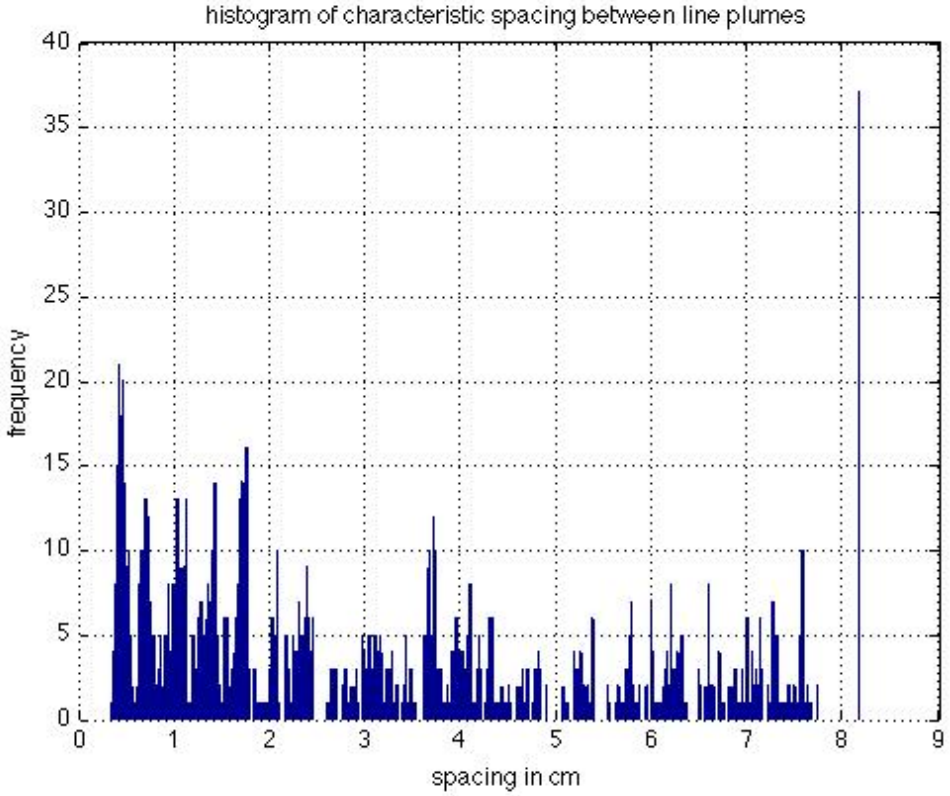
histogram of characteristic spacing between line plumes
frequency
spacing in cm
0
5
10
15
20
25
30
35
40
0
1
2
3
4
5
6
7
8
9

(V)

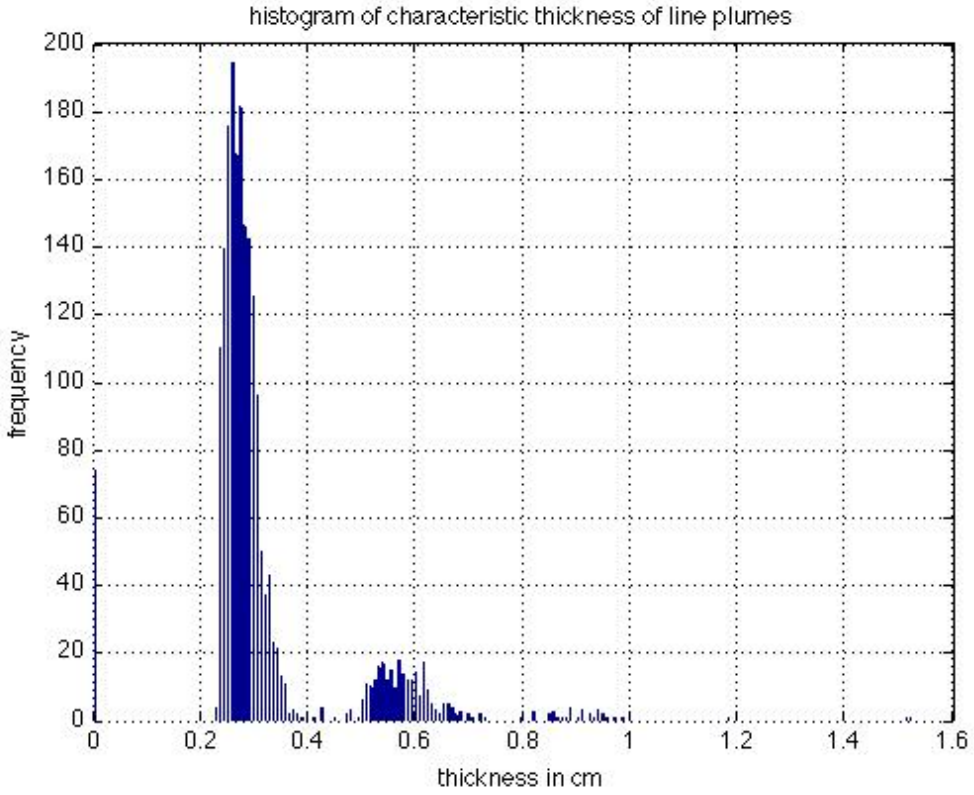
histogram of characteristic thickness of line plumes
frequency
thickness in cm
0
20
40
60
80
100
120
140
160
180
200
0.2
0.4
0.6
0.8
1
1.2
1.4
1.6

(H)

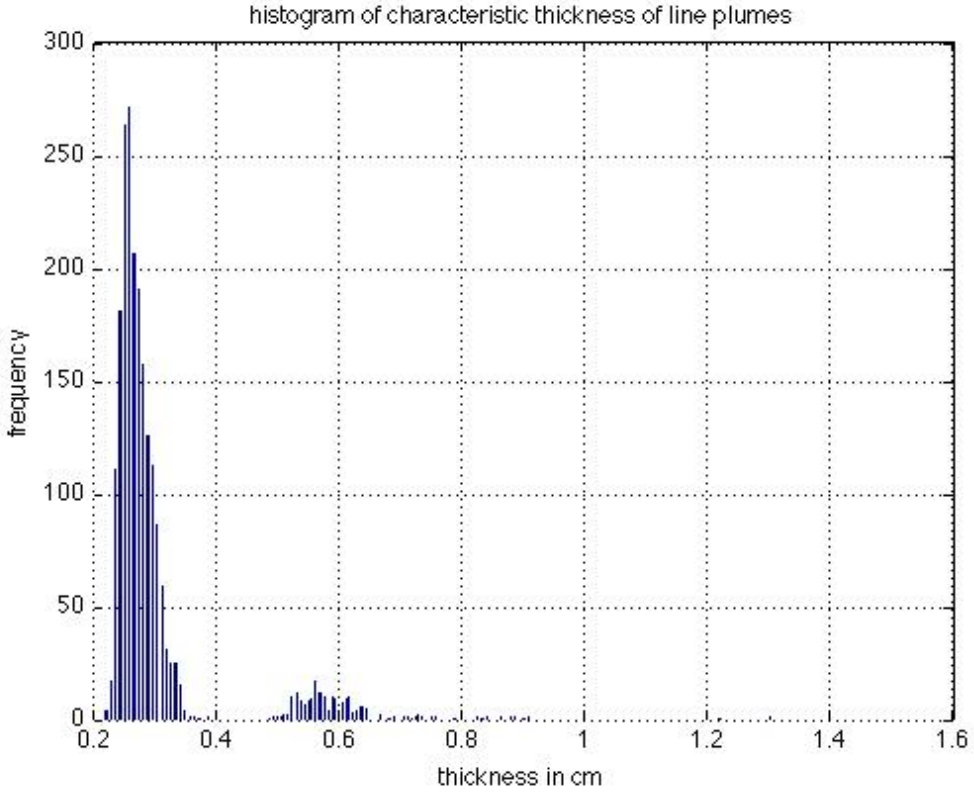
histogram of characteristic thickness of line plumes
frequency
thickness in cm
0
50
100
150
200
250
300
0.2
0.4
0.6
0.8
1
1.2
1.4
1.6

(V)

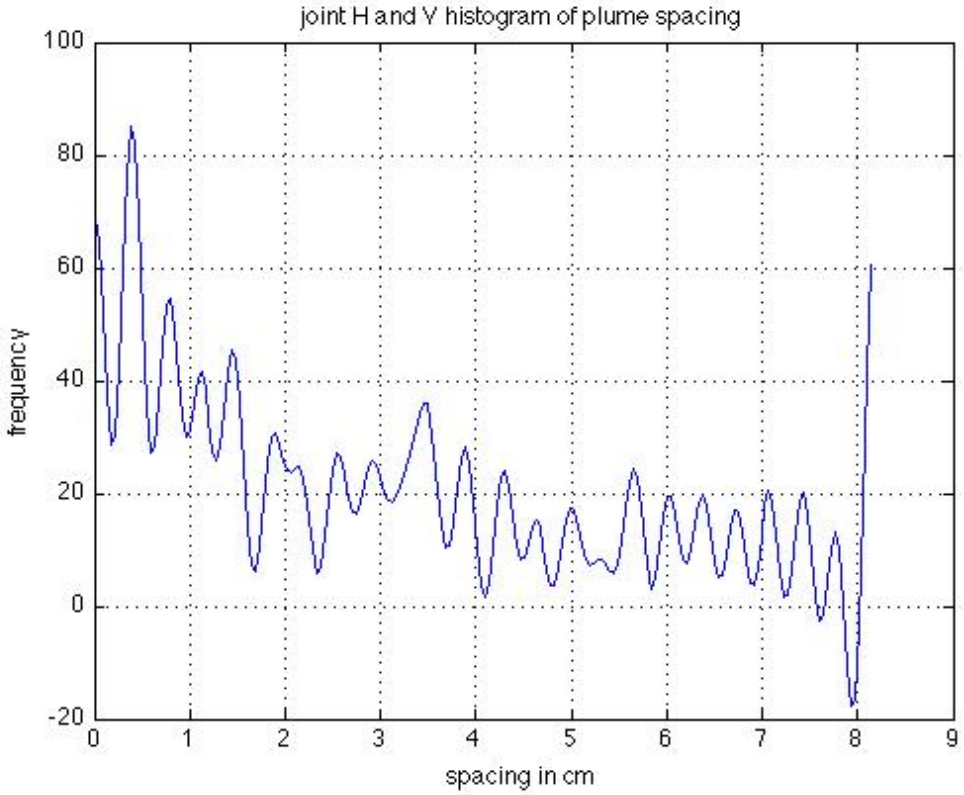
joint H and V histogram of plume spacing
frequency
spacing in cm
100
80
60
40
20
0
-20
0
1
2
3
4
5
6
7
8
9

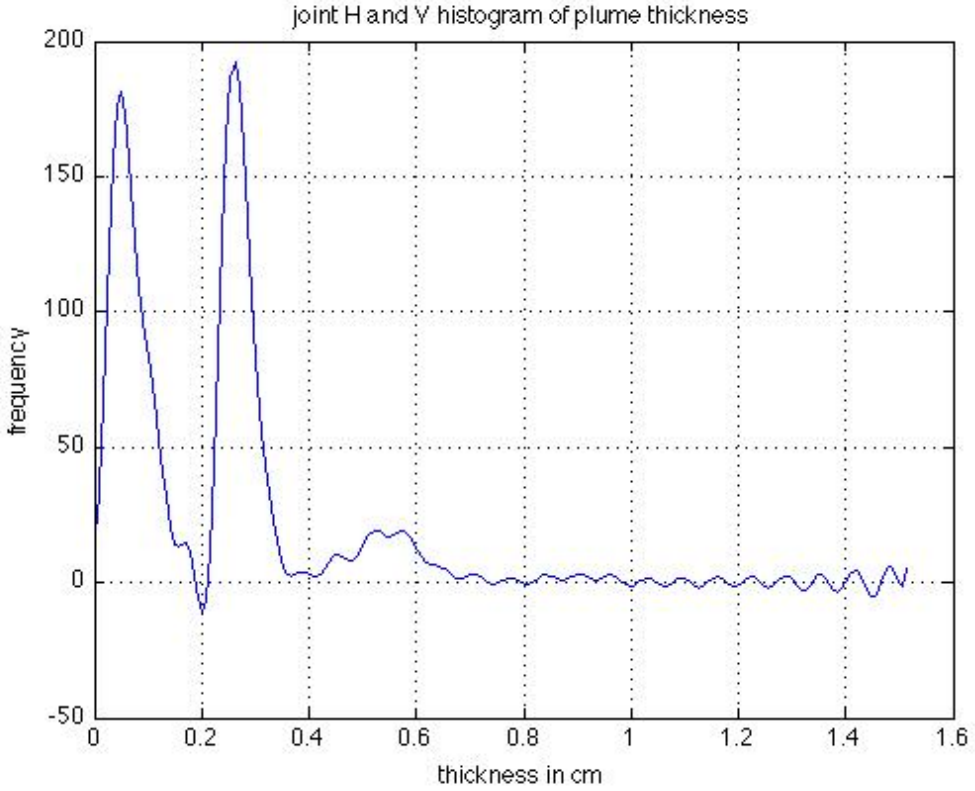
joint H and V histogram of plume thickness
frequency
thickness in cm
200
150
100
50
0
-50
0
0.2
0.4
0.6
0.8
1
1.2
1.4
1.6

PExpt3, U = 5

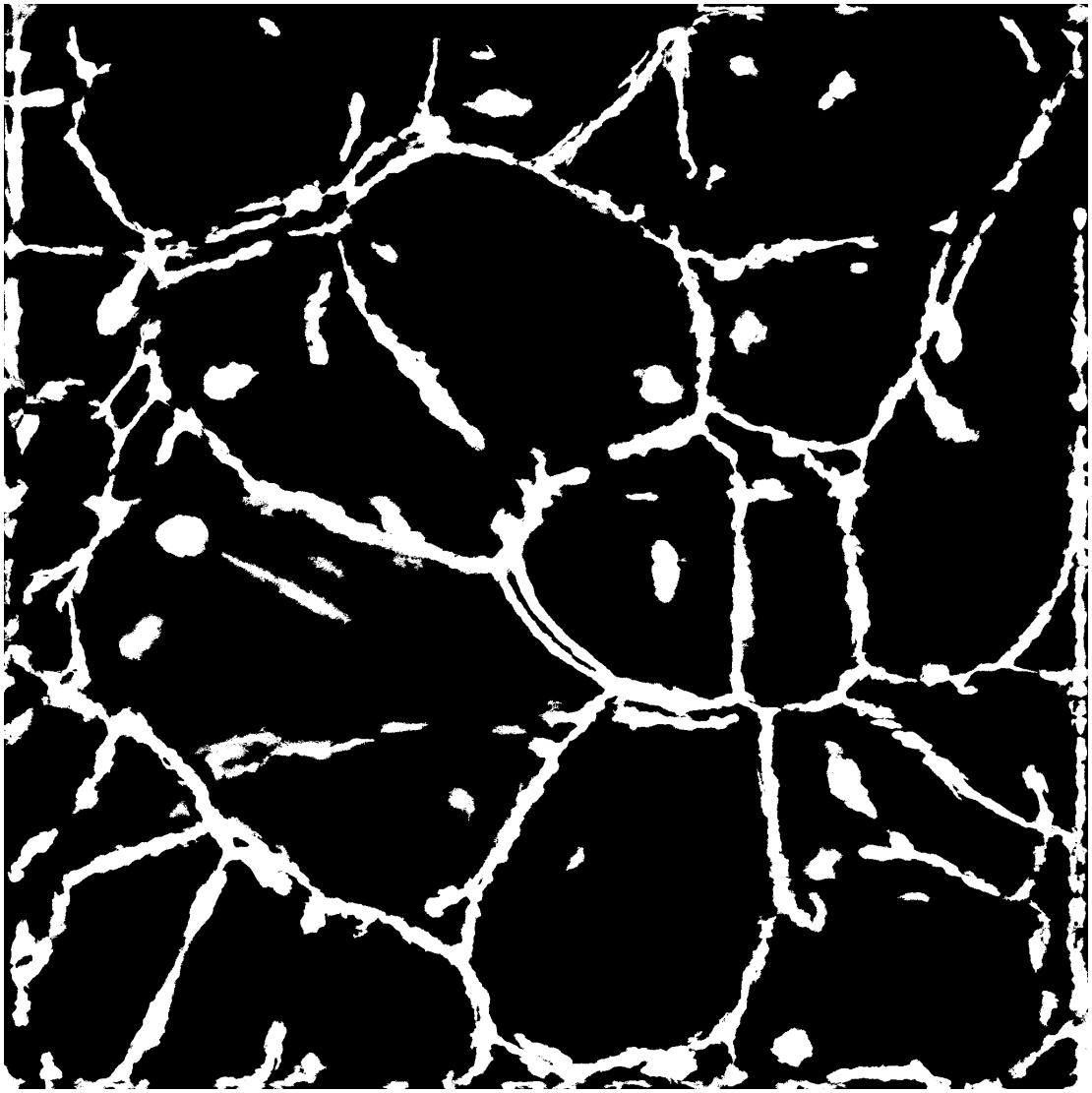

Spacing in cm (frequency of occurrence)

0.39(60)
1.4(35)
3.65(35)
5.5(35)
2.1(27)

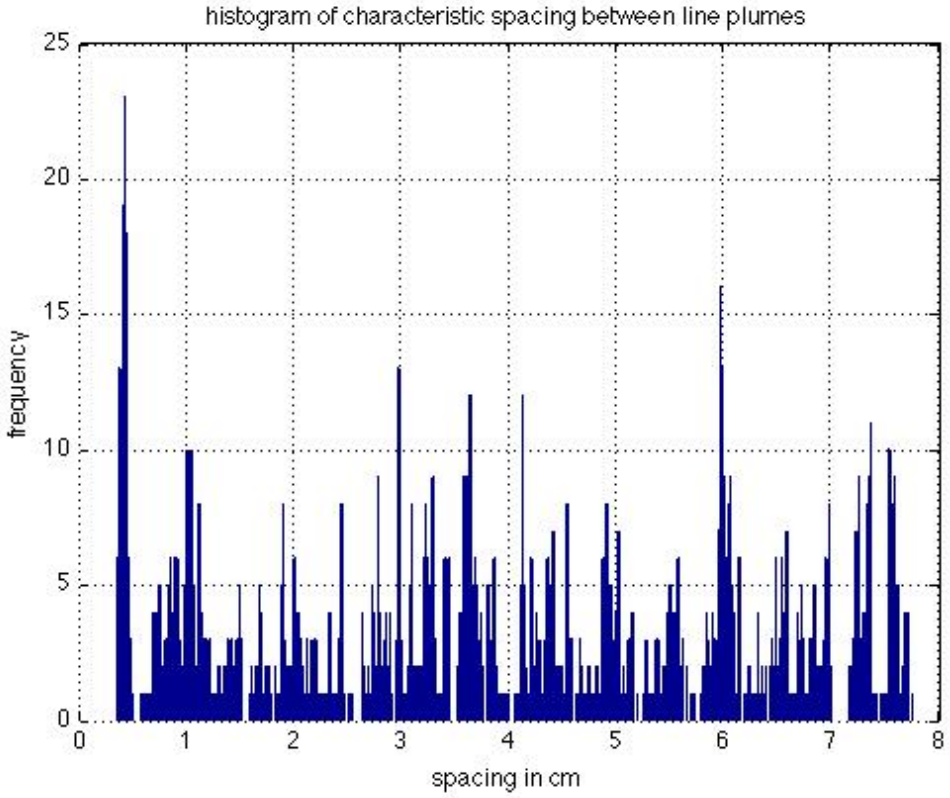
histogram of characteristic spacing between line plumes
frequency
spacing in cm
0
5
10
15
20
25
0
1
2
3
4
5
6
7
8

(H

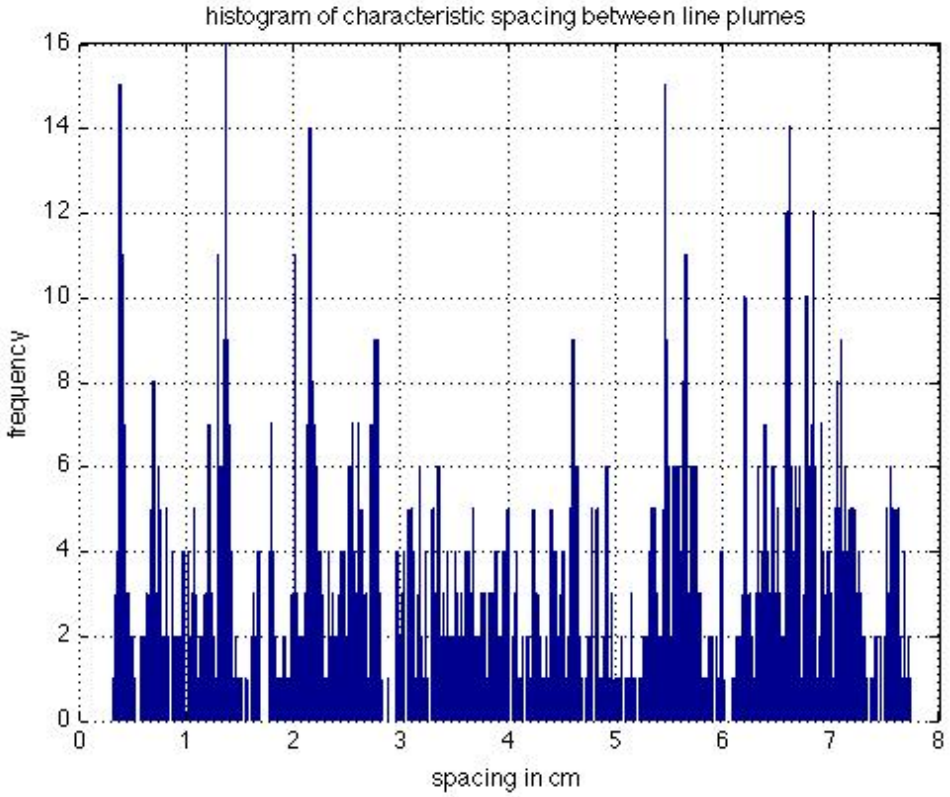
histogram of characteristic spacing between line plumes
frequency
spacing in cm
0
2
4
6
8
10
12
14
16
0
1
2
3
4
5
6
7
8

(V)

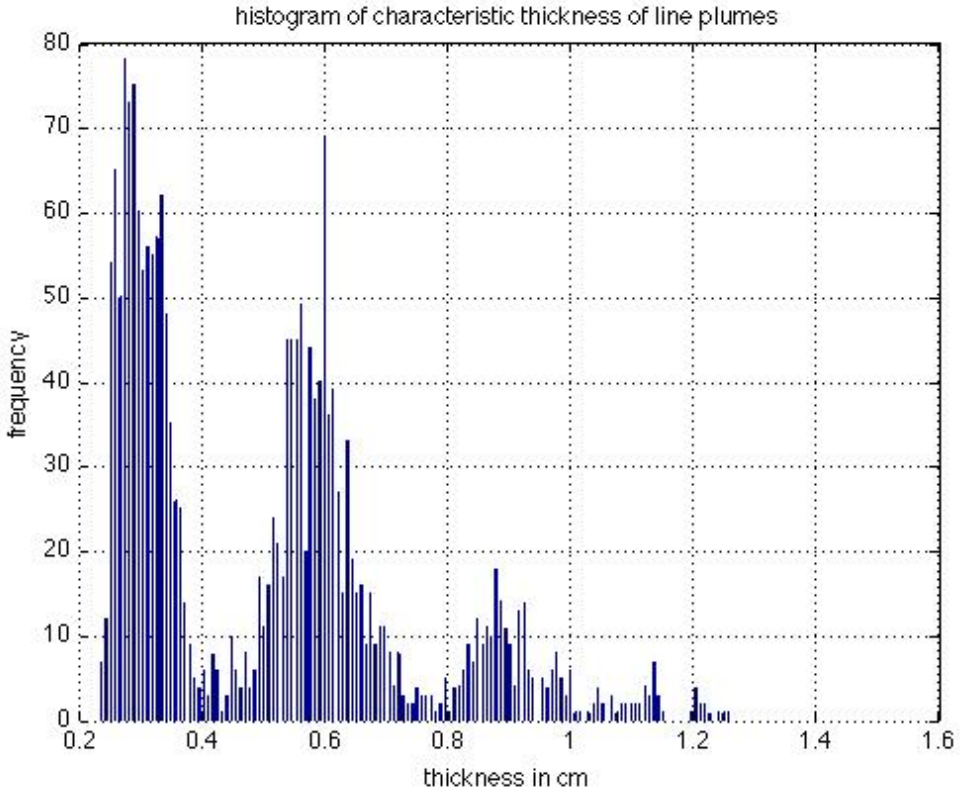
histogram of characteristic thickness of line plumes
frequency
thickness in cm
0
10
20
30
40
50
60
70
80
0.2
0.4
0.6
0.8
1
1.2
1.4
1.6

(H)

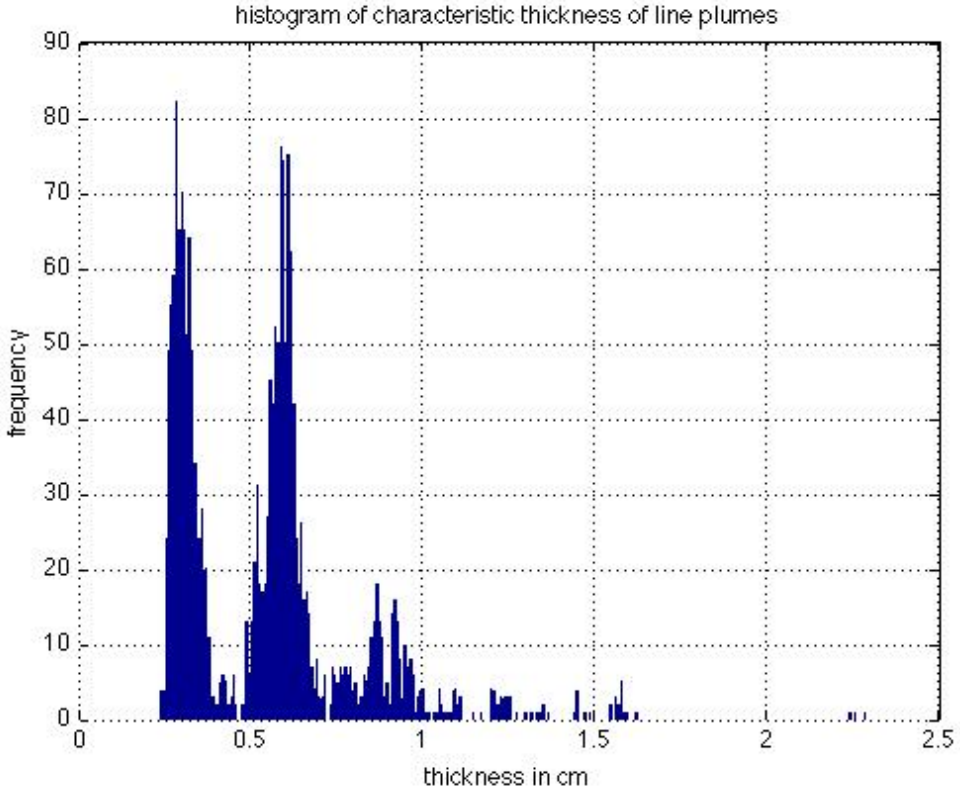
histogram of characteristic thickness of line plumes
frequency
thickness in cm
0
10
20
30
40
50
60
70
80
90
0
0.5
1
1.5
2
2.5

(V)

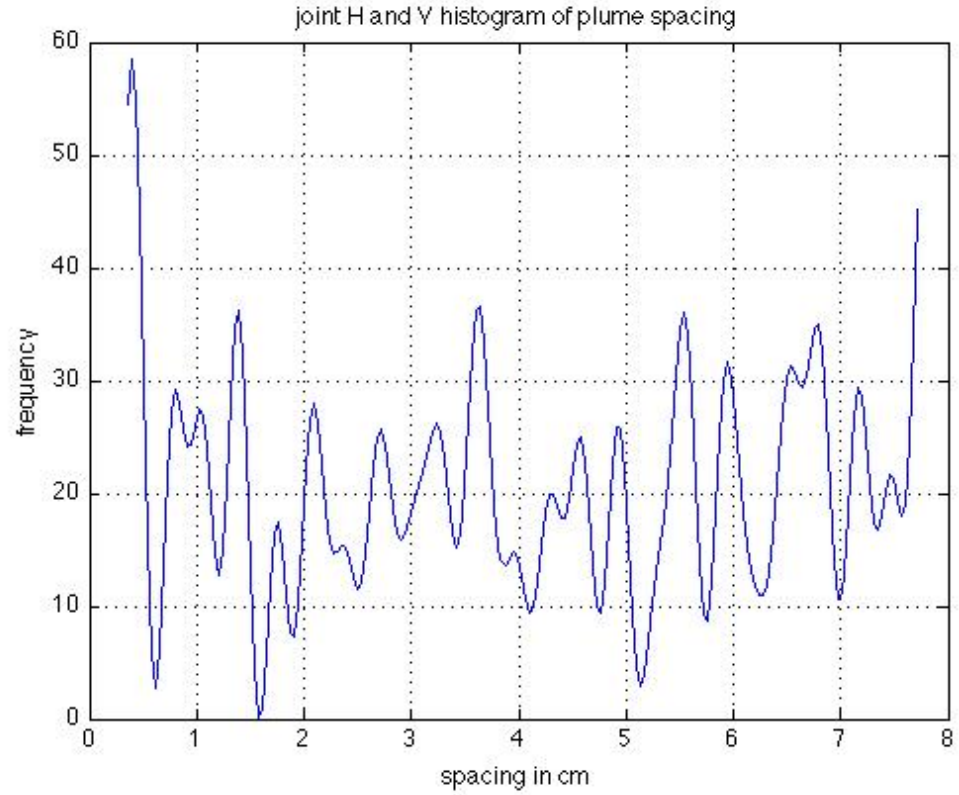
joint H and V histogram of plume spacing
frequency
spacing in cm
0
10
20
30
40
50
60
0
1
2
3
4
5
6
7
8

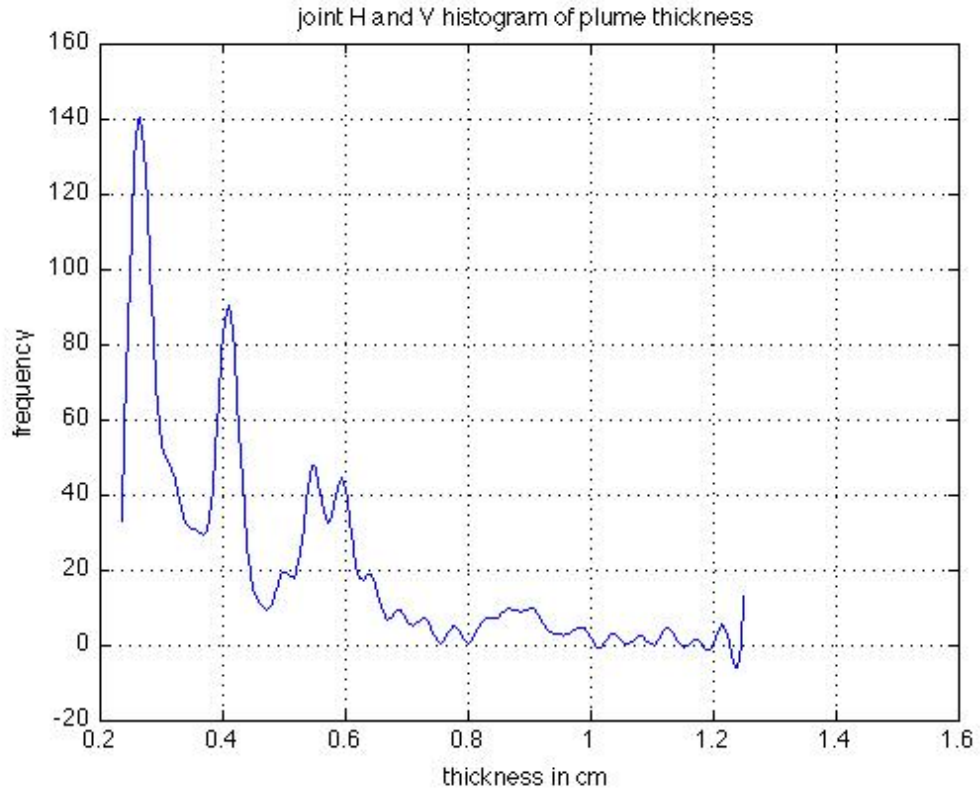
joint H and V histogram of plume thickness
frequency
thickness in cm
-20
0
20
40
60
80
100
120
140
160
0.2
0.4
0.6
0.8
1
1.2
1.4
1.6

PExpt4, U = 7

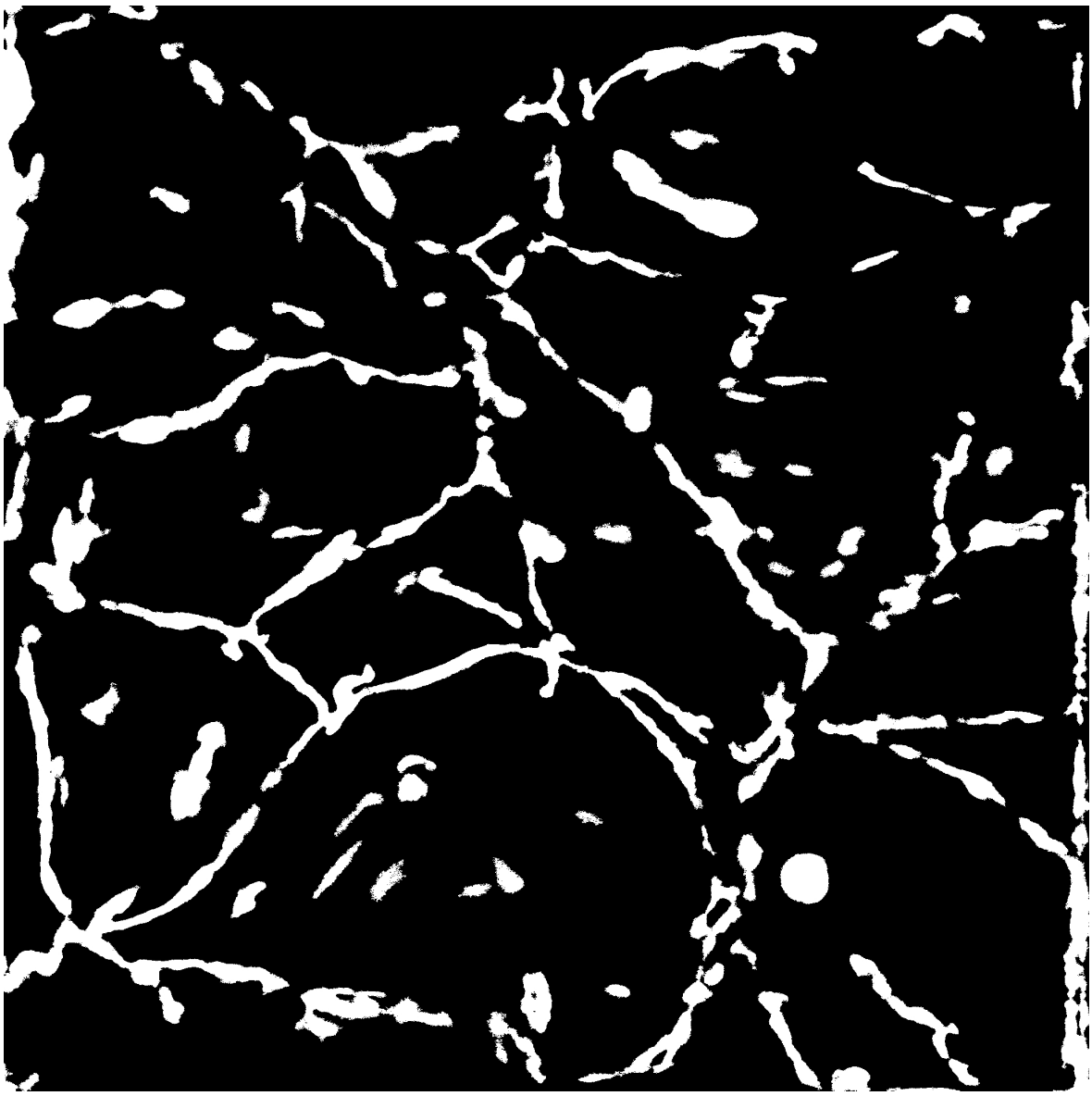

Spacing in cm (frequency of occurrence)

0.39(50)
3.75(38)
2.1(35)
4.45(33)
0.75(33)

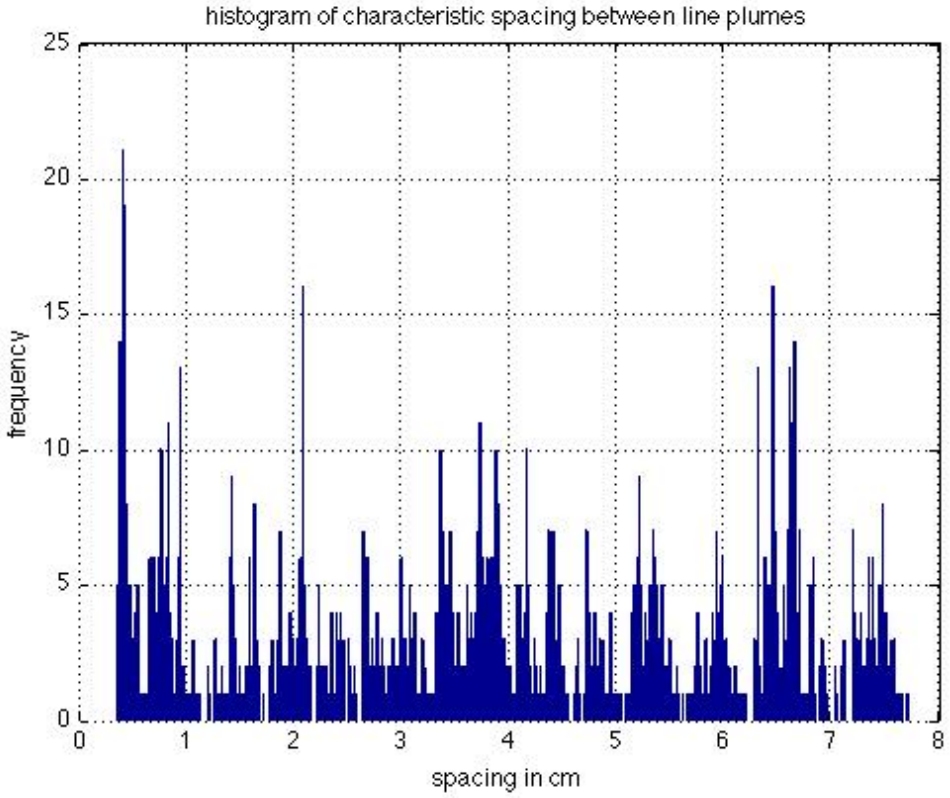
histogram of characteristic spacing between line plumes
frequency
spacing in cm
0
5
10
15
20
25
0
1
2
3
4
5
6
7
8

(H)

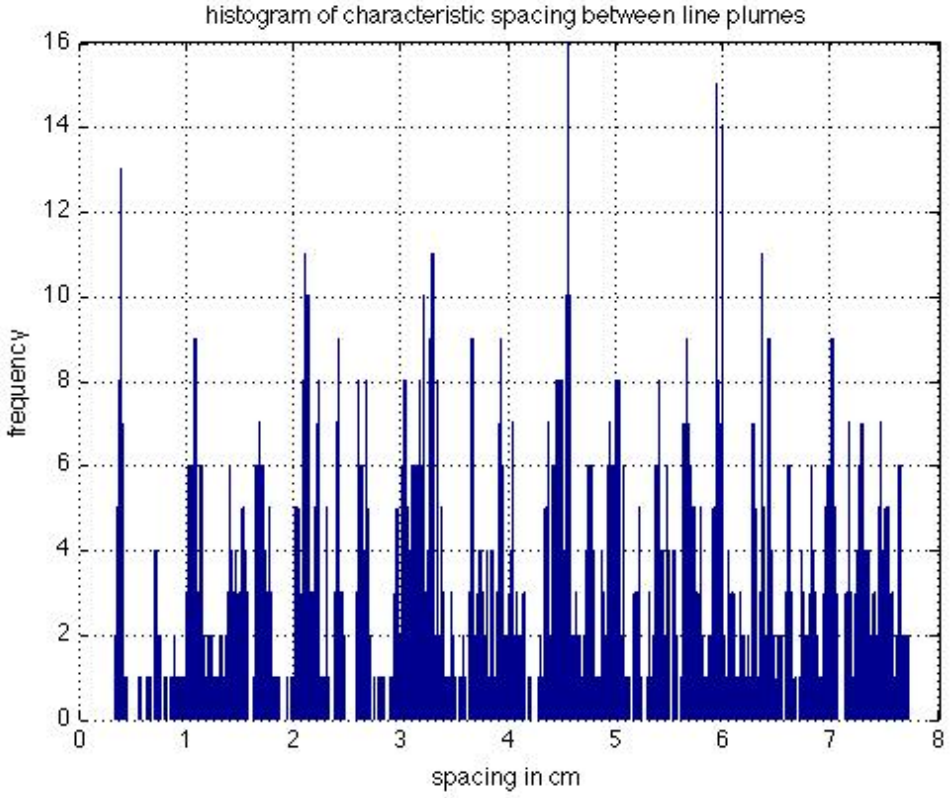
histogram of characteristic spacing between line plumes
frequency
spacing in cm
0
2
4
6
8
10
12
14
16
0
1
2
3
4
5
6
7
8

(V)

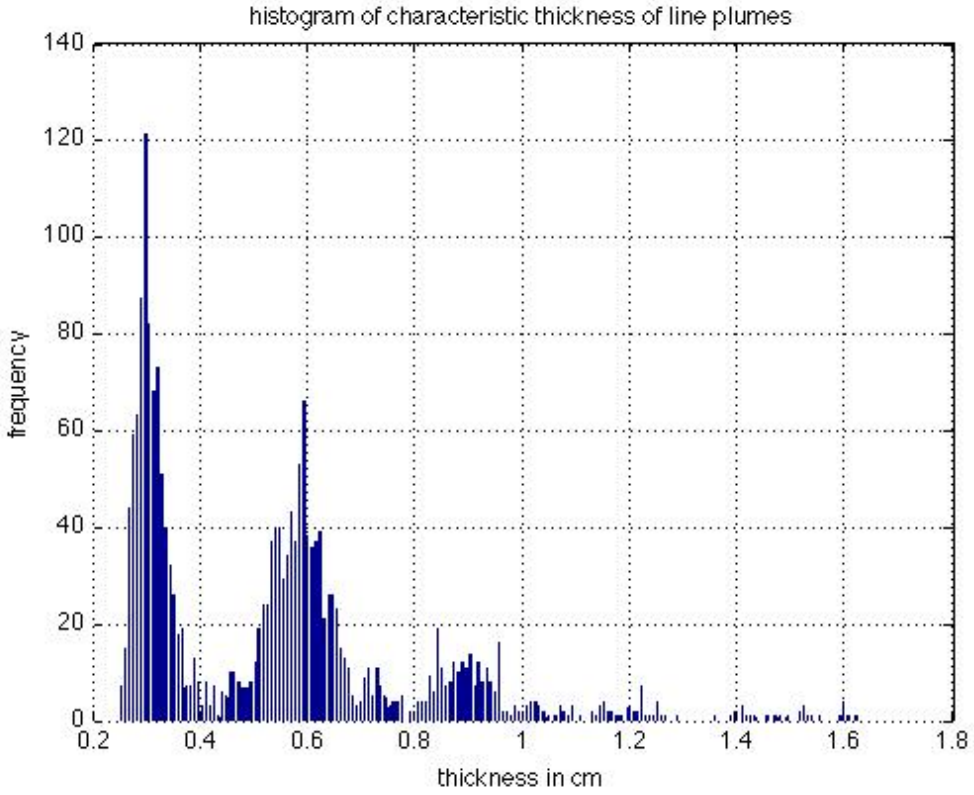
histogram of characteristic thickness of line plumes
frequency
thickness in cm
0
20
40
60
80
100
120
140
0.2
0.4
0.6
0.8
1
1.2
1.4
1.6
1.8

(H)

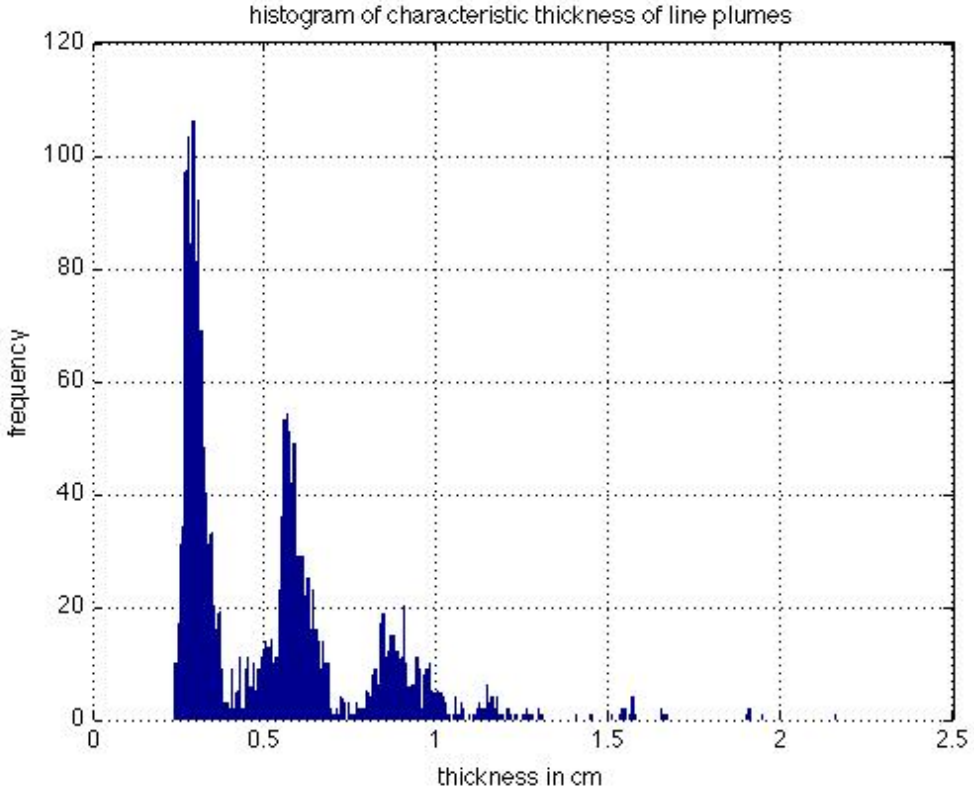
histogram of characteristic thickness of line plumes
frequency
thickness in cm
0
20
40
60
80
100
120
0
0.5
1
1.5
2
2.5

(V)

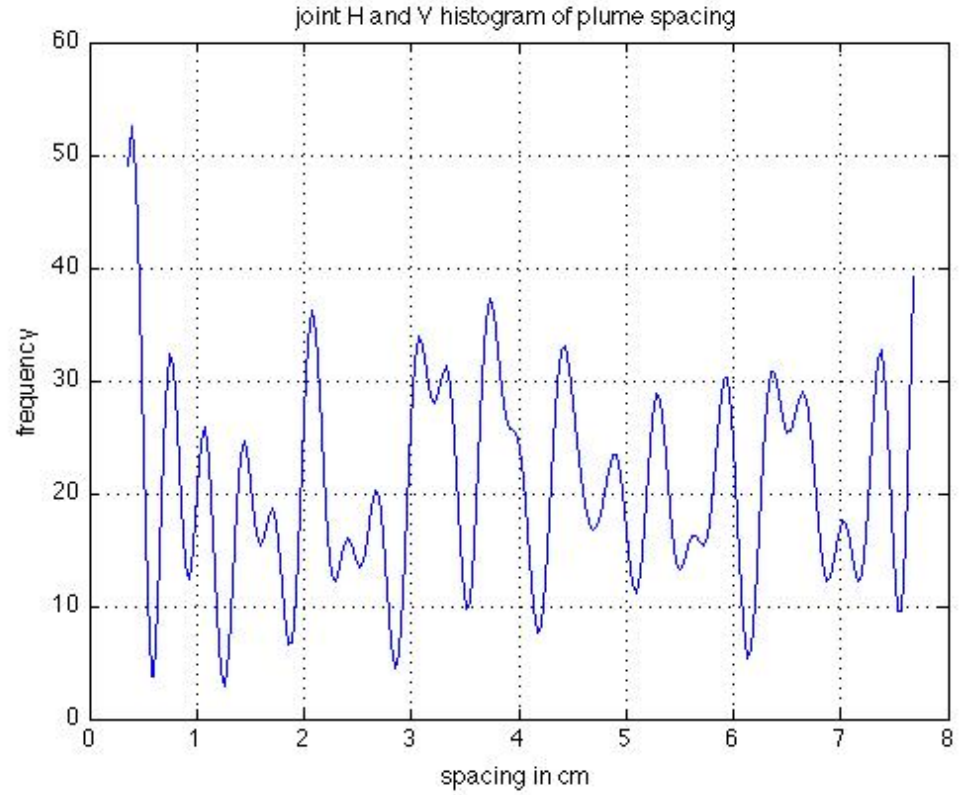
joint H and V histogram of plume spacing
frequency
spacing in cm
0
10
20
30
40
50
60
0
1
2
3
4
5
6
7
8

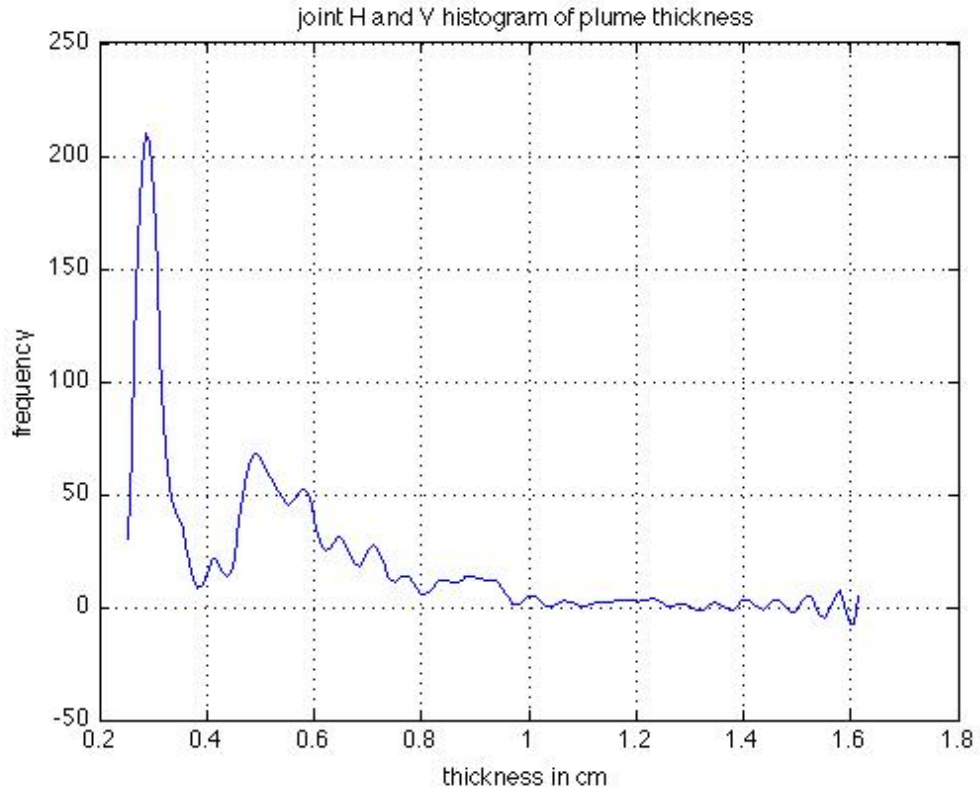
joint H and V histogram of plume thickness
frequency
thickness in cm
-50
0
50
100
150
200
250
0.2
0.4
0.6
0.8
1
1.2
1.4
1.6
1.8

PExpt5, U =15

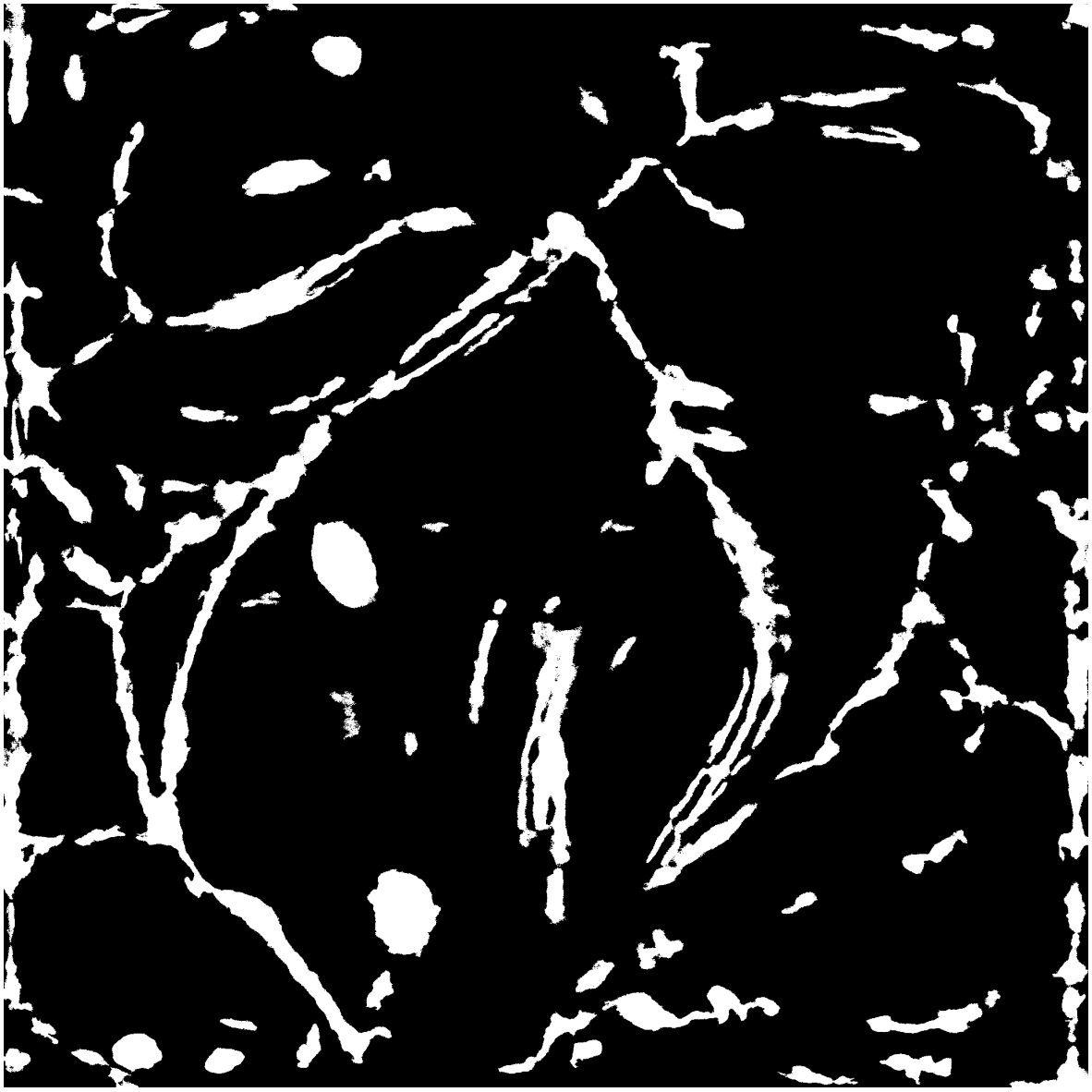

Spacing in cm (frequency of occurrence)

0.4(80)
4.9(55)
2.1(30)
1.45(30)_
7(30)

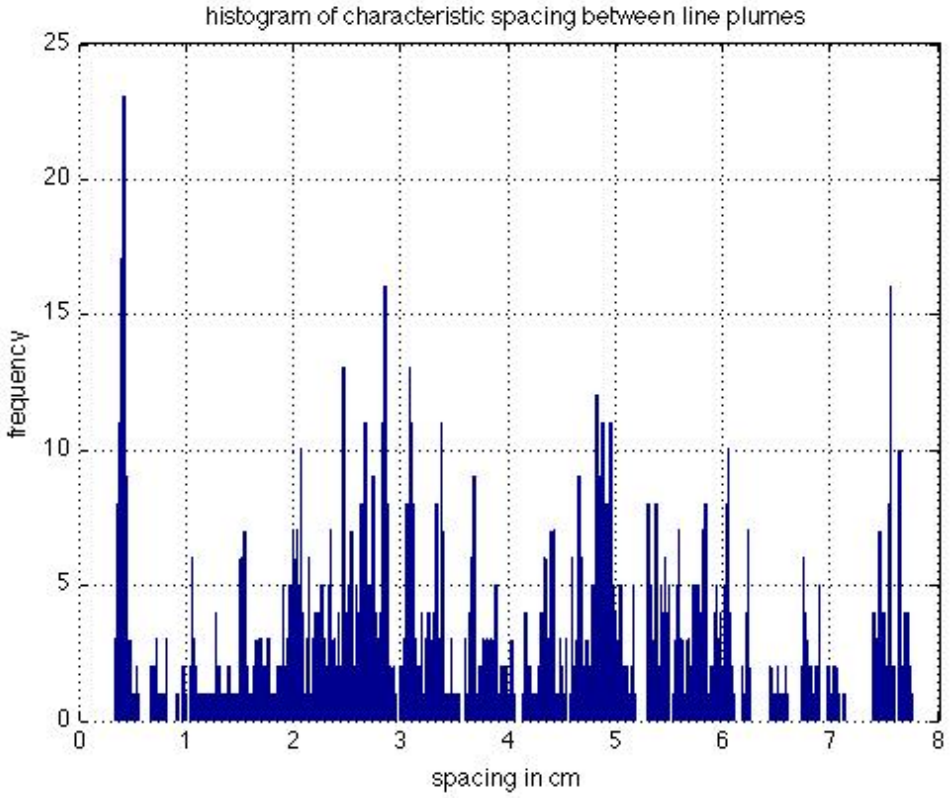
histogram of characteristic spacing between line plumes
frequency
spacing in cm
0
5
10
15
20
25
0
1
2
3
4
5
6
7
8

(H)

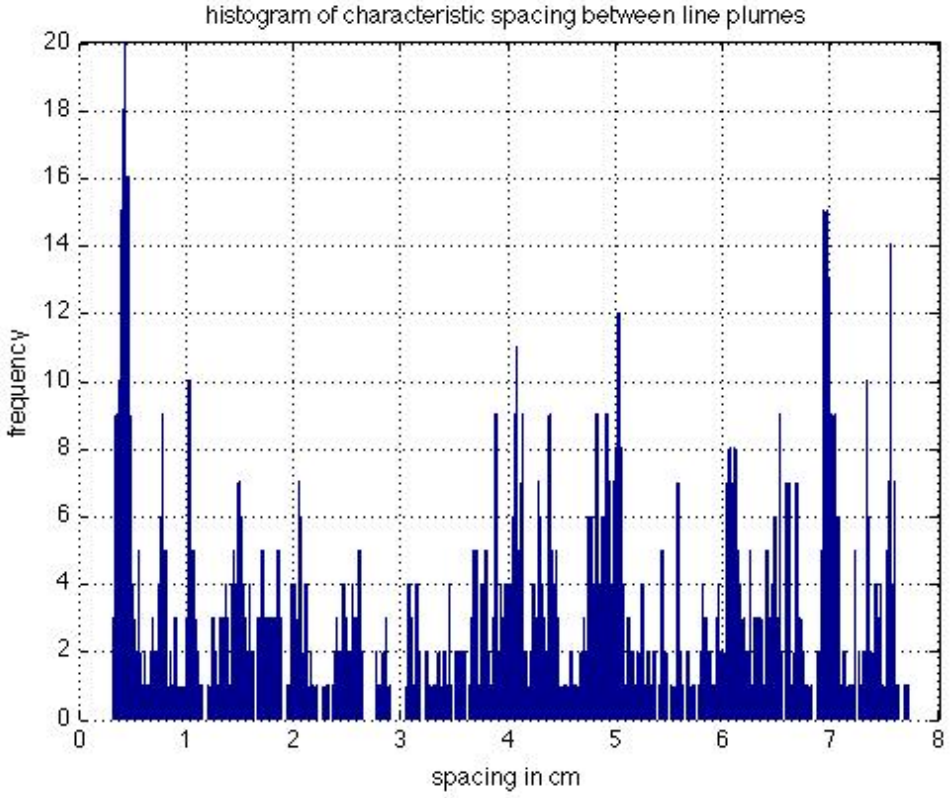
histogram of characteristic spacing between line plumes
frequency
spacing in cm
0
2
4
6
8
10
12
14
16
18
20
0
1
2
3
4
5
6
7
8

(V)

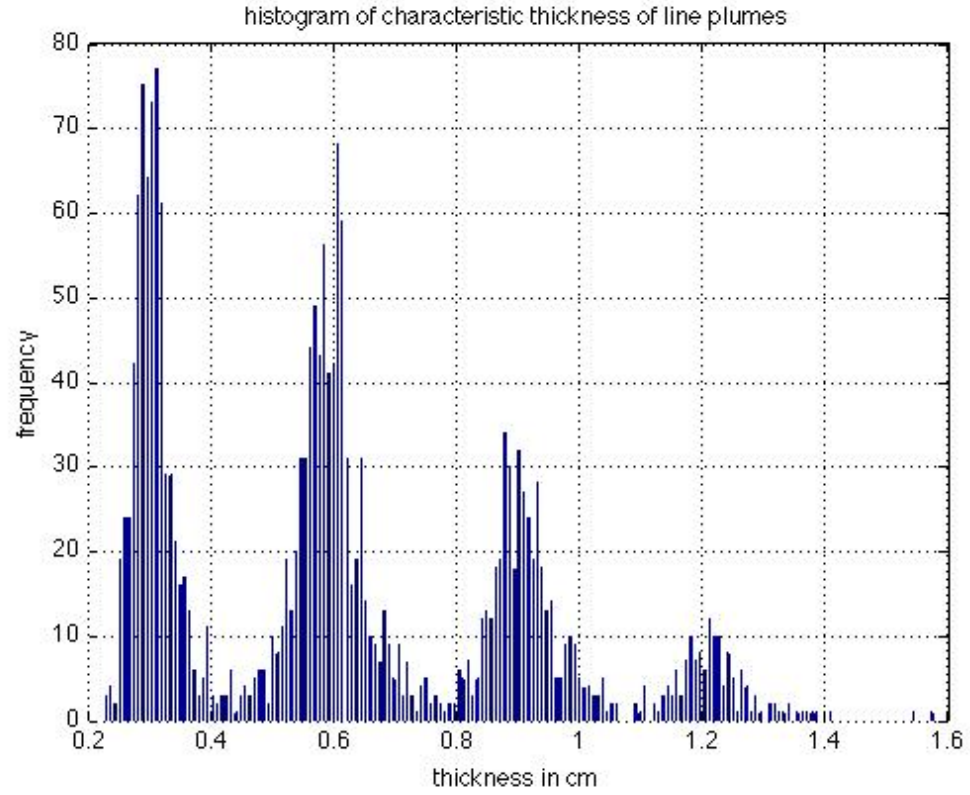
histogram of characteristic thickness of line plumes
frequency
thickness in cm
0
10
20
30
40
50
60
70
80
0.2
0.4
0.6
0.8
1
1.2
1.4
1.6

(H)

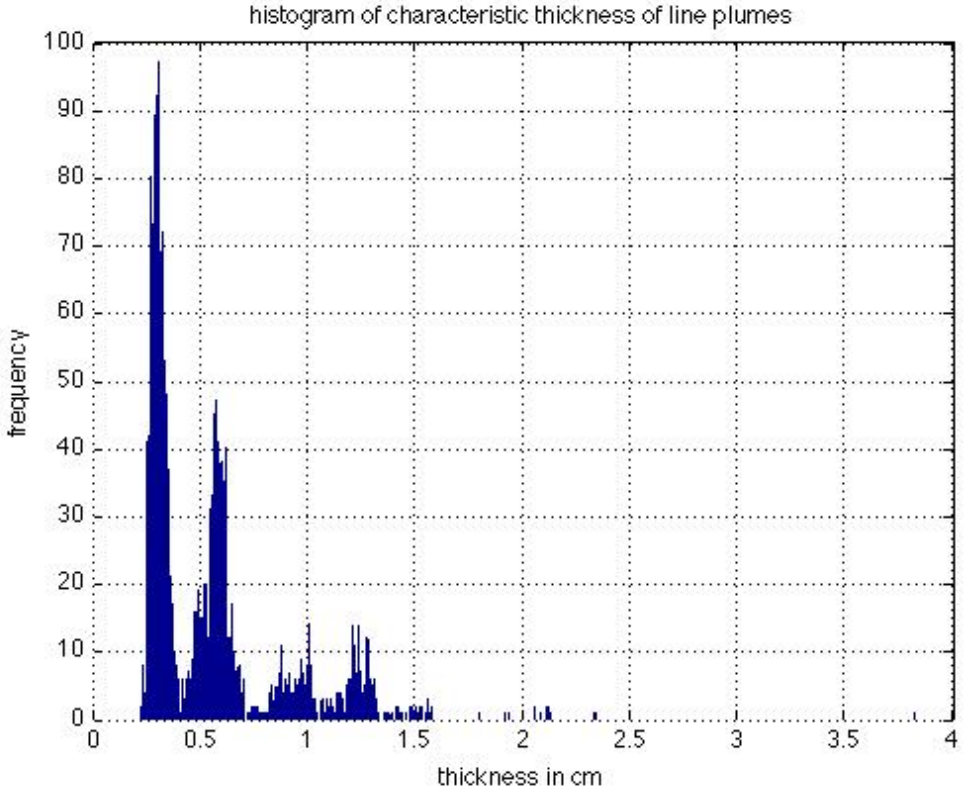
histogram of characteristic thickness of line plumes
frequency
thickness in cm
0
10
20
30
40
50
60
70
80
90
100
0
0.5
1
1.5
2
2.5
3
3.5
4

(V)

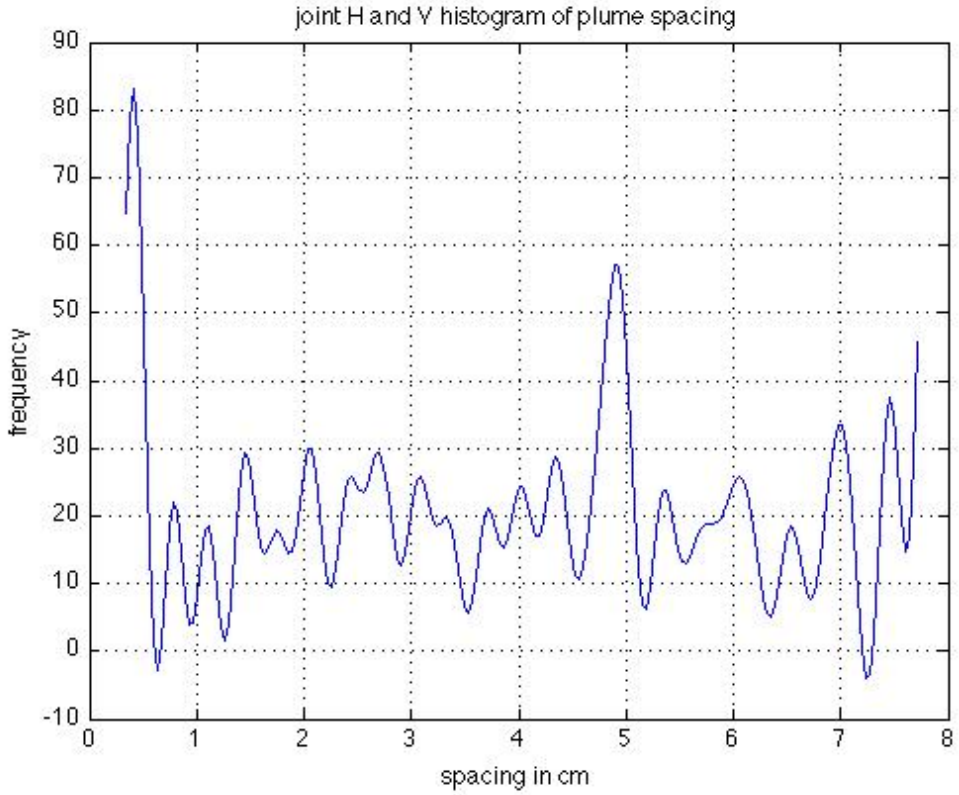
joint H and V histogram of plume spacing
frequency
spacing in cm
90
80
70
60
50
40
30
20
10
0
-10
0
1
2
3
4
5
6
7
8

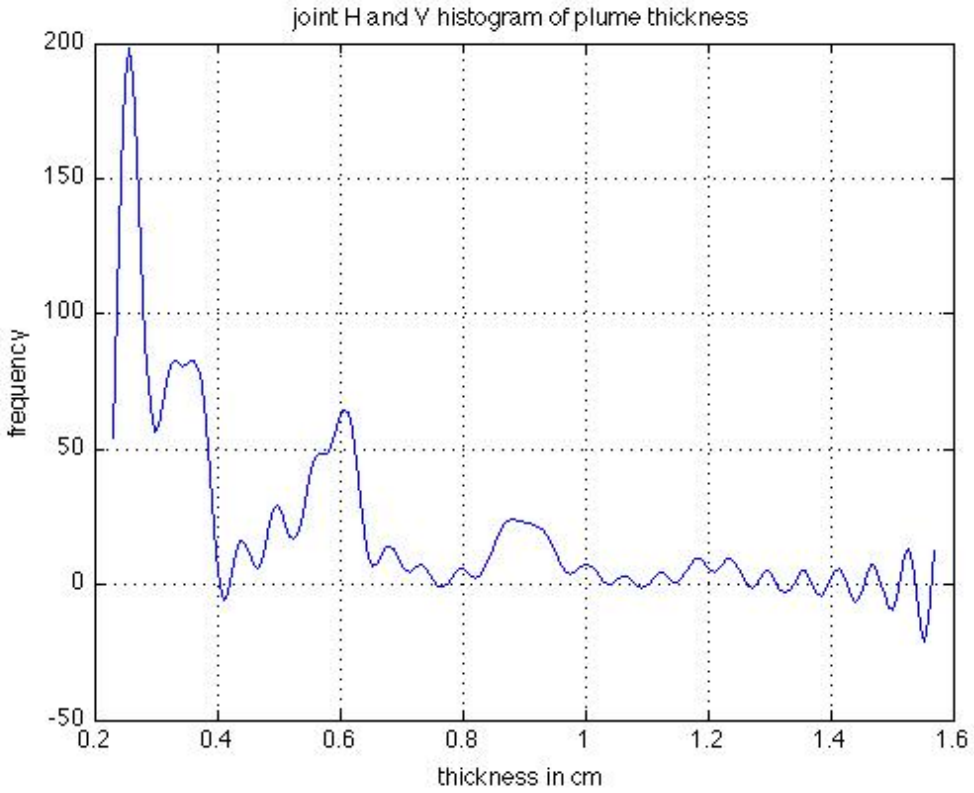
joint H and V histogram of plume thickness
frequency
thickness in cm
200
150
100
50
0
-50
0.2
0.4
0.6
0.8
1
1.2
1.4
1.6

PExpt6, U = 25

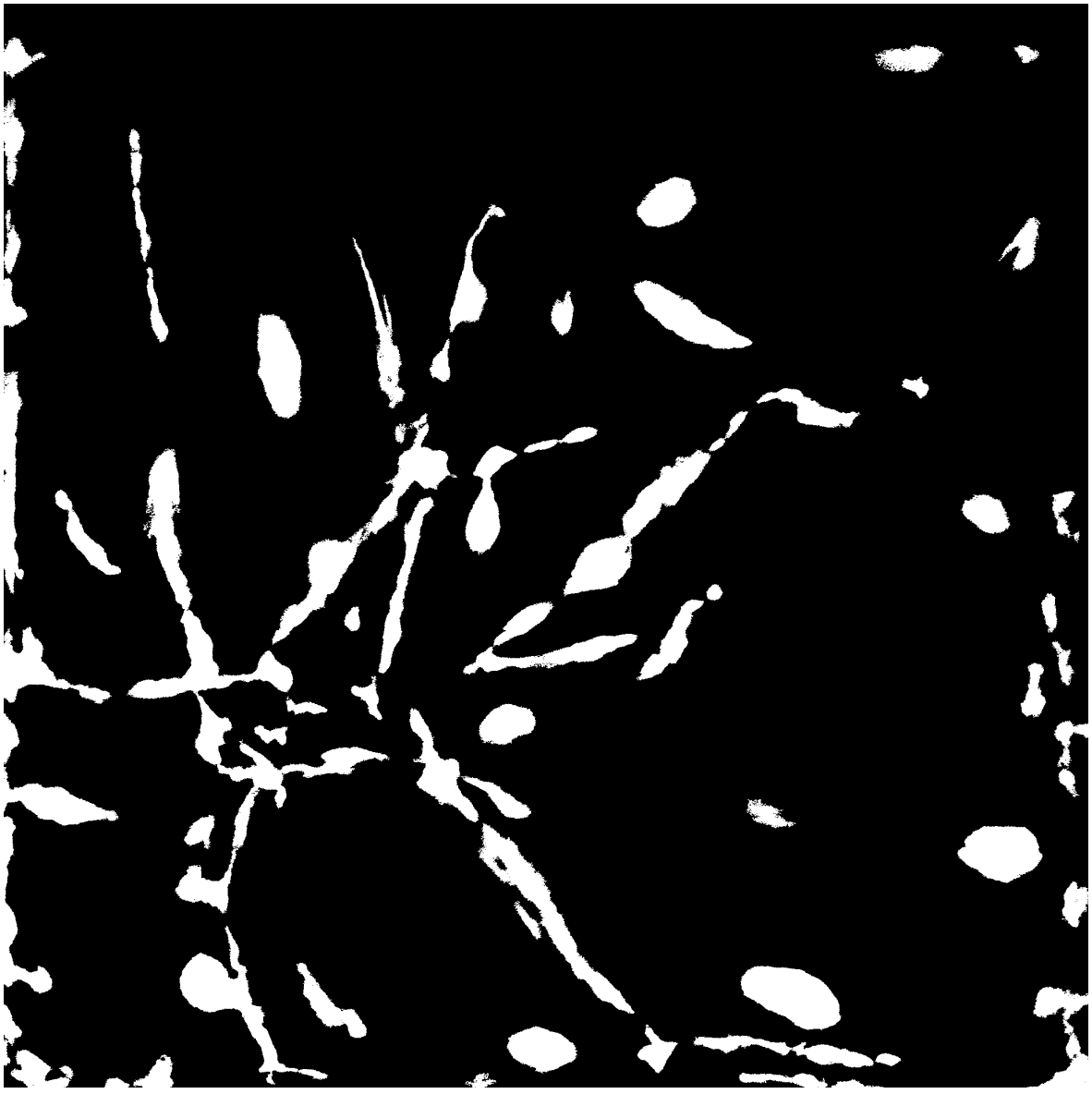

Spacing in cm (frequency of occurrence)

2.2(45)
0.9(40)
1.75(40)
4.7(40)
2.65(35)

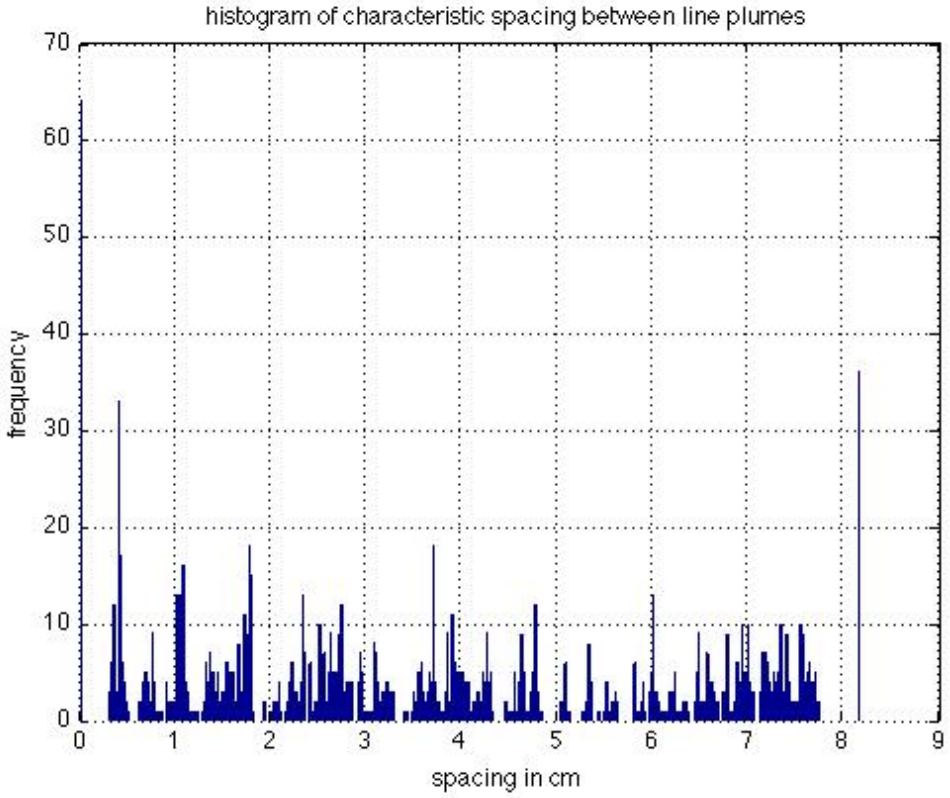
histogram of characteristic spacing between line plumes
frequency
spacing in cm
0
10
20
30
40
50
60
70
0
1
2
3
4
5
6
7
8
9

(H)

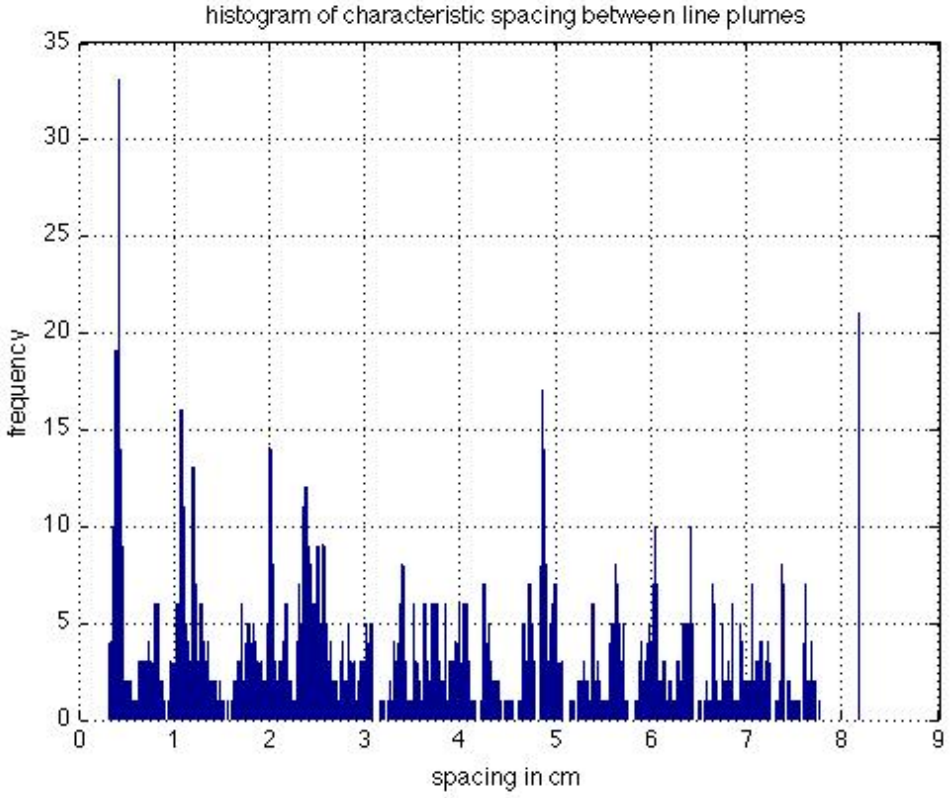
histogram of characteristic spacing between line plumes
frequency
spacing in cm
0
5
10
15
20
25
30
35
0
1
2
3
4
5
6
7
8
9

(V)

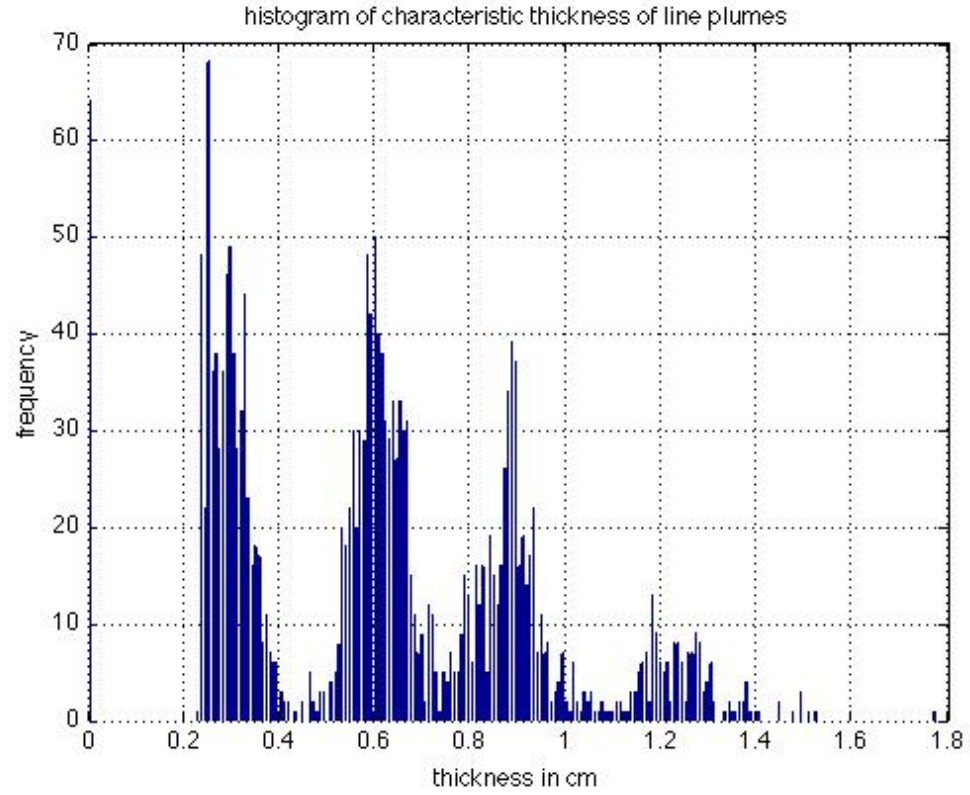
histogram of characteristic thickness of line plumes
frequency
thickness in cm
0
10
20
30
40
50
60
70
0
0.2
0.4
0.6
0.8
1
1.2
1.4
1.6
1.8

(H)

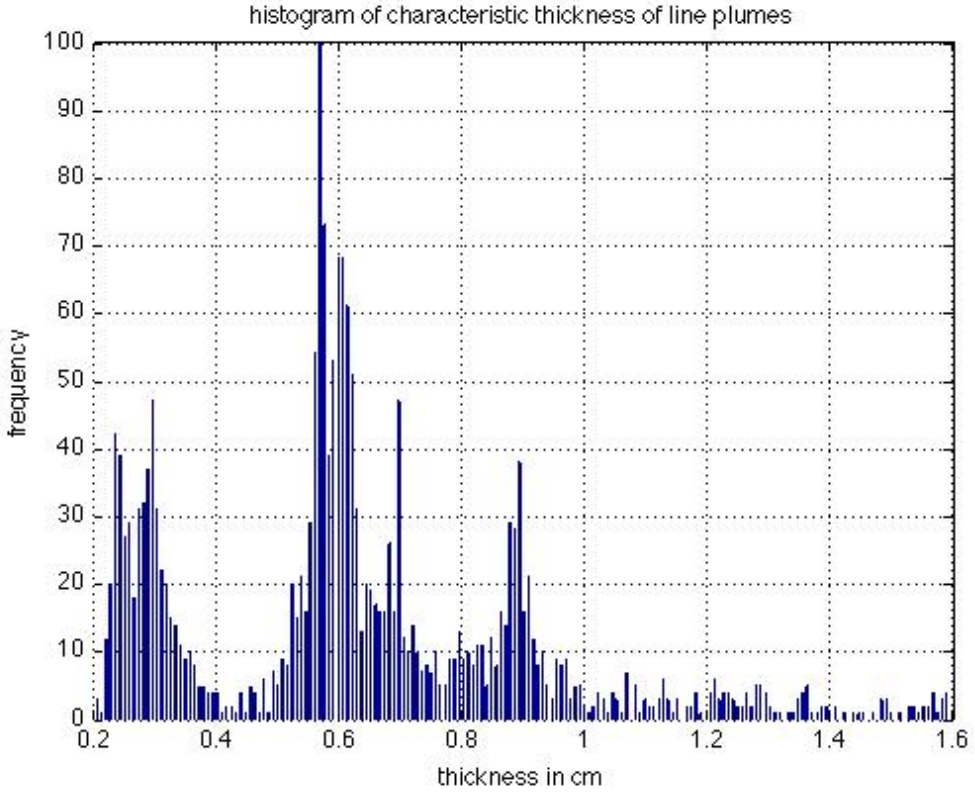
histogram of characteristic thickness of line plumes
frequency
thickness in cm
0
10
20
30
40
50
60
70
80
90
100
0.2
0.4
0.6
0.8
1
1.2
1.4
1.6

(V)

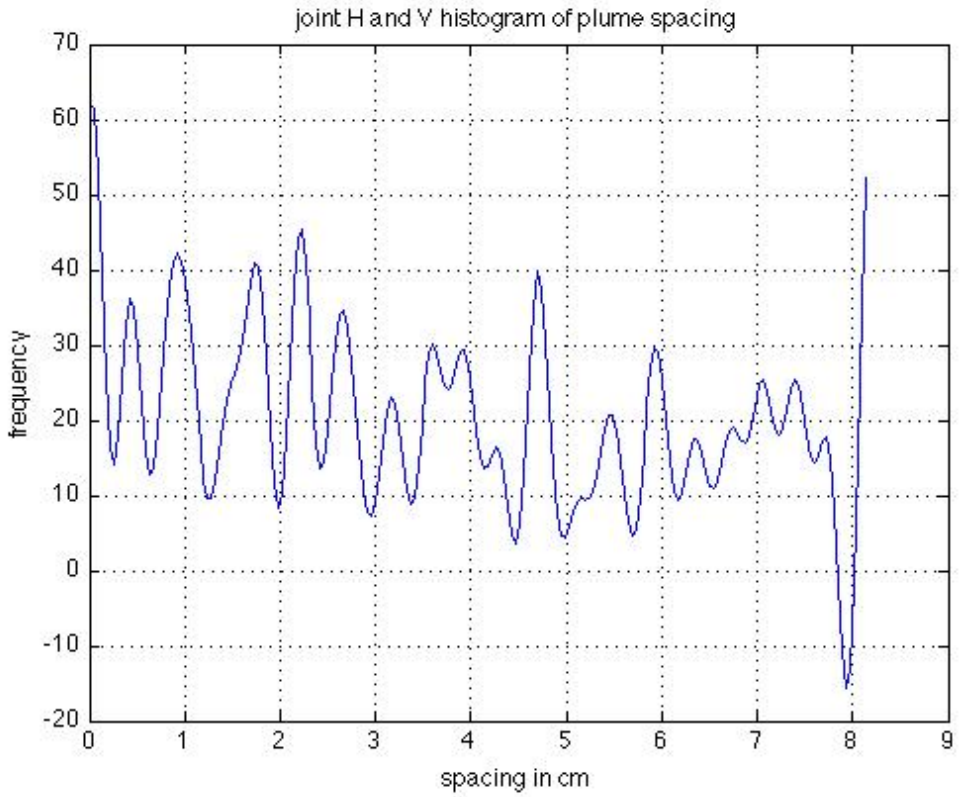
joint H and V histogram of plume spacing
frequency
spacing in cm
70
60
50
40
30
20
10
0
-10
-20
0
1
2
3
4
5
6
7
8
9

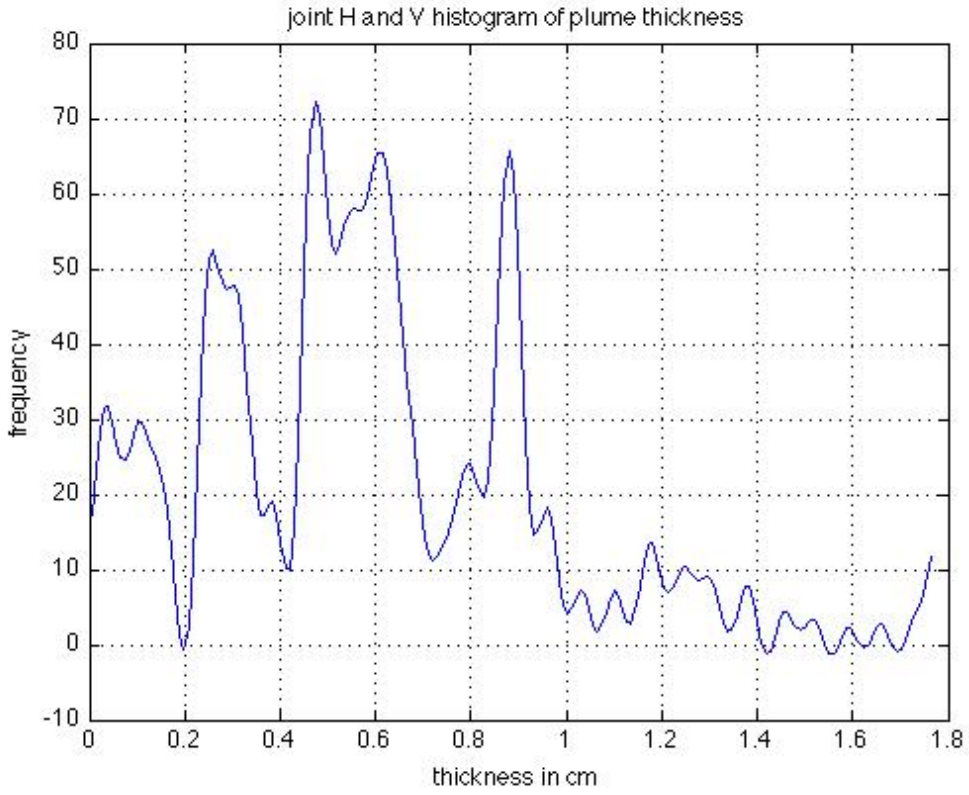
joint H and V histogram of plume thickness
frequency
thickness in cm
80
70
60
50
40
30
20
10
0
-10
0
0.2
0.4
0.6
0.8
1
1.2
1.4
1.6
1.8

PExpt7, U = 65

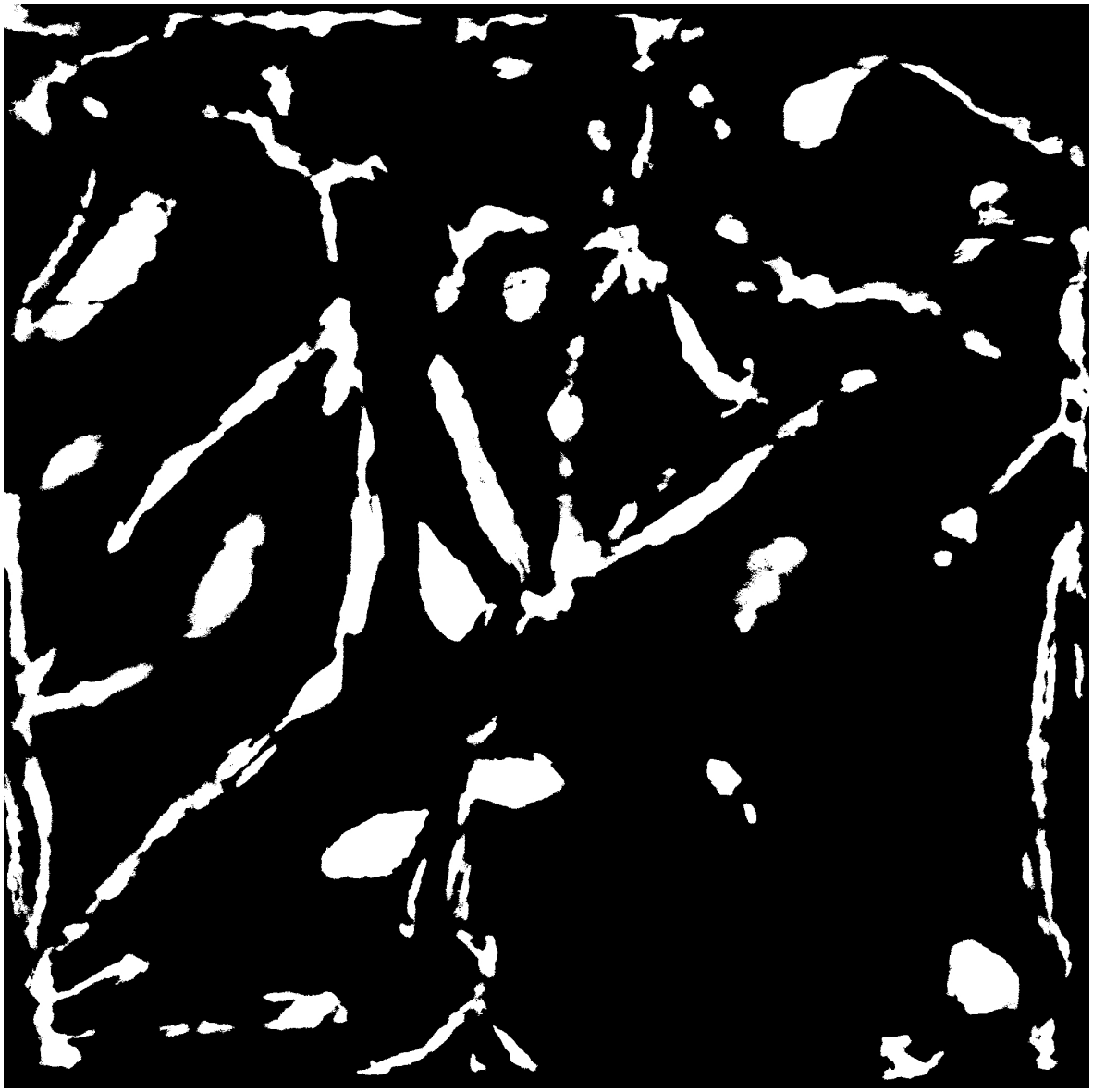

Spacing in cm (frequency of occurrence)

0.4(75)
5.1(45)
2.7(38)
3(38)
5.4(35)
7(35)

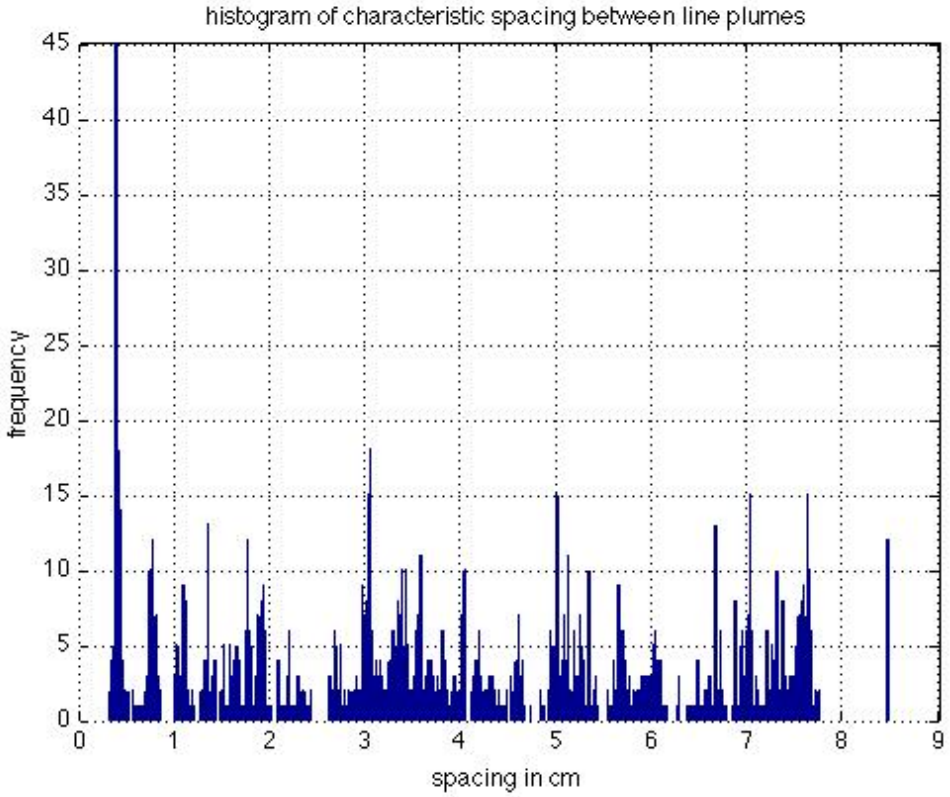
histogram of characteristic spacing between line plumes
frequency
spacing in cm
0
5
10
15
20
25
30
35
40
45
0
1
2
3
4
5
6
7
8
9

(H)

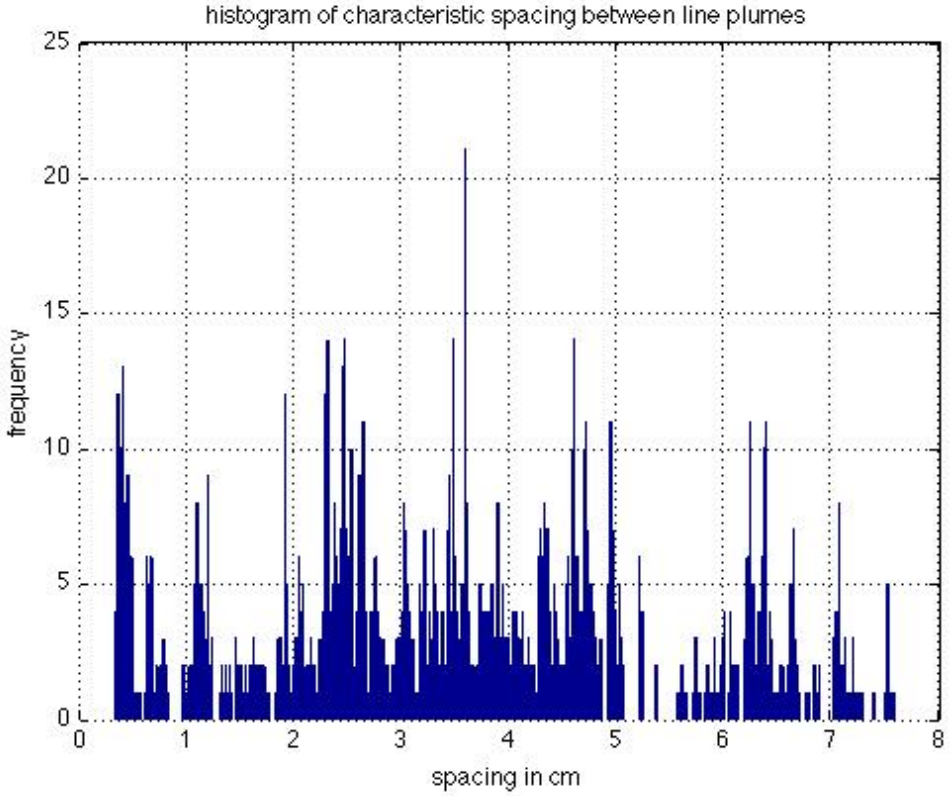
histogram of characteristic spacing between line plumes
frequency
spacing in cm
0
5
10
15
20
25
0
1
2
3
4
5
6
7
8

(V)

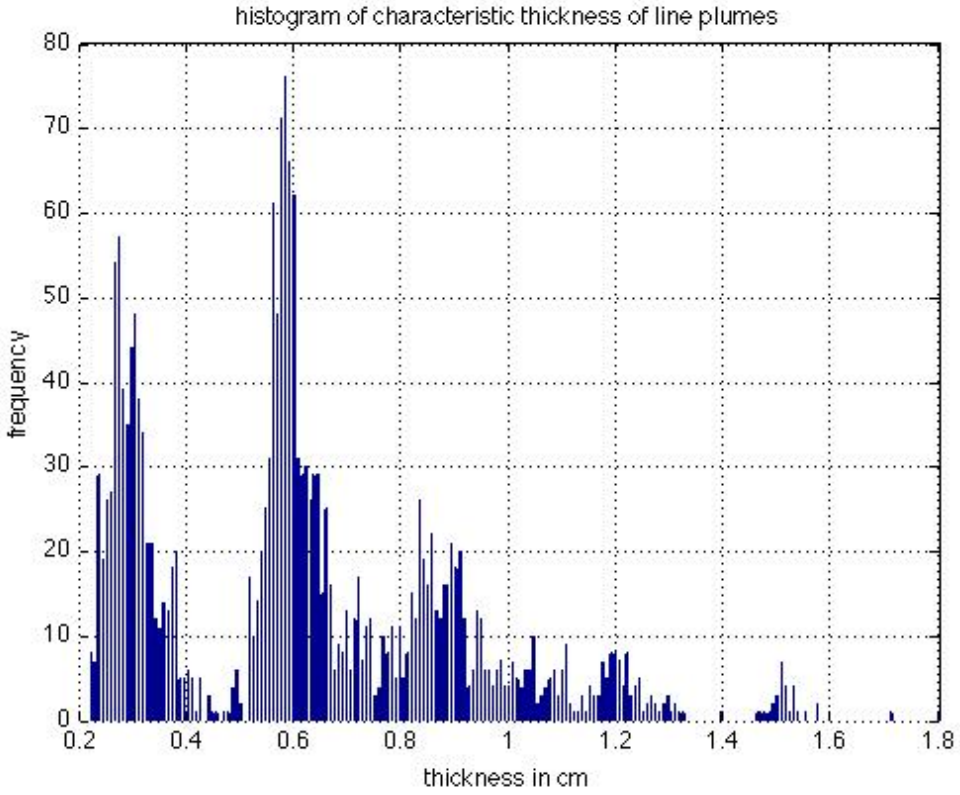
histogram of characteristic thickness of line plumes
frequency
thickness in cm
0
10
20
30
40
50
60
70
80
0.2
0.4
0.6
0.8
1
1.2
1.4
1.6
1.8

(H)

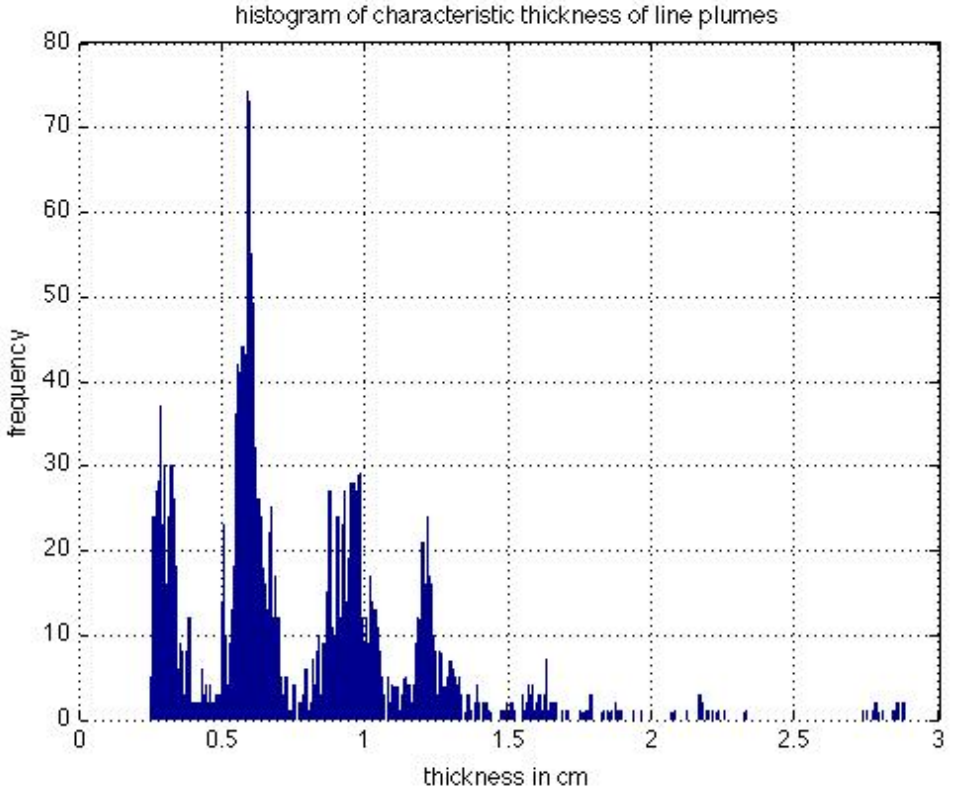
histogram of characteristic thickness of line plumes
frequency
thickness in cm
0
10
20
30
40
50
60
70
80
0
0.5
1
1.5
2
2.5
3

(V)

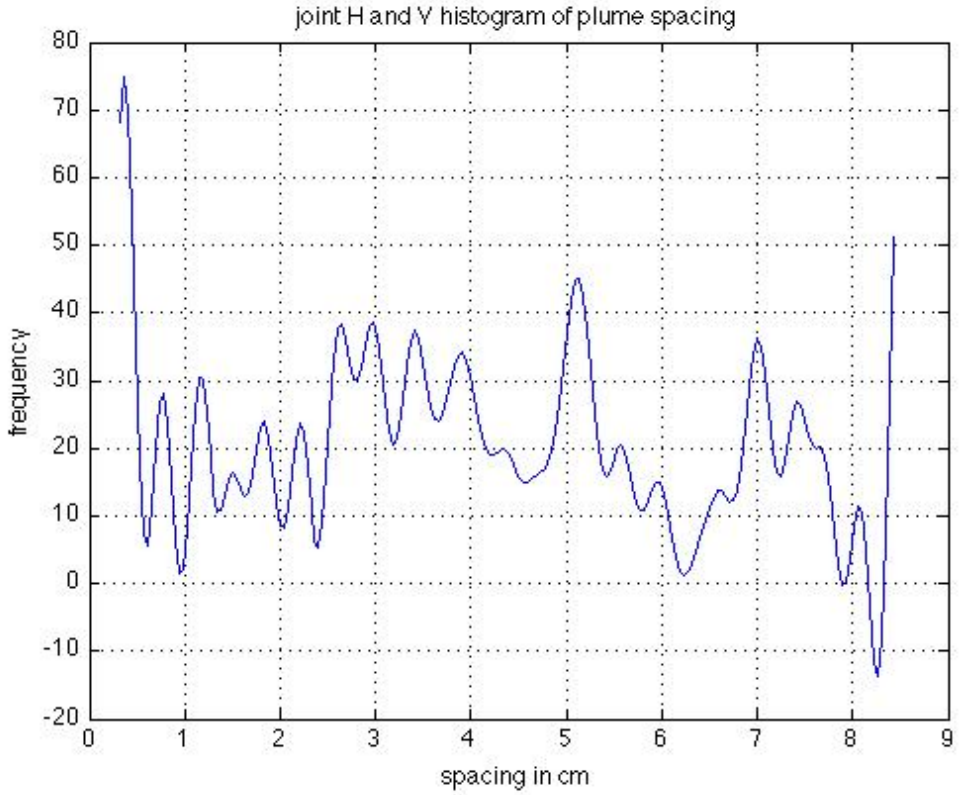
joint H and V histogram of plume spacing
frequency
spacing in cm
80
70
60
50
40
30
20
10
0
-10
-20
0
1
2
3
4
5
6
7
8
9

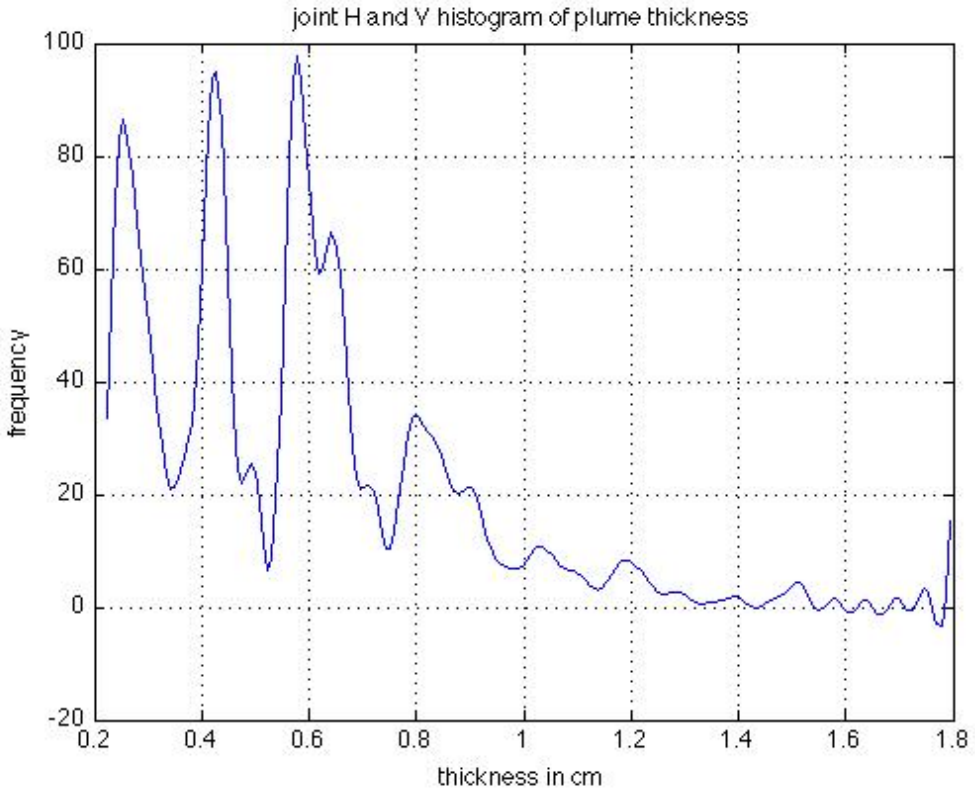
joint H and V histogram of plume thickness
frequency
thickness in cm
100
80
60
40
20
0
-20
0.2
0.4
0.6
0.8
1
1.2
1.4
1.6
1.8

PExpt8, U = 130

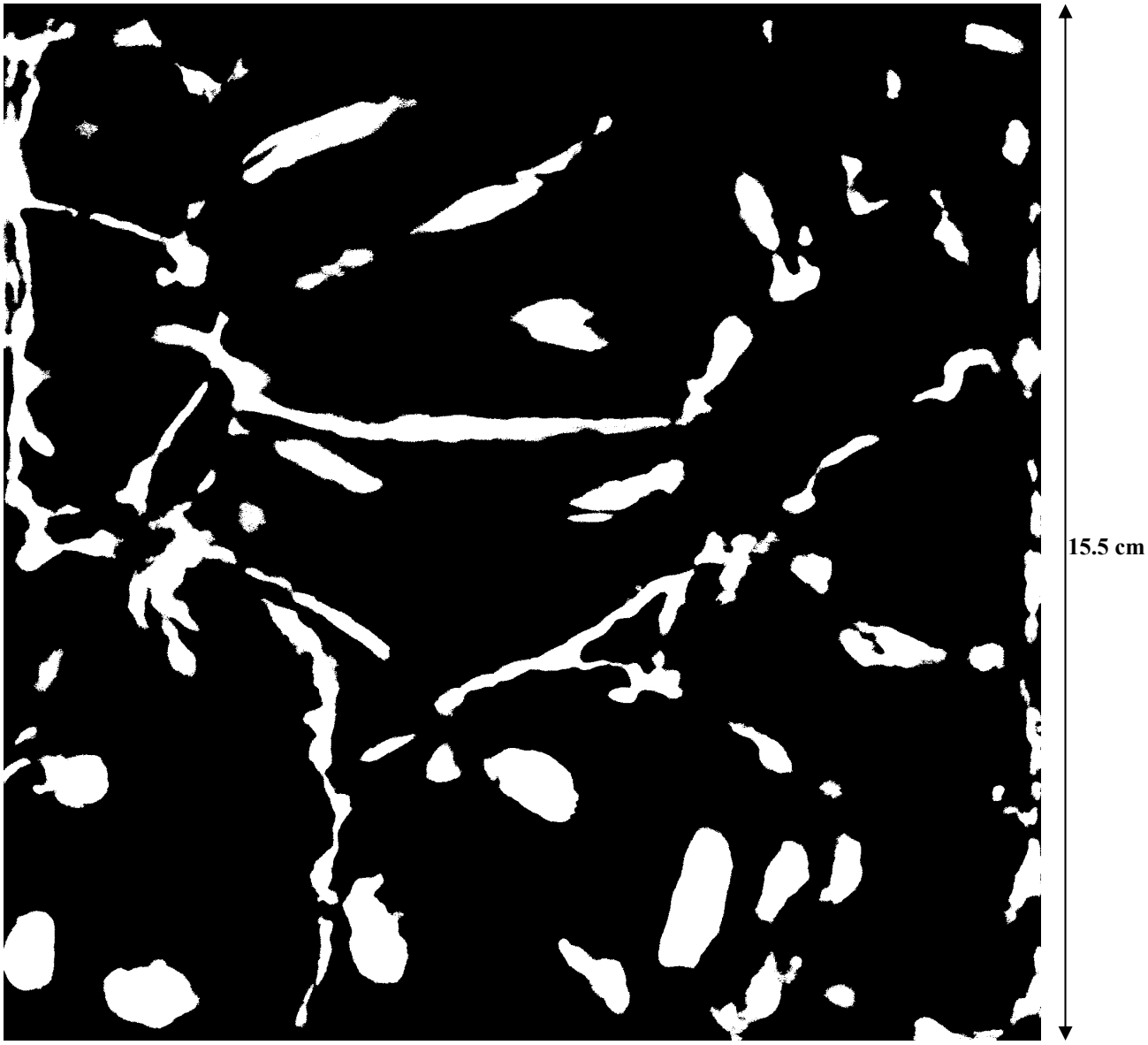

Spacing in cm (frequency of occurrence)

7(60)
6.65(50)
5.1(35)
2.65(30)
0.35(30)
4.3(30)

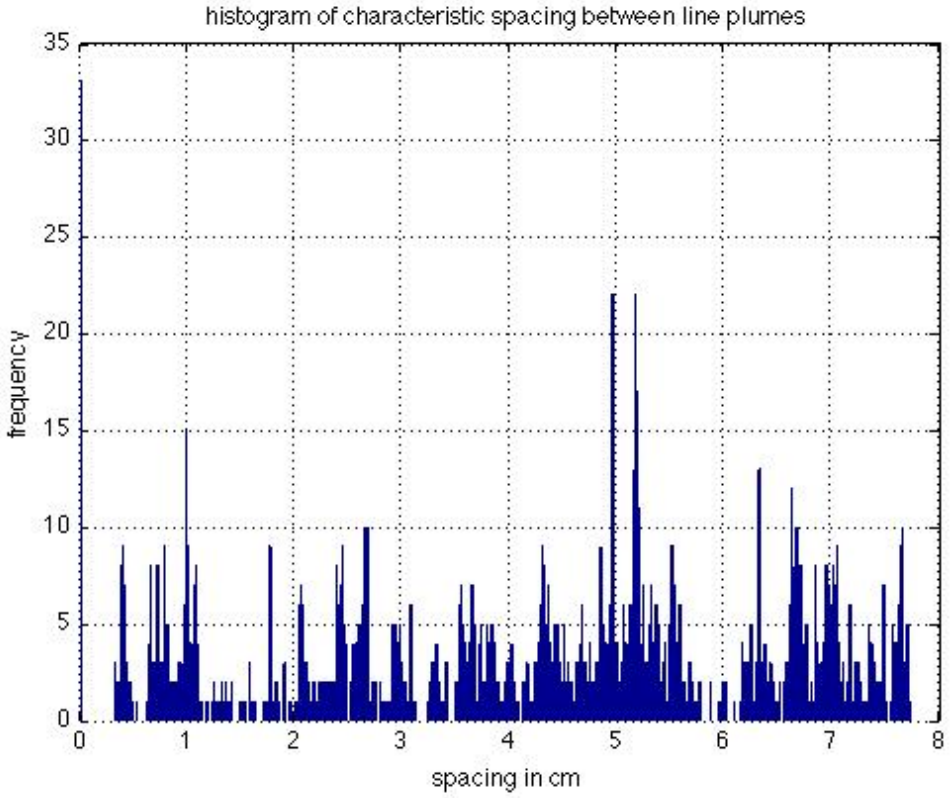
histogram of characteristic spacing between line plumes
frequency
spacing in cm
0
5
10
15
20
25
30
35
0
1
2
3
4
5
6
7
8

(H)

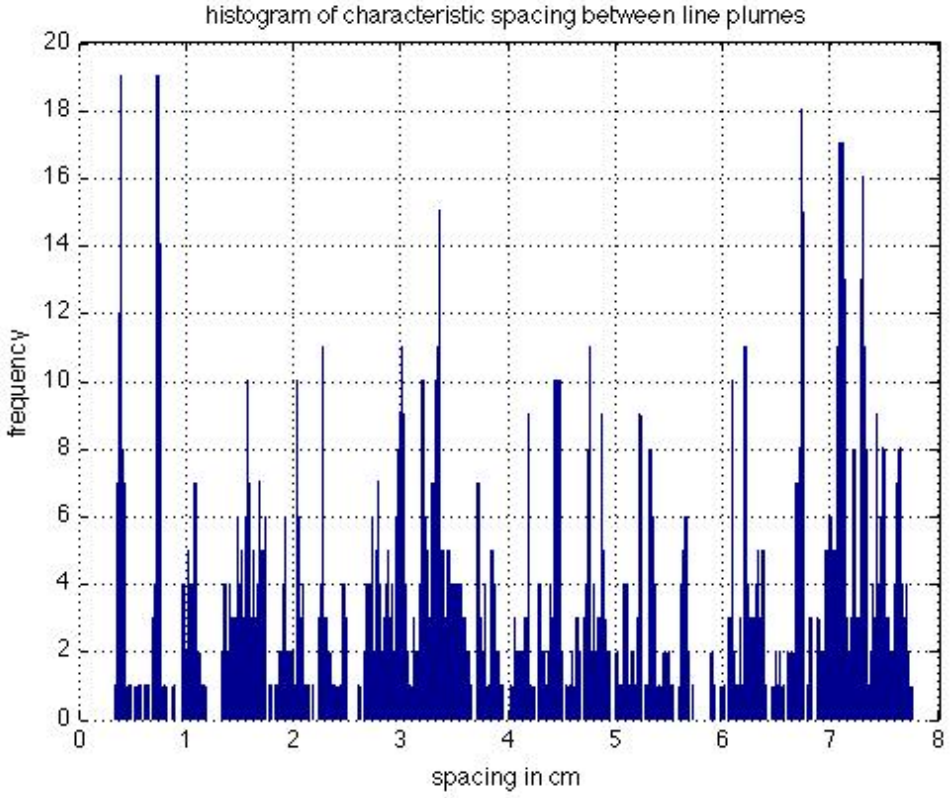
histogram of characteristic spacing between line plumes
frequency
spacing in cm
0
2
4
6
8
10
12
14
16
18
20
0
1
2
3
4
5
6
7
8

(V)

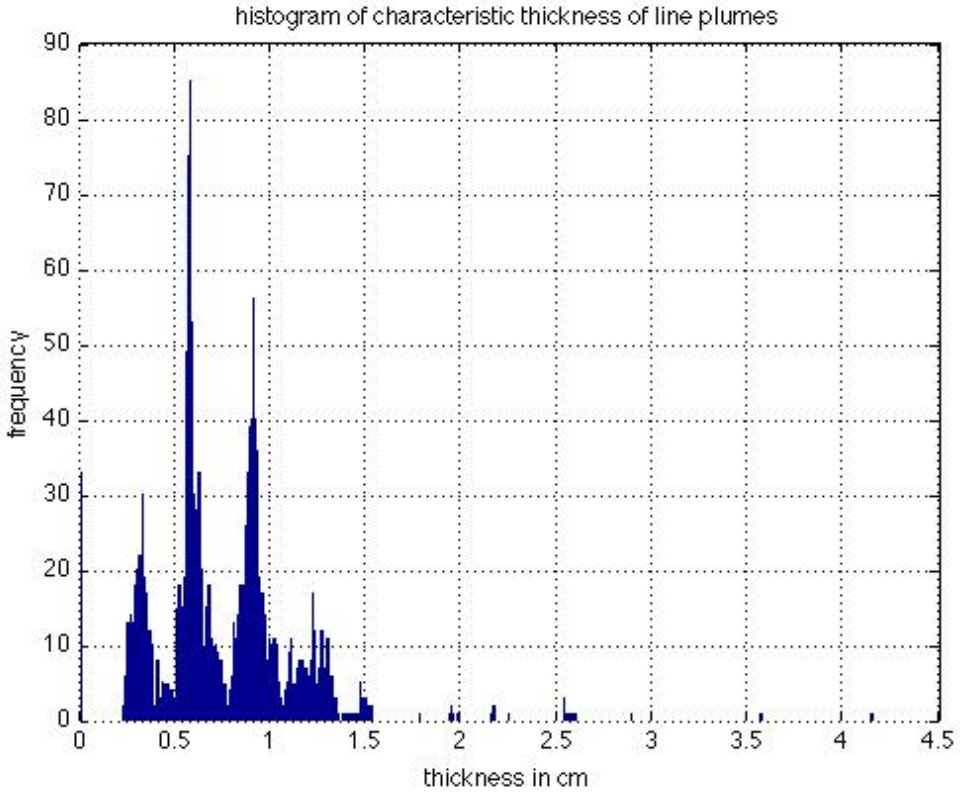
histogram of characteristic thickness of line plumes
frequency
thickness in cm
0
10
20
30
40
50
60
70
80
90
0
0.5
1
1.5
2
2.5
3
3.5
4
4.5

(H)

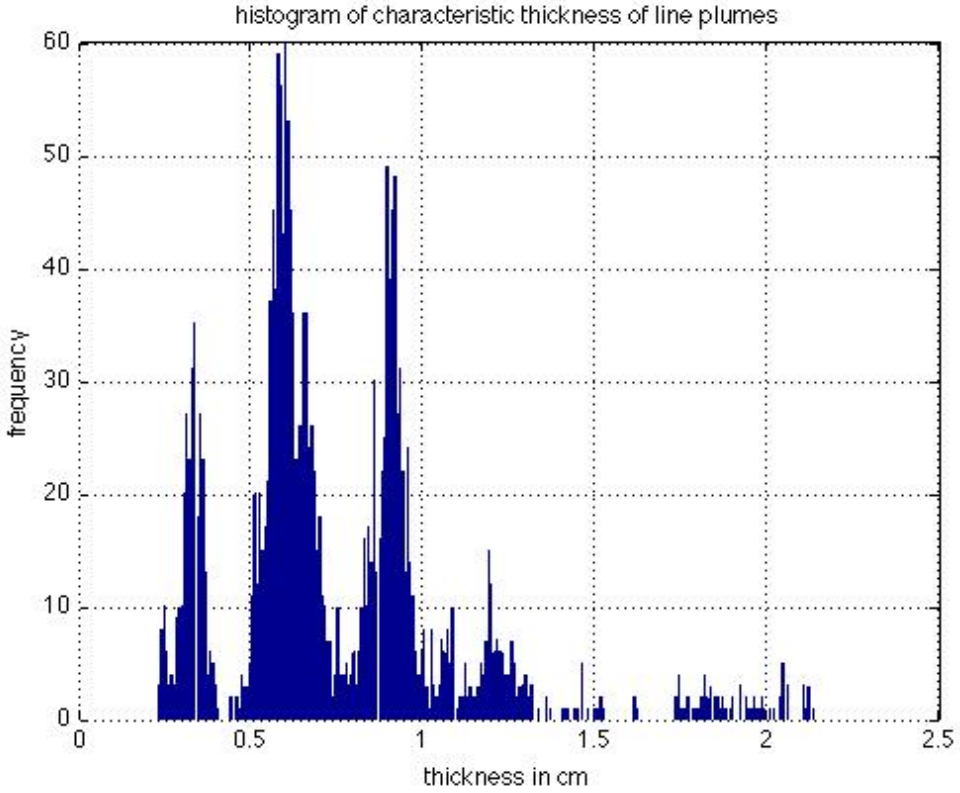
histogram of characteristic thickness of line plumes
frequency
thickness in cm
0
10
20
30
40
50
60
0
0.5
1
1.5
2
2.5

(V)

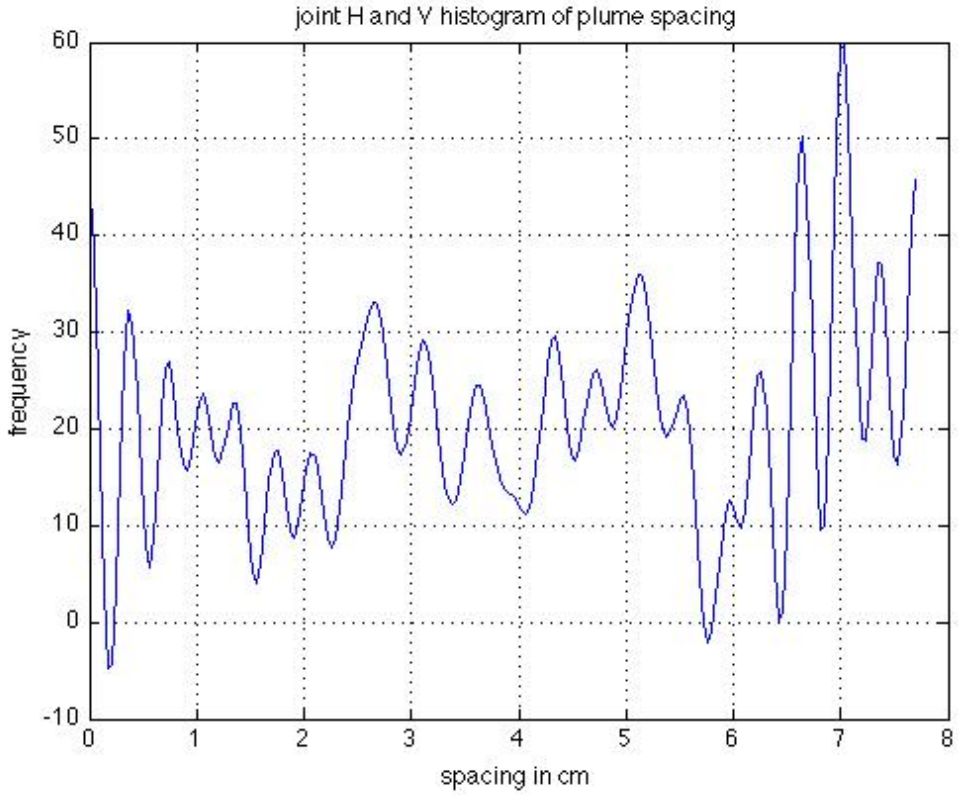
joint H and V histogram of plume spacing
frequency
spacing in cm
60
50
40
30
20
10
0
-10
0
1
2
3
4
5
6
7
8

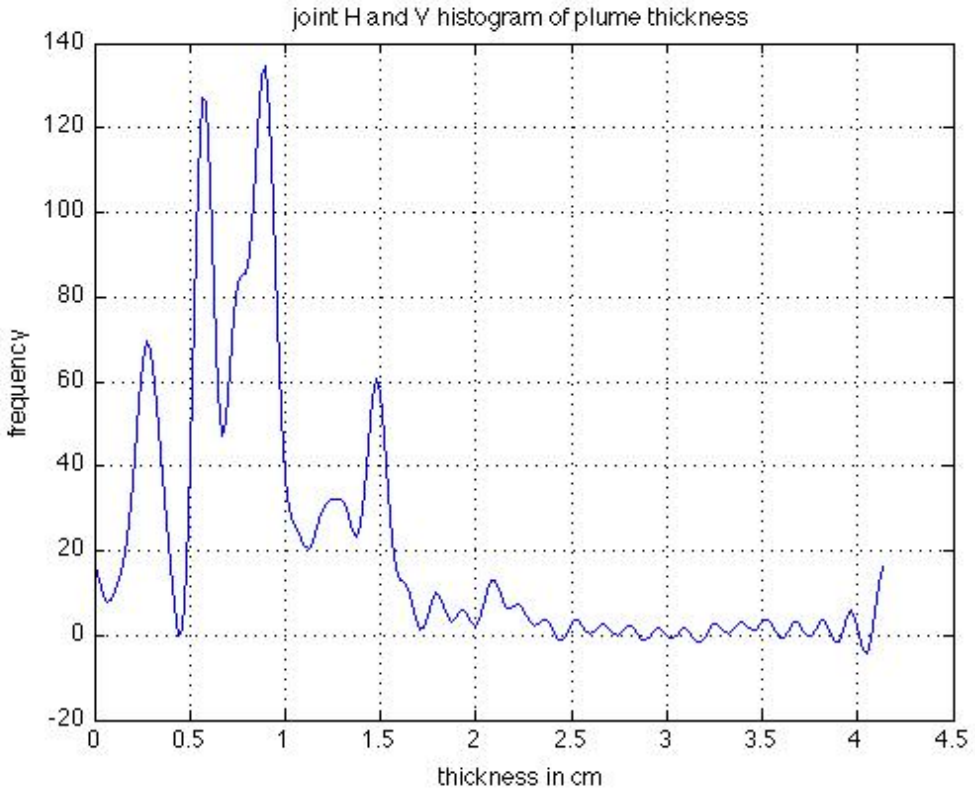
joint H and V histogram of plume thickness
frequency
thickness in cm
140
120
100
80
60
40
20
0
-20
0
0.5
1
1.5
2
2.5
3
3.5
4
4.5

PExpt9, U = 300

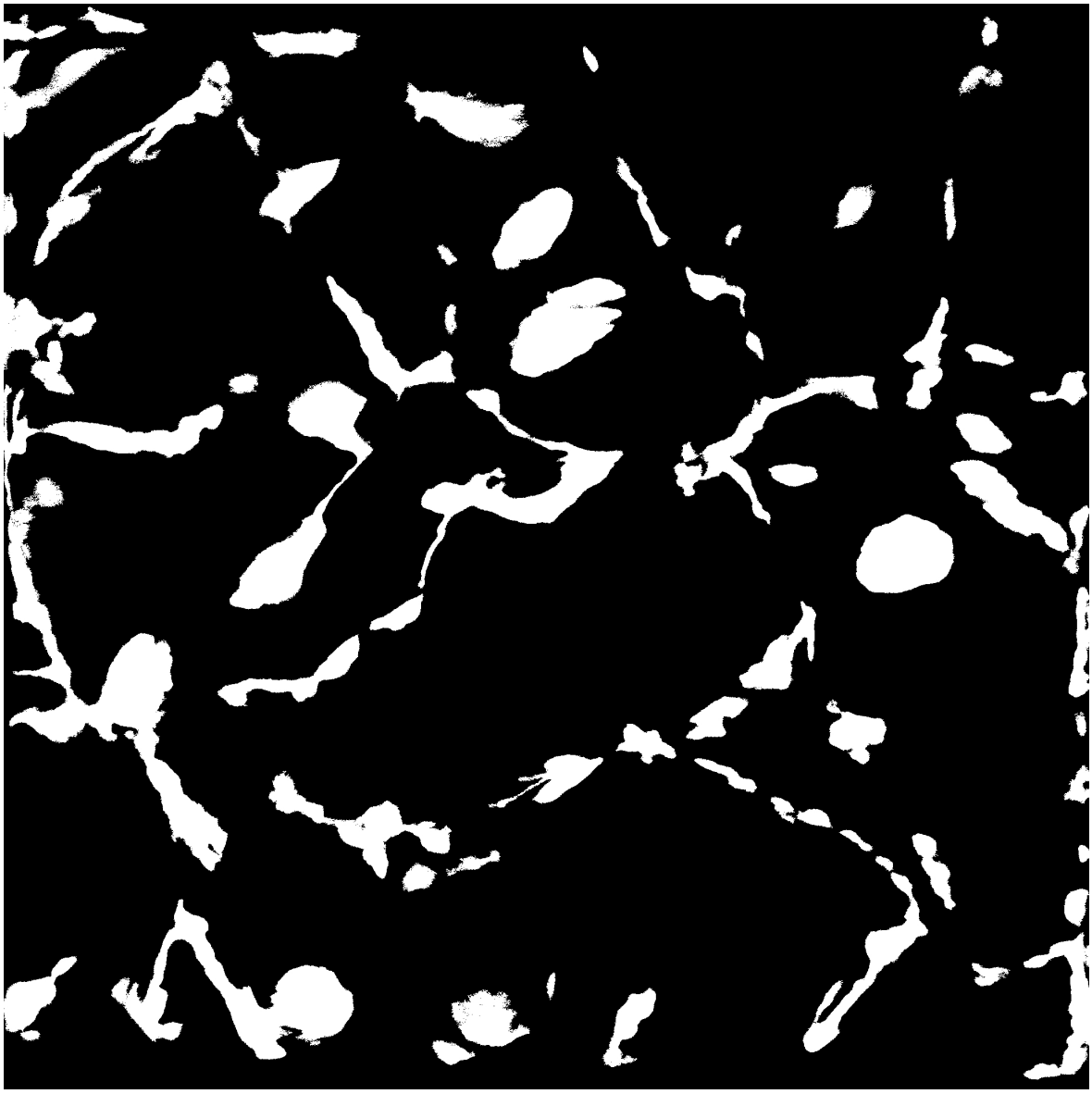

Spacing in cm (frequency of occurrence)

7.45(50)
6.65(45)
2.25(45)
1.85(45)
1.5(45)
0.4(45)

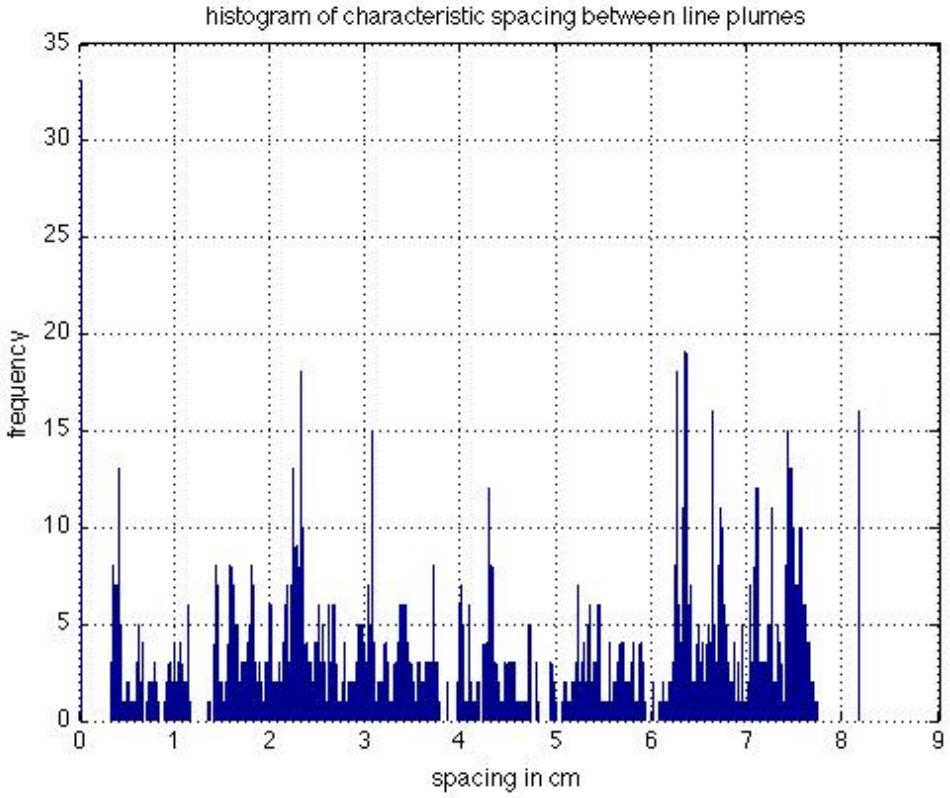
histogram of characteristic spacing between line plumes
frequency
spacing in cm
0
5
10
15
20
25
30
35
0
1
2
3
4
5
6
7
8
9

(H)

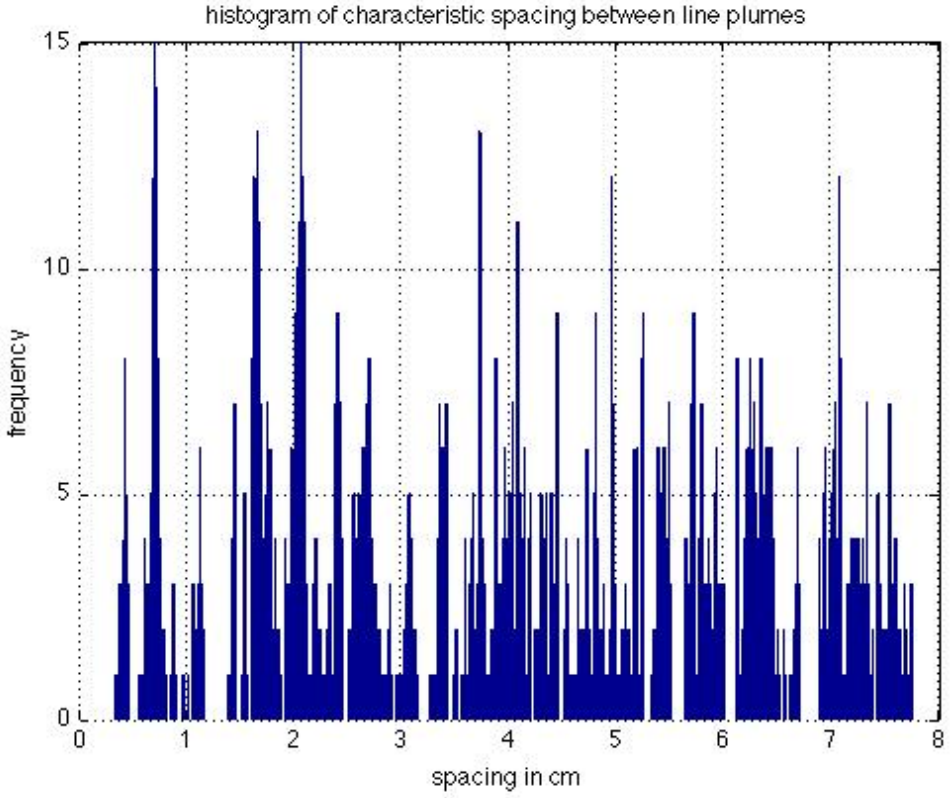
histogram of characteristic spacing between line plumes
frequency
spacing in cm
0
5
10
15
0
1
2
3
4
5
6
7
8

(V)

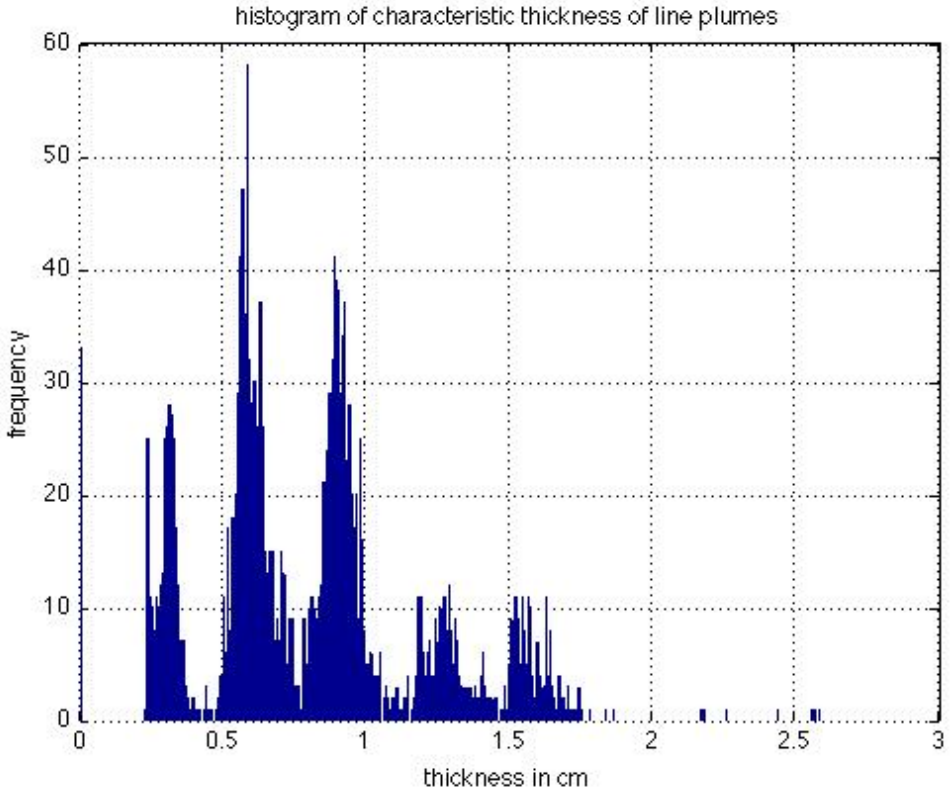
histogram of characteristic thickness of line plumes
frequency
thickness in cm
0
10
20
30
40
50
60
0
0.5
1
1.5
2
2.5
3

(H)

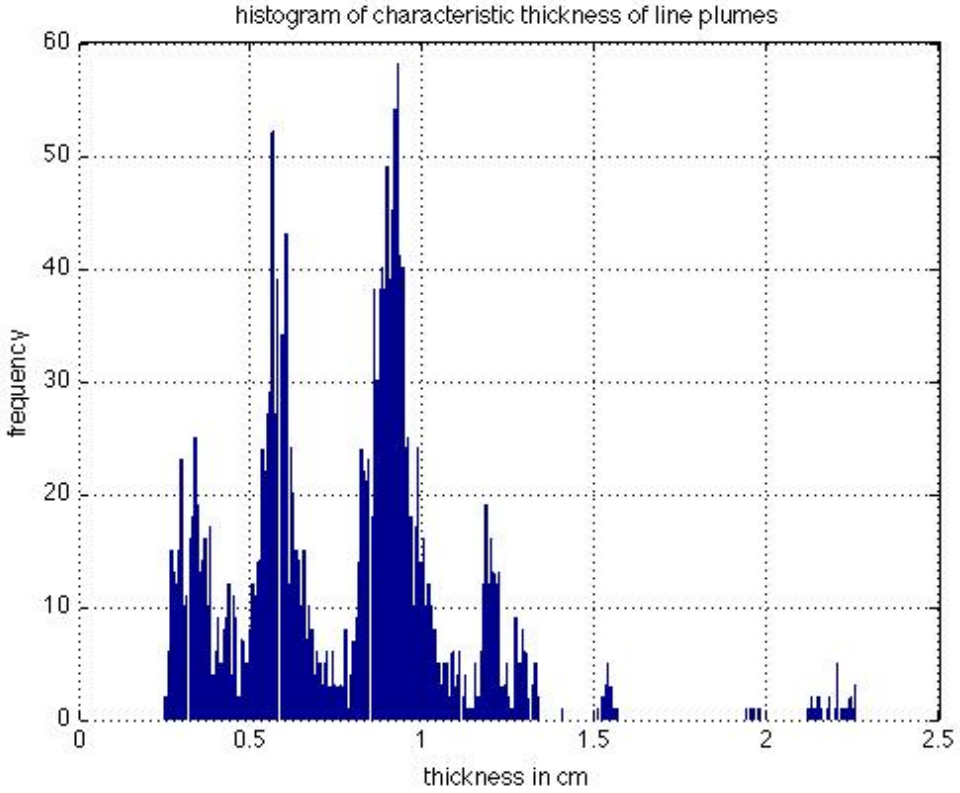
histogram of characteristic thickness of line plumes
frequency
thickness in cm
0
10
20
30
40
50
60
0
0.5
1
1.5
2
2.5

(V)

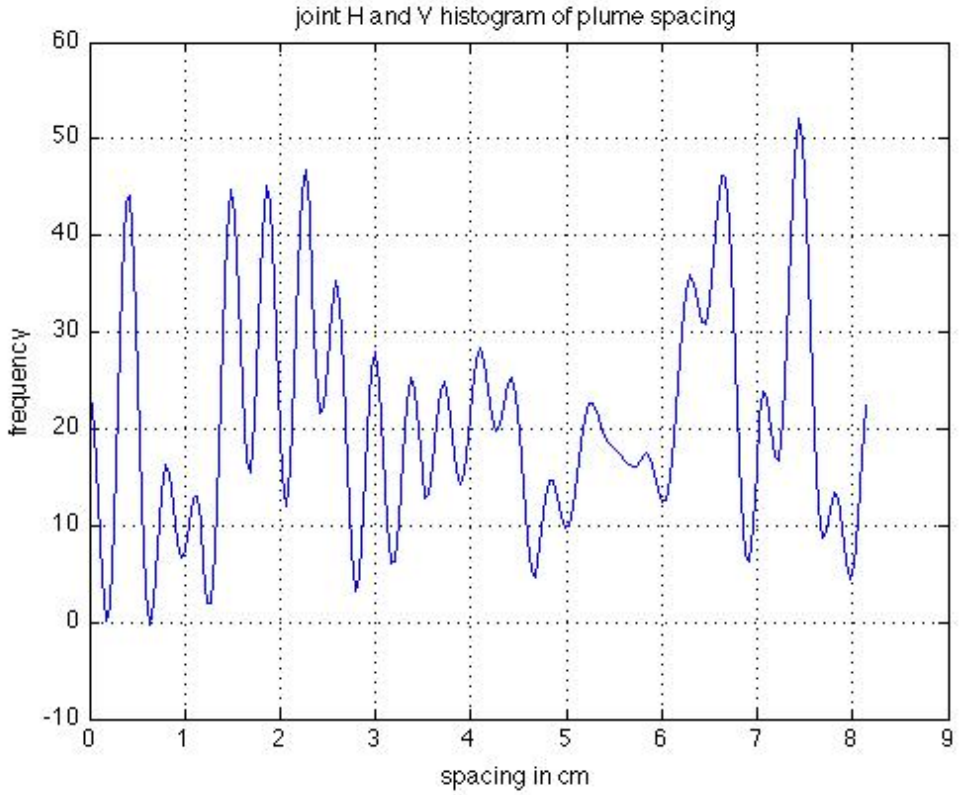
joint H and V histogram of plume spacing
frequency
spacing in cm
60
50
40
30
20
10
0
-10
0
1
2
3
4
5
6
7
8
9

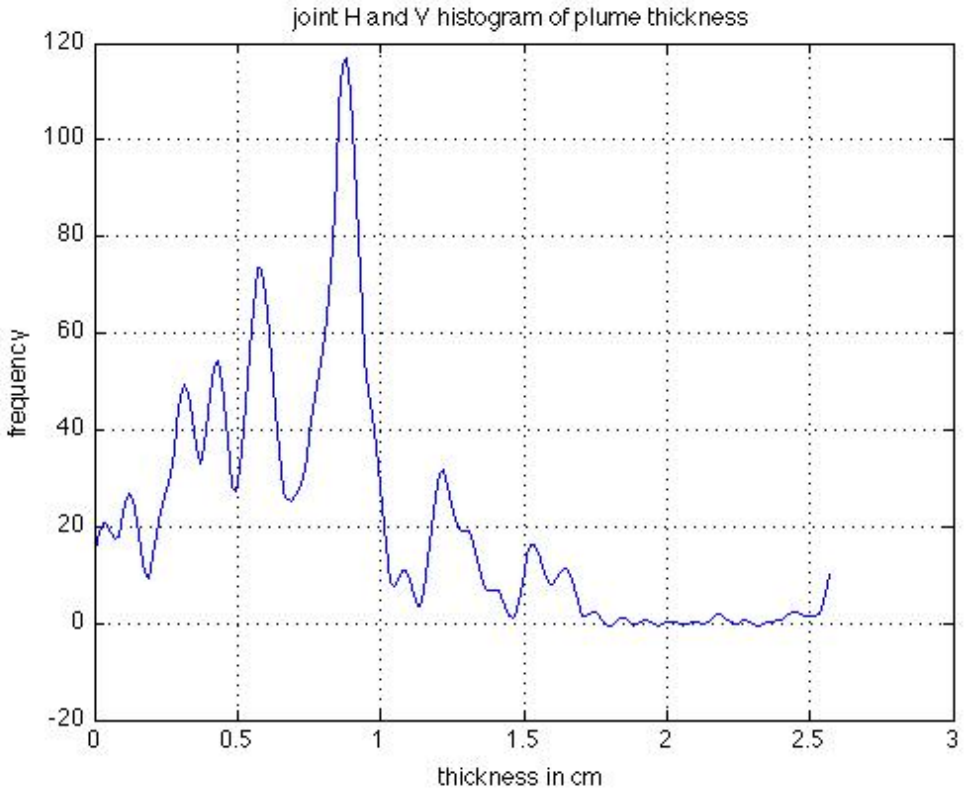
joint H and V histogram of plume thickness
frequency
thickness in cm
120
100
80
60
40
20
0
-20
0
0.5
1
1.5
2
2.5
3

PExpt10, U = 470

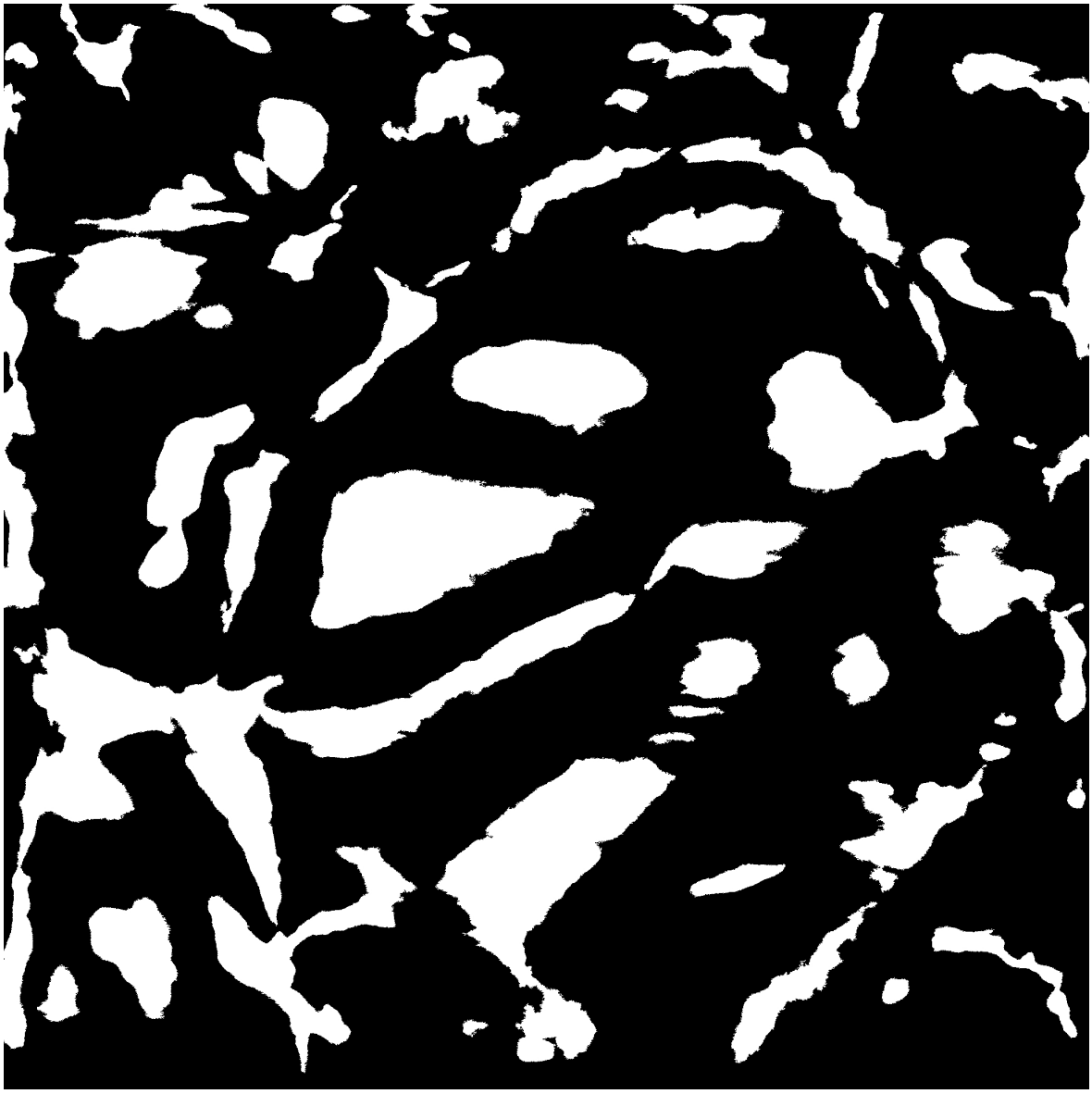

Spacing in cm (frequency of occurrence)

6.55(50)
3.8(48)
2.75(40)
7.6(35)
1.1(35)
4.6(35)

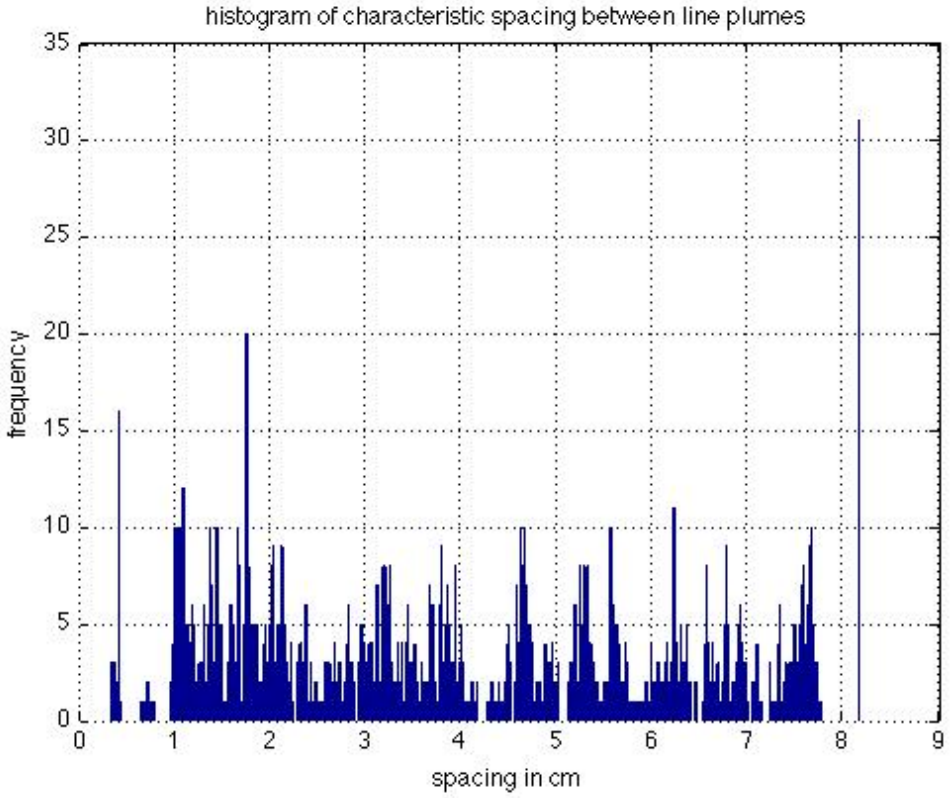
histogram of characteristic spacing between line plumes
frequency
spacing in cm
0
5
10
15
20
25
30
35
0
1
2
3
4
5
6
7
8
9

(H)

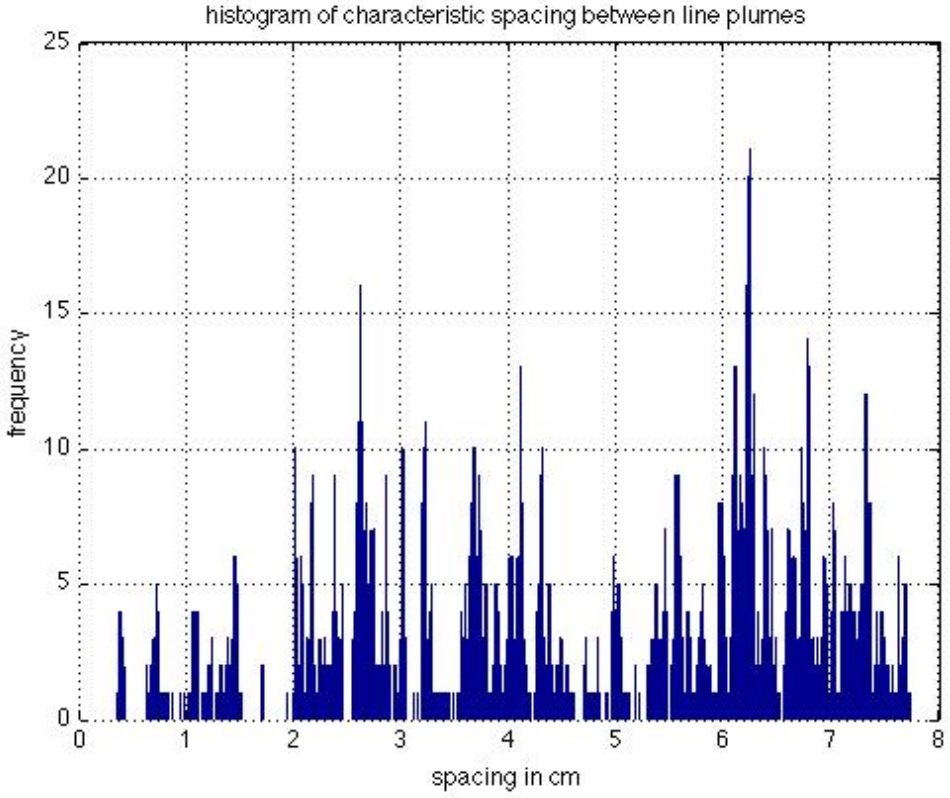
histogram of characteristic spacing between line plumes
frequency
spacing in cm
0
5
10
15
20
25
0
1
2
3
4
5
6
7
8

(V)

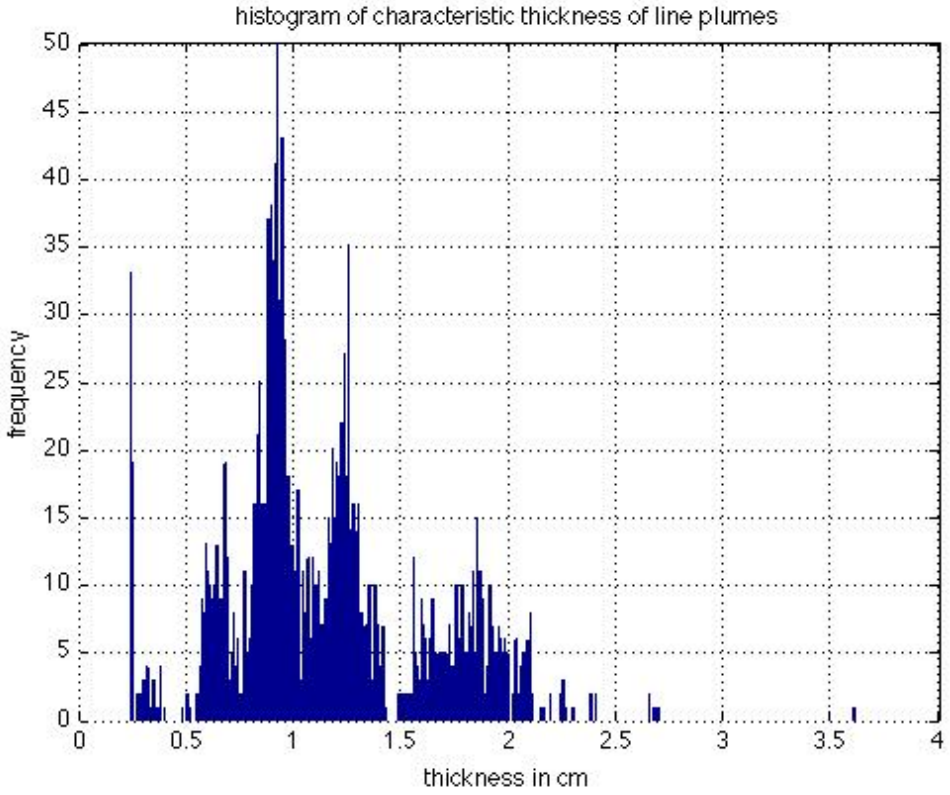
histogram of characteristic thickness of line plumes
frequency
thickness in cm
0
5
10
15
20
25
30
35
40
45
50
0
0.5
1
1.5
2
2.5
3
3.5
4

(H)

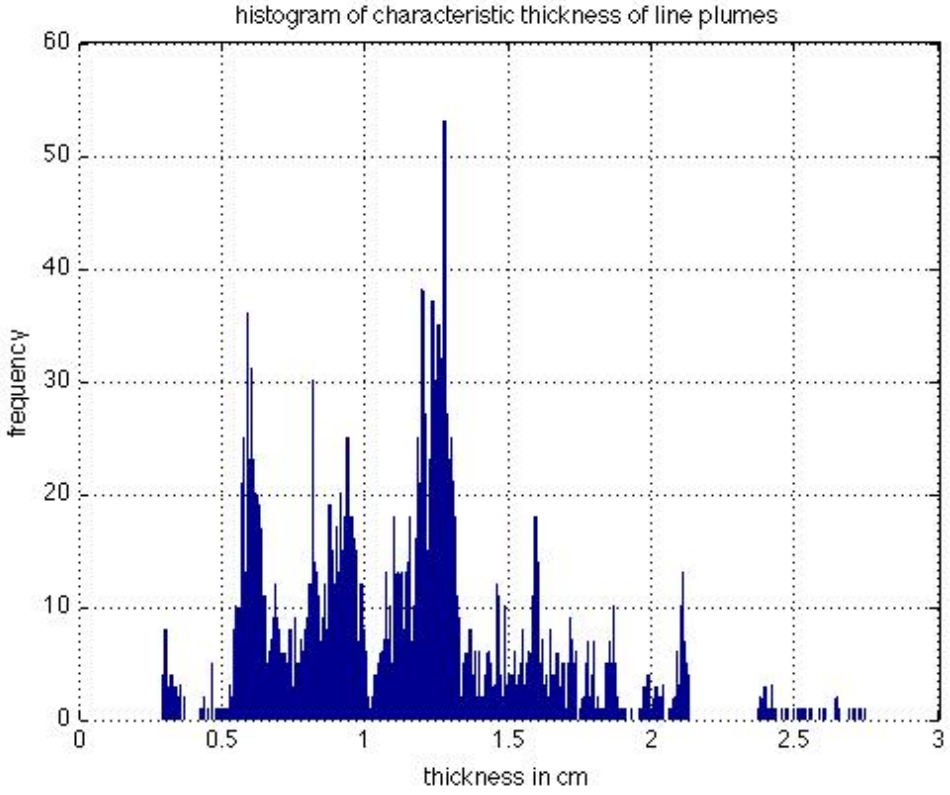
histogram of characteristic thickness of line plumes
frequency
thickness in cm
0
10
20
30
40
50
60
0
0.5
1
1.5
2
2.5
3

(V)

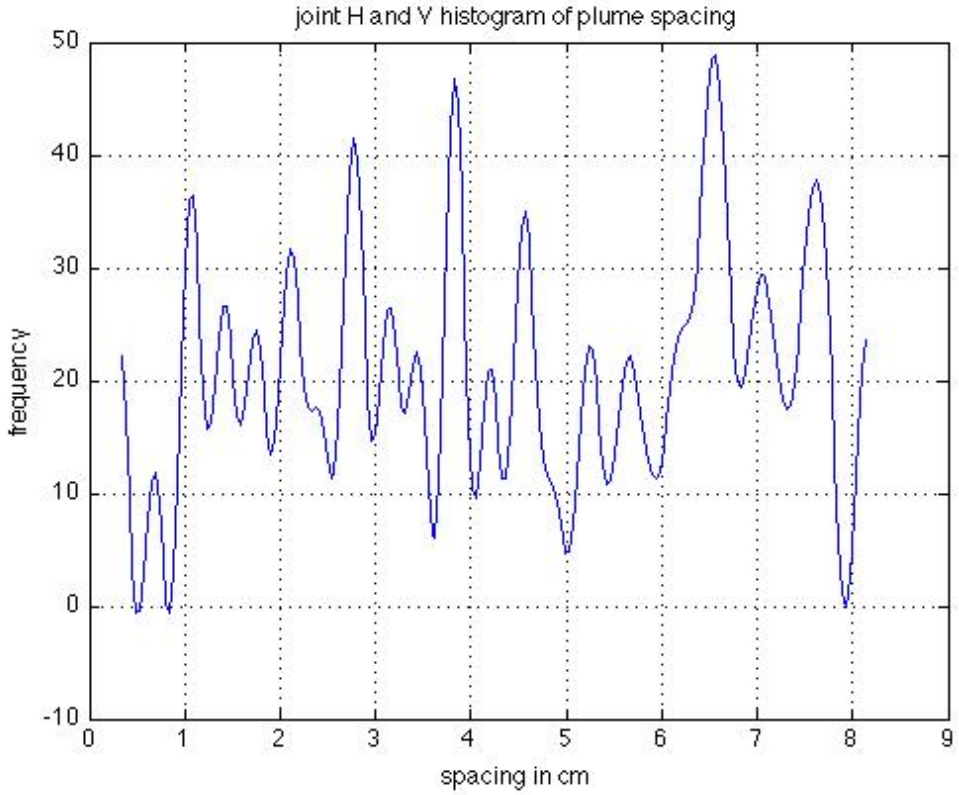
joint H and V histogram of plume spacing
frequency
spacing in cm
50
40
30
20
10
0
-10
0
1
2
3
4
5
6
7
8
9

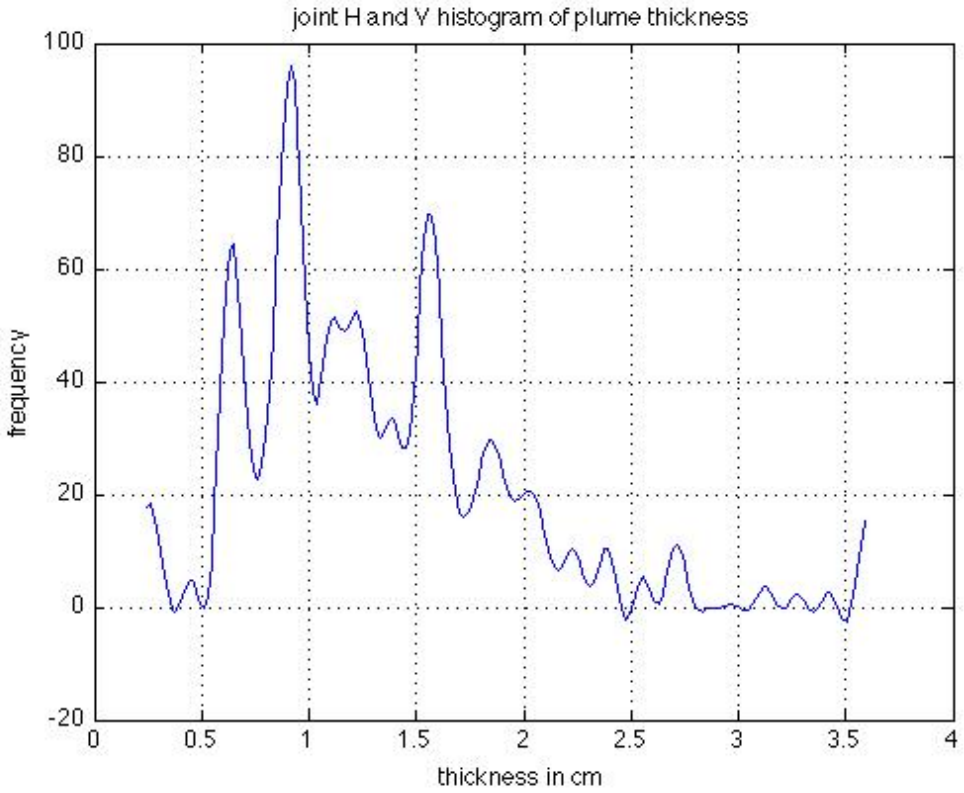
joint H and V histogram of plume thickness
frequency
thickness in cm
100
80
60
40
20
0
-20
0
0.5
1
1.5
2
2.5
3
3.5
4

PExpt11, U = 930

Spacing in cm (frequency of occurrence)

0.35(70)
0.73(55)
3.9(50)
4.35(40)
5.2(38)
6(32)

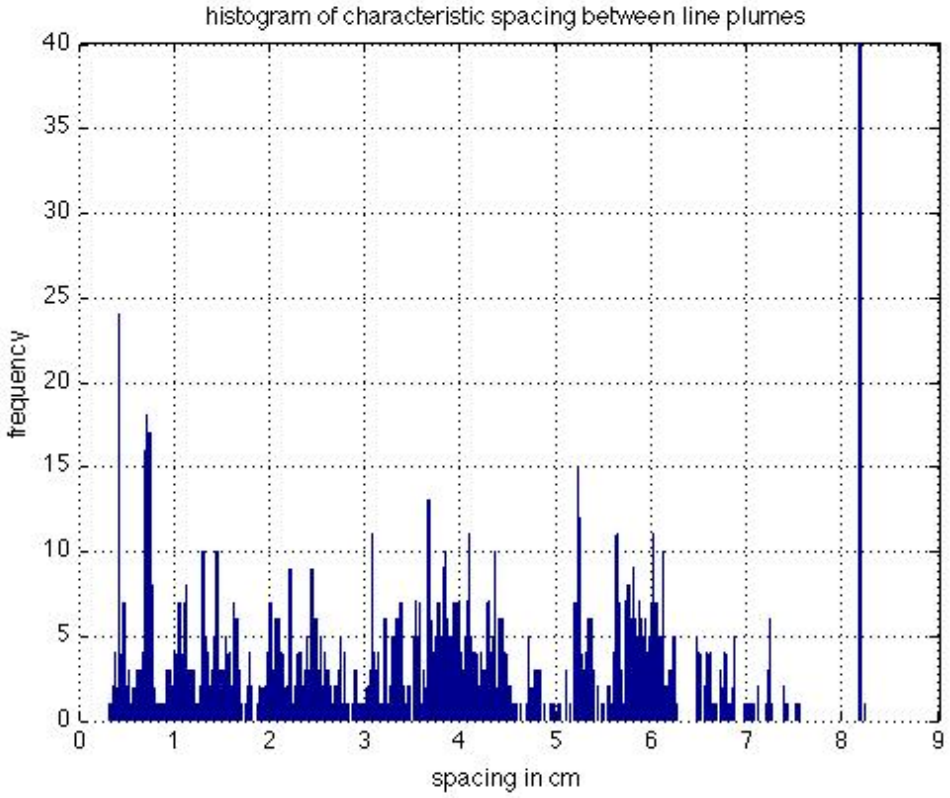
histogram of characteristic spacing between line plumes
frequency
spacing in cm
0
5
10
15
20
25
30
35
40
0
1
2
3
4
5
6
7
8
9

(H)

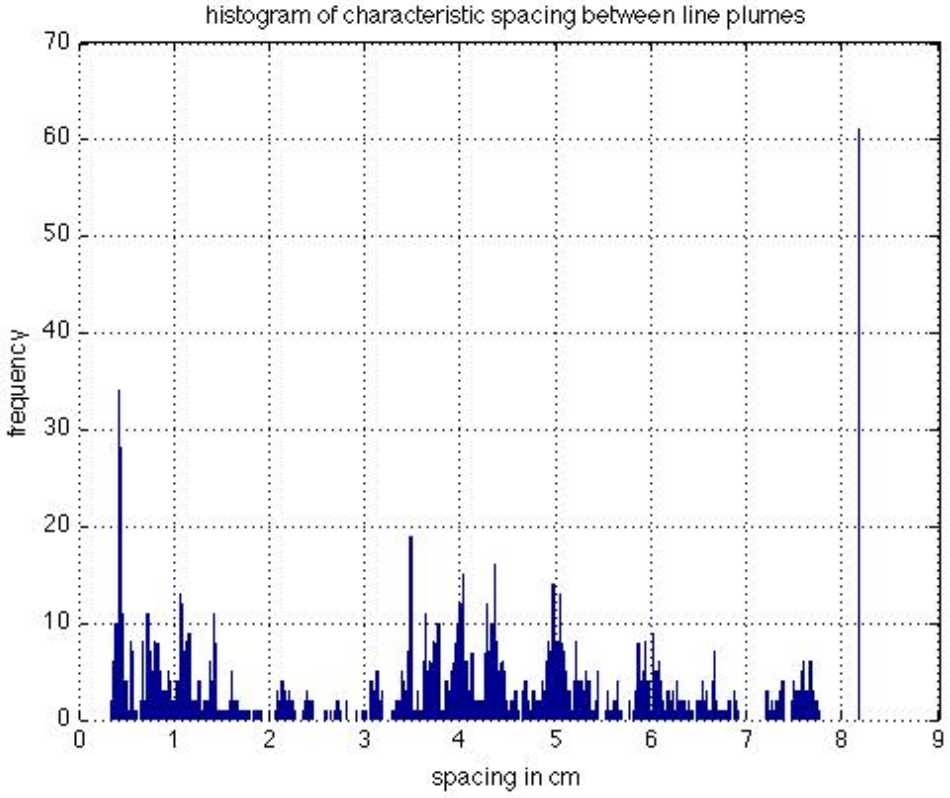
histogram of characteristic spacing between line plumes
frequency
spacing in cm
0
10
20
30
40
50
60
70
0
1
2
3
4
5
6
7
8
9

(V)

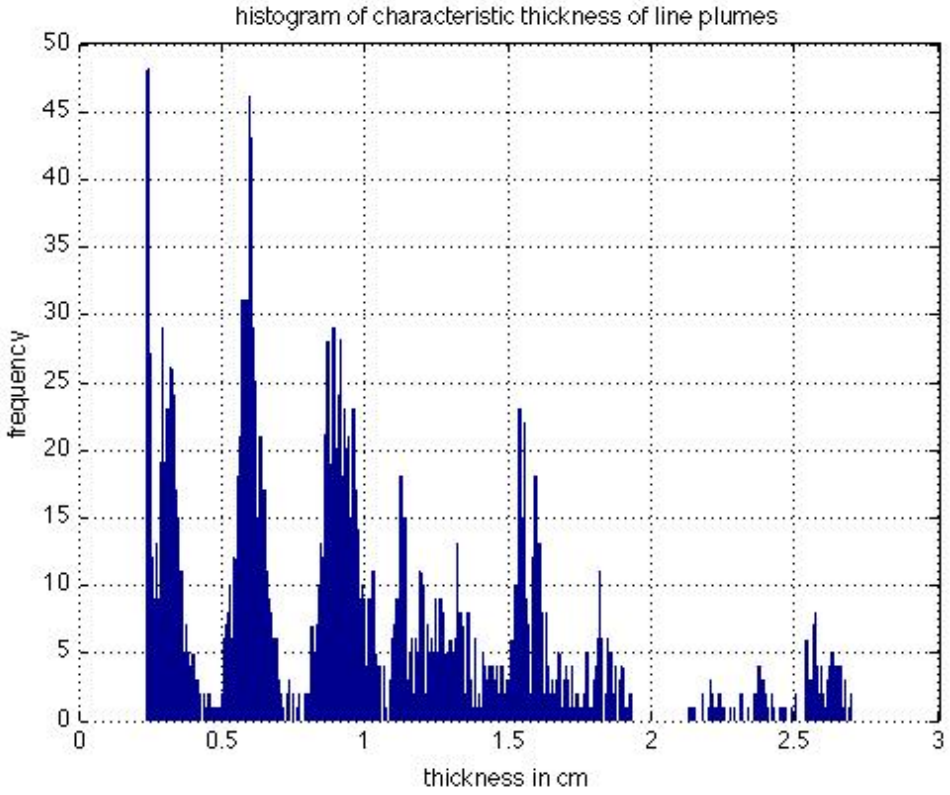
histogram of characteristic thickness of line plumes
frequency
thickness in cm
0
5
10
15
20
25
30
35
40
45
50
0
0.5
1
1.5
2
2.5
3

(H)

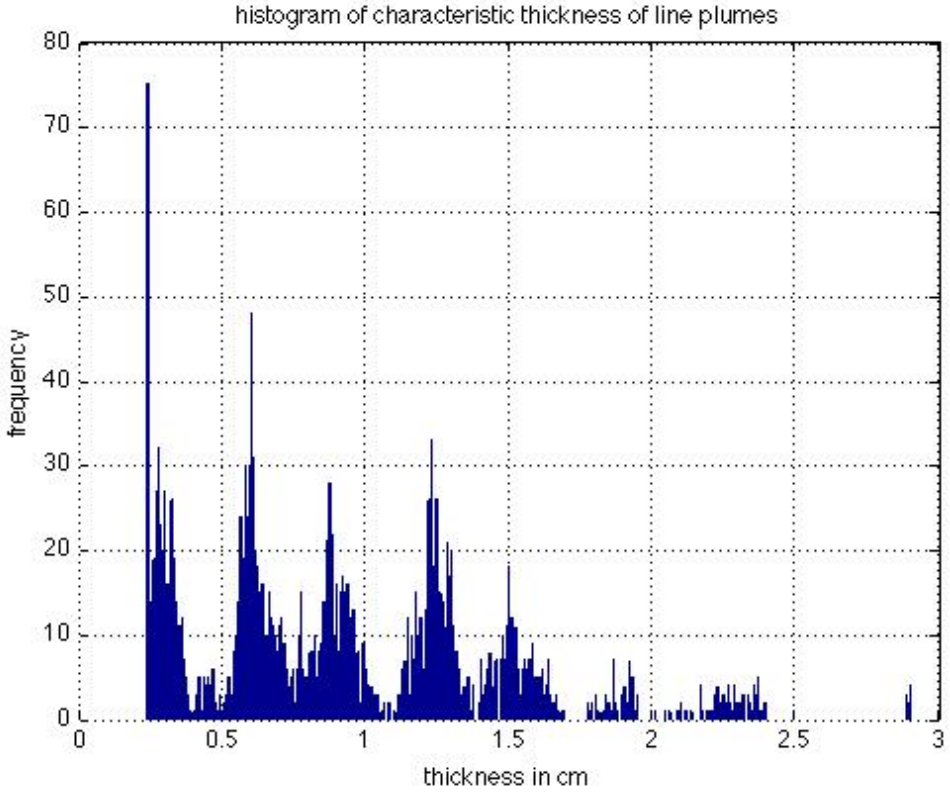
histogram of characteristic thickness of line plumes
frequency
thickness in cm
0
10
20
30
40
50
60
70
80
0
0.5
1
1.5
2
2.5
3

(V)

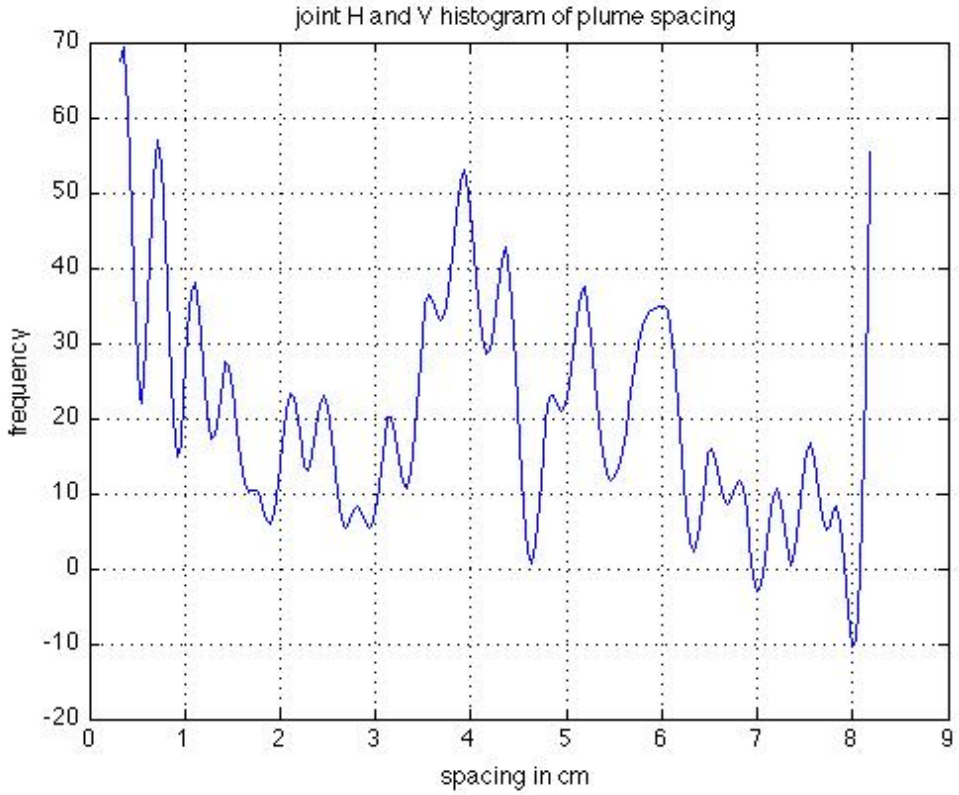
joint H and V histogram of plume spacing
frequency
spacing in cm
70
60
50
40
30
20
10
0
-10
-20
0
1
2
3
4
5
6
7
8
9

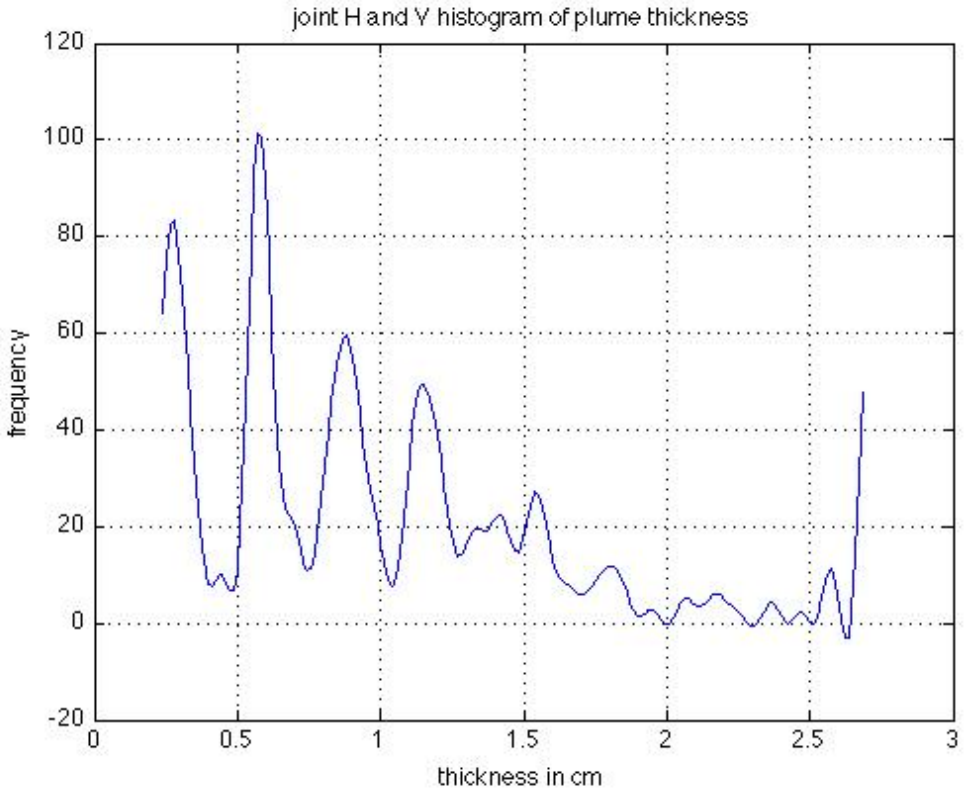
joint H and V histogram of plume thickness
frequency
thickness in cm
120
100
80
60
40
20
0
-20
0
0.5
1
1.5
2
2.5
3

PExpt12, U =2500

Spacing in cm (frequency of occurrence)

0.35(90)
4.4(35)
7.4(40)
1.1(40
6.5(30)
5.8(30)

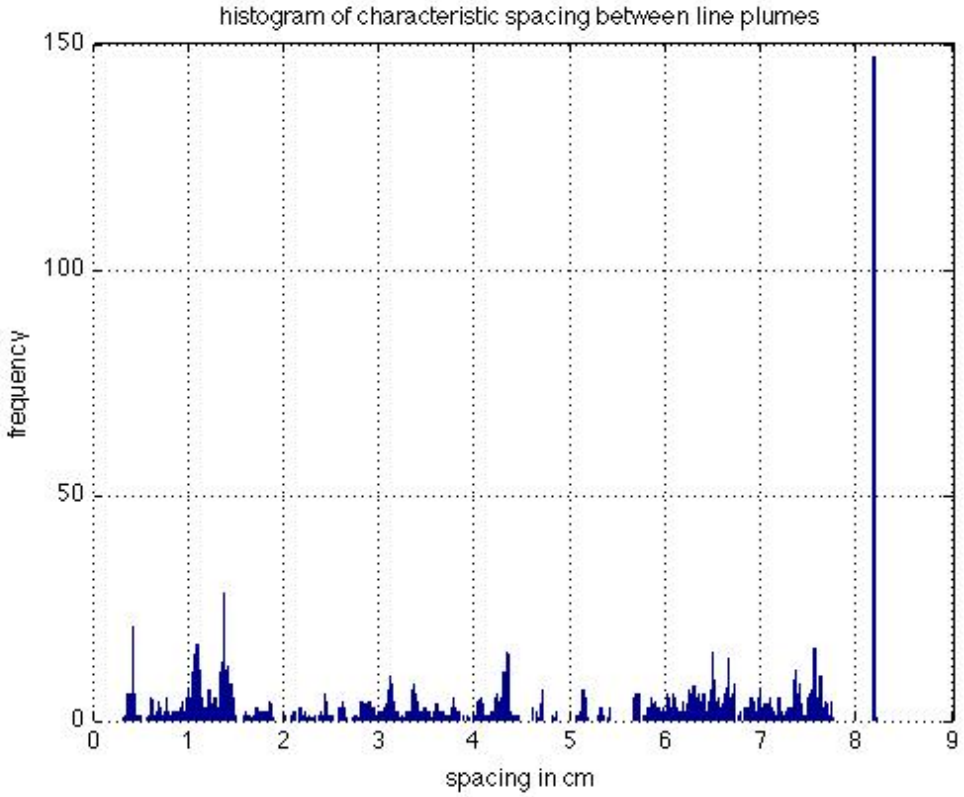
histogram of characteristic spacing between line plumes
frequency
spacing in cm
0
50
100
150
0
1
2
3
4
5
6
7
8
9

(H)

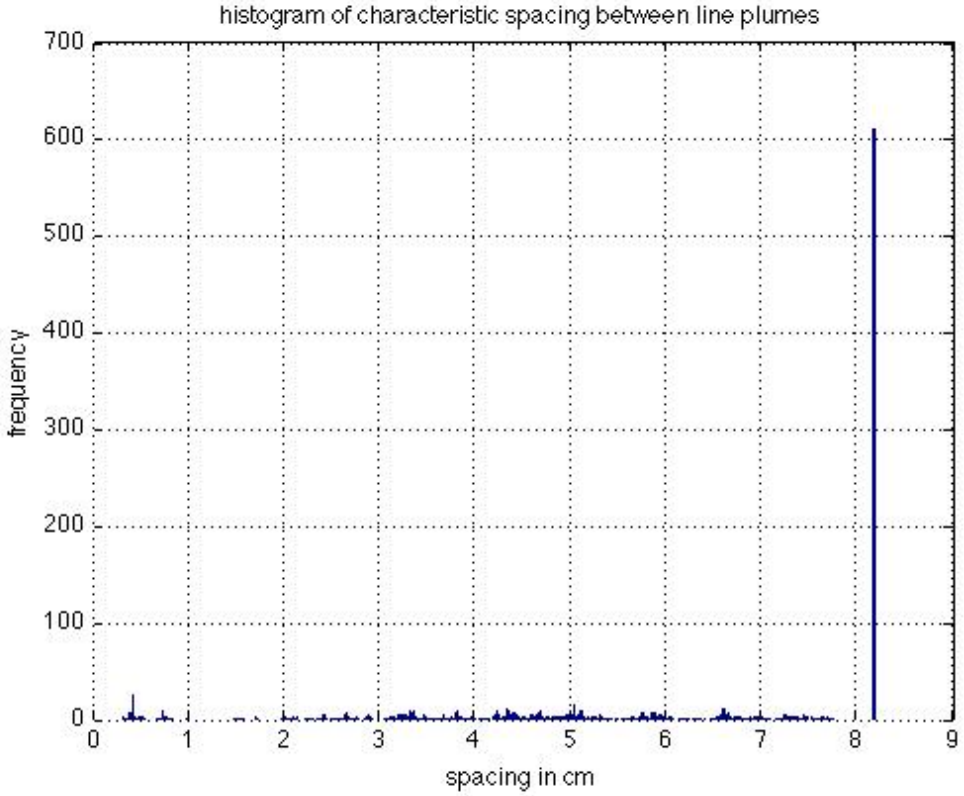
histogram of characteristic spacing between line plumes
frequency
spacing in cm
0
100
200
300
400
500
600
700
0
1
2
3
4
5
6
7
8
9

(V)

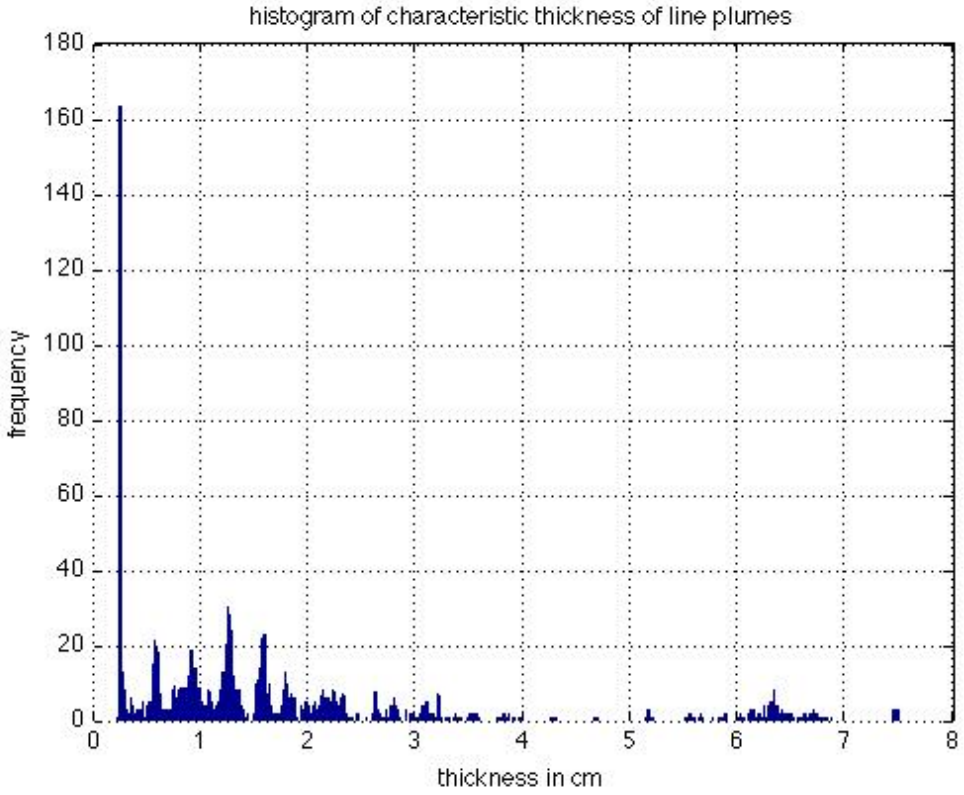
histogram of characteristic thickness of line plumes
frequency
thickness in cm
0
20
40
60
80
100
120
140
160
180
0
1
2
3
4
5
6
7
8

(H)

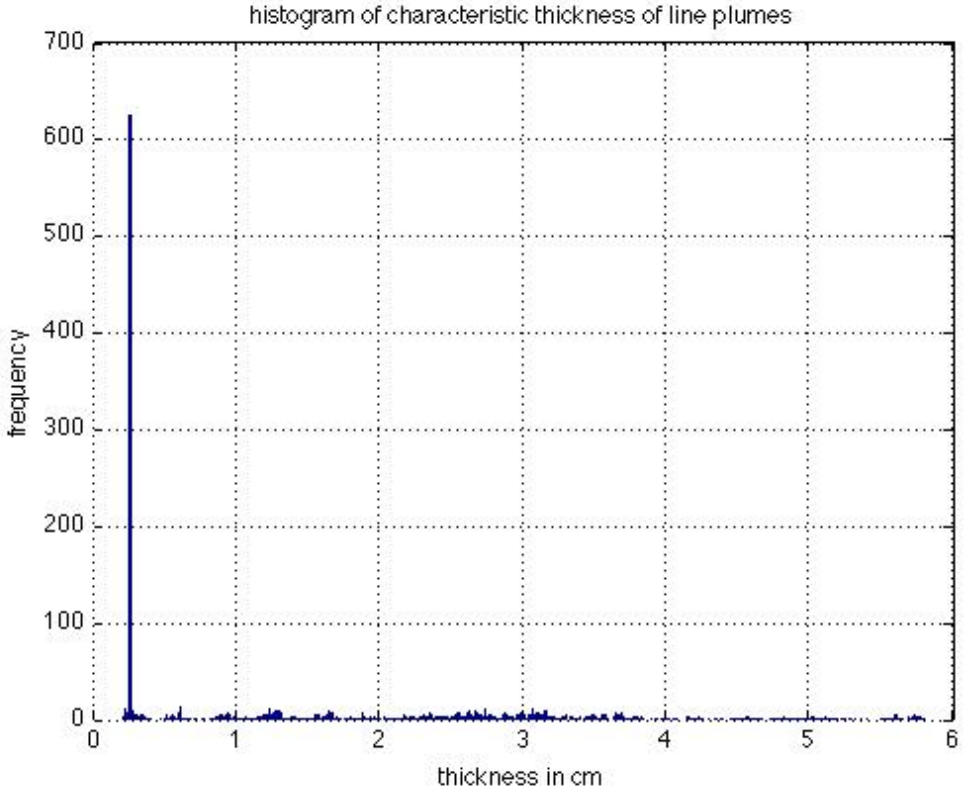
histogram of characteristic thickness of line plumes
frequency
thickness in cm
0
100
200
300
400
500
600
700
0
1
2
3
4
5
6

(V)

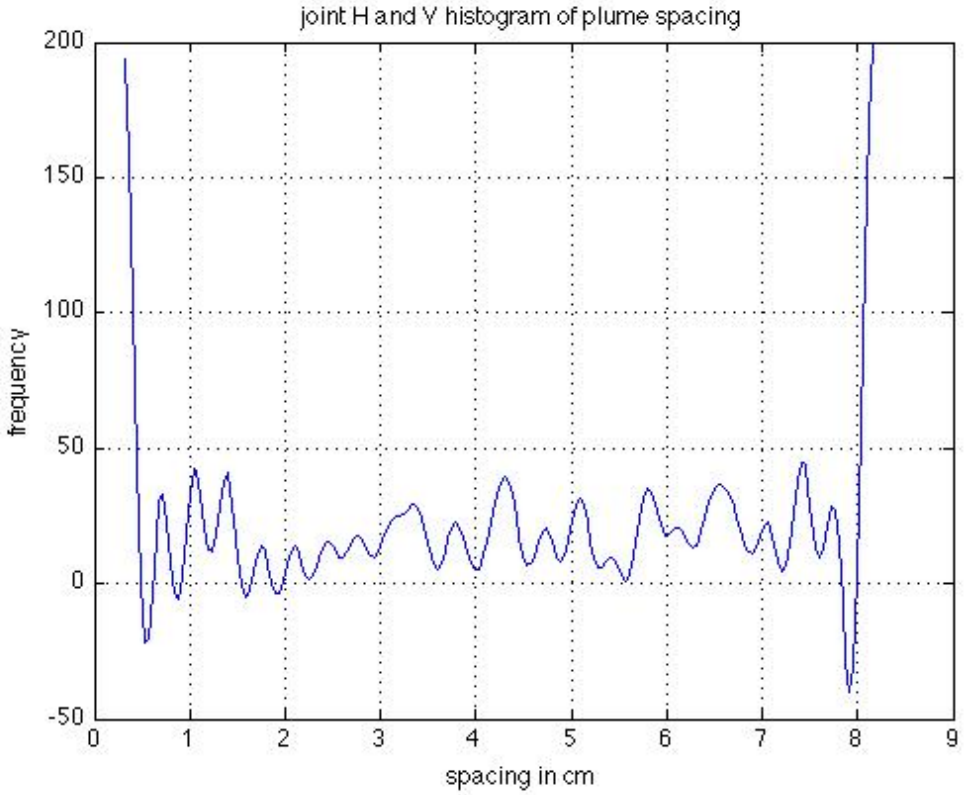
joint H and V histogram of plume spacing
frequency
spacing in cm
200
150
100
50
0
-50
0
1
2
3
4
5
6
7
8
9

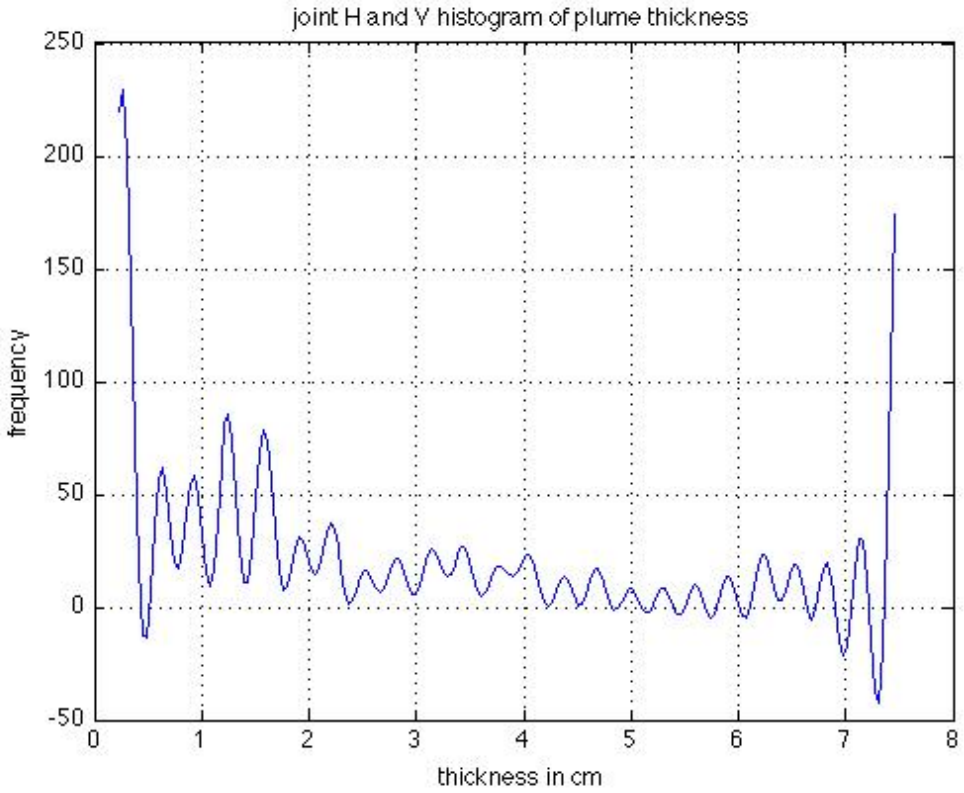
joint H and V histogram of plume thickness
frequency
thickness in cm
250
200
150
100
50
0
-50
0
1
2
3
4
5
6
7
8

TExpt6, U=1/300

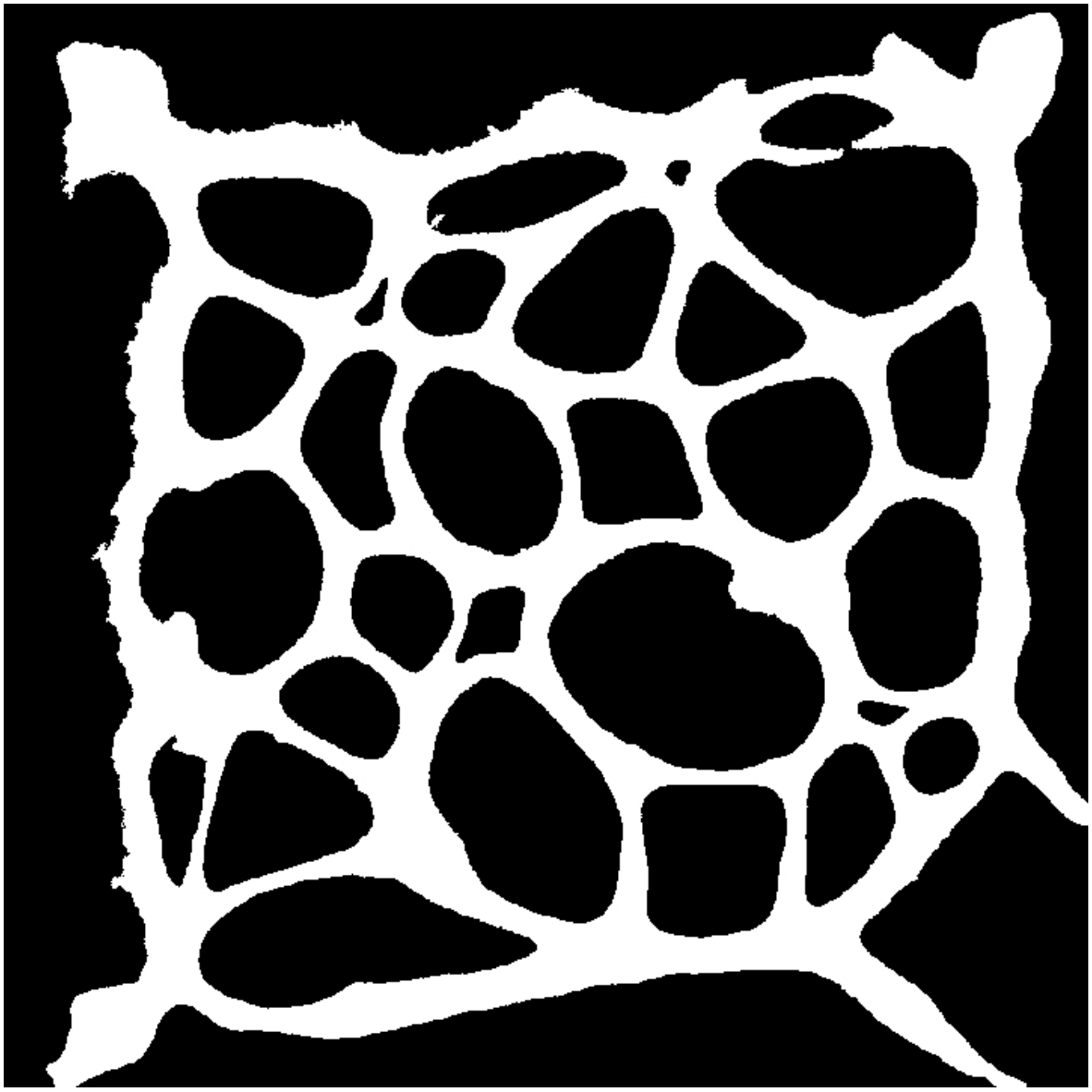

Spacing in cm (frequency of occurrence)

4.4(18)
3.05(17)
6.35(17)
3.65(14)
5.7(11)
5.2(10)
2.05(9)

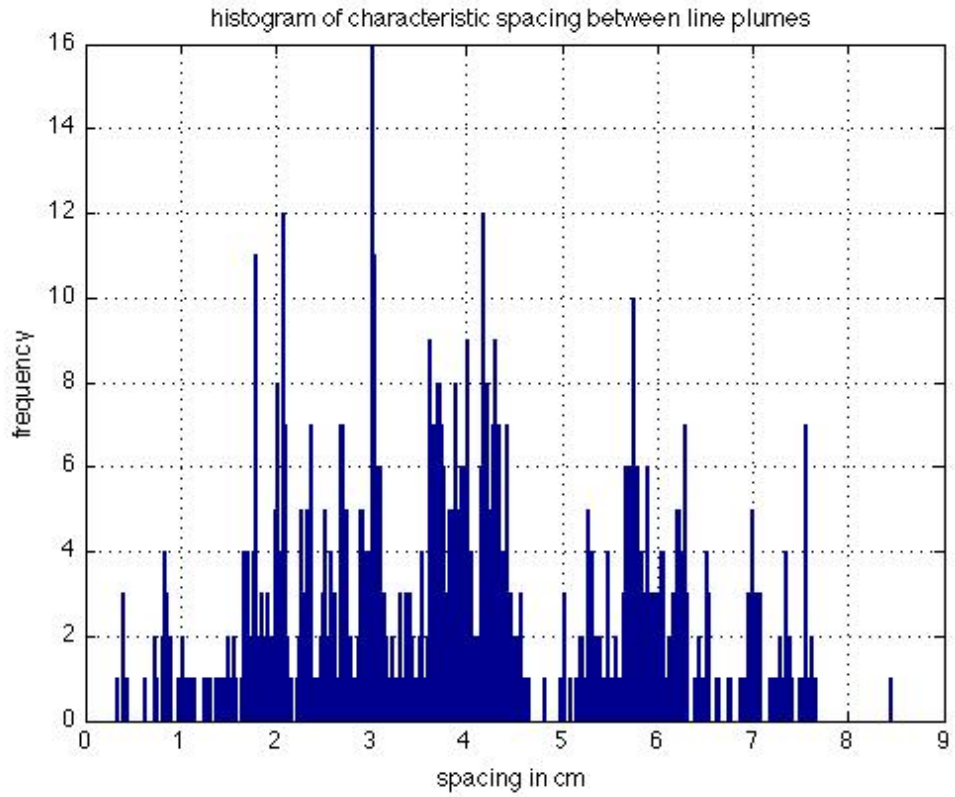
histogram of characteristic spacing between line plumes
frequency
spacing in cm
0
2
4
6
8
10
12
14
16
0
1
2
3
4
5
6
7
8
9

(H)

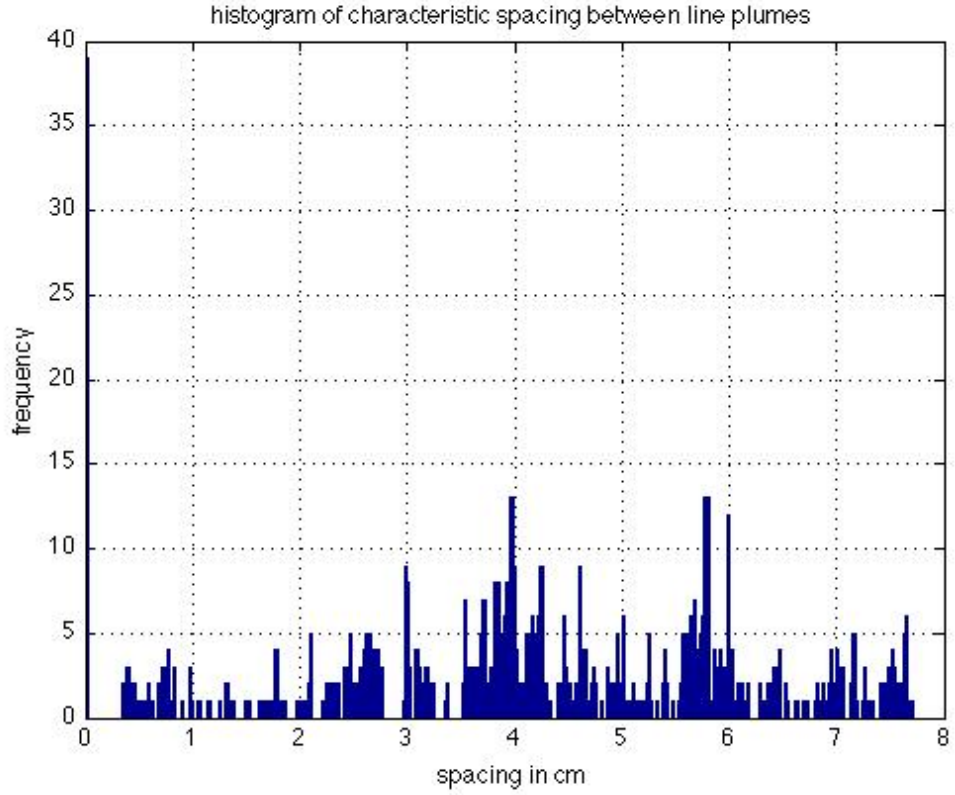
histogram of characteristic spacing between line plumes
frequency
spacing in cm
0
5
10
15
20
25
30
35
40
0
1
2
3
4
5
6
7
8

(V)

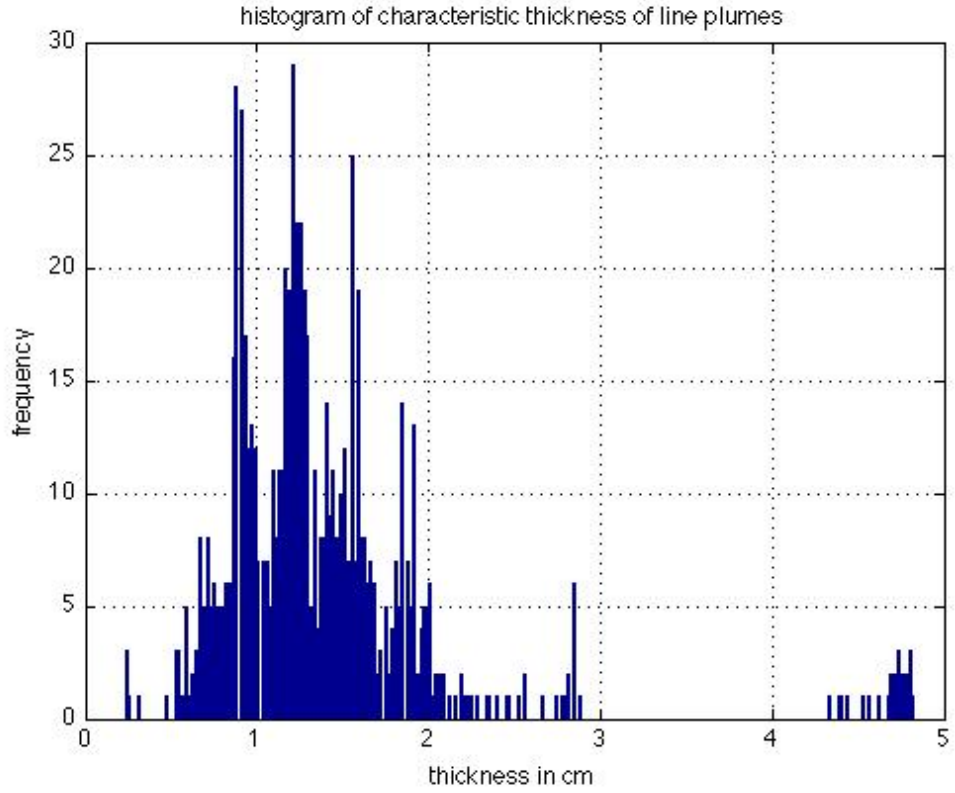
histogram of characteristic thickness of line plumes
frequency
thickness in cm
0
5
10
15
20
25
30
0
1
2
3
4
5

(H)

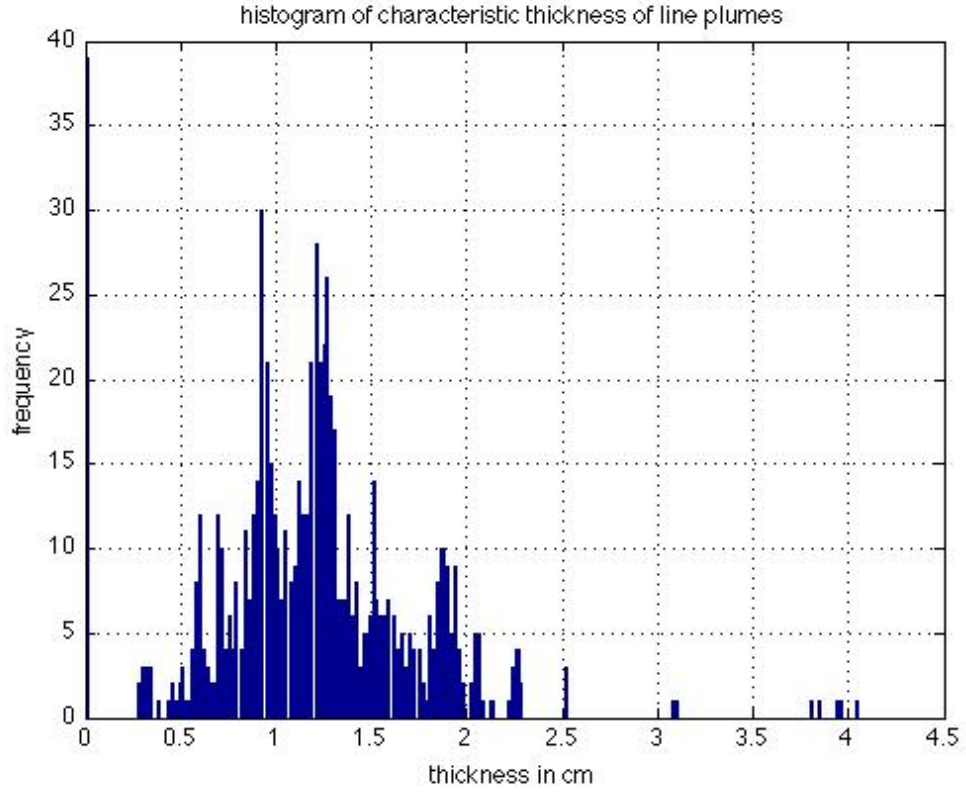
histogram of characteristic thickness of line plumes
frequency
thickness in cm
0
5
10
15
20
25
30
35
40
0
0.5
1
1.5
2
2.5
3
3.5
4
4.5

(V)

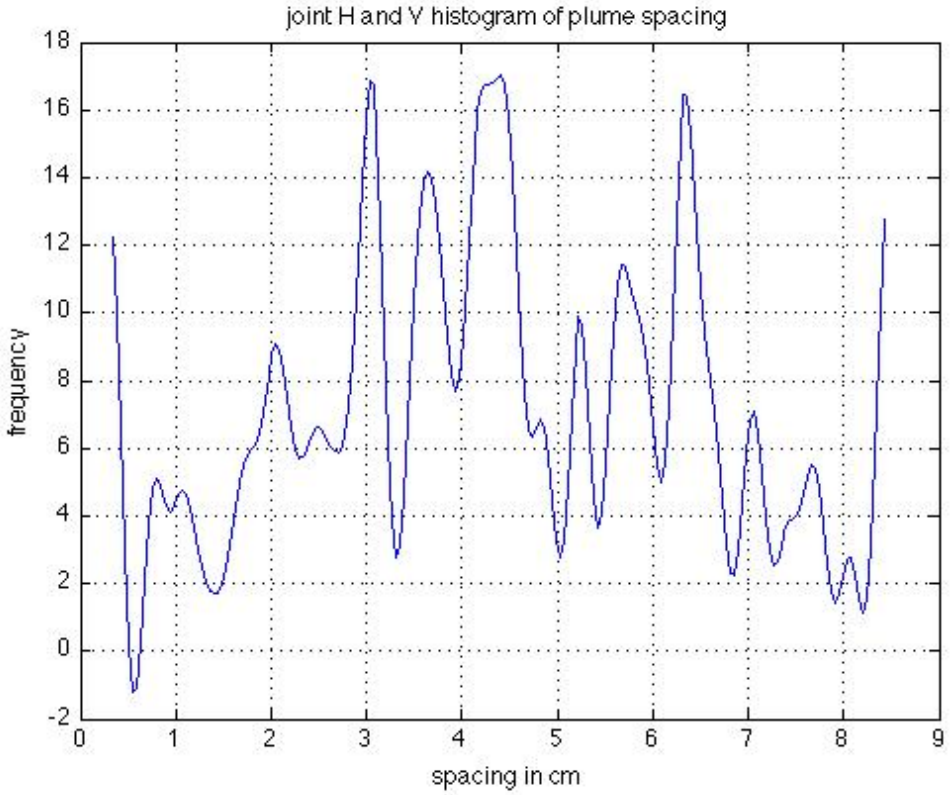
joint H and V histogram of plume spacing
frequency
spacing in cm
18
16
14
12
10
8
6
4
2
0
-2
0
1
2
3
4
5
6
7
8
9

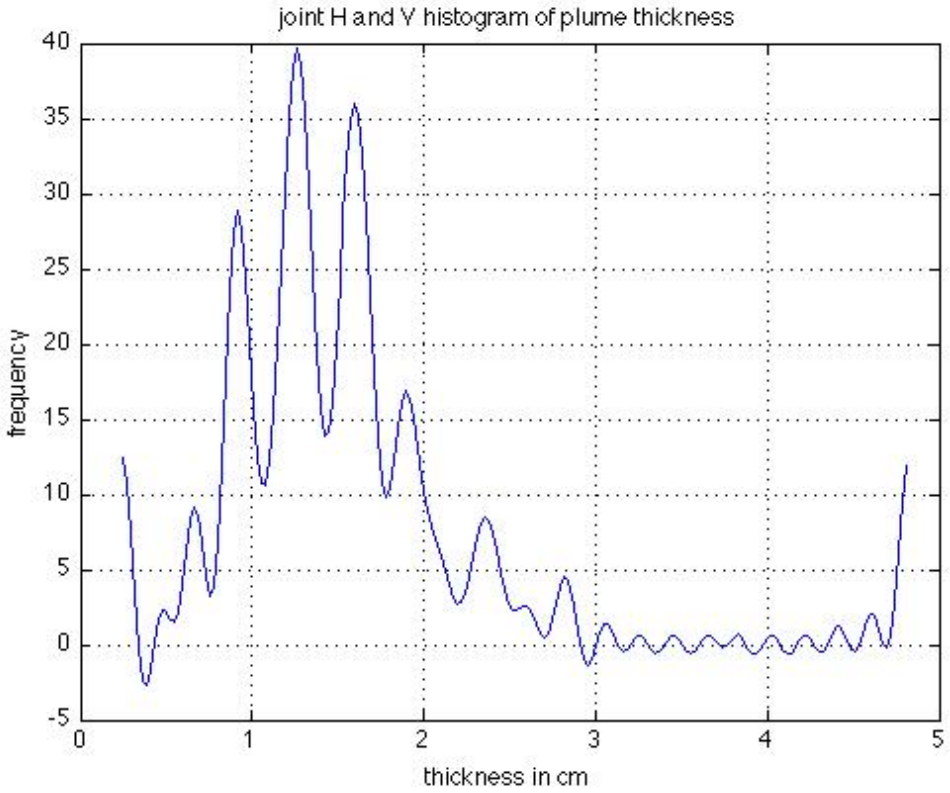
joint H and V histogram of plume thickness
frequency
thickness in cm
40
35
30
25
20
15
10
5
0
-5
0
1
2
3
4
5

MExpt1, U = 1/130

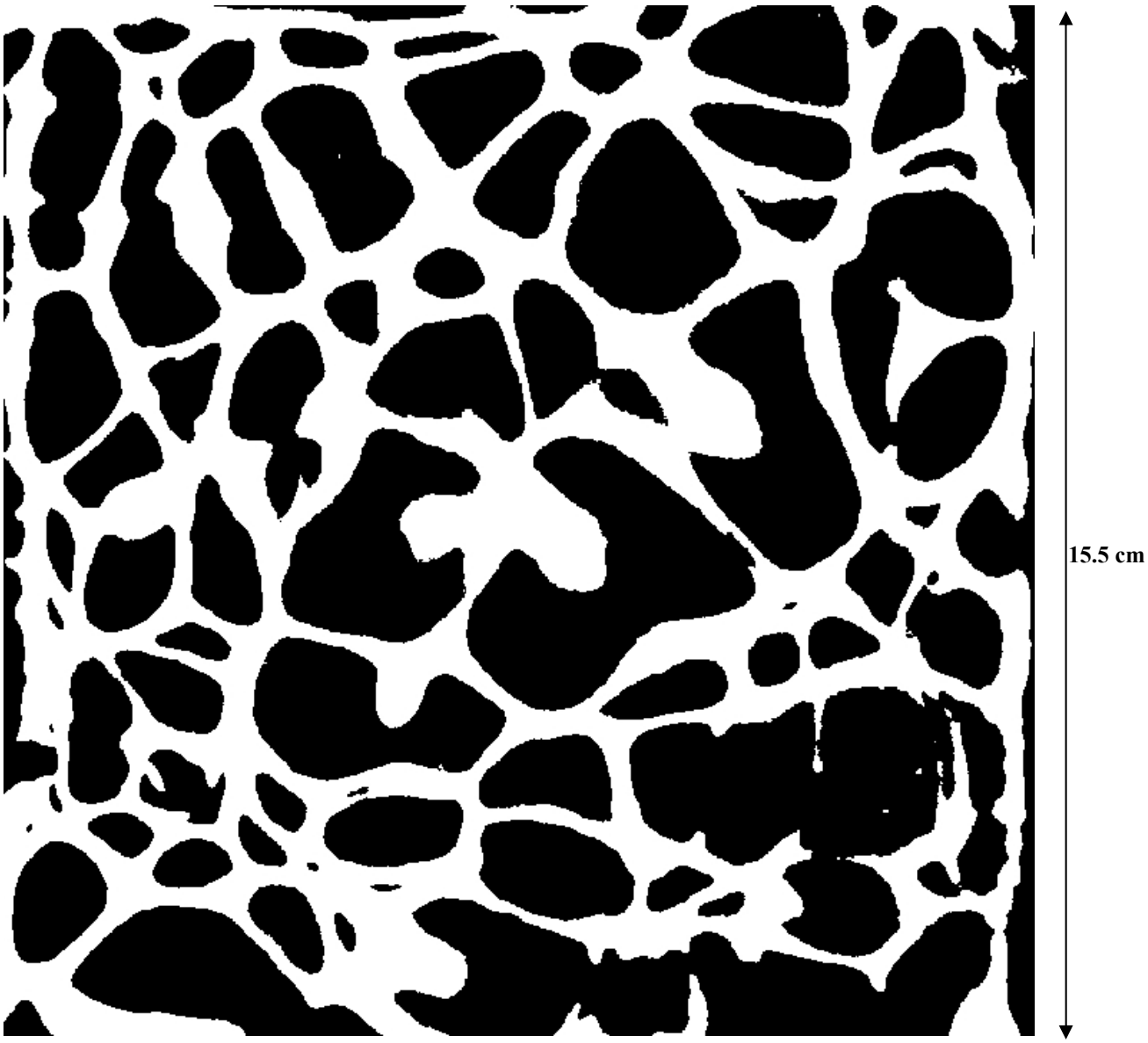

Spacing in cm (frequency of occurrence)

5.25(28)
4.4(14)
3(11)
5.8(12)
6.2(11)
1.6(10)

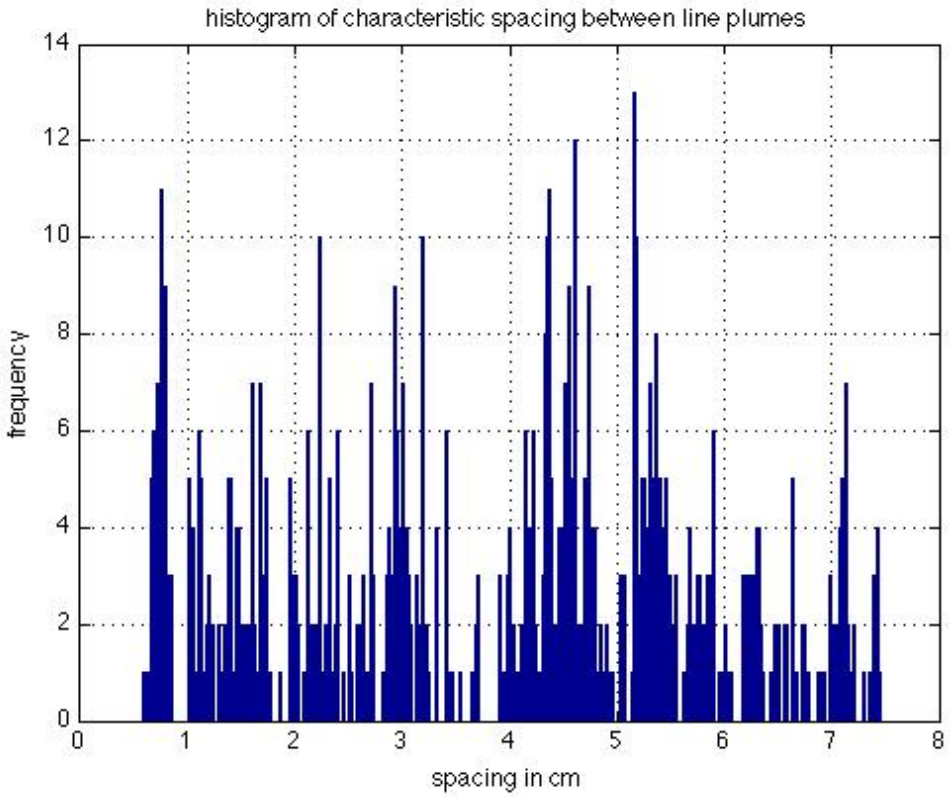
histogram of characteristic spacing between line plumes
frequency
spacing in cm
0
2
4
6
8
10
12
14
0
1
2
3
4
5
6
7
8

(H)

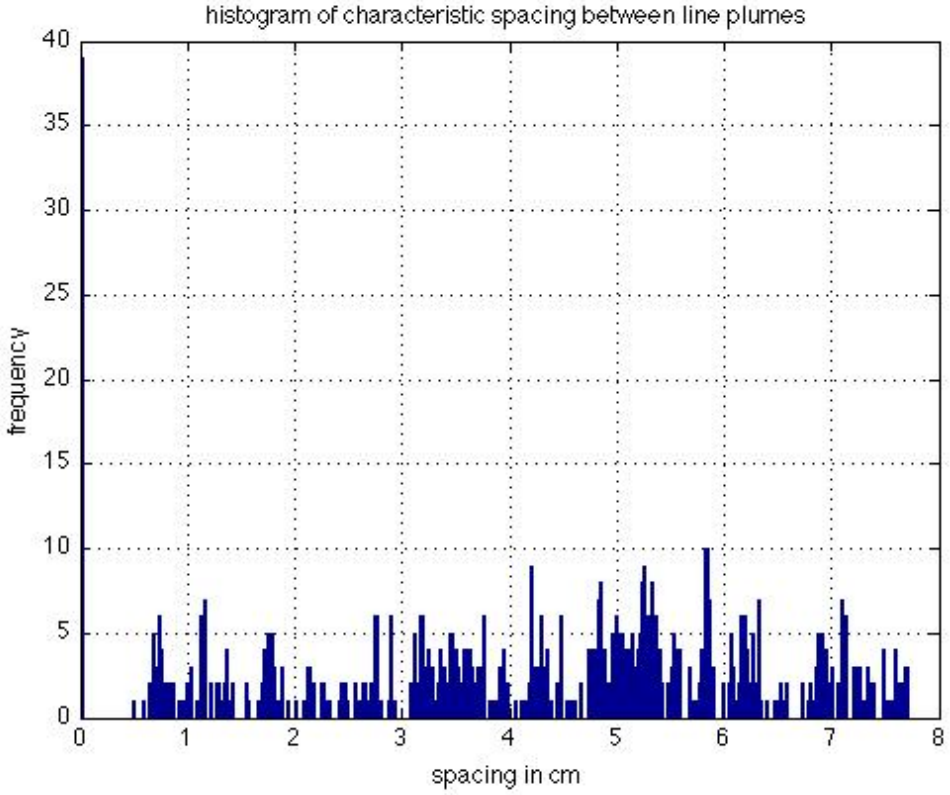
histogram of characteristic spacing between line plumes
frequency
spacing in cm
0
5
10
15
20
25
30
35
40
0
1
2
3
4
5
6
7
8

(V)

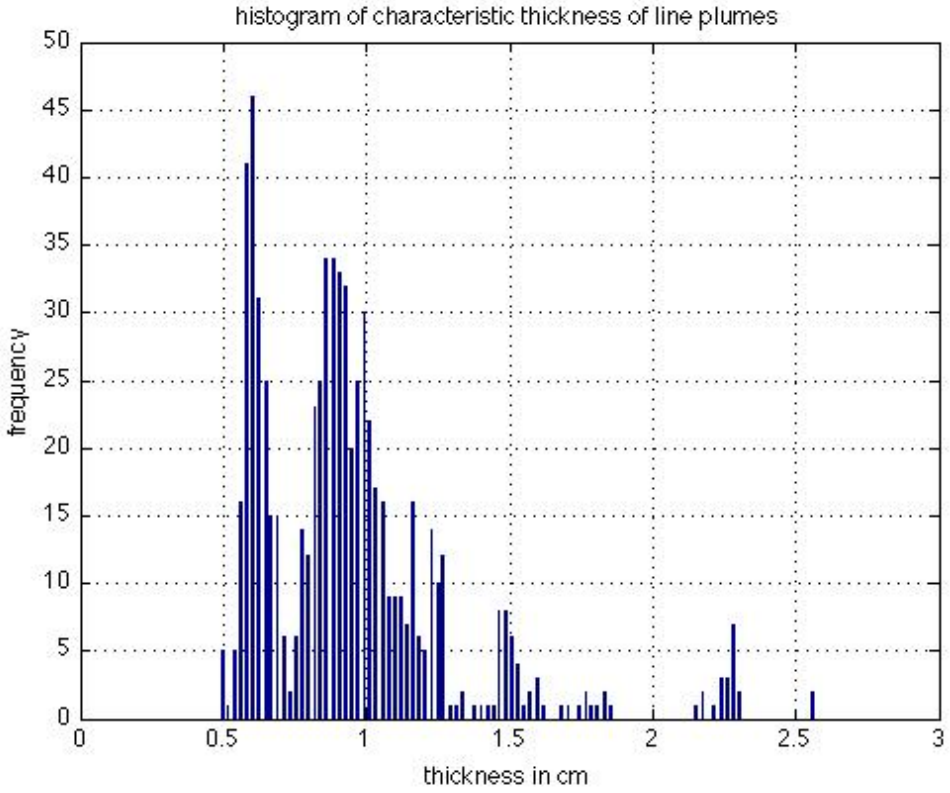
histogram of characteristic thickness of line plumes
frequency
thickness in cm
0
5
10
15
20
25
30
35
40
45
50
0
0.5
1
1.5
2
2.5
3

(H)

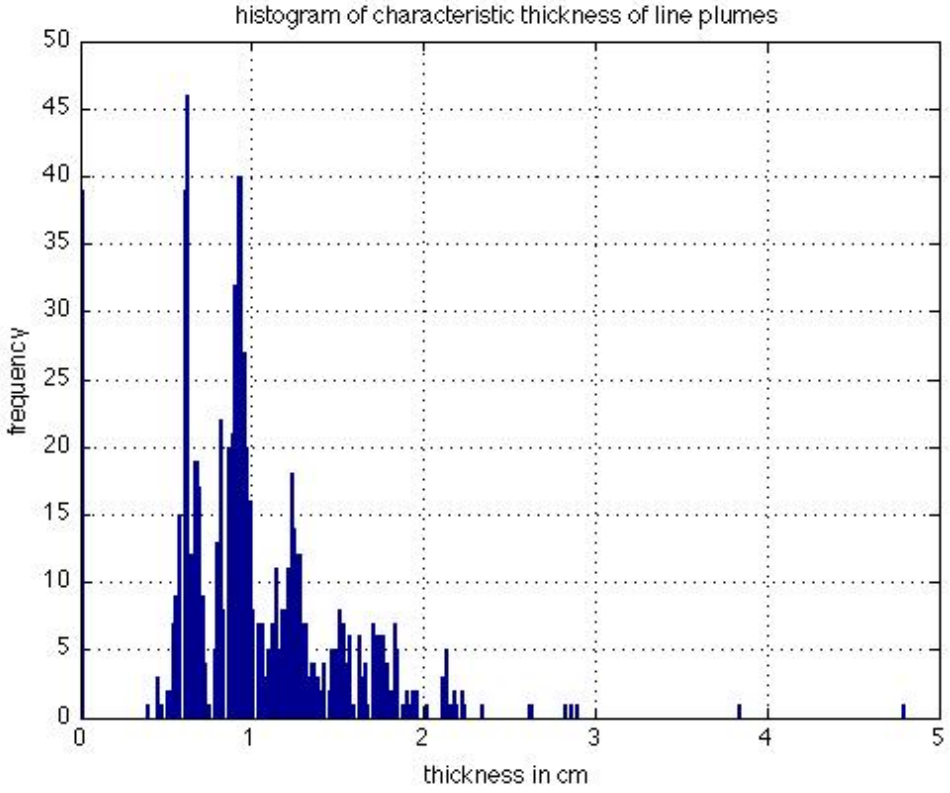
histogram of characteristic thickness of line plumes
frequency
thickness in cm
0
5
10
15
20
25
30
35
40
45
50
0
1
2
3
4
5

(V)

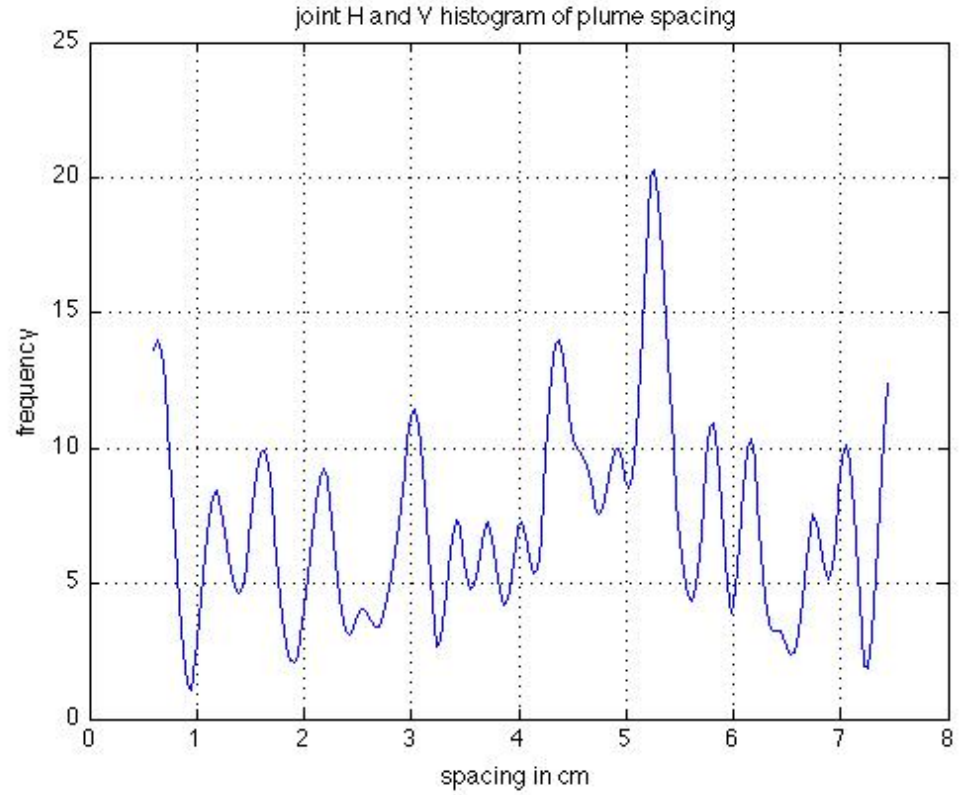
joint H and V histogram of plume spacing
frequency
spacing in cm
0
5
10
15
20
25
0
1
2
3
4
5
6
7
8

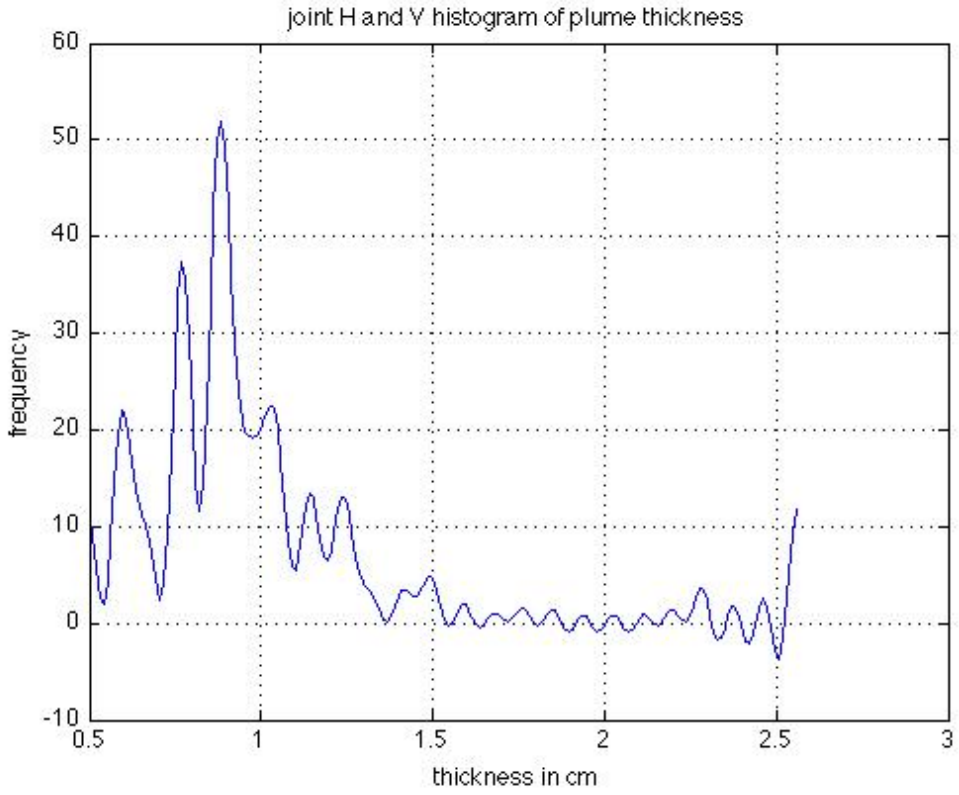
joint H and V histogram of plume thickness
frequency
thickness in cm
-10
0
10
20
30
40
50
60
0.5
1
1.5
2
2.5
3

TExpt7, U = 1/65

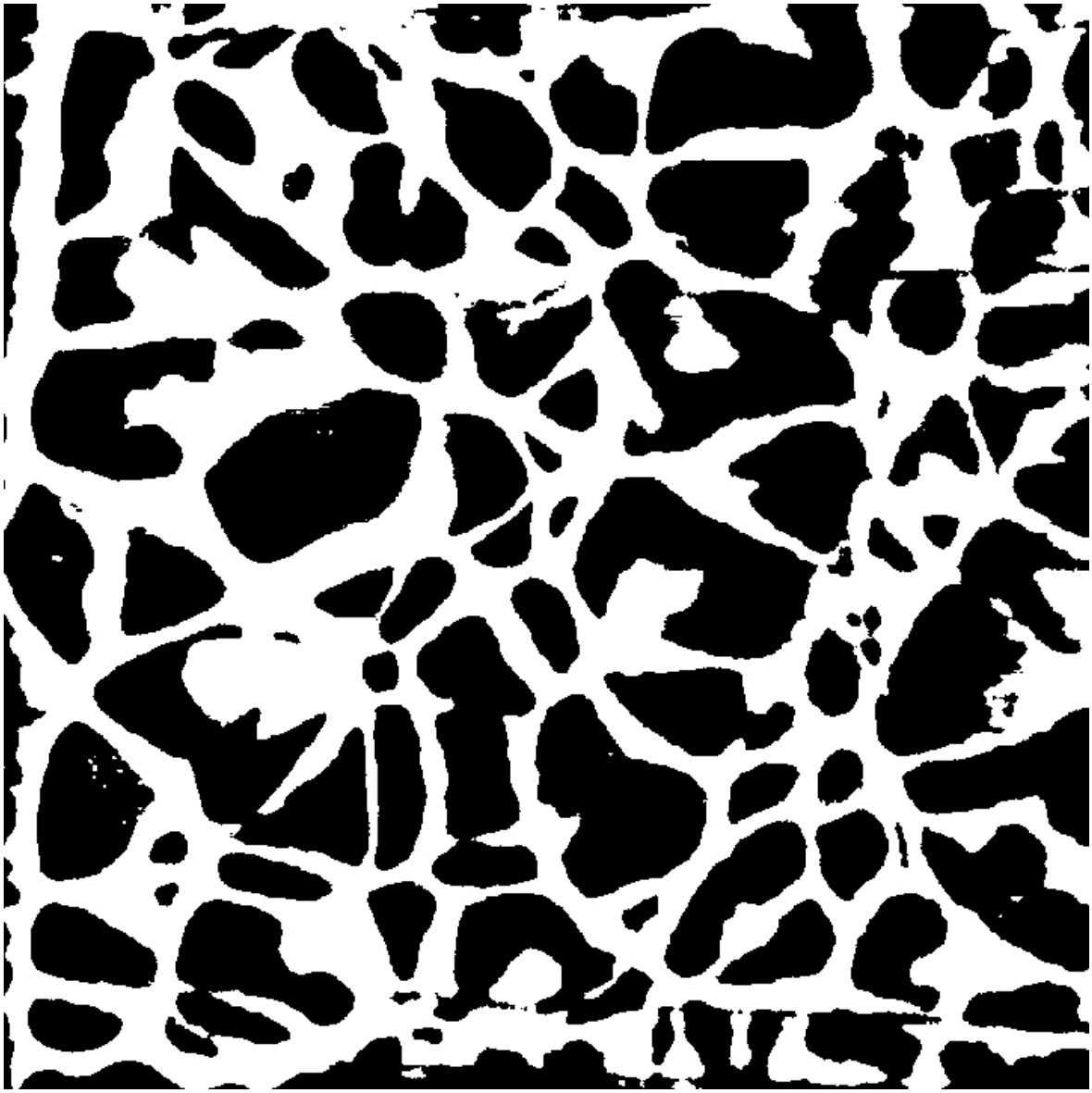

Spacing in cm (frequency of occurrence)

7.05(18)
3.5(15)
5.3(15)
5(14)
4(12)
6.4(11)

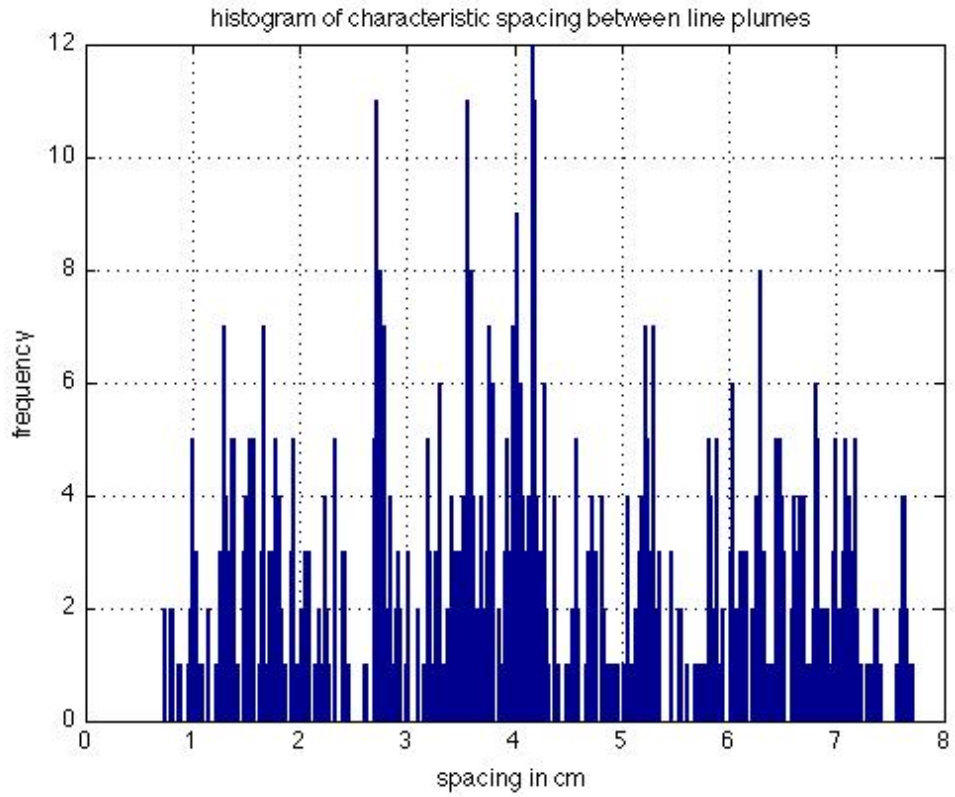
histogram of characteristic spacing between line plumes
frequency
spacing in cm
0
2
4
6
8
10
12
0
1
2
3
4
5
6
7
8

(H)

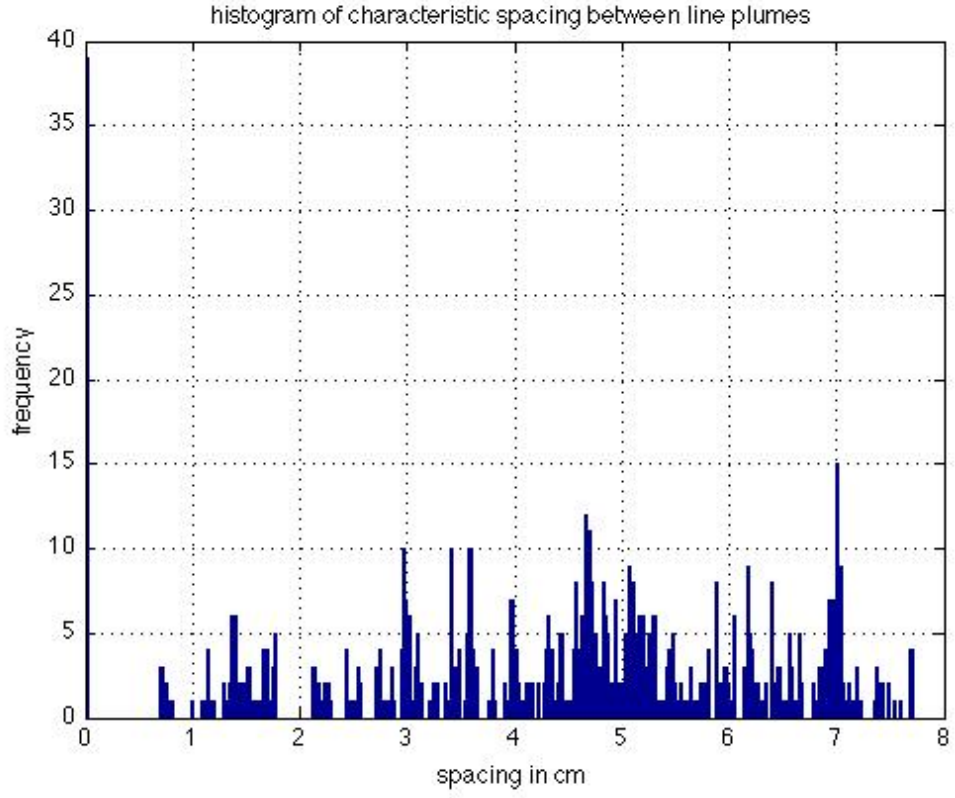
histogram of characteristic spacing between line plumes
frequency
spacing in cm
0
5
10
15
20
25
30
35
40
0
1
2
3
4
5
6
7
8

(V)

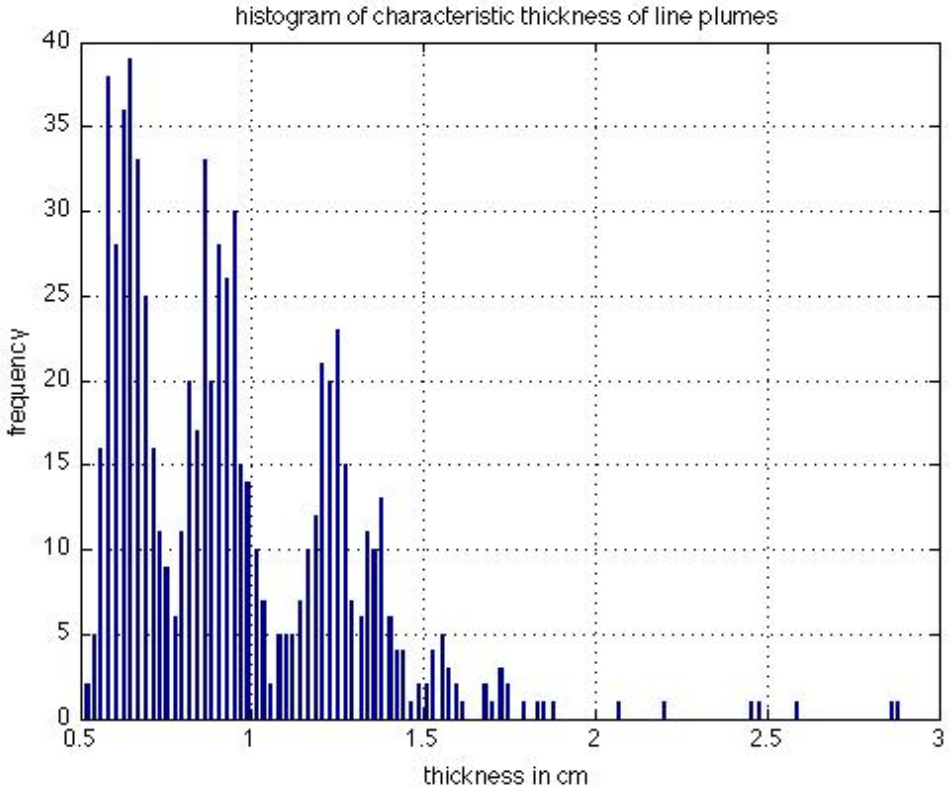
histogram of characteristic thickness of line plumes
frequency
thickness in cm
0
5
10
15
20
25
30
35
40
0.5
1
1.5
2
2.5
3

(H)

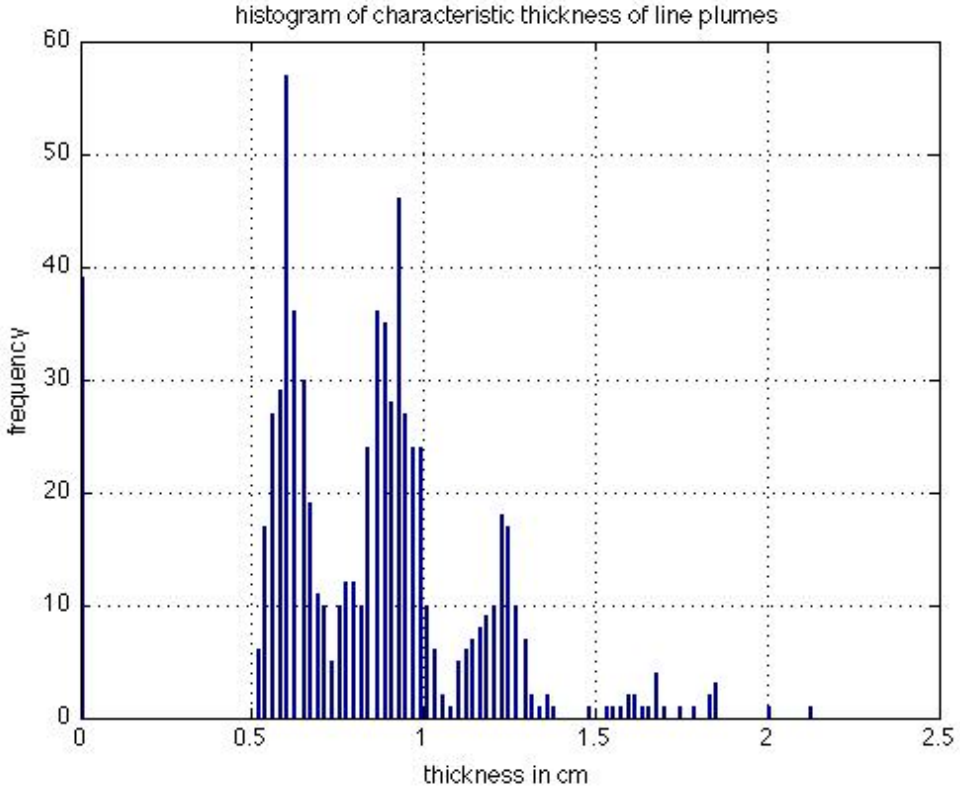
histogram of characteristic thickness of line plumes
frequency
thickness in cm
0
10
20
30
40
50
60
0
0.5
1
1.5
2
2.5

(V)

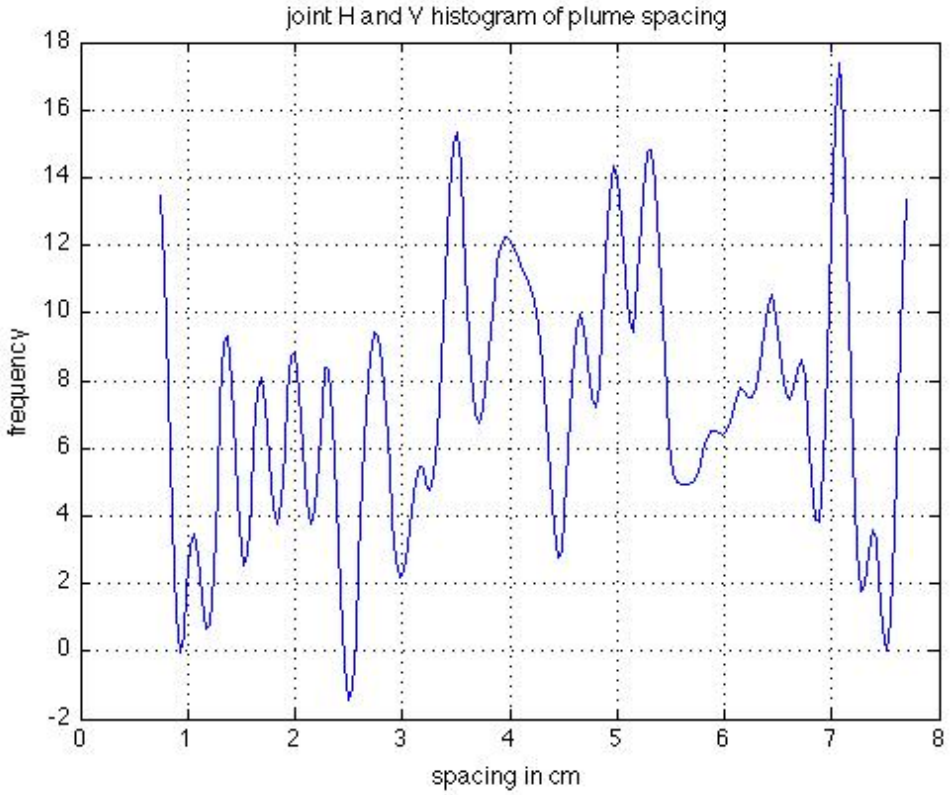
joint H and V histogram of plume spacing
frequency
spacing in cm
18
16
14
12
10
8
6
4
2
0
-2
0
1
2
3
4
5
6
7
8

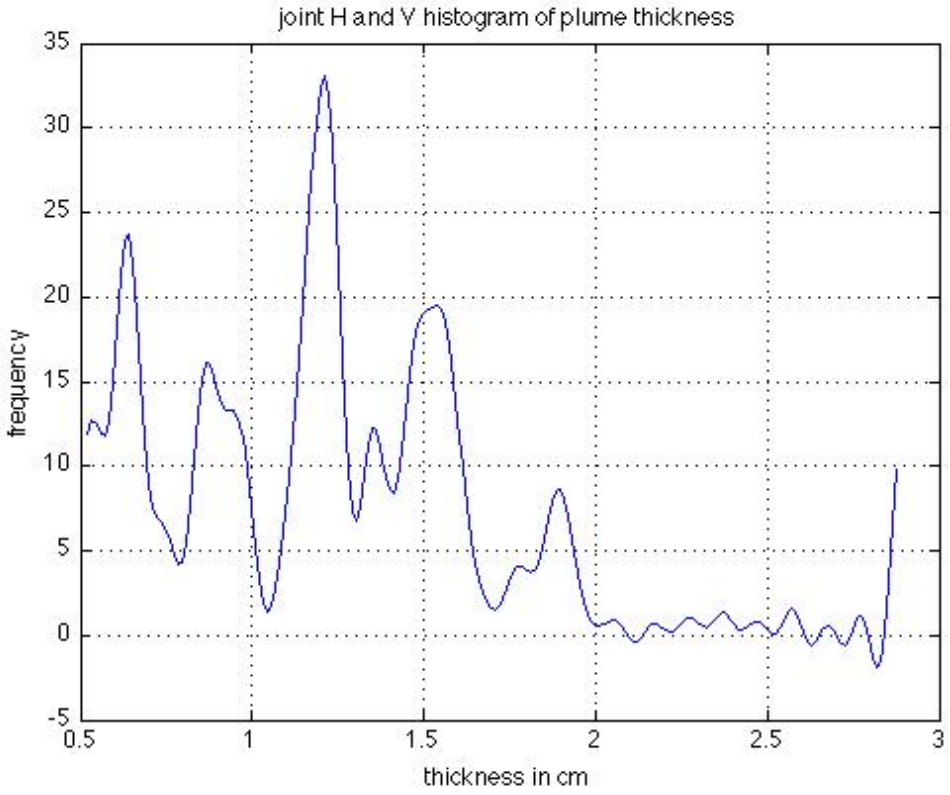
joint H and V histogram of plume thickness
frequency
thickness in cm
35
30
25
20
15
10
5
0
-5
0.5
1
1.5
2
2.5
3

MExpt2, U = 1/25

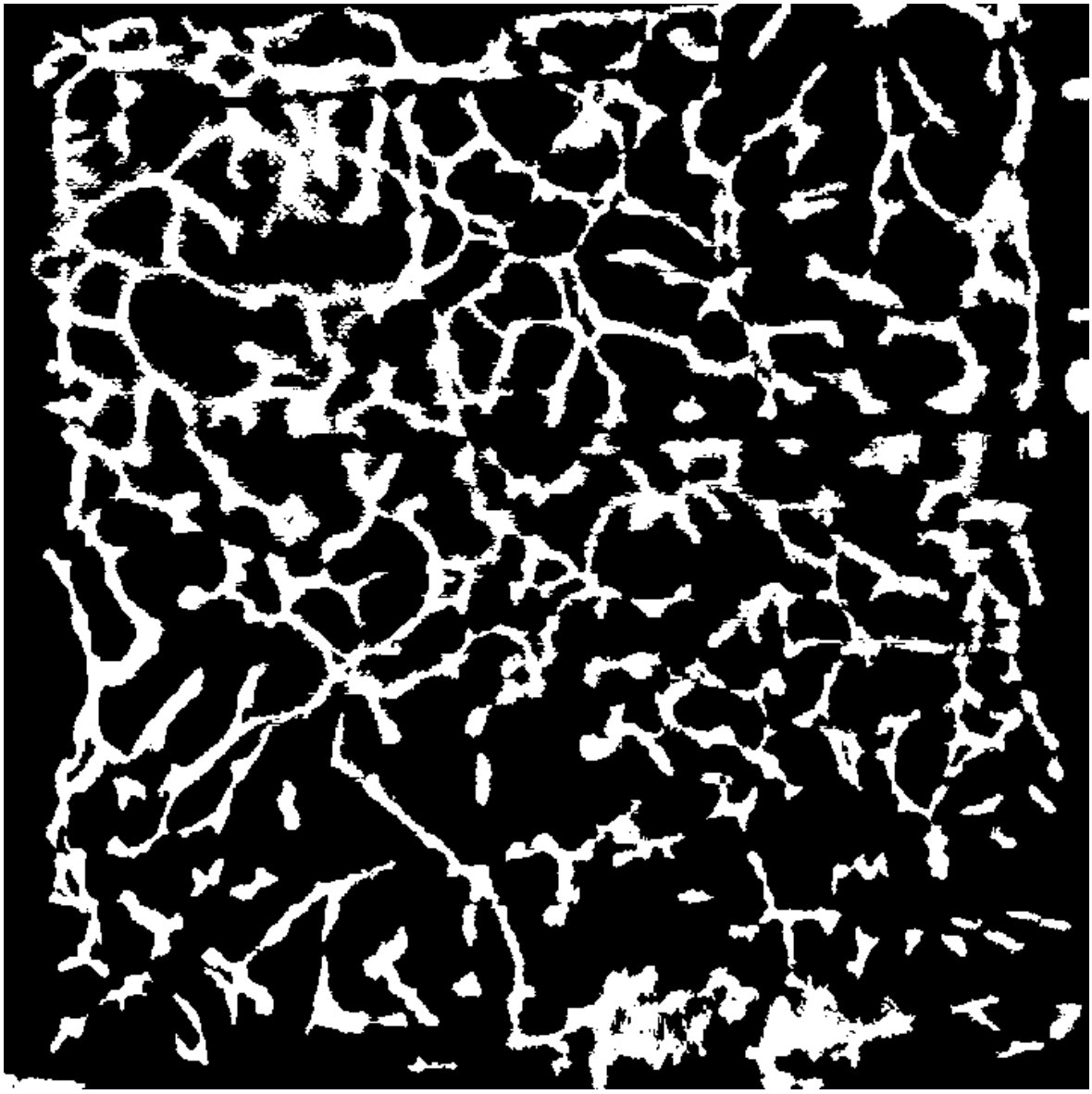

Spacing in cm (frequency of occurrence)

1.05(17)
0.73(14)
1.4(13)
3.55(12)
3(12)
2.1(11)

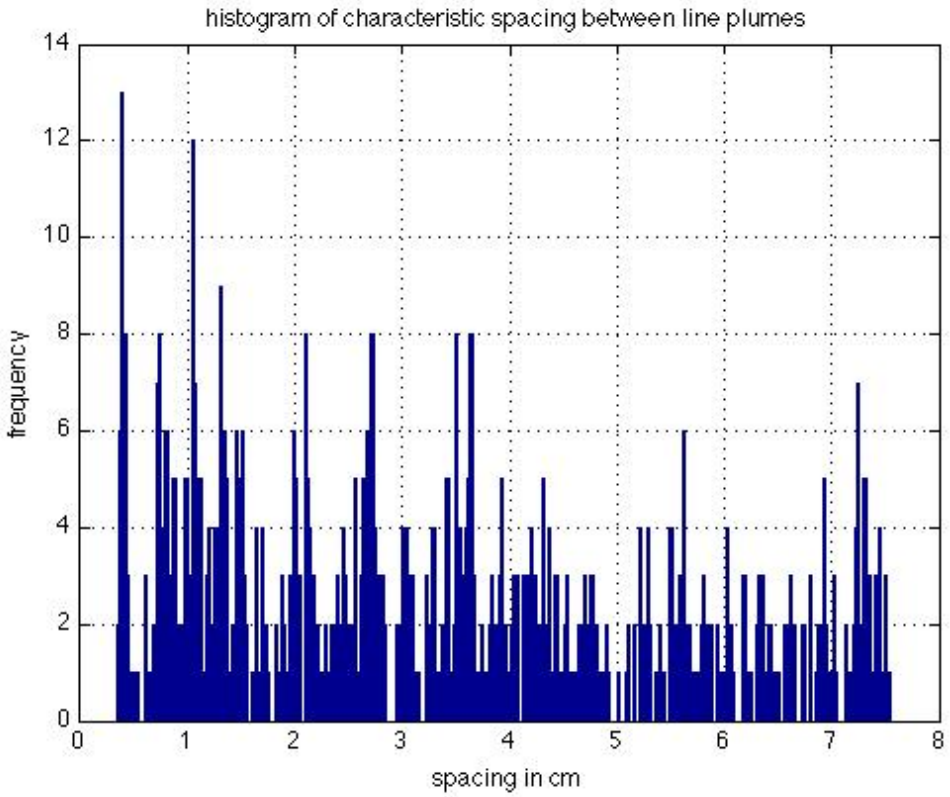
histogram of characteristic spacing between line plumes
frequency
spacing in cm
0
2
4
6
8
10
12
14
0
1
2
3
4
5
6
7
8

(H)

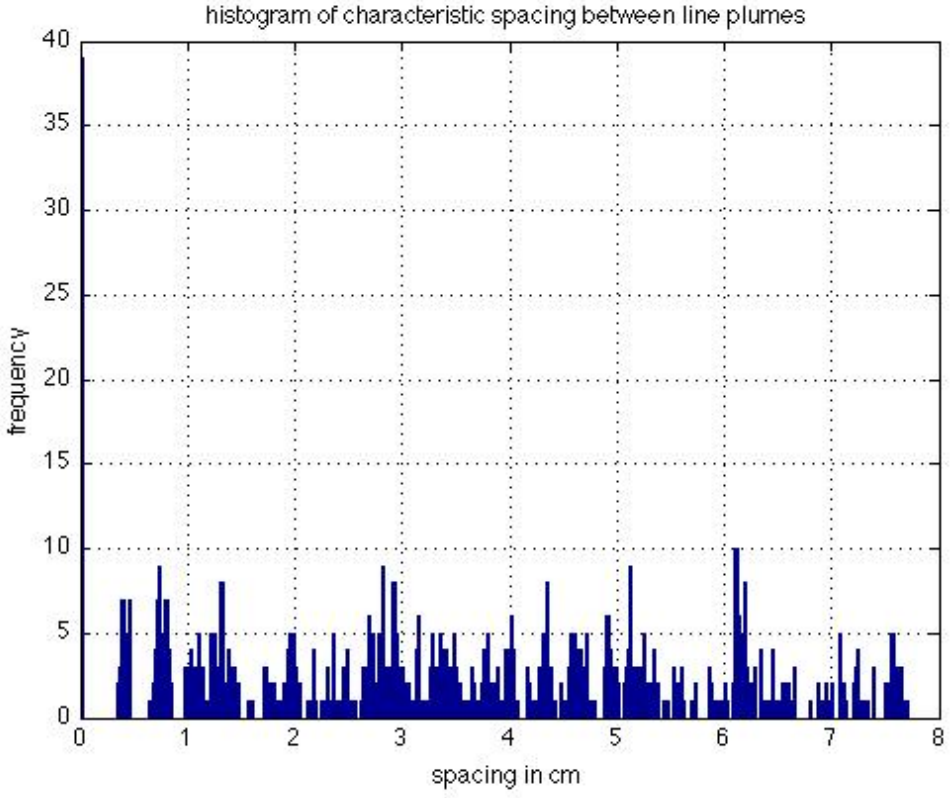
histogram of characteristic spacing between line plumes
frequency
spacing in cm
0
5
10
15
20
25
30
35
40
0
1
2
3
4
5
6
7
8

(V)

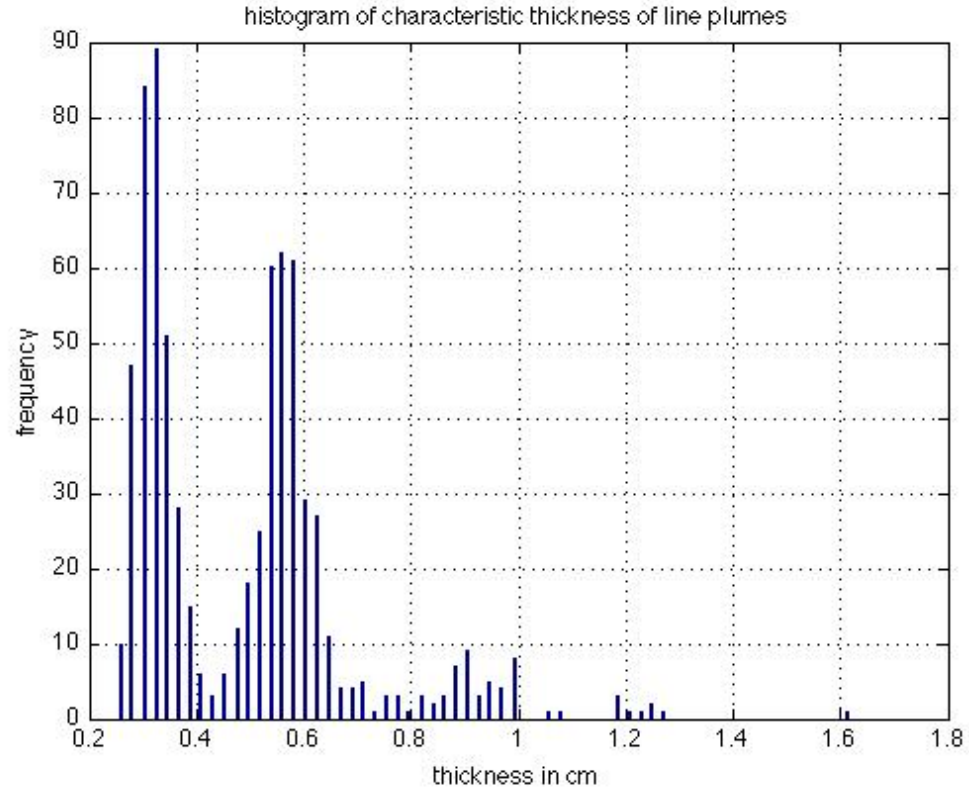
histogram of characteristic thickness of line plumes
frequency
thickness in cm
0
10
20
30
40
50
60
70
80
90
0.2
0.4
0.6
0.8
1
1.2
1.4
1.6
1.8

(H)

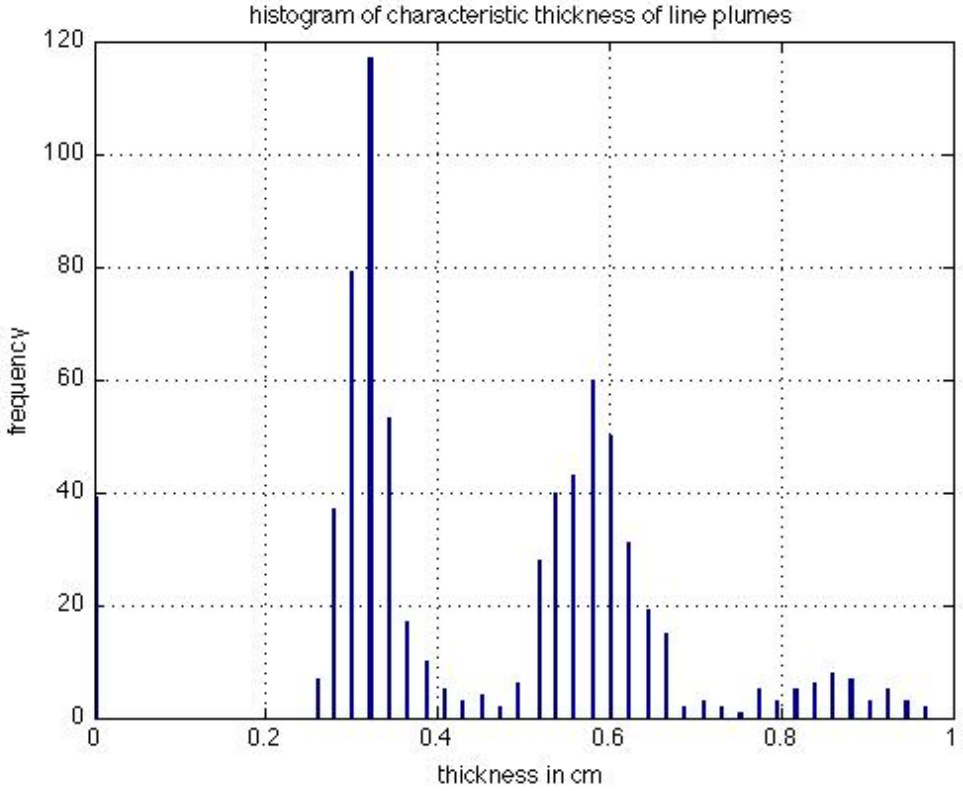
histogram of characteristic thickness of line plumes
frequency
thickness in cm
0
20
40
60
80
100
120
0
0.2
0.4
0.6
0.8
1

(V)

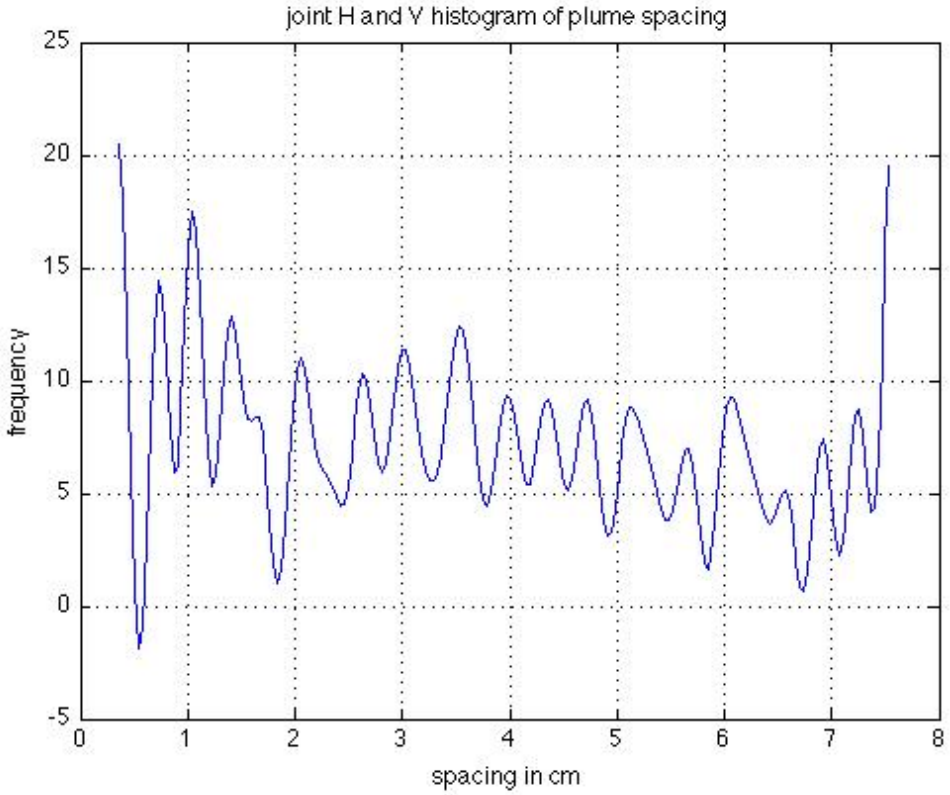
joint H and V histogram of plume spacing
frequency
spacing in cm
25
20
15
10
5
0
-5
0
1
2
3
4
5
6
7
8

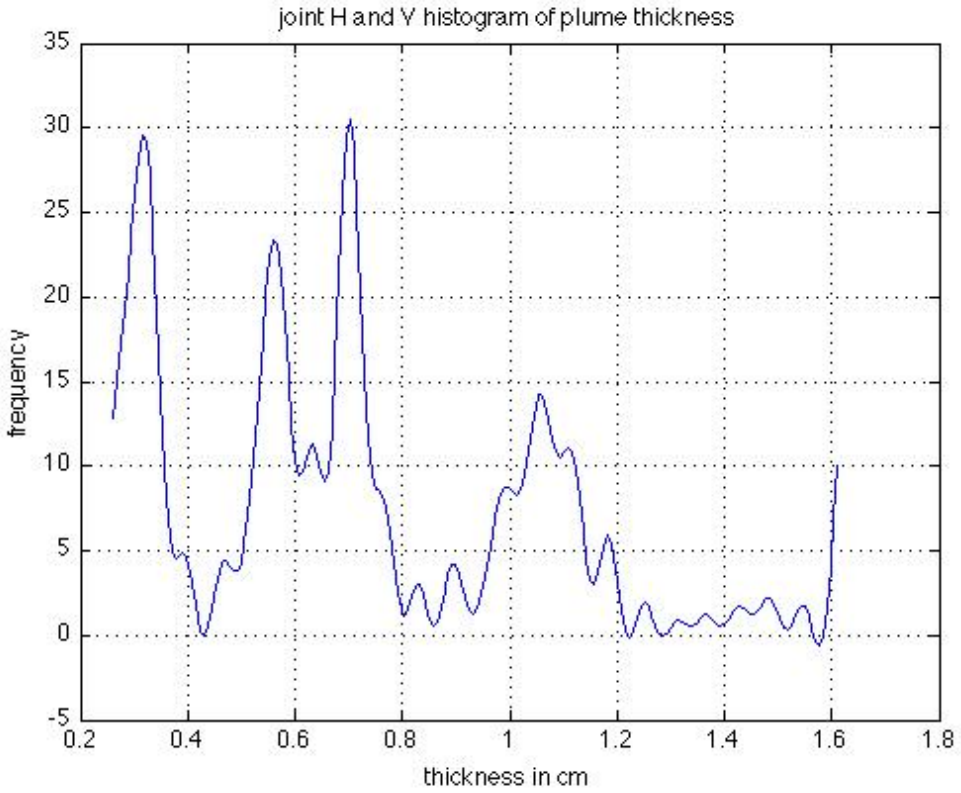
joint H and V histogram of plume thickness
frequency
thickness in cm
35
30
25
20
15
10
5
0
-5
0.2
0.4
0.6
0.8
1
1.2
1.4
1.6
1.8

Appendix – 2

Calculations

In this section, we show the details of the various calculations used in the thesis.

Calculations for Rayleigh Number:

The Rayleigh number defined in terms of density difference is defined as the compositional Rayleigh number Ra_c:

$$Ra_c = \frac{g\left(\frac{\Delta\rho}{\rho}\right)L^3}{\gamma_a \alpha}, \quad \text{where } \gamma_a \text{ is the kinematic viscosity of the ambient fluid}$$

Now, g= $9.81 ms^{-2}$, $\Delta\rho = 4 kgm^{-3}$ (constant for the experiments considered), $\rho = 989\ kgm^{-3}$ (standard for water), $L = 15.5cm$ (Fluid layer height in upper chamber, initial value), $\alpha = 5 \times 10^{-10} m^2 s^{-1}$ (Mass diffusivity of sugar in water).

(for simplicity, Ra_c will be referred to as Ra hereafter)

The Rayleigh number based on ambient fluid viscosity is:

$$Ra = \frac{9.81 \times \frac{4}{989} \times (15.5 \times 10^{-2})^3}{\gamma_a \times 5 \times 10^{-10}} = \frac{295500}{\gamma_a}$$

The viscosity may be expressed in terms of the viscosity ratio:

$$\gamma_a = \frac{\mu_a}{\rho} = \frac{U \times 1 \times 10^{-3} Pas}{(989 + 4) kgm^{-3}} = U \times 1.007 \times 10^{-6} m^2 s^{-1}$$

(assuming standard value for water, $\mu = 1\ mPas$)

The viscosity ratio is defined as:

$$U = Viscosity\ ratio = \frac{Viscosity\ of\ upper\ chamber\ fluid}{Viscosity\ of\ lower\ chamber\ fluid}$$

Or, equivalently, $U = \frac{Viscosity\ of\ ambient\ fluid}{Viscosity\ of\ plume\ fluid}$

We now proceed to calculate the Rayleigh numbers for the various experiments:

Experiment 1: $U = 1, Ra = \frac{295500}{1.007 \times 10^{-6}} = 2.934 \times 10^{11}$

For remaining experiments, till Experiment 12, i.e. $U = 2500$,

$$Ra = \frac{295500}{U(1.007 \times 10^{-6})} = \frac{2.934 \times 10^{11}}{U}$$

(These are the Ra calculations shown in Table 4)

Plume Spacing Calculations

We consider the relevant expressions for plume spacing that are available in the literature (Theerthan and Arakeri, 1998, Puthenveettil & Arakeri, 2005, Kerr, 1994).

Theerthan: Plume spacing λ_c, normalized by the characteristic length D is given by:

$\frac{\lambda_c}{D} = 67Ra^{-1/3}$ [Theerthan & Arakeri, 1998]

$\frac{\lambda_c}{D} = 67\left[\frac{g\left(\frac{\Delta\rho}{\rho}\right)D^3}{\gamma\alpha}\right]^{-1/3} \Rightarrow \lambda_c = 67{\gamma_a}^{1/3}\left[\frac{5\times10^{-10}}{9.81\times\frac{4}{989}}\right]^{1/3} = 0.155{\gamma_a}^{1/3}$ where γ_a is the ambient viscosity (all other parameters are constant)

Plume spacing in Table 4 have been calculated using this expression for different values of γ_a for experiments where $U > 1$.

Eg: for $U = 1$, $\lambda_c = 0.155(1.007 \times 10^{-6} \times 1)^{1/3} = 0.155cm$

for $U = 2500$, $\lambda_c = 0.155(1.007 \times 10^{-6} \times 2500)^{1/3} = 2.1cm$

Puthenveettil: Theoretical prediction for plume spacing in the diffusion regime (at $Sc{\sim}600$) is:

${Ra_\lambda}^{1/3} = \frac{\bar{\lambda}}{z_w} \cong 92$ [Puthenveettil & Arakeri, 2005]

Where, z_w - near wall length scale in turbulent convection (defined by Theerthan)

$z_w = \left[\frac{\gamma\alpha}{g\beta\Delta c_w}\right]^{1/3} = \left[\frac{\gamma\alpha}{g\left(\frac{\Delta\rho}{\rho}\right)}\right]^{1/3}$ where α - Mass Diffusivity, $\gamma = \gamma_a$- ambient viscosity

$$\therefore z_w = \left[\frac{\gamma_a\alpha}{g\left(\frac{\Delta\rho}{\rho}\right)}\right]^{1/3} = {\gamma_a}^{1/3}\left(\frac{5\times10^{-10}}{9.81\times\frac{4}{989}}\right)^{1/3} = {\gamma_a}^{\frac{1}{3}}(2.32\times10^{-3})$$

$\therefore \bar{\lambda} = 92\left({\gamma_a}^{\frac{1}{3}} \times 2.32 \times 10^{-3}\right) = 0.213 \times {\gamma_a}^{\frac{1}{3}}$ (all other parameters are constant)

(This expression is used to calculate spacings in the Table 4)

Eg: for $U = 1$, $\lambda_c = 0.213(1.007 \times 10^{-6} \times 1)^{1/3} = 0.213cm$

for $U = 2500$, $\lambda_c = 0.213(1.007 \times 10^{-6} \times 2500)^{1/3} = 2.89cm$

Puthenveettil: (Advection Case) Plume Spacing prediction is:

$Ra_\lambda{}^{1/3} = \frac{\bar{\lambda}}{z_w} = 2k^{2/3}Ra^{1/6}\sqrt{\frac{z_v}{H}}Sc^{1/6}$ [Puthenveettil & Arakeri, 2008]

Where $z_v = \frac{\gamma}{V_i}$ is the length scale due to advection and V_i is the through flow velocity.

$$Q = AV_i \Rightarrow 4mls^{-1} = (15.5 \times 15.5)cm^2 \times 0.2 \times V_i$$

$\therefore V_i = 0.083cms^{-1}$ (in our experiments)

$$\therefore z_v = \frac{\gamma_a}{V_i} = 1205\gamma_a$$

H=15.5cm, k=0.325 (constant assumed to fit data in Puthenveettil & Arakeri, 2008)

Hence $\bar{\lambda} = 56.27\gamma_a{}^{5/6}$ [other parameters are constant]

(These spacings are shown in the Table 4 and this case is not plotted)

Eg: for $U = 1$, $\bar{\lambda} = 0.05cm$

for $U = 2500$, $\bar{\lambda} = 38.4cm$

Kerr: Kerr has developed relations for experiments on melting driven by compositional convection. The timescale 'τ' and wavelength 'λ' for exponential growth of fastest growing linear R-T instabilities to the buoyant melt layer are:

$\tau = (P)\frac{\mu_m}{gh_m(\rho_f - \rho_m)}$ and $\lambda = (Q)\pi h_m$ [Kerr, 1994]

Where P and Q are functions of $\left(\frac{\mu_f}{\mu_m}\right)$ given by: [$\frac{\mu_f}{\mu_m} \approx U$ in our experiments]

$$P\left(\frac{\mu_f}{\mu_m}\right) = \begin{cases} 10.2988\ for\ U = 1 \\ 6.222\ for\ U \ll 1 \\ (324)^{1/3}(U)^{2/3} for\ U \gg 1 \end{cases}$$

$$Q\left(\frac{\mu_f}{\mu_m}\right) = \begin{cases} 1.1822\ for\ U = 1 \\ 0.94\ for\ U \ll 1 \\ (2/3)^{1/3}(U)^{1/3} for\ U \gg 1 \end{cases}$$

The thickness of the melt layer h_m is given by:

$$h_m = \left(\frac{PV_i\mu_m}{g(\rho_f - \rho_m)}\right)^{1/2}$$

h_m can probably be considered as the boundary layer thickness in our experiments.

Example calculations for h_m: (We need to be careful about P & Q)

Experiment 1: $U = 1,\ h_m = \left(\frac{10.2988\times0.083\times10^{-2}\times1\times10^{-3}}{9.81\times4}\right)^{1/2} = 0.046cm$

Experiment 2: $U = 2500$, $h_m = \left(\frac{(324)^{\frac{1}{3}}(2500)^{2/3}\times0.083\times10^{-2}\times1\times10^{-3}}{9.81\times4}\right)^{1/2} = 0.51cm$

h_m values for $U < 1$ have been tabulated.

To calculate plume spacing values from Kerr's work, we have used 3 different expressions:

$\boldsymbol{\lambda_1}$ (in the Table 4)

$\lambda = (Q)\pi h_m$ as given Kerr (1994). Q is selected carefully, depending on U

Eg: $U = 2500$, $\lambda = \left(\frac{2}{3}\right)^{1/3} \times (2500)^{1/3} \times \pi \times 0.51 \times 10^{-2} = 18.9cm$

$\boldsymbol{\lambda_2}$ (in the Table 4)
$\lambda = \pi h_m$ (this is mentioned in Jellinek et al (1999))

Eg: $U = 2500$, $\lambda = \pi \times 0.51 \times 10^{-2} = 1.6\ cm$

$\boldsymbol{\lambda_3}$ (in the Table 4)
$\lambda = h_m(U)^{1/3}$

(Whitehead & Luther, (1975), and mentioned in Jellinek et al, (1999))

Eg:$U = 2500$, $\lambda = (2500)^{1/3} \times 0.51 \times 10^{-2} = 6.92\ cm$

(λ_3 spacing values have been plotted as Kerr's scaling in the plot)

In the Table 4, in the last column, we list the plume spacing values obtained from using the weighted average definition.

Appendix – 3

Data from Traverse Experiments

In this Appendix, we provide additonal data from the Traverse Experiments (TExpt1 to TExpt7). Here, we show additional plots of fractional area v/s height of traverse and also montage sets of the images used for analysis of area fraction and mixing. Figure 47 (a) to (f) shows plots of fractional area v/s height of traverse above the mesh for TExpt2 to TExpt7. Note that the plot of fractional area v/s height of traverse above the mesh for TExpt1 has been shown in Figure 37.

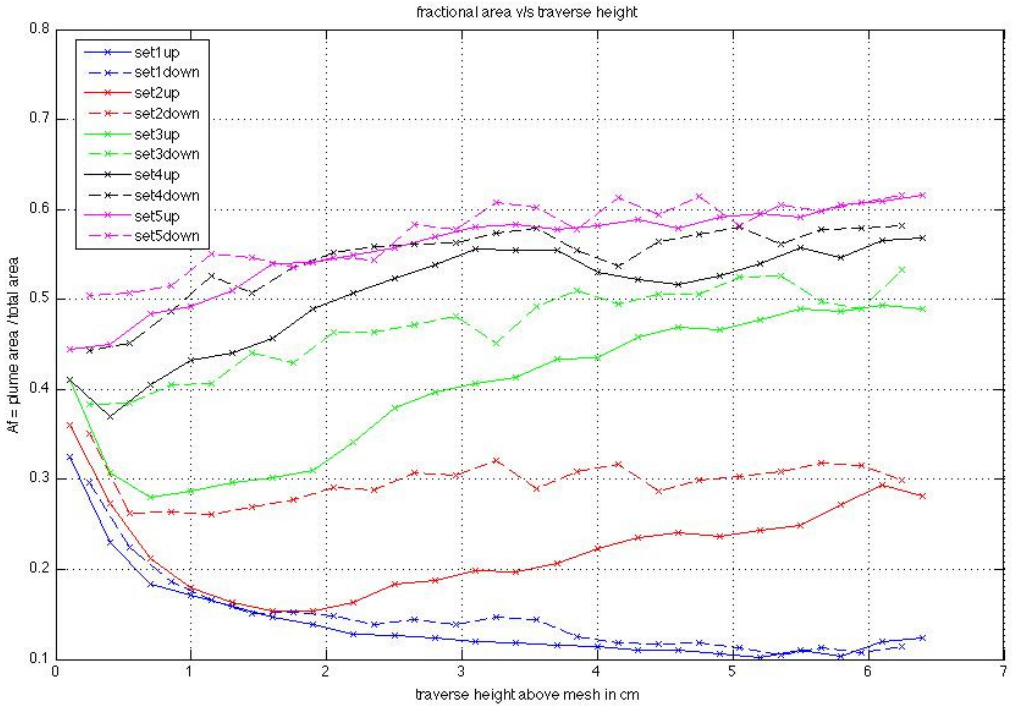

Figure 47: (a) Fractional area v/s traverse height, TExpt2, U = 65

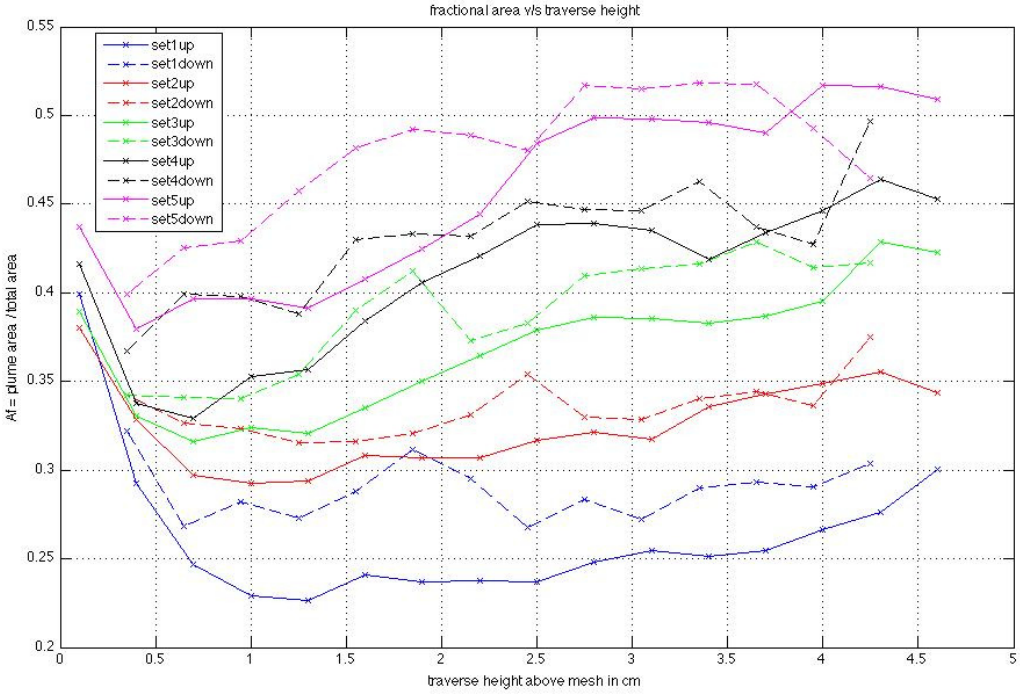

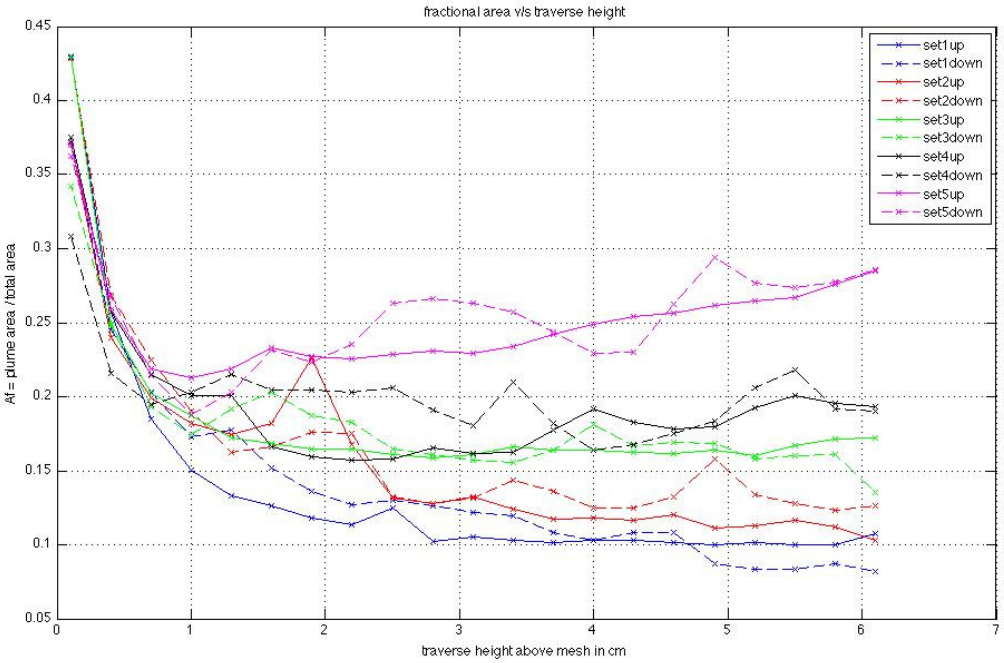

Figure 47: (c) Fractional area v/s traverse height, TExpt4, U = 930

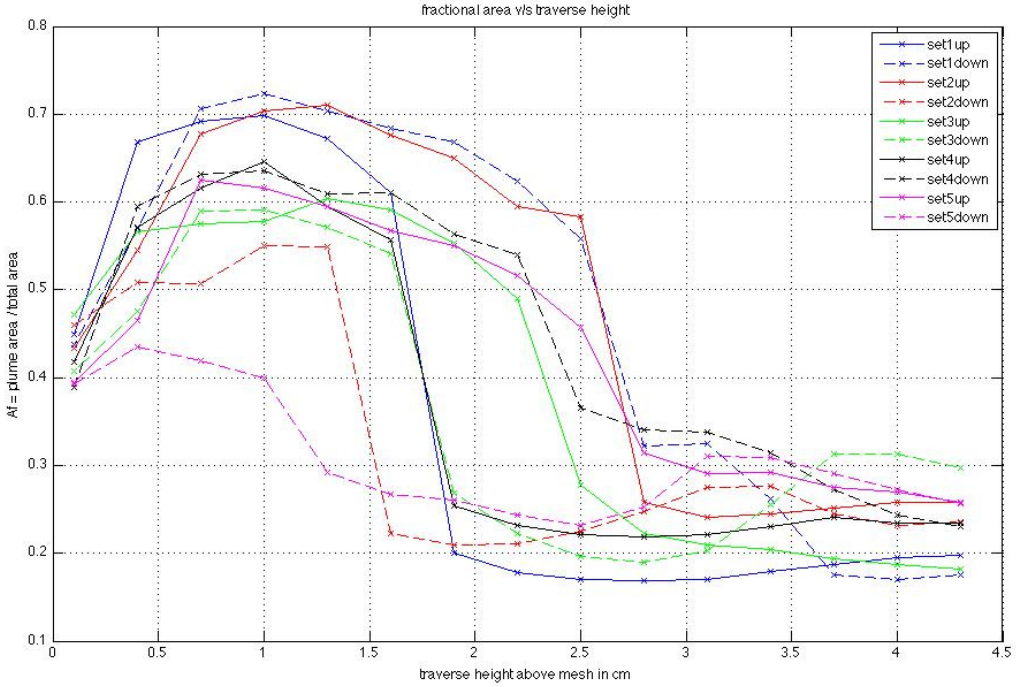

Figure 47: (d) Fractional area v/s traverse height, TExpt5, U = 2500

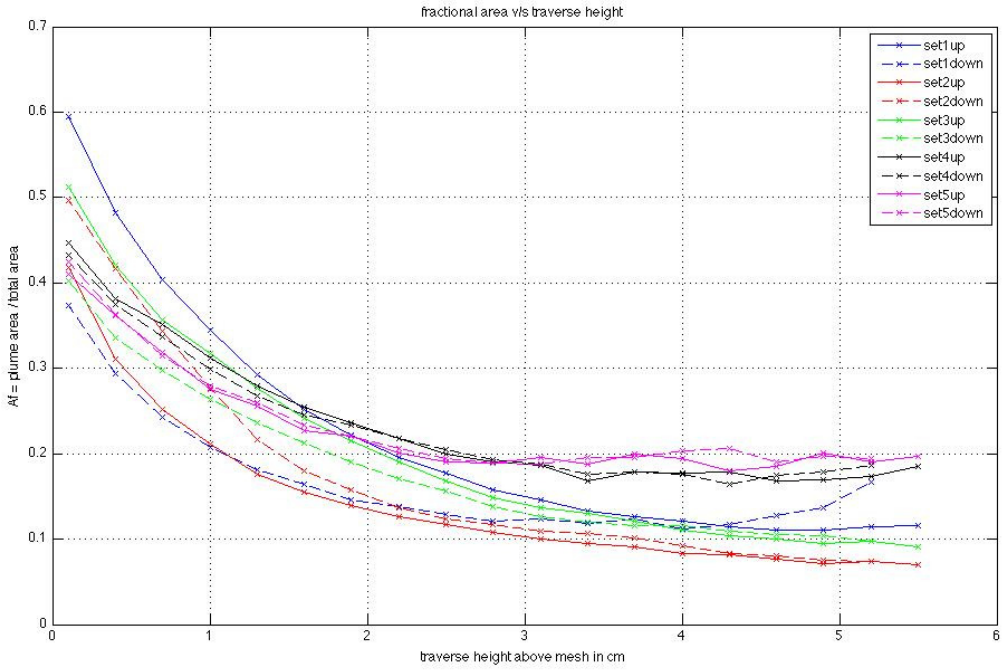

Figure 47: (e) Fractional area v/s traverse height, TExpt6, U = 1/300

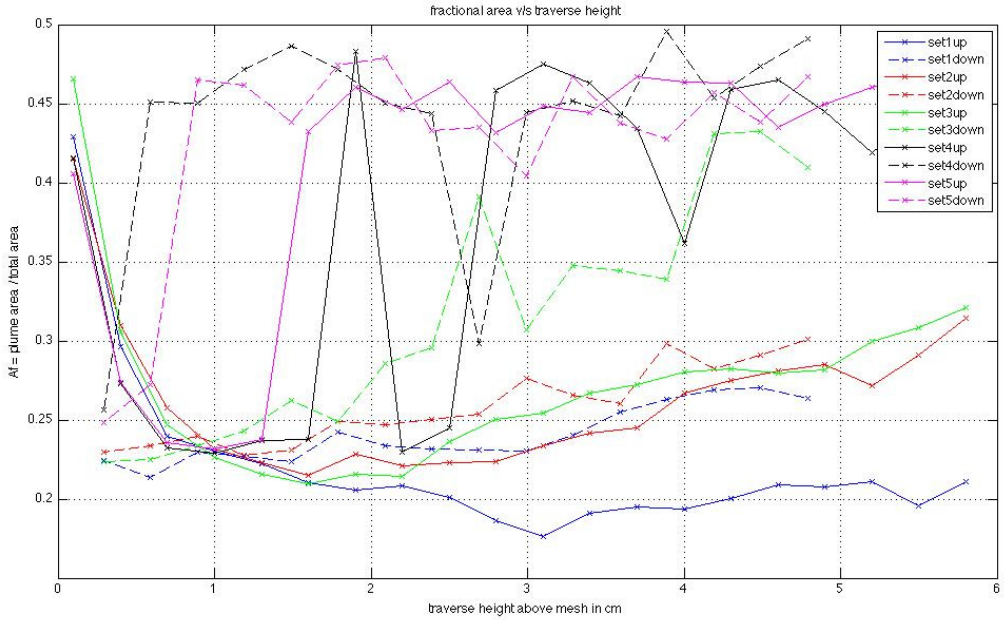

Figure 47: (f) Fractional area v/s traverse height, TExpt7, U = 1/65

The figures that follow are montage sets of images from the Traverse Experiments (TExpt1 to TExpt7). The sequence of images shown is spaced 1 second apart in time, and corresponds to a change in 3 mm height of traverse. The images start with the near-wall planform structure and the next images in sequence are for the laser sheet moving up. The images are shown at a difference of 3 mm height. Black markers are visible in the centre of the montage sets, these indicate that the maximum height has been reached and now onwards all the images are those which correspond to the laser sheet moving downwards. Figures 48 (a) to (g) show montage sets of raw images from the Traverse experiments for the third traverse cycle (set 3).

TExpt1

U = 1

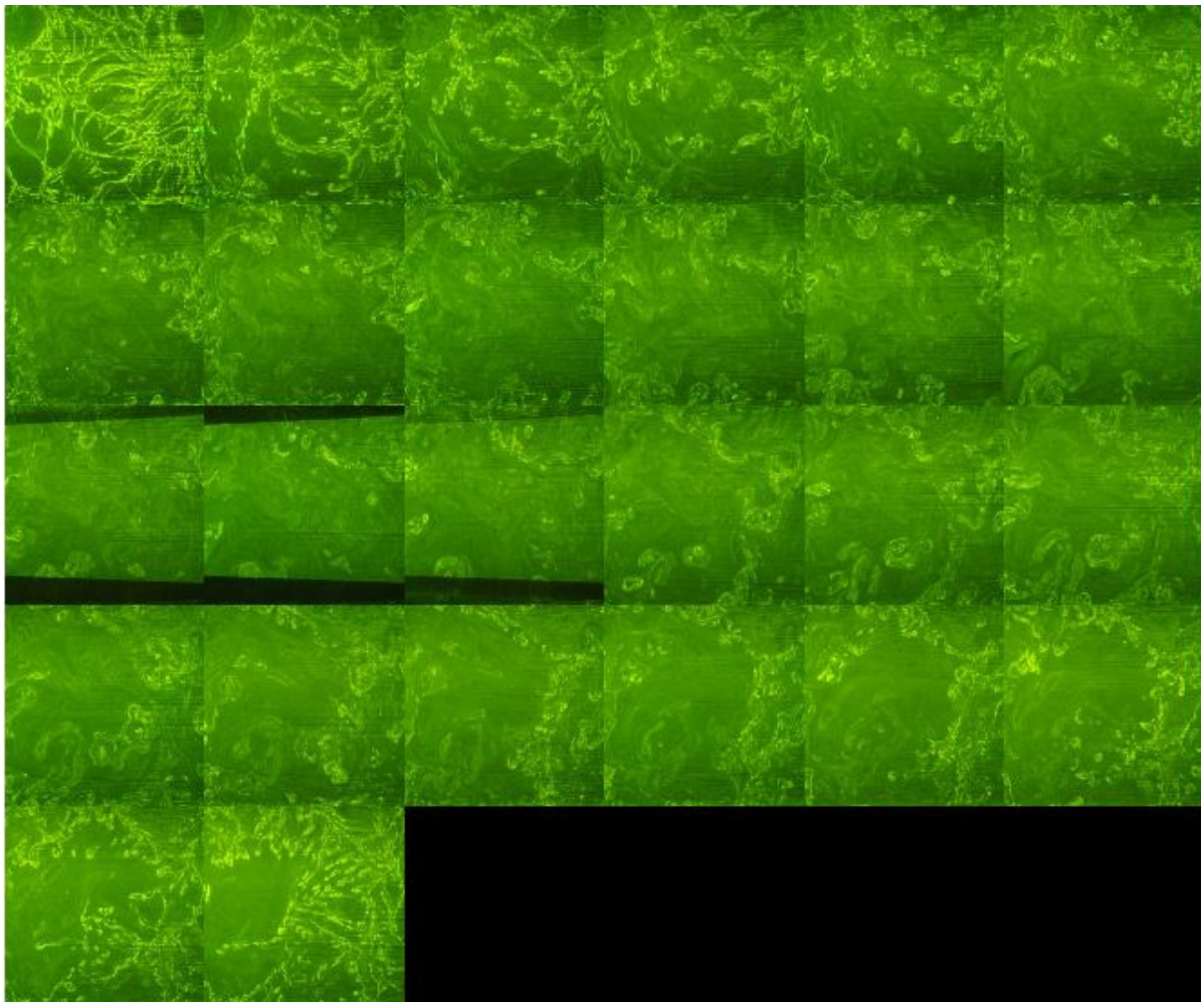

Figure 48: (a) Montage set of raw images for TExpt1, U =1

TExpt2

U = 65

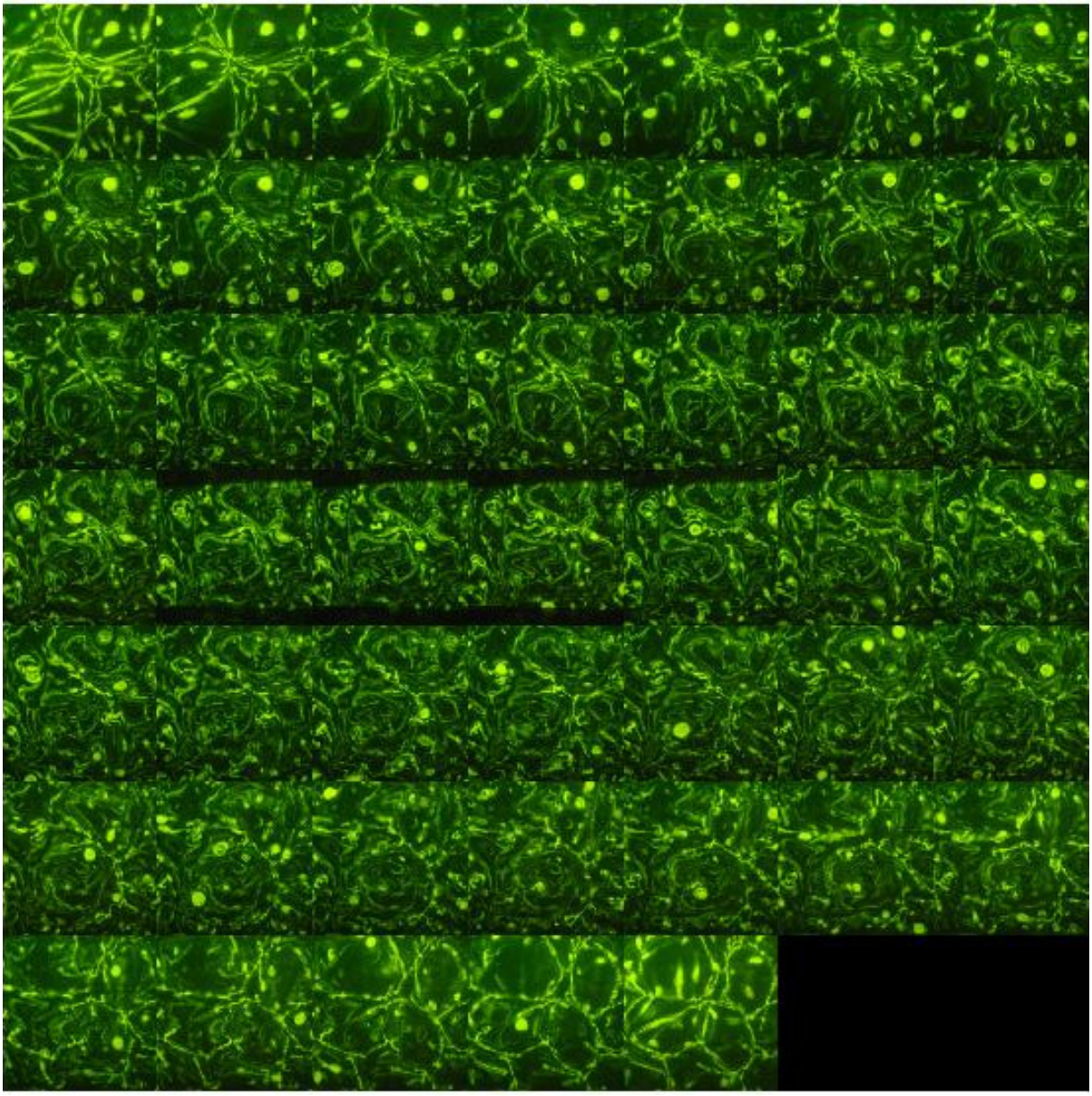

Figure 48: (b) Montage set of raw images for TExpt2, U = 65

TExpt3

U = 300

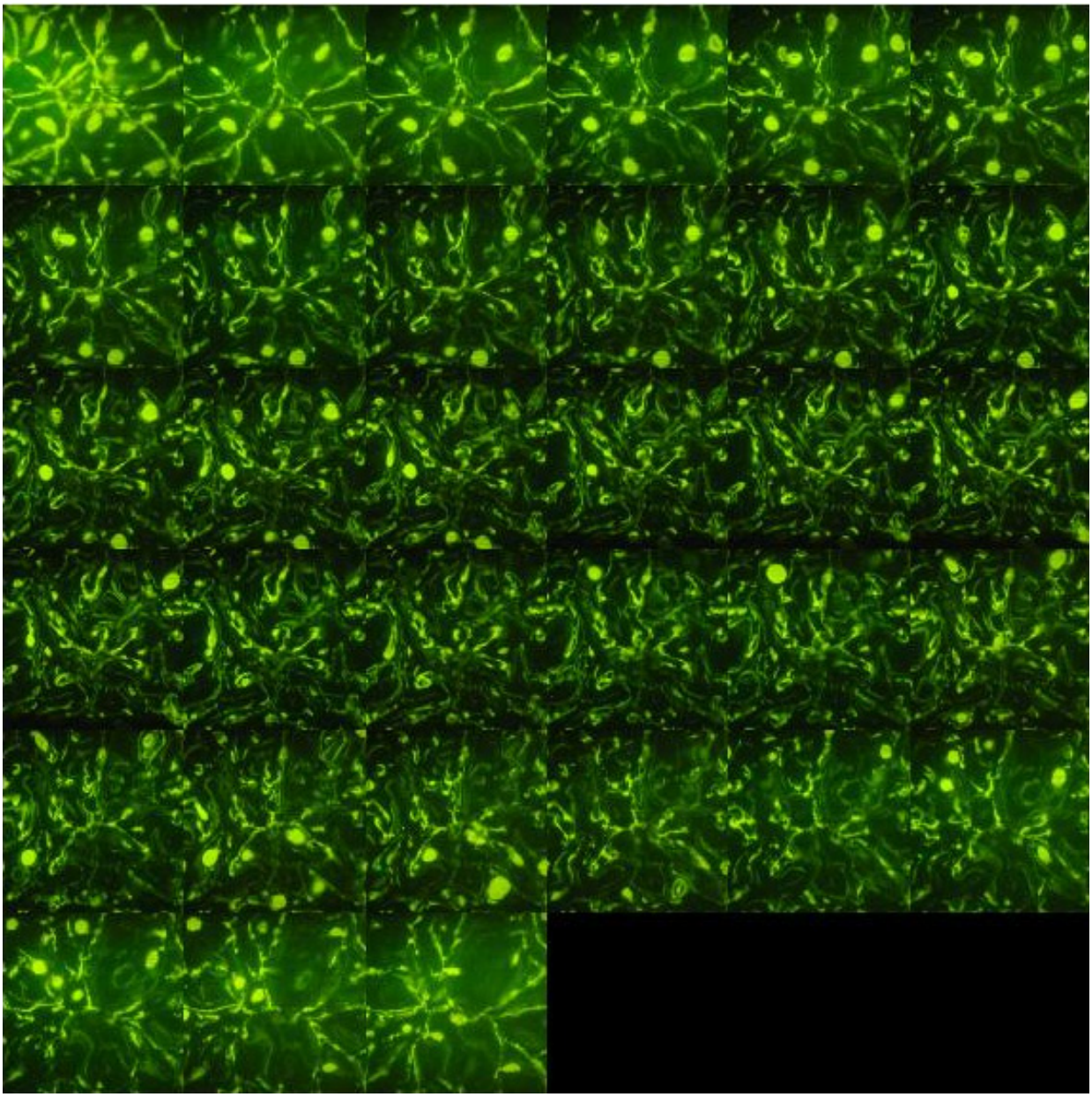

Figure 48: (c) Montage set of raw images for TExpt3, U = 300

TExpt4

U = 930

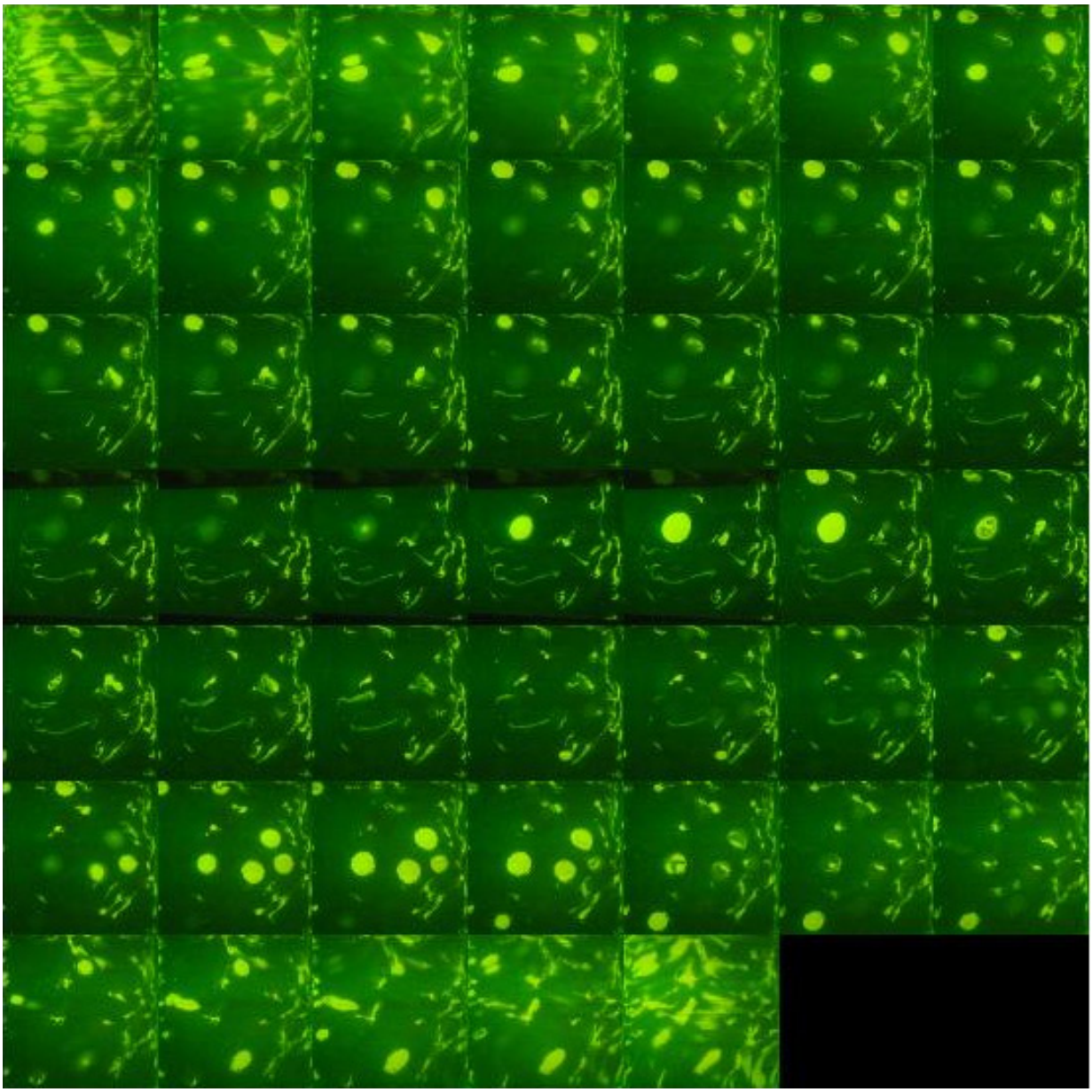

Figure 48: (d) Montage set of raw images for TExpt4, U = 930

TExpt5

U = 2500

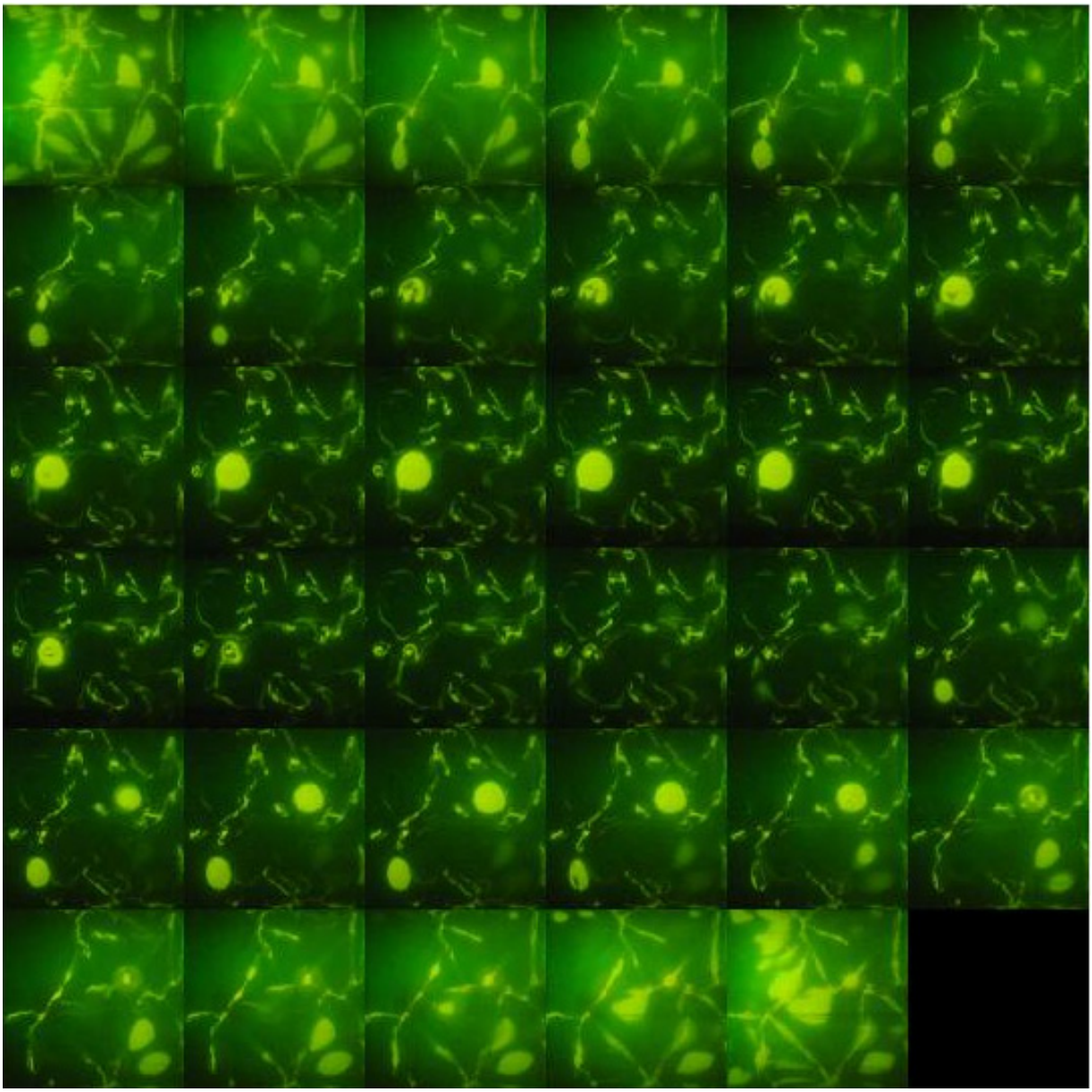

Figure 48: (e) Montage set of raw images for TExpt5, U = 2500

TExpt6

U = 1/300

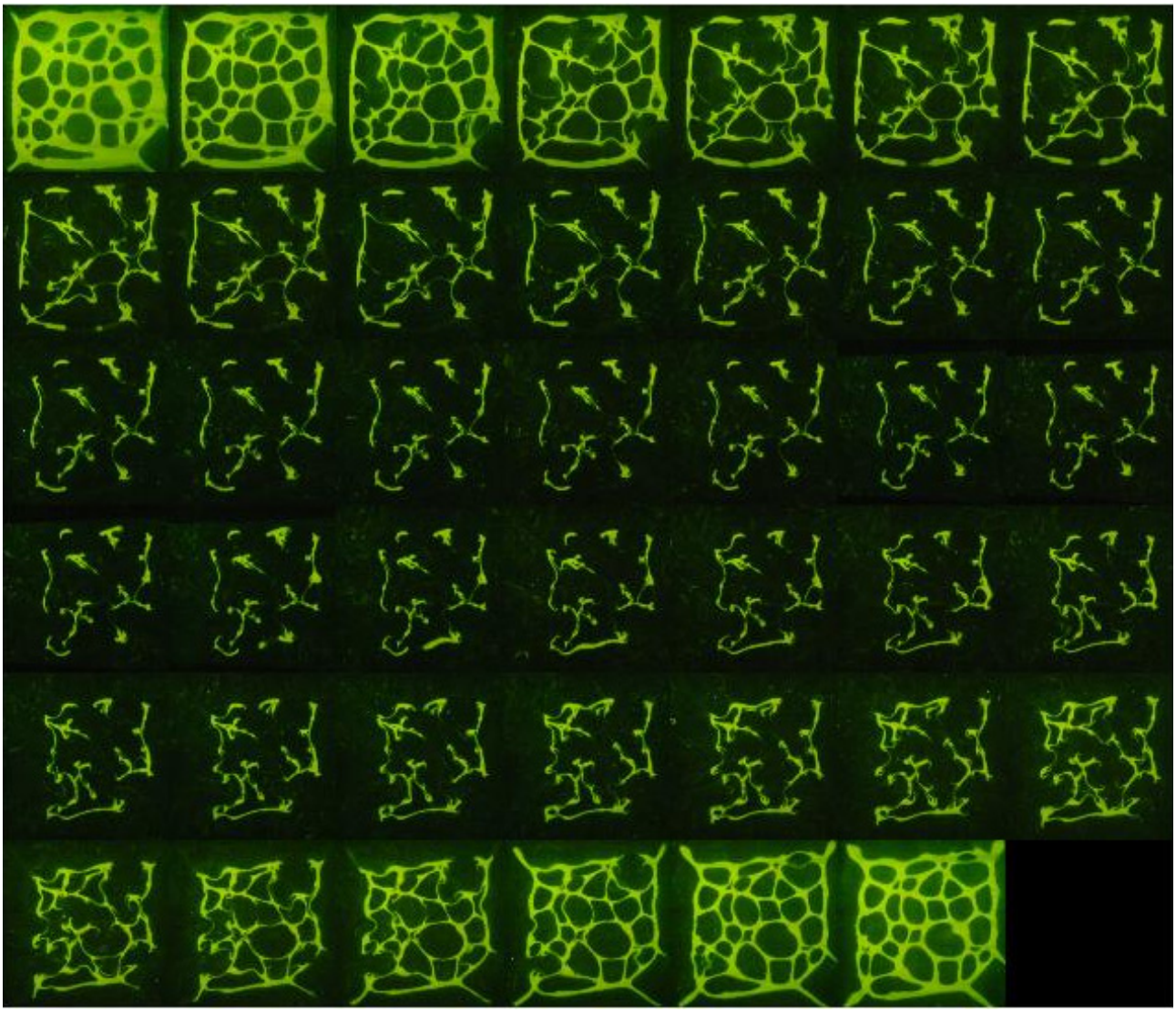

Figure 48: (f) Montage set of raw images for TExpt6, U = 1/300

TExpt7

U = 1/65

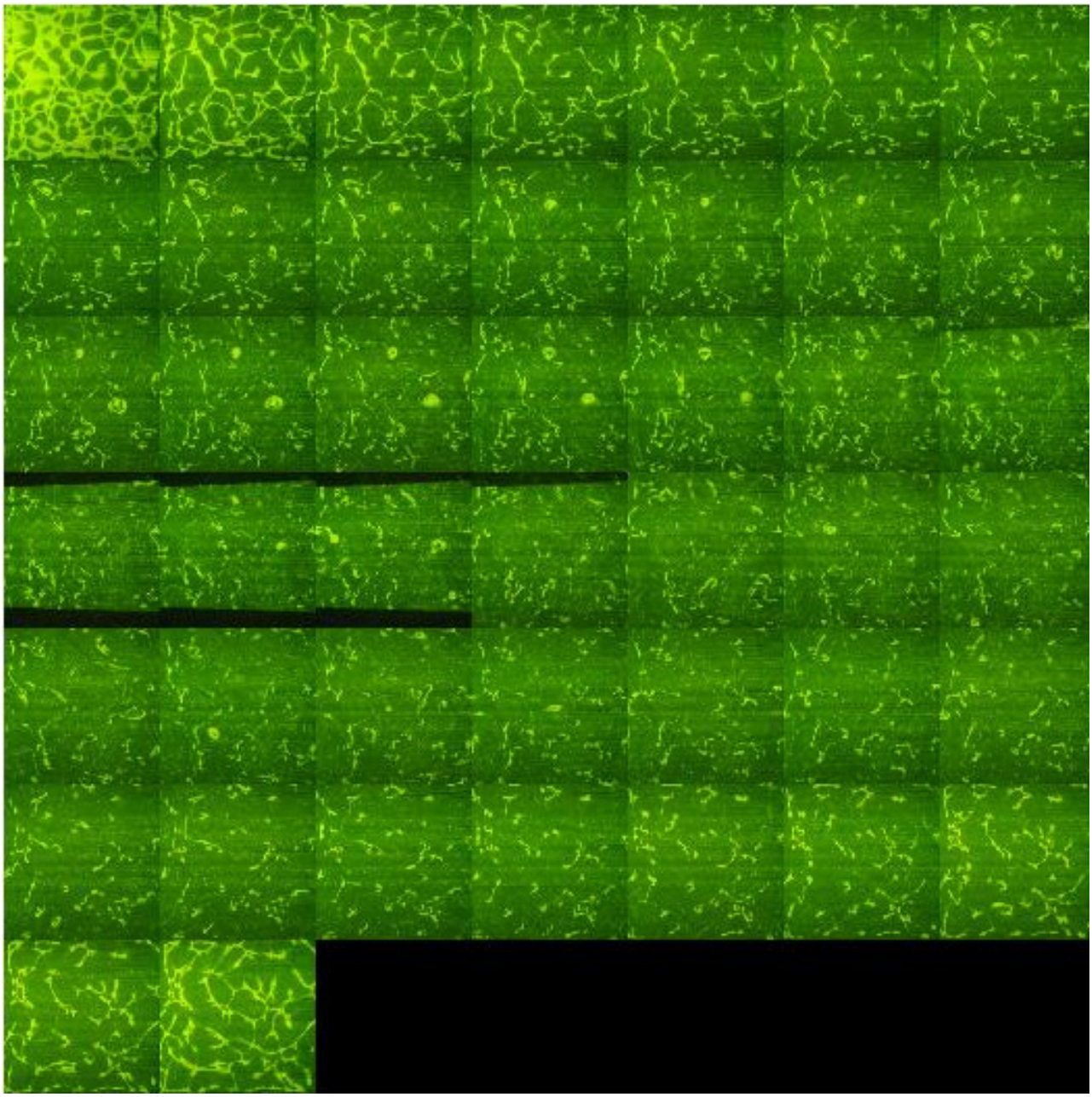

Figure 48: (g) Montage set of raw images for TExpt7, U = 1/65

References

Ahlers, G., Grossmann, S., & Lohse. D. Heat transfer and large scale dynamics in turbulent Rayleigh-Bénard convection. Rev. of Mod. Phys. 81, 503-538 (2009)

Aqualon Sodium Carboxymethylcellulose, Physical and chemical properties, 1999. Booklet 250, Hercules Inc.

Bunge, H-P, Richards, M. A., Baumgardner, J. R. 1996 Effect of depth-dependent viscosity on the planform of mantle convection. Nature. 379, 436-438.

Busse, F. H., & Whitehead, J. A. 1971Instabilities of convection rolls in a high Prandtl number fluid, J. Fluid Mech., 47, 305-320.

Courtillot , V., Davaille, A., Besse, J., Stock, J. 2003 Three distinct types of hotspots in the Earth's mantle. Earth Planet. Sci. Lett, 205, 295-308

Davaille, A. 1999a Two-layer thermal convection in miscible viscous fluids. J. Fluid Mech. 379, 223–253

Davaille, A. 1999b Simultaneous generation of hotspots and superswells by convection in a heterogeneous planetary mantle. Nature 402,756–760

Davaille, A., Girard, F., Le Bars M 2002 How to anchor plumes in a convecting mantle? Earth Planet Sci Lett 203,62–634.

Davaille, A., Le Bars M, Carbonne C 2003 Thermal convection in a heterogeneous mantle, C R Acad Sci G´eosciences, 335, 141–156.

Davaille, A. & Vatteville, J. 2005 On the transient nature of mantle plumes. Geophys Res Lett. 32.

Davies, G. F., 1999 Dynamic Earth: Plates, Plumes and Mantle Convection, Cambridge University Press

Debopam Das, Sreenivas K.R., Jaywant H. Arakeri, Srinivasan J. 1993 On the bifurcation of laminar buoyant jets discharged horizontally. Proceedings of the third world conference on Experimental Heat Transfer, Fluid mechanics and Thermodynamics, 855-862, USA

Duncan, R. A. & Richards, M. A. 1991 Hotspots, mantle plumes, flood basalts, and true polar wander, Rev. Geophys. 29, 31-50.

Foulger, G. R., Natland, J. H. 2003 Is hotspot volcanism a consequence of plate tectonics? Science, 300, 921-922

Griffiths, R.W., 1986 Thermals in extremely viscous fluids, including the effects of temperature-dependant viscosity. J. Fluid Mech., 166, 115-138.

Griffiths, R.W. & Campbell, I.H., 1990 Stirring and structure in mantle starting plumes. Earth Planet. Sci. Lett., 99, 66-78.

Grossman, S. & Lohse, D. 2000 Scaling in thermal convection: a unifying theory. J. Fluid. Mech. 407, 27-56.

Heslot, F., Castaing B., Libchaber A. 1987 Transitions to turbulence in helium gas. Phys. Rev. A. 36, 12

Jellinek, A. M., Kerr, R. C., Griffiths, R. W. 1999a Mixing and compositional stratification produced by natural convection: 1. The experiments and their application to Earth's core and mantle, J. Geophys. Res., 104, 7183–7202

Jellinek, A. M., Kerr, R. C., Griffiths, R. W. 1999b Mixing and compositional stratification produced by natural convection: 2. Applications to the differentiation of basaltic and silicic magma chambers and komatiite lva flows, J. Geophys. Res., 104, 7203–7218

Jellinek, A. M., Manga, M. 2002 The influence of a chemical boundary layer on the fixity, spacing and lifetime of mantle plumes. Nature 41, 760–763

Jellinek, A. M., Lenardic, A., Manga, M. 2002 The influence of interior mantle temperature on the structure of plumes: Heads for Venus, tails for the Earth, Geophys. Res. Lett., 29.

Jellinek, A. M., & Manga, M 2004 Links between long-lived hot spots, mantle plumes, D", and plate tectonics, Rev. Geophys., 42, 1-35

Kadanoff, L. P. 2001 Turbulent heat flow: structures and scaling. Phys. Today 54, 34–39.

Kellogg, L. H. & King, S. D. 1997 The effect of temperature dependent viscosity on the structure of new plumes in the mantle: Results of a finite element model in a spherical, axisymmetric shell. Earth Planet. Sci. Lett. 148, 13-26.

Kelly, A. & Bercovici, D. 1997 The clustering of rising diapirs and plume heads. Geophys. Res. Lett., 24, 201–204.

Kenjeres, S. & Hanjalic, K.2002 Numerical Insight into flow structure in ultraturbulent thermal convection. Phys. Rev. E, 66.

Kerr, R. C., Melting driven by vigorous compositional convection. 1994 J. Fluid Mech. 280, 255-285

Krishnamurti, R. 1970 On the transition to turbulent convection. J. Fluid. Mech. 42, 295–320.

Kumagai, I., Kurita, K., 2000 On the fate of mantle plumes at density interfaces. Earth Planet. Sci. Lett. 179, 63-71

Kumagai, I. 2002 On the anatomy of mantle plumes: effect of the viscosity ratio on entrainment and stirring. Earth Planet. Sci. Lett. 198, 211-224.

Kumagai, I., Davaille, A., Kurita, K., 2007 On the fate of thermally buoyant mantle plumes at density interfaces. Earth Planet. Sci. Lett. 254, 180-193.

Lithgow-Bertelloni, C., Richards, M. A., Griffiths, R. W., Conrad, C. 2001 Plume generation in natural thermal convection at high Rayleigh and Prandtl numbers, J. Fluid Mech., 434, 1–21.

Manga, M. 1997 Interactions between mantle diapirs. Geophys. Res. Lett., 24, 1871–1874.

Manga, M., & Weeraratne, D. 1999 Experimental study of non-Boussinesq Rayleigh-Benard convection at high Rayleigh and Prandtl numbers, Phys. Fluids, 11, 2969–2976.

Manga, M., Weeraratne, D., Morris, S. J. S. 2001 Boundary layer thickness and instabilities in Benard convection of a liquid with a temperature-dependent viscosity, Phys. Fluids, 13, 802–805.

Morgan, W. J. 1971 Convection plumes in the lower mantle. Nature. 230, 42-43.

Niemela, J. J., Skrbek, L., Sreenivasan, K. R. & Donelly, R. J. 2000 Turbulent convection at very high Rayleigh numbers. Nature. 404, 837–840.

Olson, P., Singer, H., 1985 Creeping plumes. J. Fluid Mech., 158, 511-531.

Olson, P. & Christensen, U. 1986 Solitary wave propagation in a fluid conduit within a viscous matrix, J. Geophys. Res. 91, 6367-6374.

Puthenveettil, B. A. 2004 Investigations on high Rayleigh number turbulent free convection, PhD Thesis, IISc, Bangalore, India.

Puthenveettil, B. A. & Arakeri, J. H. 2005 Plume structure in high-Rayleigh-number convection. J. Fluid Mech. 542, 217–249.

Puthenveettil, B. A. & Arakeri, J. H. 2008 Convection due to an unstable density difference across a permeable membrane. J. Fluid Mech. 609, 139–170.

Ribe, N., A. Davaille, U. Christensen, 2007 Fluid dynamics of mantle plumes, Mantle Plumes–A Multidisciplinary Approach. Springer

Schaeffer, N., & Manga, M. 2001 Interactions between rising and sinking mantle plumes. Geophys. Res. Lett., 28, 455–458.

Scott, D. R., Stevenson, D. J., Whitehead, J. A. 1987 Observations of solitary waves in a viscously deformable pipe. Nature. 319.

Siggia, E. D. 1994 High Rayleigh number convection. Annu. Rev. Fluid Mech. 26, 137–168.

Sleep, N. H., 1990 Hotspots and Mantle Plumes: Some Phenomenology. J. Geophys. Res. 95, 6715-6736

Theerthan, S. A. & Arakeri, J. H. 1998 A model for near-wall dynamics in turbulent Rayleigh–Benard convection. J. Fluid Mech. 373, 221–254.

Theerthan, S. A. & Arakeri, J. H. 2000 Plan form structure and heat transfer in turbulent free convection over horizontal surfaces. Phys. Fluids 12, 884–894.

van Keken , P. 1997 Evolution of starting mantle plumes: a comparison between numerical and laboratory models. Earth Planet. Sci. Lett. 148, 1-11.

Whitehead, J.A., Luther, D.S., 1975 Dynamics of laboratory diapir and plume models, J. Geophys. Res., 80,705-717.

Whitehead J. A., 1988 Fluid models of geological hotspots, Ann. Rev. Fluid. Mech, 20, 61-87

White D. B., 1988 The planforms and onset of convection with a temperature-dependent viscosity. J. Fluid Mech., 191, 247-286

Xi, H-D, Lam, S., Xia, K-Q 2004 From laminar plumes to organized flows: the onset of large-scale circulation in turbulent thermal convection. J. Fluid Mech. 503,47–56

Young, Y.-N., Tufo, H., Dubey, A. & Rosner, R. 2001 On the miscible Rayleigh–Taylor instability: two- and three-dimensions. J. Fluid Mech. 447, 377–408.

Zhao, D. 2001. Seismic structure and origin of hotspots and mantle plumes. Earth Planet. Sci. Lett. 192, 251-265